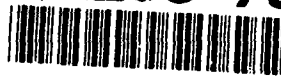AD-A268 790

WL-TR-93-1030

WIDEBAND ELECTROMAGNETIC
SCATTERING/ANALYSIS PROGRAM

FAR ZONE ELECTROMAGNETIC SCATTERING
FROM COMPLEX SHAPES USING
GEOMETRICAL THEORY OF DIFFRACTION

N. Akhter and R.J. Marhefka
THE OHIO STATE UNIVERSITY
ELECTROSCIENCE LABORATORY
1320 KINNEAR ROAD
COLUMBUS, OHIO 43212

December 1992

Interim Report for Period May 1991 to December 1992

DTIC
SELECTE
SEP 0 1 1993
B D

AVIONICS DIRECTORATE
WRIGHT LABORATORY
AIR FORCE MATERIEL COMMAND
WRIGHT-PATTERSON AIR FORCE BASE, OHIO 45433-7734

93 8 31 130

93-20421

NOTICE

When Government drawings, specifications, or other data are used for any purpose other than in connection with a definitely Government-related procurement, the United States Government incurs no responsibility or any obligation whatsoever. The fact that the government may have formulated or in any way supplied the said drawings, specifications, or other data, is not to be regarded by implication, or otherwise in any manner construed, as licensing the holder, or any other person or corporation; or as conveying any rights or permission to manufacture, use, or sell any patented invention that may in any way be related thereto.

This report is releasable to the National Technical Information Service (NTIS). At NTIS, it will be available to the general public, including foreign nations.

This technical report has been reviewed and is approved for publication.

RICHARD J. KOESEL
PROJECT ENGINEER

DENNNIS M. MUKAI, ACTG SEC CHIEF
TECHNOLOGY DEVELOPMENT SECTION

GALE D. URBAN
ACTG DIRECTOR
MISSION AVIONICS DIVISION
AVIONICS DIRECTORATE

If your address has changed, if you wish to be removed from our mailing list, or if the addressee is no longer employed by your organization please notify WL/AARM, WPAFB, OH 45433-7734 to help us maintain a current mailing list.

Copies of this report should not be returned unless return is required by security considerations, contractual obligations, or notice on a specific document.

REPORT DOCUMENTATION PAGE

Public reporting burden for this collection of information is estimated to average 1 hour per response, including the time for reviewing instructions, searching existing data sources, gathering and maintaining the data needed, and completing and reviewing the collection of information. Send comments regarding this burden estimate or any other aspect of this collection of information, including suggestions for reducing this burden to Washington Headquarters Services, Directorate for Information Operations and Reports, 1215 Jefferson Davis Highway, Suite 1204, Arlington, VA 22202-4302, and to the Office of Management and Budget, Paperwork Reduction Project (0704-0188), Washington, DC 20503

1. AGENCY USE ONLY (Leave blank)	2. REPORT DATE	3. REPORT TYPE AND DATES COVERED
	DEC 1992	INTERIM 05/01/91--12/31/92

4. TITLE AND SUBTITLE WIDEBAND ELECTOMAGNETIC SCATTERING/ANALYSIS PROGRAM Far Zone Electromagnetic Scattering from Complex Shapes Using Geometric Theory of Diffraction

6. AUTHOR(S) N. AKHTER AND R.J. MARHEFKA

5. FUNDING NUMBERS
C F33615-91-C-1729
PE 62204
PR 7622
TA 07
WU 71

7. PERFORMING ORGANIZATION NAME(S) AND ADDRESS(ES)

THE OHIO STATE UNIVERSITY
ELECTROSCIENCE LABORATORY
1320 KINNEAR ROAD
COLUMBUS OHIO 43212

8. PERFORMING ORGANIZATION REPORT NUMBER

724733-1

9. SPONSORING/MONITORING AGENCY NAME(S) AND ADDRESS(ES)

AVIONICS DIRECTORATE
WRIGHT LABORATORY
AIR FORCE MATERIEL COMMAND
WRIGHT PATTERSON AFB OH 45433-7409

10. SPONSORING/MONITORING AGENCY REPORT NUMBER
WL-TR-93-1030

11. SUPPLEMENTARY NOTES

12a. DISTRIBUTION/AVAILABILITY STATEMENT

Approved for public release; distribution is unlimited.

12b. DISTRIBUTION CODE

13. ABSTRACT (Maximum 200 words)

Backscatter and bistatic scattering in the far zone using the uniform theory of diffraction (UTD) from shapes which require second and higher order interactions to get an accurate solution over a wide range of angles is considered. One of the simplest of these shapes is the two-dimensional dihedral. The solution contains interactions of up to third order, which provide excellent results for the dihedrals of 60° or greater and for sizes larger than one wavelength in extent. The dihedral solution is modified for curvature and caustic corrections to get results for the top-hat, bruderhedral, and bi-cone. Another extension to the dihedral is the parallel plate cavity and the circular cavity. First and second order caustic corrections for the donut are included. Also, the result of the dihedral is modified to get results for the multi-joined cylinders made of PVC pipes filled with absorber. Analytical results are validated against method of moments or measurements.

14. SUBJECT TERMS UTD, SCATTERING, RADAR CROSS SECTION	**15. NUMBER OF PAGES** 196
	16. PRICE CODE

17. SECURITY CLASSIFICATION OF REPORT	18. SECURITY CLASSIFICATION OF THIS PAGE	19. SECURITY CLASSIFICATION OF ABSTRACT	20. LIMITATION OF ABSTRACT
UNCLASSIFIED	UNCLASSIFIED	UNCLASSIFIED	UL

DTIC QUALITY INSPECTED 1

Contents

Figures

viii

SECTION 1

Introduction

In recent years, electromagnetic scattering from complex structures has become an important field of research. Accurate and efficient solutions to scattering from complex structures can enhance the ability to understand how targets can be detected in the presence of clutter. Many approaches are available, but for high frequency scattering, the Uniform Theory of Diffraction (UTD) is one of the most efficient and accurate techniques. UTD can provide the characteristic scattering properties of local features of the target such as frequency response, polarization, and angular behavior.

It is well known that due to the highly local nature of high frequency scattering, the solution to complex structures can be modeled approximately as a superposition of scattered fields from simpler shapes such as plates, ellipsoids, cylinders, dihedrals, trihedrals, et cetera. These can be used to represent component parts of vehicles such as trucks, aircraft, etc., as well as natural objects such as tree trunks and branches.

The object of this research is to find far zone backscatter and bistatic scattered fields from some of the most common shapes which require second and higher order interactions to get an accurate result over a wide range of angles and frequencies. The basic shapes important to this discussion are the dihedral, bruderhedral, trihedral, top-hat, bi-cone, parallel plate cavity, cake pan (shallow circular cavity),

1

donut and multi-joined cylinders. All the shapes considered are assumed to be perfectly conducting except the multi-joined cylinders which may be made of dielectric materials. For these shapes, the most important higher order interactions will be determined. Where possible the expressions will be simplified to show the connection between the UTD results and the more classical PO approximations. It should be pointed out that many of the targets do not have easily found references to their scattering properties.

Some background information on UTD [1] is presented in Section 2. The double diffraction formulation presented here is derived in Reference [2]. In Section 3, the UTD analysis of a two-dimensional dihedral is discussed. Parallel ray formulation of the UTD is used here for the far zone problem. This means, in two dimensions, that only edge diffractions, their images, and various combinations of double diffractions are needed. This is a very efficient and accurate means of analyzing the far zone problem. It avoids any integrations and non physical "imposed" edged conditions. Basic dihedral mechanisms are studied, and it is shown how the various interactions ensure continuity of the total field. It is found that excellent comparisons with Method of Moments results are obtained using fields of up to third order interactions for dihedrals of 60° or greater. Also, it is observed that this solution is good for dihedrals that are as small as about one wavelength (maximum width of the dihedral). Higher order interactions are required to get results for less than 60° dihedrals or for smaller sizes. For the case of maximum scattering from a general angled dihedral, the UTD terms that are dominant in between the strips of the dihedral are reduced to simple forms.

UTD, being a ray technique, predicts infinite fields at caustics. It is therefore necessary to introduce caustic corrections to obtain a bounded field at the caustics. Caustic corrections of first, second and higher order are discussed in Section 4. In Section 5 and 6, the two-dimensional dihedral solution, modified by the spread factor and the caustic corrections discussed in Section 4, is used to get results for the top-

2

hat and bi-cone, respectively. It is shown that the curvature modifications and the caustic corrections to the two-dimensional solution gives appropriate results when compared with the body of revolution results even for very small sizes.

A modification to the two-dimensional dihedral is the parallel plate cavity. The parallel plate cavity modified for curvature and caustics effects is the cake pan (shallow circular cavity). In Section 7, the parallel plate cavity and the cake pan are discussed. For the cake pan, ray terms which contribute only in the principal plane are included. It is found that for shallow and wide circular cavities good results can be obtained, over a wide range of angles, by including only the ray terms that contribute in the principal plane.

For the donut, in Section 8, the first and second order GO terms and its caustic corrections are discussed. No creeping wave terms are included in this solution.

In Section 9, techniques developed for the two-dimensional dihedral solution and the cylinder solution is also used to get backscatter results from multi-joined cylinders. This model is used to investigate the scattering from geometries similar to tree trunks and branches. In particular, two types of "tree" crook models are examined. The UTD results are compared with the measurements and reasonable agreement is found.

3

SECTION 2

Theoretical Background

1 Introduction

This chapter contains a brief description of the techniques of Geometrical Optics (GO), and the Uniform Theory of Diffraction (UTD) needed for the solution of the configurations analyzed in this work. Details on these high frequency approximate-solution methods can be found in References [1, 3, 4, 5]. Also, a recently developed far-zone double diffraction coefficient is presented [2].

It is assumed that the fields exhibit a time dependence of $e^{j\omega t}$ which is suppressed throughout this work.

2 Geometrical Optics (GO)

A brief summary of geometrical optics is given here. The propagation of electromagnetic energy at high frequencies through isotropic, lossless media can be described using GO. Thus GO provides a high frequency approximate solution to the incident, reflected and refracted fields. In our problem, we will be concerned with the reflected field. The GO can be obtained from an asymptotic solution of Maxwell's equations and it corresponds to the leading term of the Luneberg-Kline asymptotic expansion for large values of angular frequency [1]. According to GO, electromagnetic energy can be viewed as travelling along well-defined paths known as rays. The ray path, in

any continuous medium, may be determined using Fermat's principle which states the energy will flow along the path of shortest electrical length between any two points. The shortest electrical path is one which results in the shortest propagation time between two points. From Fermat's principle, the law of reflection and the law of refraction can be obtained. In geometrical optics, phase is proportional to the distance along the ray path from some reference point, and the amplitude is governed by the conservation of power in a tube of rays. Figure 1 shows one such tube of rays. The distances ρ_1 and ρ_2 are from a fixed reference point to the "caustics", where a family of rays merge or intersect.

In geometrical optics, like all other ray techniques, the fields can not be evaluated at the caustics. At caustics, the approximation of power conservation in a tube of rays is no longer valid. The field near a caustic appears to become infinite as a finite amount of power gets squeezed into a vanishing area. The fields near caustics must be found by other means. Chapter 4 discusses some of the caustics encountered in this work.

2.1 GO Reflected Field

The GO reflected field from a smooth conducting convex surface with radius of curvature greater than λ, see Figure 2, is given as

$$\vec{E}^r(\vec{r}) = \vec{E}^i(Q_r) \cdot \overline{\overline{R}} \sqrt{\frac{\rho_1^r \rho_2^r}{(\rho_1^r + s^r)(\rho_2^r + s^r)}}\, e^{-jk s^r}, \tag{1}$$

where

Q_r = reflection point,

$\vec{E}^i(Q_r)$ = incident field at Q_r,

s^r = distance from Q_r to receiver,

$\overline{\overline{R}}$ = the dyadic reflection coefficient,

$\overline{\overline{R}} = R_s \hat{e}_\perp^i \hat{e}_\perp^r + R_h \hat{e}_\parallel^i \hat{e}_\parallel^r,$

$R_{s,h} = \mp 1,$
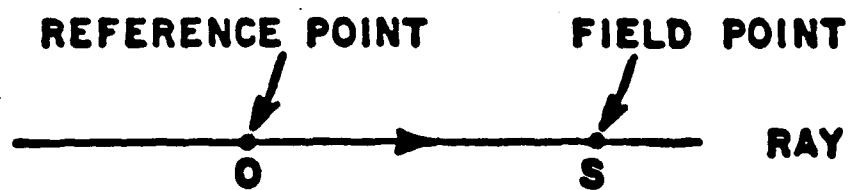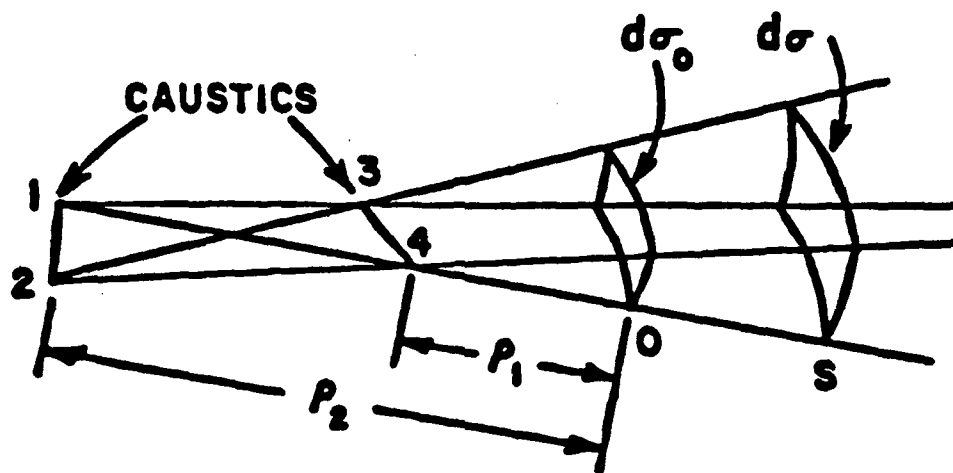
Figure 1: An astigmatic tube of rays.

REFLECTED RAY

INCIDENT RAY

$\hat{e}^r_{\parallel}$

$\hat{e}^i_{\parallel}$

$\hat{n}$

θ^i

$\hat{s}^r$

$\hat{e}_\perp$

$\hat{s}^i$

$\hat{e}_\perp$

Q_R
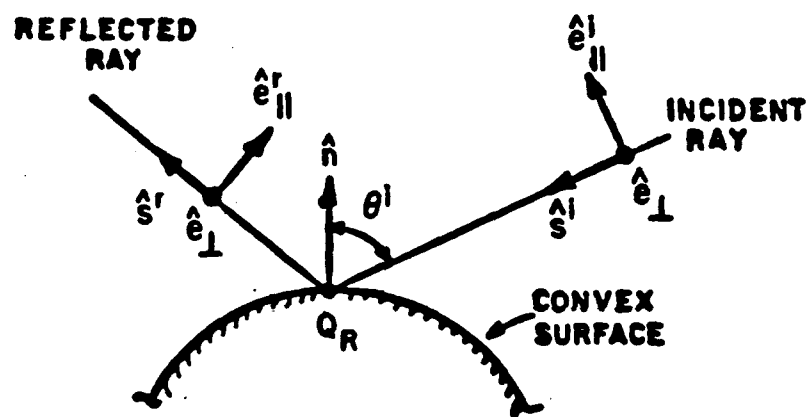
CONVEX SURFACE

$\hat{s}$ = UNIT OUTWARD NORMAL VECTOR TO THE CONVEX SURFACE AT Q_R

$\hat{e}^i_{\parallel} = \hat{e}_\perp \times \hat{s}^i$

$\hat{e}^r_{\parallel} = \hat{e}_\perp \times \hat{s}^r$

Figure 2: Reflection off a convex conducting surface.

7

$\rho^r_{1,2}=$ principal radii of curvature of the reflected wavefront, and

$$\frac{1}{\rho^r_{1,2}} = \frac{1}{2}\left(\frac{1}{\rho^i_1}+\frac{1}{\rho^i_2}\right) + \frac{\cos\theta^i}{|\Theta|^2}\left[\frac{(\Theta_{22})^2+(\Theta_{12})^2}{R_1}+\frac{(\Theta_{21})^2+(\Theta_{11})^2}{R_2}\right]$$

$$\pm\frac{1}{2}\left\{\left(\frac{1}{\rho^i_1}-\frac{1}{\rho^i_2}\right)^2+\left(\frac{1}{\rho^i_1}-\frac{1}{\rho^i_2}\right)\frac{4\cos\theta^i}{|\Theta|^2}\left[\frac{(\Theta_{22})^2+(\Theta_{12})^2}{R_1}+\frac{(\Theta_{21})^2+(\Theta_{11})^2}{R_2}\right]\right.$$

$$\left.+\frac{4\cos^2\theta^i}{|\Theta|^4}\left[\left(\frac{(\Theta_{22})^2+(\Theta_{12})^2}{R_1}+\frac{(\Theta_{21})^2+(\Theta_{11})^2}{R_2}\right)^2-\frac{4|\Theta|^2}{R_1R_2}\right]\right\}^{\frac{1}{2}}, \quad (2)$$

where the plus sign is associated with ρ^r_1 and the minus sign with ρ^r_2, and

$$\Theta_{jk} = \hat{X}^i_j.\hat{U}_k \tag{3}$$

or

$$\Theta = \begin{bmatrix} \hat{X}_1.\hat{U}_1 & \hat{X}_1.\hat{U}_2 \\ \hat{X}_2.\hat{U}_1 & \hat{X}_2.\hat{U}_2 \end{bmatrix}. \tag{4}$$

$\hat{X}^i_1$ and $\hat{X}^i_2$ are the principal directions of the incident wavefront on the curved surface S at Q_r with the principal radii of curvature ρ^i_1 and ρ^i_2, and θ^i is the angle of incidence. (See Figure 3) $\hat{U}_1$ and $\hat{U}_2$ are unit vectors in the principal directions of S at Q_r with the principal radii of curvature R_1 and R_2.

For the far-zone case, the Equation (2) can be simplified as

$$\frac{1}{\rho^r_{1,2}} = \frac{1}{\cos\theta^i}\left[\frac{\sin^2\theta_2}{R_1}+\frac{\sin^2\theta_1}{R_2}\right]$$

$$\pm\sqrt{\frac{1}{\cos^2\theta^i}\left[\frac{\sin^2\theta_2}{R_1}+\frac{\sin^2\theta_1}{R_2}\right]^2-\frac{4}{R_1R_2}} \tag{5}$$

where θ_1 is the angle between the direction of the incident ray $\hat{s}^i$ and $\hat{U}_1$, and θ_2 is the angle between $\hat{s}^i$ and $\hat{U}_2$.

3 Uniform Theory of Diffraction (UTD)

Keller's generalization of fermat's principle allows one to include a class of rays diffracted from electrical and/or geometrical discontinuities on a scattering or a
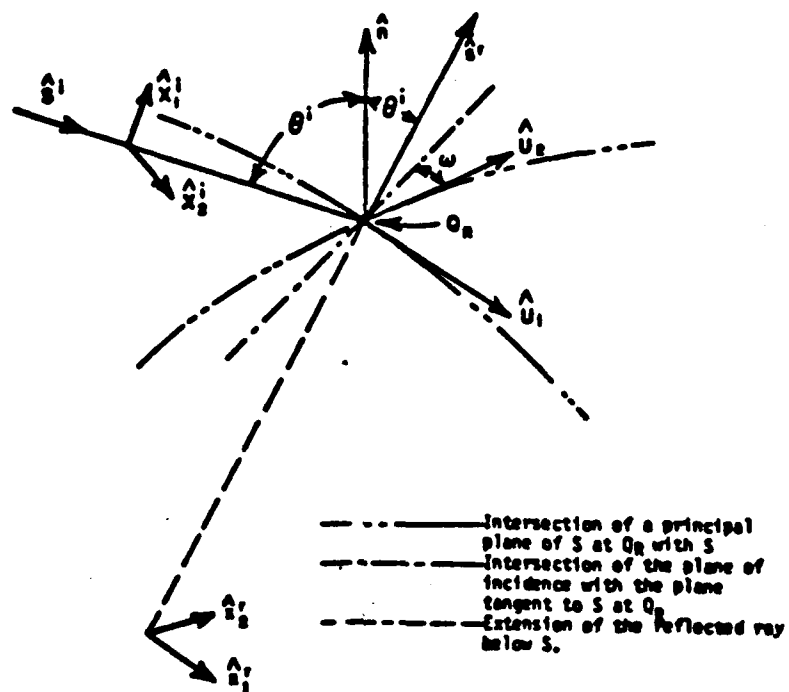
Figure 3: Geometry of the description of the wavefront reflected from the curved surface S.

radiating object; these diffracted rays exist in addition to the rays of GO which describe incident, reflected and refracted rays.

In GTD, the initial value of the diffracted rays are obtained by multiplying the incident field with a diffraction coefficient at the point of diffraction, analogous to the reflection coefficient for the reflected ray. The expression for the diffraction coefficient depends on the scattering mechanism (edge diffraction, tip diffraction, etc.). The application of GTD is limited only by the availability of accurate coefficients. The Uniform Theory of Diffraction (UTD) is an improved version of the GTD in that the diffraction coefficients remain valid at and near the shadow boundaries, where the Keller's original coefficient had failed.

Two major contributors to the diffracted field considered by UTD are diffraction from the edge and the diffraction from a curved surface (or the creeping wave diffraction). In this work, only the edge diffraction will be considered.

4   UTD Edge Diffracted Field

The singly edge diffracted UTD field as developed by Kouyoumjian and Pathak [1] is now introduced. The three-dimensional wedge diffraction geometry is shown in Figure 4. Let an arbitrarily polarized field $\overline{E}^i(s')$ which may be plane, cylindrical or spherical wave be incident on the wedge. Such a field $\overline{E}^i(s')$ can be represented as a GO incident ray field. When an incident ray strikes the edge at Q_r (say), then it generates a cone of edge diffracted rays which emanate from Q_e so that the cone half angle = angle made be the incident ray into the edge tangent at Q_e (i.e., $\beta_o = \beta_o'$). This is a consequence of the generalization of the fermat's principle to the incident edge diffracted.

The authors of [1] expressed the dyadic diffraction coefficients in a ray fixed coordinate system which is centered at the diffraction point Q_r. The orthogonal unit vectors associated with the ray fixed coordinate system are defined as:

$$\hat{s}' = \hat{\beta}_o' \times \hat{\phi}', \tag{6}$$

10
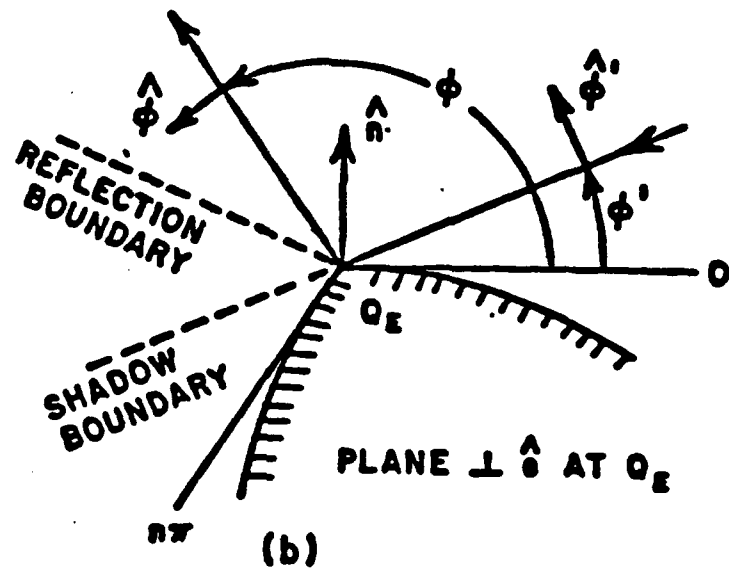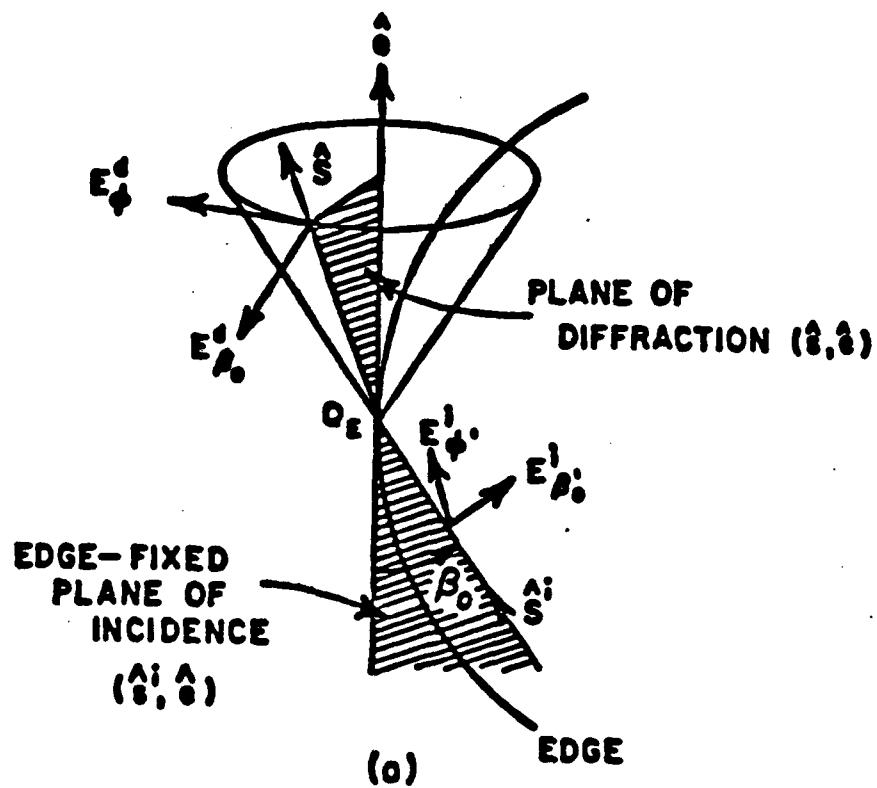
Figure 4: Geometry for the three-dimensional wedge diffraction problem.

11

and

$$\hat{s} = \hat{\beta}_o \times \hat{\phi}. \tag{7}$$

These vectors are shown in Figure 4. The diffracted field from a semi-infinite perfectly-conducting curved wedge is given by the following expression:

$$\overline{E}^d(s) \sim \overline{E}^i(Q_e) \cdot \overline{\overline{D}} \sqrt{\frac{\rho^d}{s(\rho^d + s)}}\, e^{-jks}, \tag{8}$$

where

Q_e = point of diffraction on the edge,

$\vec{E}^i(Q_e)$ = incident field at Q_e,

s = distance from Q_e to receiver,

ρ^d = caustic distance for the diffracted ray,

$\overline{\overline{D}}$ = the dyadic edge diffraction coefficient,

$$\overline{\overline{D}} = -\hat{\beta}'_o\hat{\beta}_o D_s - \hat{\phi}'\hat{\phi}D_h, \tag{9}$$

or in matrix form

$$\begin{bmatrix} E^d_{\beta_o} \\ E^d_{\phi} \end{bmatrix} \sim \begin{bmatrix} -D_s & 0 \\ 0 & -D_h \end{bmatrix} \begin{bmatrix} E^i_{\beta'_o} \\ E^i_{\phi'} \end{bmatrix} \sqrt{\frac{\rho^d}{s(\rho^d + s)}} e^{-jks}. \tag{10}$$

The ray fixed coordinate system ensures that the diffraction coefficient dyadic, $\overline{\overline{D}}$, matrix is diagonal.

The soft diffraction coefficient, D_s, is associated with the component of E-field that is parallel to the edge, i.e.,

$$\hat{z} \cdot \overline{E} = 0. \tag{11}$$

The hard diffraction coefficient, D_h, is associated with the component of E-field that is perpendicular to the edge, i.e.,

$$\hat{n} \cdot \nabla \left(\hat{z} \cdot \overline{H} \right) = 0. \tag{12}$$

12

The soft and hard diffraction coefficients are defined as

$$D_{s,h} = \frac{-e^{-j\pi/4}}{2n\sqrt{2\pi k}\sin\beta_o}\left[\cot\left(\frac{\pi+\beta^-}{2n}\right)F\left(kLa^+(\beta^-)\right)\right.$$

$$+\cot\left(\frac{\pi-\beta^-}{2n}\right)F\left(kLa^-(\beta^-)\right)$$

$$\mp\left\{\cot\left(\frac{\pi+\beta^+}{2n}\right)F\left(kLa^+(\beta^+)\right)\right.$$

$$\left.\left.+\cot\left(\frac{\pi-\beta^+}{2n}\right)F\left(kLa^-(\beta^+)\right)\right\}\right], \tag{13}$$

where

$$a^\pm(\beta) = 2\cos^2\left(\frac{2n\pi N^\pm-(\beta)}{2}\right), \tag{14}$$

and $N^\pm$ are integers which most nearly satisfy the equations

$$2\pi n N^+ - (\beta) = \pi, \tag{15}$$

and

$$2\pi n N^- - (\beta) = -\pi, \tag{16}$$

with

$$\beta = \beta^\pm = \phi\pm\phi' \tag{17}$$

F(x), where x=kLa, is a transition function defined as

$$F(x) = 2j \mid \sqrt{x} \mid e^{jx}\int_{|\sqrt{x}|}^{\infty}e^{-j\tau^2}d\tau \tag{18}$$

The magnitude and phase of F(x) is shown in the Figure 5. For x small ($X < 0.3$),

$$F(x) \sim \left(\sqrt{\pi x} - 2xe^{j\frac{\pi}{4}} - \frac{2}{3}x^2e^{-j\frac{\pi}{4}}\right)e^{j\left(\frac{\pi}{4}+X\right)}. \tag{19}$$

When $0.3 < x < 3.5$, linear interpolation is used as an efficient numerical means of determining F(x) so that

$$F(x) = F(x_n) + A_n(x - x_n). \tag{20}$$

13
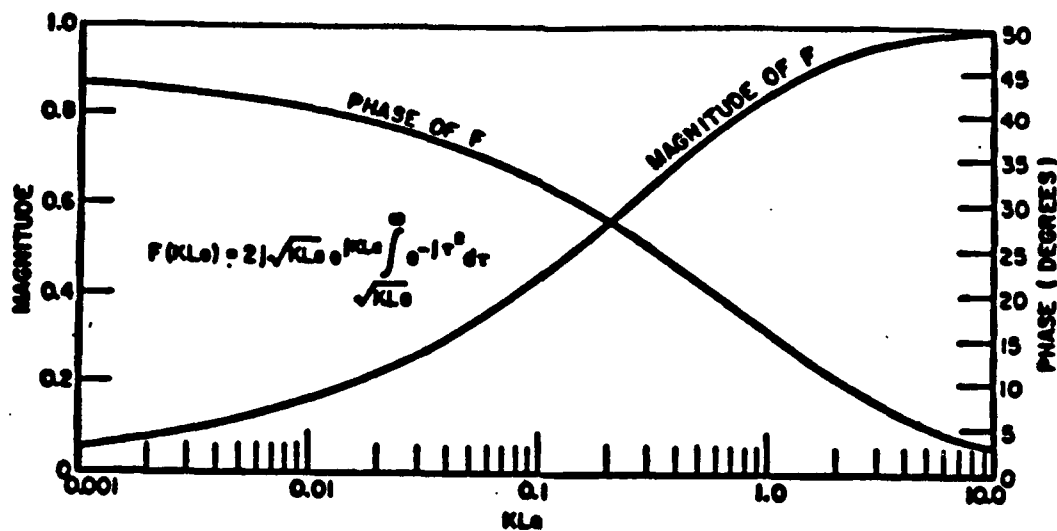
Figure 5: Magnitude and phase of F(x).

For $x > 5.5$ one finds that

$$F(x) \sim 1 + \frac{j}{2x} - \frac{3}{4x^2} - j\frac{15}{8x^3} + \frac{75}{16x^4}.$$ (21)

The diffracted caustic distance, ρ^d, is defined as

$$\frac{1}{\rho^d} = \frac{1}{\rho^i_e} - \frac{\hat{n}_c \cdot (\hat{s}' - \hat{s})}{a_e \sin^2 \beta_o}.$$ (22)

L is a distance parameter, where

$$L^{i,r} = s\frac{(\rho^{i,r}_e + s)\,\rho^{i,r}_1\rho^{i,r}_2}{\rho^{i,r}_e\left(\rho^{i,r}_1 + s\right)\left(\rho^{i,r}_2 + s\right)} \sin^2 \beta_o.$$ (23)

The parameters $\rho^{i,r}_c$ are the (incident, reflected) radii of curvature at Q_e in the plane containing the (incident, reflected) ray and $\hat{e}$ is the unit vector tangent to the edge at Q_e, $\hat{n}_e$ is the associated unit normal vector to the edge directed away from the center of curvature, $a_e > 0$ is the radius of curvature of the edge at Q_e and β_o is the angle between the incident ray and the tangent to the edge as shown in Figure 4. The

14

unit vectors $\hat{s}'$ and $\hat{s}$ are in the direction of incidence and diffraction, respectively. $\rho_{1,2}^{i,r}$ are the principal radii of curvature of the (incident, reflected) wavefront at Q_r. The superscript n, o on L denote that the radii of curvature are determined at the reflection shadow boundaries of the n and o faces, respectively. The reflected field caustic distance in the plane of the reflected ray and edge tangent is given by

$$\frac{1}{\rho_c^r} = \frac{1}{\rho_c^i} - \frac{2\,(\hat{n}.\hat{n}_c)\,(\hat{s}'.\hat{n})}{a_c \sin^2 \beta_o}, \tag{24}$$

where

$\hat{n}$ = normal to the surface at Q_e,

$\hat{n}_c$ = normal to the edge curvature at Q_e,

$\hat{s}'$ = incident ray direction,

a_c = radius of the edge curvature.

The diffraction coefficient in Equation (13) may be simplified for the special case when the source and the receiver are in the far field so that F[x] is approximately equal to 1. For this case the diffraction coefficients, $D_{s,h}$ reduce to the Keller's diffraction coefficients in Reference [3], or

$$D_{s,h}(L, \phi, \phi', \beta_o) = \frac{-e^{-j\frac{\pi}{4}}}{2n\sqrt{2\pi k}\sin\beta_o} \left[\cot\left(\frac{\pi + \beta^-}{2n}\right) + \cot\left(\frac{\pi - \beta^-}{2n}\right) \right.$$
$$\left. \mp \left\{ \cot\left(\frac{\pi + \beta^+}{2n}\right) + \cot\left(\frac{\pi - \beta^+}{2n}\right) \right\} \right], \tag{25}$$

which may also be written as

$$D_{s,h}(L, \phi, \phi', \beta_o) = \frac{-e^{-j\frac{\pi}{4}}\sin\frac{\pi}{n}}{n\sqrt{2\pi k}\sin\beta_o}$$
$$\left[\frac{1}{\cos\left(\frac{\pi}{n}\right) - \cos\left(\frac{\phi-\phi'}{n}\right)} \mp \frac{1}{\cos\left(\frac{\pi}{n}\right) - \cos\left(\frac{\phi+\phi'}{n}\right)} \right]. \tag{26}$$

The diffraction coefficient may also be simplified for the special case when n=2 (half-plane)

$$D_{s,h}(L, \phi, \phi', \beta_o) = \frac{-e^{-j\frac{\pi}{4}}}{2\sqrt{2\pi k}\sin\beta_o} \left[\frac{F[kLa(\beta^-)]}{\cos(\beta_o^-/2)} \mp \frac{F[kLa(\beta^+)]}{\cos(\beta_o^+/2)} \right]. \tag{27}$$

15

5 Scattering from a Strip in the Far-zone

A study of the scattering from a strip is considered because the strip is the basic building block for the structures discussed in this work. For the case of far-zone illumination and observer, the first order bistatic scattered field from the strip contains only the diffracted field from two edges. The GO information need not be specifically included, since it is contained in the GTD far zone diffracted fields. Consider the geometry shown in Figure 6. The length of the strip is given as l. The basic geometrical parameters needed are

$$\phi_1 - \phi_1' = \phi - \phi' \tag{28}$$

$$\phi_1 + \phi_1' = \phi + \phi' - 2\phi_o \tag{29}$$

$$\phi_2' = \begin{cases} \pi + \phi_o - \phi' & , 0 < \phi' < \pi + \phi_o \\ 3\pi + \phi_o - \phi' & , \pi + \phi_o < \phi' < 2\pi \end{cases} \tag{30}$$

$$\phi_2 = \begin{cases} \pi + \phi_o - \phi & , 0 < \phi < \pi + \phi_o \\ 3\pi + \phi_o - \phi & , \pi + \phi_o < \phi < 2\pi \end{cases} \tag{31}$$

$$\overline{U}'_{s,h} = \hat{z} U^i_{s,h} \left[D_{s,h}(Q_1) + D_{s,h}(Q_2) \right] e^{-jks} \tag{32}$$

where

$$U^i_{\,h} = \begin{cases} E_o & , \text{E parallel to wedge} \\ H_o & , \text{E perpendicular to wedge} \end{cases} \tag{33}$$

and

$$U^t_{\,h} = U^i_{\,h} \frac{-e^{-j\pi/4}}{2\sqrt{2\pi k}} \left(\frac{1}{\cos\left(\frac{\phi_1 - \phi_1'}{2}\right)} \mp \frac{1}{\cos\left(\frac{\phi_1 + \phi_1'}{2}\right)} \right) +$$

$$U^i_{\,h} \frac{-e^{-j\pi/4}}{2\sqrt{2\pi k}} \left(\frac{1}{\cos\left(\frac{\phi_2 - \phi_2'}{2}\right)} \mp \frac{1}{\cos\left(\frac{\phi_2 + \phi_2'}{2}\right)} \right) e^{jkl\left(\cos\phi_1 + \cos\phi_1'\right)}. \tag{34}$$

It is observed that both diffraction coefficients become infinite at the reflection shadow boundaries (i.e. $\phi_1 + \phi_1' = \pi$ and $\phi_2 + \phi_2' = \pi$; or $\phi + \phi' = 2\phi_o + \pi$) and at the incident shadow boundary (forward scatter) (i.e. $\phi_1 - \phi_1' = \pi$ and $\phi_2 - \phi_2' = \pi$).
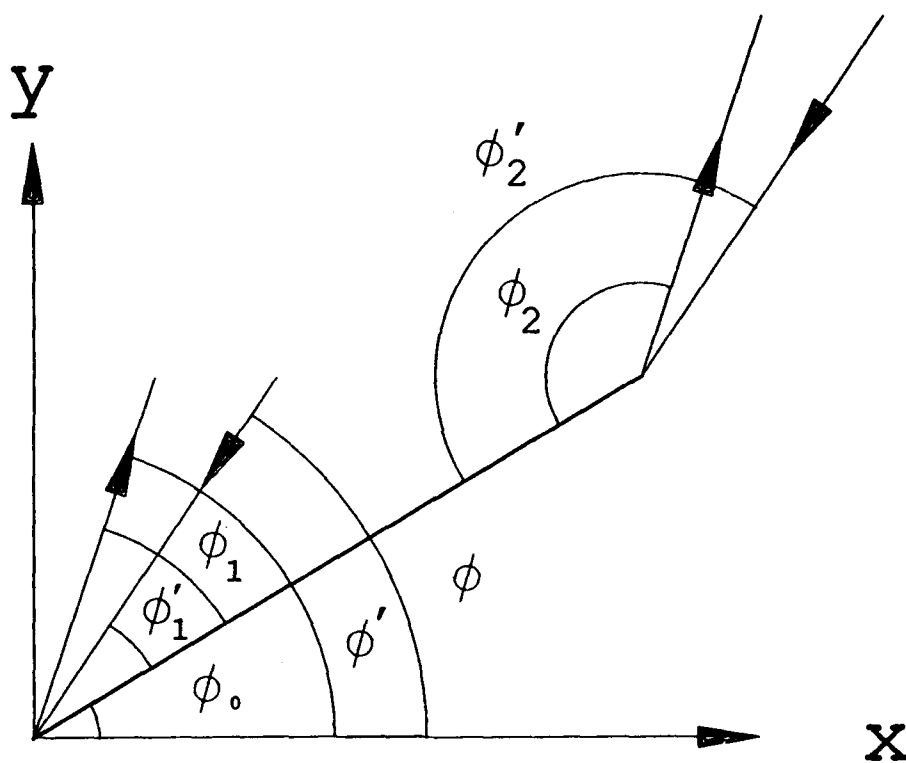
Figure 6: Geometry of the strip.

Using Equations (28) through (31) into Equation (34) and constraining to the region $0 < \phi < \pi + \phi_o$ and $0 < \phi' < \pi + \phi_o$, gives

$$U_{h}^{t} = U_{h}^{i} \frac{-e^{-j\pi/4}}{2\sqrt{2\pi k}} \left(\frac{1}{\cos\left(\frac{\phi-\phi'}{2}\right)} \mp \frac{1}{\cos\left(\frac{\phi+\phi'-2\phi_o}{2}\right)} \right)$$

$$+ U_{h}^{i} \frac{-e^{-j\pi/4}}{2\sqrt{2\pi k}} \left(\frac{1}{\cos\left(\frac{\phi-\phi'}{2}\right)} \pm \frac{1}{\cos\left(\frac{2\phi_o-\phi-\phi'}{2}\right)} \right) e^{jkl(\cos(\phi-\phi_o)+\cos(\phi'-\phi_o))}. \qquad (35)$$

Notice that for this range the scattering along the incident shadow boundary is not possible. Combining terms results

$$U_{h}^{t} = U_{h}^{i} \frac{-e^{-j\pi/4}}{2\sqrt{2\pi k}} e^{jkl\cos\left(\frac{\phi+\phi'-2\phi_o}{2}\right)\cos\left(\frac{\phi-\phi'}{2}\right)}$$

$$\left\{ \pm \frac{2j \sin\left(kl\cos\left(\frac{\phi+\phi'-2\phi_o}{2}\right)\cos\left(\frac{\phi-\phi'}{2}\right)\right)}{\cos\left(\frac{\phi+\phi'-2\phi_o}{2}\right)} \right.$$

$$\left. + \frac{2 \cos\left(kl\cos\left(\frac{\phi+\phi'-2\phi_o}{2}\right)\cos\left(\frac{\phi-\phi'}{2}\right)\right)}{\cos\left(\frac{\phi-\phi'}{2}\right)} \right\}. \qquad (36)$$

In general, the case of infinity along the reflection shadow is more common and is treated in detail to show how a continuous result is obtained. Near the reflection shadow boundary

$$\cos\left(\frac{\phi+\phi'-2\phi_o}{2}\right) = \cos(\pi/2 \pm \epsilon) \simeq \mp \epsilon. \qquad (37)$$

Using Equation (37) in Equation (36) gives

$$U_{h}^{t} = U^{i} \frac{-e^{-j\pi/4}}{\sqrt{2\pi k}} \left\{ \pm jkl \cos\left(\frac{\phi-\phi'}{2}\right) + \frac{1}{\cos\left(\frac{\phi-\phi'}{2}\right)} \right\}. \qquad (38)$$

For broadside backscatter case

$$U_{h}^{t} = U_{h}^{i} \frac{-e^{-j\pi/4}}{\sqrt{2\pi k}} [\pm jkl + 1] = U_{h}^{po} + U^{c} \qquad (39)$$

where U_{h}^{po} is the PO term and U^{c} is the correction to PO. Simplifying the U_{h}^{po} term

$$U_{h}^{po} = \mp U_{h}^{i} \frac{e^{j\pi/4}}{\sqrt{2\pi k}} kl \qquad (40)$$

18

$$\sigma^{po}_{strip} = 2\pi \left[\frac{U'}{U'}\right]^2 = 2\pi \frac{l^2}{\lambda} \qquad (41)$$

gives the expected PO result for backscatter from broadside of a 2-D strip.

Results of fields backscattered from a strip are presented in Figures 7 and 8. The UTD solution is obtained by the above formulation. Comparing the UTD result with the moment method result, it is observed that using the single edge diffracted fields from the edges gives a good approximation to the exact solution for the main and a few side lobes. For the TE_z case, we note that near $\phi = 0^\circ$ and 180° the first order UTD solution is not accurate. This is a consequence of the higher order terms not being taken into account. However for the TM_z case the higher order terms are negligible. See References [6, 7, 8, 9] for higher order effects on the strip.

6 Double Diffraction Formulation

Previous solutions of the field diffracted by double-edge structures used the UTD in its original formulation argumented by slope diffraction (especially for the soft polarization) to give useful results when the distance between the two edges is very large. However, difficulties are present whenever the second edge is located in the transition region of the first edge and the diffracted field is calculated in the transition regions adjacent to the incident or reflection shadow boundaries of the second edge. These problems are caused by the rapid, spatial variation together with a non-ray optical behavior of the field incident on the second edge after diffraction from the first. It is obvious that the angular range of the overlapping transition regions broadens as the distance between the edges decreases. Part of the difficulties are removed by a spectral extension of the UTD in References [6] and [7]. This solution is uniformly valid at any incidence aspect, but it is restricted to those observation aspects which coincide with diffraction shadow boundary (DSB) or the diffraction reflection shadow boundary (DRSB). (See Figure 25.)

19
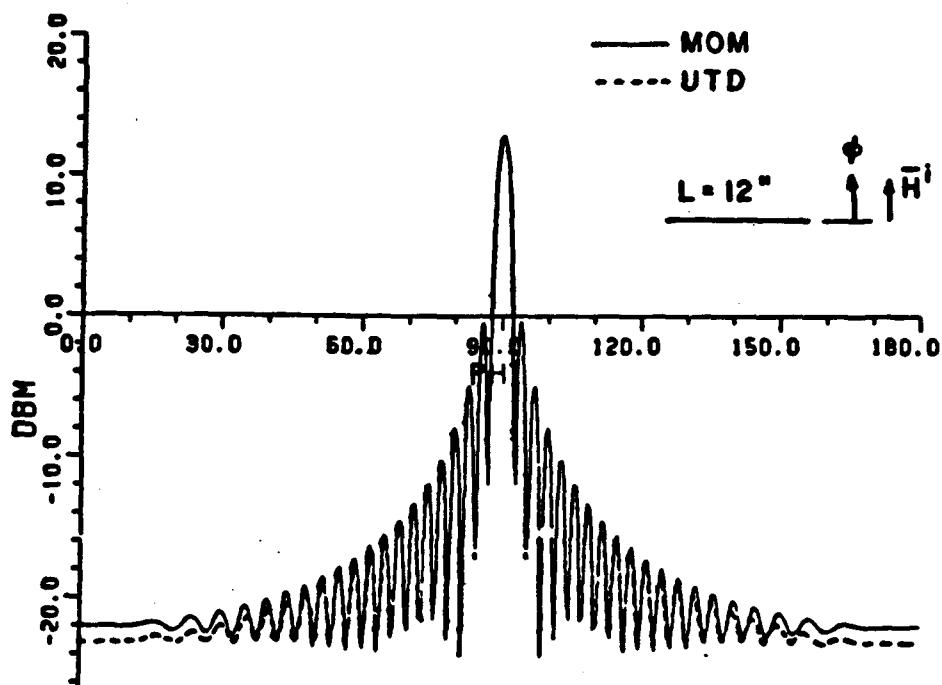
Figure 7: Backscatter field from a 12 in strip at 10 GHz (soft case).
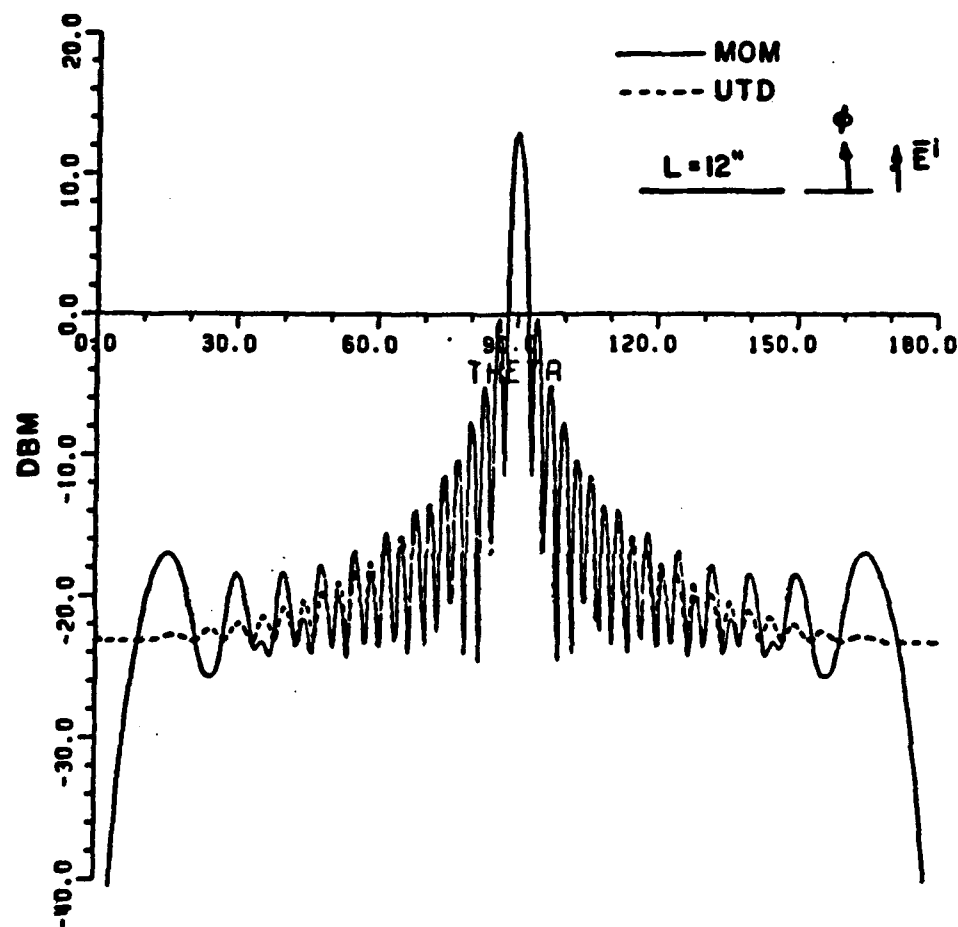
Figure 8: Backscatter field from a 12 in strip at 10 GHz (hard case).

A closed form solution for the doubly diffracted field in the far zone from a pair of parallel wedges is presented in Reference [2]. As shown in Section 3, these expressions exhibit the proper discontinuities and singularities so that when combined with the singly diffracted field, the field is continuous and uniform. For joined wedges, shown in Figure 9, the angle parameters are defined as

$$\Phi_p = \pi + (-1)^p (n_1\pi - \phi_1'); \quad p = 1,2, \tag{42}$$

and

$$\Phi_q = \pi + (-1)^q (n_2\pi - \phi_2'); \quad q = 1,2. \tag{43}$$

The pattern function of the field doubly diffracted from Q_1 and Q_2 is given as

$$P_m^{\dot{}}(Q_1, Q_2) \sim \sum_{p=1}^{2} \sum_{q=1}^{2} P_{h}^{\dot{}}(\Phi_p, \Phi_q). \tag{44}$$

By only retaining the first nonvanishing term in the asymptotic expansion for kd large, the following closed form expressions are obtained

$$P_s(\Phi_p, \Phi_q) \sim \frac{(-1)^p(-1)^q}{8\pi j(n_1 n_2)^2} \frac{a_p a_q}{\sin^2(\frac{\Phi_p}{2n_1})\sin^2(\frac{\Phi_q}{2n_2})}$$
$$\frac{F[kda_p] - F[kda_q]}{a_p - a_q} \left(\frac{e^{-jkd}}{\sqrt{kd}}\right), \tag{45}$$

for a TM plane wave (with the electric field parallel). For a TE plane wave (with the electric field perpendicular),

$$P_h(\Phi_p, \Phi_q) \sim -\frac{1}{4\pi j n_1 n_2} \cot\left(\frac{\Phi_p}{2n_1}\right) \cot\left(\frac{\Phi_q}{2n_2}\right)$$
$$\frac{a_q F[kda_p] - a_p F[kda_q]}{a_p - a_q} \left(\frac{e^{-jkd}}{\sqrt{kd}}\right), \tag{46}$$

and

$$a_i = 2\cos^2[(\Phi_i - \pi - (-1)^i 2n\pi N_i)/2] \tag{47}$$

where $n = n_1$ for i = p, $n = n_2$ for i = q, and N_i is the integer that most nearly satisfies

$$N_i = (-1)^i \frac{\Phi_i}{2n\pi}. \tag{48}$$

22

$F(x)$ is the transition function that has been defined for the single diffraction case.

If the two wedges are separate, the above equations are slightly varied. For the separated wedges shown in Figure 10, the angle parameters are defined as

$$\Phi_p = \pi + (-1)^r(\phi_1 - \eta_p\phi_1'); \quad p = 1,4 , \tag{49}$$

$$\Phi_q = \pi + (-1)^q(\phi_2 - \eta_q\phi_2'); \quad q = 1,4 , \tag{50}$$

with $\eta_i = 1$ for i=1, 2 and $\eta_i = -1$ for i=3, 4. The pattern function of the field double diffracted from Q_1 and Q_2 is given as

$$P_{\bar{m}}^{\xi}(Q_1,Q_2) \sim \sum_{p=1}^{4}\sum_{q=1}^{4} \frac{\chi_p\chi_q}{2} \left[P_s(\Phi_p,\Phi_q) + P_h(\Phi_p,\Phi_q)\right], \tag{51}$$

where $\chi_i = \eta_i$ in the TM case and $\chi_i = 1$ in the TE case.

7 Limit Forms of Double Diffraction Coefficients

When a_p and a_q are such that they are approximately equal but not close to zero, Equations (45) and (46) tend to become of indeterminate form. This can cause numerical problems on the computer. Equations (52) and (53) are parts of Equations (45) and (46), respectively, that may have such a behavior. To get around this problem on the computer, limit forms are used in the approximate region. Defining

$$T_s = \frac{F[kda_p] - F[kda_q]}{a_p - a_q} \tag{52}$$

and

$$T_h = \frac{a_q F[kda_p] - a_p F[kda_q]}{a_p - a_q}, \tag{53}$$

and noting that

$$kd\lim_{\epsilon \to 0} \frac{F[kda_q + \epsilon] - F[kda_q]}{kda_q + \epsilon - kda_q} = kdF'[kda]\,|_{a=a_q} \tag{54}$$

where the $'$ denotes diffraction with respect to the argument of the transition function,

$$\frac{d}{dp}\int_p^\eta f(x)dx = -f(p), \tag{55}$$

23
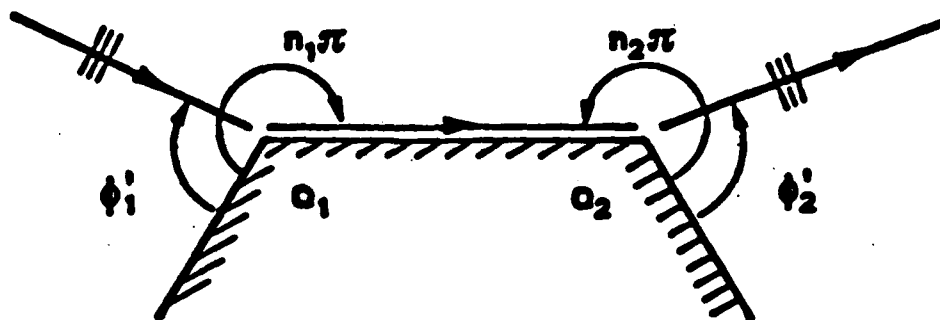
Figure 9: Joined wedges geometry.
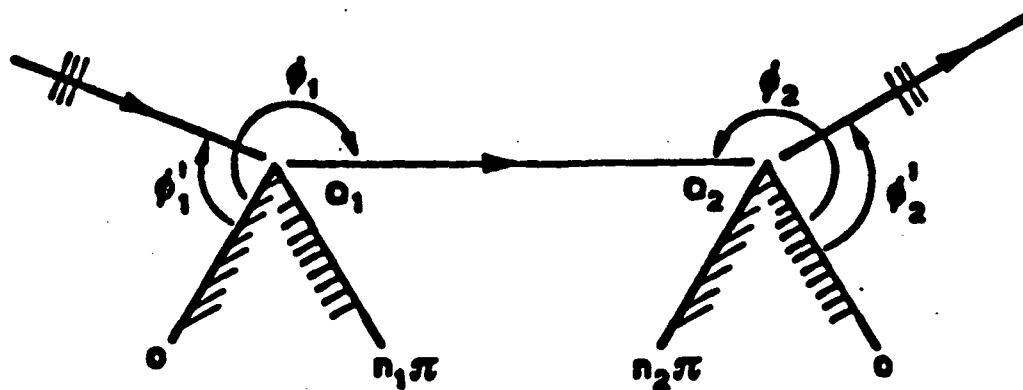
Figure 10: Geometry used for separated wedges.

and

$$F[x] = 2j\sqrt{x}e^{jx} \int_{\sqrt{x}}^{\infty} e^{-j\tau^2} d\tau, \tag{56}$$

equations for T_s and T_h, that are valid when a_p approaches a_q may be derived. From Equations (54) to (56) one obtains,

$$\frac{dF}{dx} = -j\left[1 - (\frac{1}{\sqrt{x}} + 2j\sqrt{x})e^{jx} \int_{\sqrt{x}}^{\infty} e^{-j\tau^2} d\tau\right] \tag{57}$$

$$\frac{dF}{dx} = -\frac{1}{2x}\left[2jx - (1 + 2jx) F(x)\right], \tag{58}$$

and as $a_p \to a_q$, from Equation (52)

$$\lim_{a_q \to a_p} T_s = \left[\left(\frac{1}{2a_p} + jkd\right) F[kda_p] - jkd\right]. \tag{59}$$

Equation (53) may be rearranged as

$$T_h = a_p a_q \frac{\frac{F[kda_p]}{a_p} - \frac{F[kda_q]}{a_q}}{a_p - a_q}, \tag{60}$$

and

$$\lim_{a_q \to a_p} T_h = (kd)^2 a_p a_p \frac{d}{dx}\left[\frac{F[x]}{x}\right]. \tag{61}$$

Using Equation (58) in Equation (61)

$$\lim_{a_q \to a_p} T_h = kda_p \left[\left(j - \frac{1}{2kda_p}\right) F[x] - j\right]. \tag{62}$$

Thus, when a_p and a_q are almost equal but not close to zero, Equations (59) and (62) may be replaced by Equations (45) and (46) for T_s and T_h to insure correct results and prevent computer errors.

25

SECTION 3

UTD 2-D Analysis of a Dihedral

1 Introduction

The dihedral has been in use as a scattering device for many years. Some studies conducted on the dihedral at The Ohio State University ElectroScience Laboratory are given in References [10, 11, 12, 13]. They entail mostly measurement studies with some basic analyses. More recently, renewed interest in the dihedral has led to more detailed analytic studies. A Physical Optics for a right angled dihedral is analyzed with full polarization scattering matrix in Reference [14]. Physical Optics and the Physical Theory of Diffraction are used to predict the results for dihedrals in Reference [15]. In Reference [16], a near zone type UTD plus an "imposed" edge diffraction extension is used to get the backscatter results for the dihedral in the "far zone" by extending the distance parameter for the near zone case. The use of UTD to study plate interactions in the far zone is conducted in Reference [17]. This type of solution is improved and extended to specific dihedral problems in Reference [13], and also briefly discussed in this report as a foundation for the other scatter objects analyzed in this work.

As seen in the previous section, the field of a strip can be obtained by including the diffracted fields from the two edges, and the infinity from edge diffractions combines to give a bounded result in the specular direction. When more than one strip is used in a model, the singly diffracted field from the edges will act as a near-field

26

source which can create reflected and diffracted fields from the other strip. Thus, interactions between the strips are necessary to provide a more accurate pattern. In general, these interactions are present only over a limited region which may be determined geometrically. These higher order interactions also provide the cancellation of infinities to provide a bounded result. It will be shown that interactions up to third order are sufficient to obtain results with engineering accuracy for the case of two-dimensional dihedrals of 60° or greater and for sizes larger than one wavelength in total length.

The UTD interactions that have been included in the analysis which are contained in the 2-D computer code are shown in Figure 11. The single interaction fields included are simply edge diffraction (D) terms. The second order interaction fields are the reflected - diffracted (RD), diffracted - reflected (DR), and diffracted - diffracted (DD) (double diffracted) terms. The third order interaction fields are the reflected - reflected - diffracted (RRD), diffracted - reflected - reflected (DRR), reflected - diffracted - reflected (RDR), reflected -diffracted - diffracted (RDD), diffracted - diffracted - reflected (DDR), and diffracted - reflected - diffracted (DRD) terms. Triple diffractions have not been included. Any of these terms could be critical especially at a shadow boundary. As a general rule, by knowing the position of the source and the receiver, and by drawing ray diagrams, it is simple to predict the important terms by observing the directions of the bounces.

The solution discussed here is based on a study of strip interactions given in Reference [17] and a study of double diffraction in Reference [2]. The strip interaction in the previous study, however, did not provide the necessary accuracy for dihedral configurations. The two dimensional geometry studied is shown in Figure 12. The characteristic features of our analysis allows that : (i) the length of each strip may be different, (ii) the angle between the strips may be varied, (iii) back and bistatic scattering may be treated, (iv) linear and elliptical polarization can be handled, (v) the solution is valid for small sizes in terms of a wavelength.

27
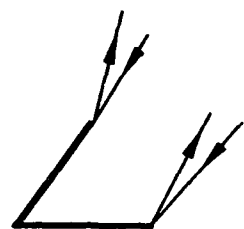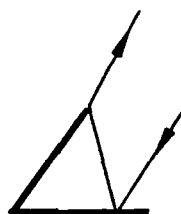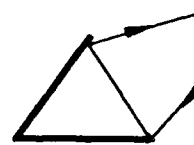
(1) D   (2) RD   (3) DR
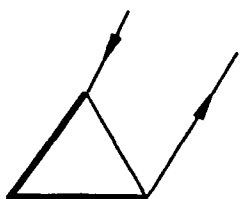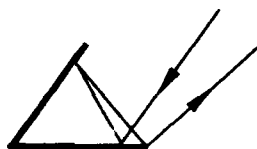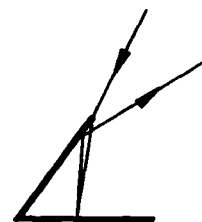
(4) DD   (5) RRD   (6) DRR

(7) RDR   (8) RDD   (9) DDR

(10) DRD

Figure 11: The interactions considered.
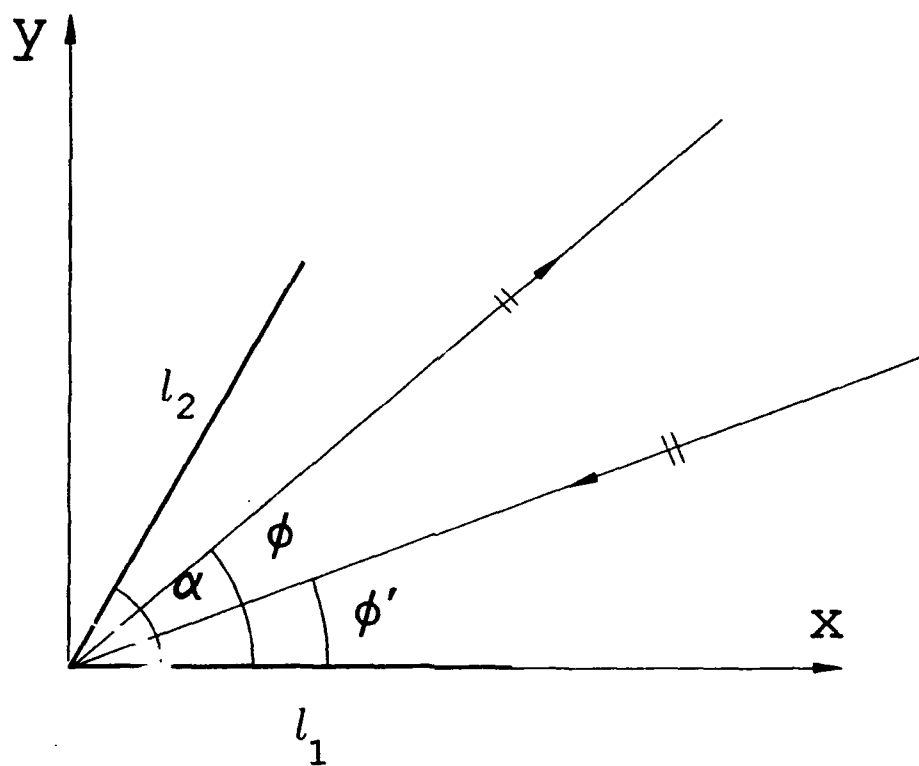
Figure 12: Two-dimensional view of the geometry studied.

2 Basic Dihedral UTD Mechanisms

This section discusses the basic UTD terms that provide the characteristic dihedral pattern. In the case of the main beam of the pattern, the RD and the DR UTD terms along with the single diffracted (D) term from the wedge formed at the junction between the two intersecting strips provide the necessary fields. The specular from the individual strip faces is produced by single diffraction (D) from the ends of the strips and the DR, RD and DRD terms between the strips. The double diffraction (DD) across the face of the dihedral can also be important.

As mentioned above, the RD and DR terms along with the D term from the junction provide the starting point for determining the scattering from an arbitrarily angled dihedral. These terms, in general, look quite complicated. In some special cases, they can be reduced to simpler formulas. As expected, in the case of backscatter for a wedge angle of $\alpha = 90°$, the well known PO result for a dihedral can be derived.

From the equations in Section 2 and for angles derived from Figure 13 for bistatic scattering from a general angled dihedral, the diffracted term from the junction is

$$
U^{D} = U^{i}_{s,h} \frac{-e^{-j\pi/4}}{2n\sqrt{2\pi k}} \left\{ \cot\left(\frac{\pi + (\phi - \phi')}{2n}\right) + \cot\left(\frac{\pi - (\phi - \phi')}{2n}\right) \right.
$$
$$
\left. + R_{s,h} \left[\cot\left(\frac{\pi + (\phi + \phi')}{2n}\right) + \cot\left(\frac{\pi - (\phi + \phi')}{2n}\right) \right] \right\}. \tag{63}
$$

In Figure 13, $D_1 R$ and RD_1 terms are due to reflection from strip 2. The terms $D_2 R$ and RD_2 are due to reflection from strip 1. The basic geometrical parameters for the $D_1 R$ term are

$$
\phi'_1 = \pi - \phi' \quad ; \quad \phi_1 = \pi - 2\alpha - \phi \tag{64}
$$

$$
\phi_1 + \phi'_1 = 2\pi - 2\alpha + \phi - \phi' \tag{65}
$$

$$
\phi_1 - \phi'_1 = -2\alpha + \phi + \phi'. \tag{66}
$$

30
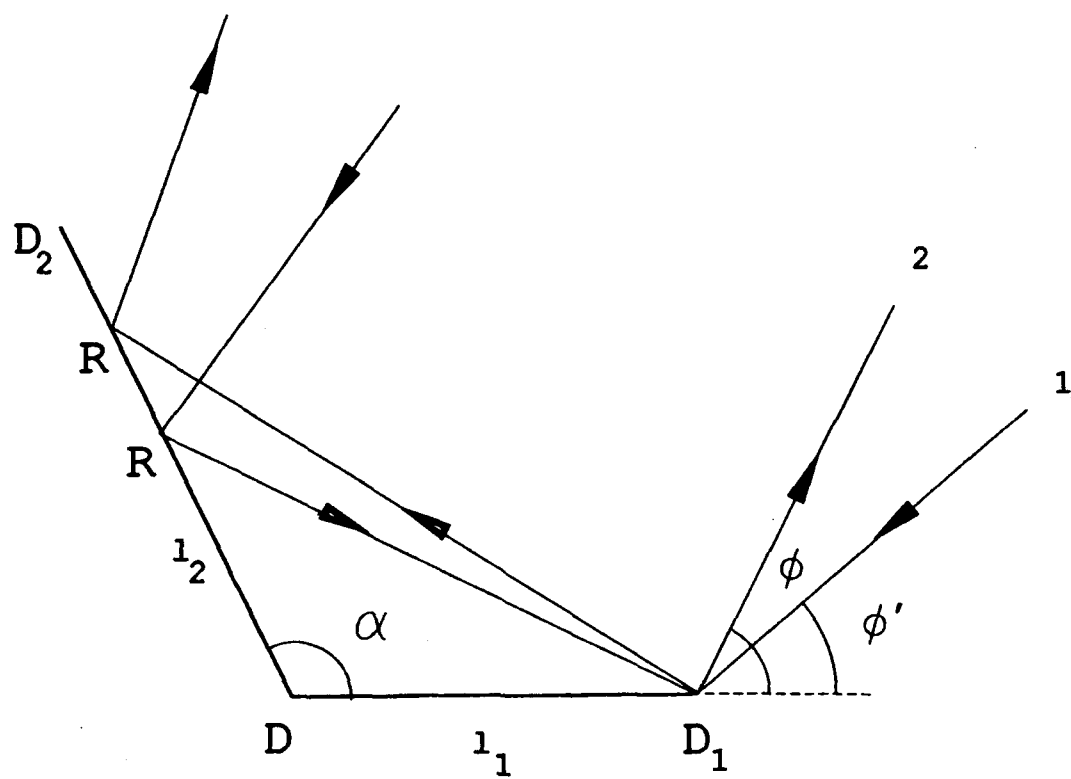
Figure 13: The DR and the RD terms (only D_1R and RD_1 shown).

For the RD_1 term, the angles are the same as for D_1R with ϕ and ϕ' interchanged. The term RD_2 has the following parameters

$$\phi'_2 = \pi - (\alpha + \phi') \quad ; \quad \phi_2 = \pi - \alpha + \phi \tag{67}$$

$$\phi_2 + \phi'_2 = 2\pi - 2\alpha + \phi - \phi' \tag{68}$$

$$\phi_2 - \phi'_2 = \phi + \phi', \tag{69}$$

and for the D_2R term, the angles are the same as for RD_2 with ϕ and ϕ' interchanged. The RD and DR fields are given by

$$U^{D_1R} + U^{RD_1} = U^i_{s,h} R_{s,h} \frac{-e^{-j\pi/4}}{2\sqrt{2\pi k}}$$

$$\left[\left(\frac{1}{\cos\left(\frac{\phi+\phi'-2\alpha}{2}\right)} - R_{s,h} \frac{1}{\cos\left(\frac{\phi-\phi'-2\alpha}{2}\right)} \right) e^{2jkl_1 \cos\left(\frac{\phi+\phi'-2\alpha}{2}\right) \cos\left(\frac{\phi-\phi'-2\alpha}{2}\right)} \right.$$

$$\left. + \left(\frac{1}{\cos\left(\frac{\phi+\phi'-2\alpha}{2}\right)} - R_{s,h} \frac{1}{\cos\left(\frac{\phi-\phi'+2\alpha}{2}\right)} \right) e^{2jkl_1 \cos\left(\frac{\phi+\phi'-2\alpha}{2}\right) \cos\left(\frac{\phi-\phi'+2\alpha}{2}\right)} \right] \tag{70}$$

and

$$U^{RD_2} + U^{D_2R} = U^i_{s,h} R_{s,h} \frac{-e^{-j\pi/4}}{2\sqrt{2\pi k}}$$

$$\left[\left(\frac{1}{\cos\left(\frac{\phi+\phi'}{2}\right)} - R_{s,h} \frac{1}{\cos\left(\frac{\phi-\phi'-2\alpha}{2}\right)} \right) e^{2jkl_2 \cos\left(\frac{\phi+\phi'}{2}\right) \cos\left(\frac{\phi-\phi'-2\alpha}{2}\right)} \right.$$

$$\left. + \left(\frac{1}{\cos\left(\frac{\phi+\phi'}{2}\right)} - R_{s,h} \frac{1}{\cos\left(\frac{\phi-\phi'+2\alpha}{2}\right)} \right) e^{2jkl_2 \cos\left(\frac{\phi+\phi'}{2}\right) \cos\left(\frac{\phi-\phi'+2\alpha}{2}\right)} \right], \tag{71}$$

where the reflection coefficient, $R_{s,h}, is \mp 1$.

It is noted that the term D_1R is present in the region

$$\alpha - \frac{\pi}{2} < \phi < \arctan\left[\frac{l_2 \sin(\alpha) - l_1 \sin(2\alpha)}{l_2 \cos(\alpha) - l_1 \cos(2\alpha)} \right] \tag{72}$$

and RD_1 is present in the region

$$\alpha - \frac{\pi}{2} < \phi' < \arctan\left[\frac{l_2 \sin(\alpha) - l_1 \sin(2\alpha)}{l_2 \cos(\alpha) - l_1 \cos(2\alpha)} \right]. \tag{73}$$

$D_2 R$ is present in the region

$$\arctan \left[\frac{l_2 \sin(\alpha)}{l_1 - l_2 \cos(\alpha)} \right] < \phi < \pi - \alpha, \tag{74}$$

and RD_2 is present in the region

$$\arctan \left[\frac{l_2 \sin(\alpha)}{l_1 - l_2 \cos(\alpha)} \right] < \phi' < \pi - \alpha. \tag{75}$$

The case where α is $90°$ is considered first. It is well known that the diffracted field from the axis of the dihedral will be zero for this case. Using

$$\cos \left(\frac{\phi \pm \phi'}{2} \pm \frac{\pi}{2} \right) = \mp \sin \left(\frac{\phi \pm \phi'}{2} \right) \tag{76}$$

in Equation (70), the following is obtained

$$U^{D_1 R} + U^{RD_1} = U^i_{s,h} \frac{-e^{-j\frac{\pi}{4}}}{2\sqrt{2\pi k}}$$
$$\left\{ 2R_{s,h} \frac{\cos \left[2kl_1 \sin \left(\frac{\phi+\phi'}{2} \right) \sin \left(\frac{\phi-\phi'}{2} \right) \right]}{\sin \left(\frac{\phi+\phi'}{2} \right)} \right.$$
$$\left. -2j \frac{\sin \left[2kl_1 \sin \left(\frac{\phi+\phi'}{2} \right) \sin \left(\frac{\phi-\phi'}{2} \right) \right]}{\sin \left(\frac{\phi-\phi'}{2} \right)} \right\}. \tag{77}$$

With a small bistatic angle and kl_1 large, the second term is dominant. Thus, the above expression may be written as

$$U^{D_1 R + RD_1}_{dominant} = U^i_{s,h} e^{j\pi/4} \frac{2l_1}{\sqrt{\lambda}} \sin \left(\frac{\phi + \phi'}{2} \right) \left\{ \frac{\sin \left[2kl_1 \sin \left(\frac{\phi+\phi'}{2} \right) \sin \left(\frac{\phi-\phi'}{2} \right) \right]}{2kl_1 \sin \left(\frac{\phi+\phi'}{2} \right) \sin \left(\frac{\phi-\phi'}{2} \right)} \right\}. \tag{78}$$

For the backscatter case, with strips of equal length, from Equations (72) to (75), only $D_1 R$ and RD_1 are present for the range $0 < \phi < \pi/4$. Also, only $D_2 R$ and RD_2 are present for the range $\pi/4 < \phi < \pi/2$. For the backscatter case

$$U^{D_1 R + RD_1}_{dominant} = U^i_{s,h} e^{j\pi/4} \frac{2l_1}{\sqrt{\lambda}} \sin(\phi); \quad 0 < \phi < \pi/4, \tag{79}$$

and

$$U^{RD_2 + D_2 R}_{dominant} = U^i_{s,h} e^{j\pi/4} \frac{2l_1}{\sqrt{\lambda}} \cos(\phi); \quad \pi/4 < \phi < \pi/2. \tag{80}$$

33

Notice that for $\phi = 45°$ this result agrees with the well known PO result. Figure 14 shows an excellent agreement of the result obtained by Equations (79) and (80) with that obtained by the UTD computer code (with all terms mentioned above).

Note that in Figure 14 there is a slope discontinuity in the dominant UTD (RD
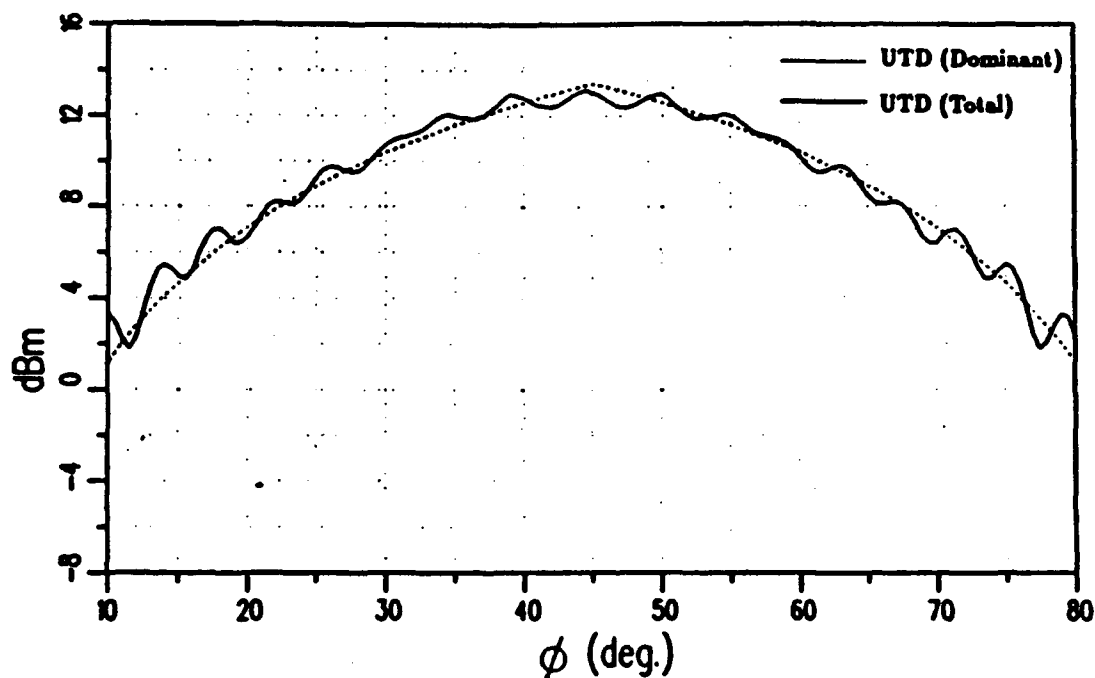
Figure 14: The dominant UTD terms and the computer code results for backscatter for 9 in 90° two-dimensional dihedral at 10 GHz.

and DR terms) at $\phi = 45°$. The DD field across the face of the dihedral balances this slope discontinuity. For the vertical and horizontal polarizations, Figures 15 and 16, respectively, compare the UTD with and without the DD field across the face of the dihedral and the Method of Moments solution [18, 19] for the backscatter case with $\phi = 45°$. To illustrate this point further, consider the 4° bistatic case. Figure 17 shows the DR and RD terms for a 4° bistatic angle. Note that the slope discontinuity of the backscatter case now spreads out and makes the pattern discontinuous. This is due to different boundaries of the various RD and DR terms (Equations (72) to (75)). Figure 18 shows that this discontinuity may be corrected by including the DD term (see Section 4) across the face of the dihedral.

34
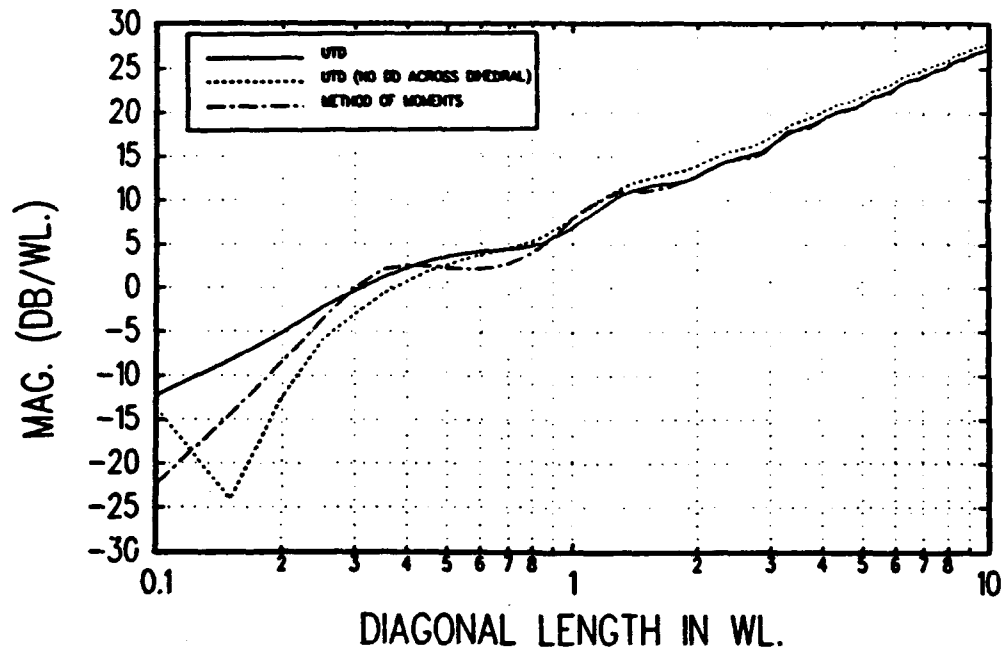
Figure 15: Contribution of the DD across the face of the dihedral for the backscatter case at 45° incident for the vertical polarization.
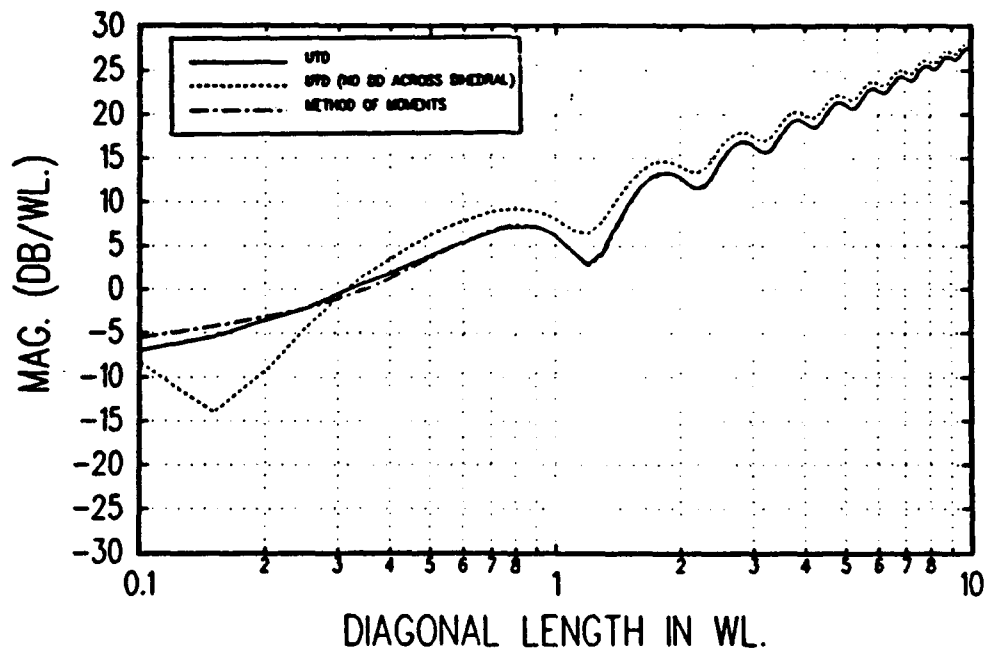
Figure 16: Contribution of the DD across the face of the dihedral for the backscatter case at 45° incident for the horizontal polarization.
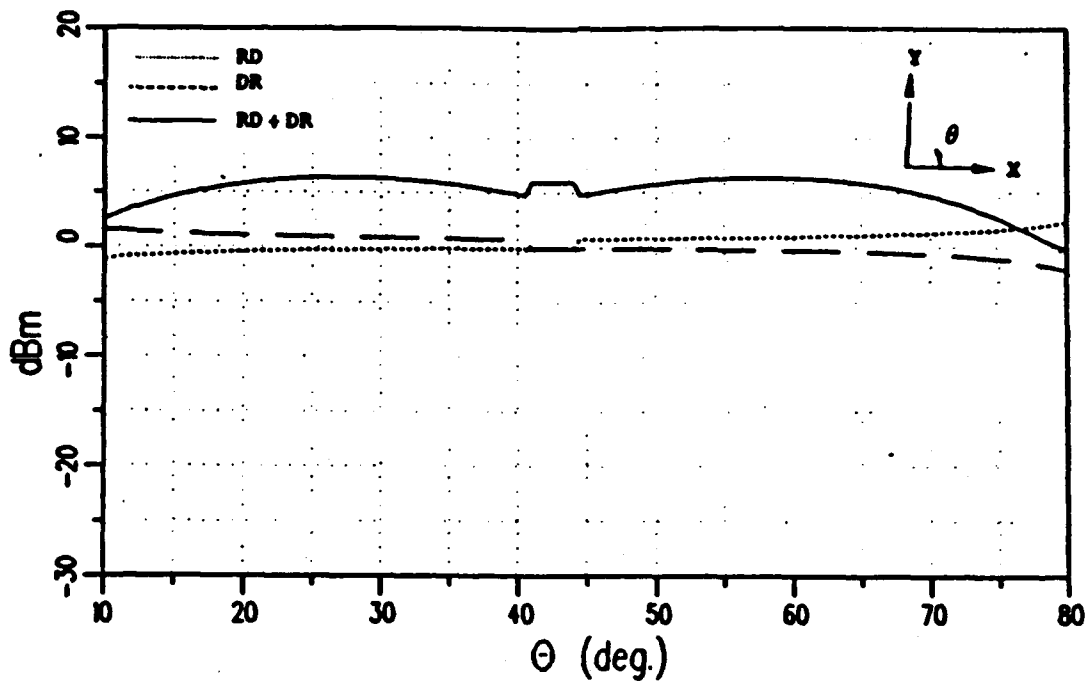
Figure 17: DR and RD terms for a 9 in 2-D dihedral at 10 GHz.
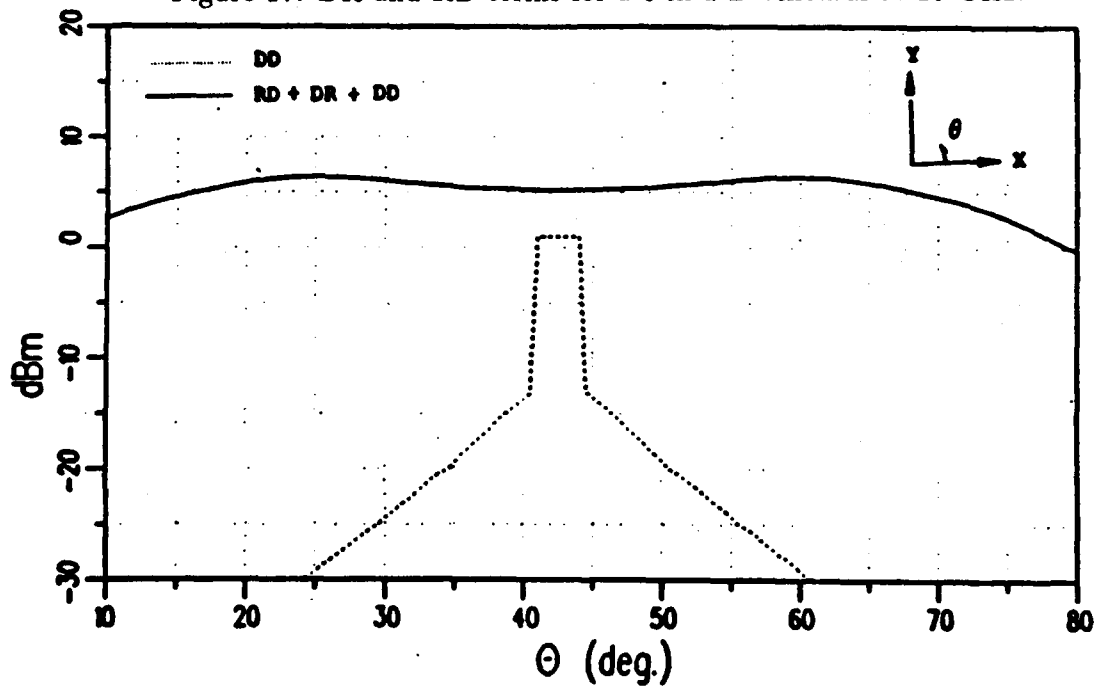
Figure 18: DD term used to eliminate the discontinuity.

Now consider the case when α is not close to $90°$. It is expected that the maximum scattering will occur when $\phi - \phi' - 2\alpha = -\pi$ or $\phi - \phi' + 2\alpha = \pi$. In this case, either the DR or RD is a major contributing factor along with the diffraction from the joint of the dihedral. Notice that the first condition is satisfied if $\phi > \phi'$ and $\alpha > 90°$, or $\phi < \phi'$ and $\alpha < 90°$ (D_1R or RD_2 term is the major contributing factor and only one term is present in a given region). The second condition is satisfied if $\phi > \phi'$ and $\alpha < 90°$, or $\phi < \phi'$ and $\alpha > 90°$ (RD_1 or D_2R term is the major contributing factor and only one term is present in a given region). Hence, it may be assumed that this is a region where diffraction from strip 1 and reflection from strip 2 is present. It is also observed that when the D_1R term is large, the first cotangent term of the singly diffracted term (Equation (63)) is also large. On the other hand, when the RD_1 term is large, the second cotangent term of the singly diffracted term (Equation (63)) is large too. For ϵ small, the case when

$$\phi - \phi' - 2\alpha = -\pi + \epsilon, \tag{81}$$

$$\cos\left(\frac{\phi - \phi' - 2\alpha}{2}\right) = \frac{\epsilon}{2}, \tag{82}$$

and

$$\cot\left(\frac{\pi + (\phi - \phi')}{2n}\right) = \frac{2\alpha}{\epsilon\pi}, \tag{83}$$

is considered. First, the contribution from D_1R and the first cotangent term of the single diffraction may be simplified to

$$U_{dominant}^{D_1R+D_{1st.cot}} = U_{s,h}^i \frac{-e^{-j\pi/4}}{2\sqrt{2\pi k}}\left[\frac{-2}{\epsilon}e^{jkl_1\cos\left(\frac{\phi+\phi'-2\alpha}{2}\right)\epsilon} + \frac{2}{\epsilon}\right] \tag{84}$$

$$U_{dominant}^{D_1R+D_{1st.cot}} = U_{s,h}^i e^{j\pi/4} \frac{l_1}{\sqrt{\lambda}}\cos\left(\frac{\phi+\phi'-2\alpha}{2}\right). \tag{85}$$

Using Equation (81) in (85) gives

$$U_{dominant}^{D_1R+D_{1st.cot}} = U_{s,h}^i e^{j\pi/4} \frac{l_1}{\sqrt{\lambda}}\sin(\phi'). \tag{86}$$

37

Next, the contribution of RD_1 and the second cotangent term of the single diffraction are obtained as

$$U_{dominant}^{RD_1 + D_{2nd,cot}} = U_{s,h}^i \frac{-e^{-j\pi/4}}{2\sqrt{2\pi k}}$$

$$\left[-\frac{e^{2jkl_1 \cos\left(\frac{\phi+\phi'-2\alpha}{2}\right)} \sin\left(2\alpha+\frac{\epsilon}{2}\right)}{\sin\left(2\alpha+\frac{\epsilon}{2}\right)} + \frac{\pi}{\alpha} \cot\left(\frac{\pi^2 - \frac{\epsilon\pi}{2}}{\alpha}\right) \right]. \tag{87}$$

At this stage, to simplify Equation (87) further, it is necessary to assume that α is close to 90°. Consider δ to be a small angle such that

$$\alpha = \pi/2 + \delta. \tag{88}$$

Now Equation (87) may be written as

$$U_{dominant}^{RD_1 + D_{2nd,cot}} = U_{s,h}^i e^{j\pi/4} e^{-2jkl_1\delta \cos\left(\frac{\phi+\phi'-2\alpha}{2}\right)}$$

$$\frac{l_1}{\sqrt{\lambda}} \cos\left(\frac{\phi+\phi'-2\alpha}{2}\right) \left\{ \frac{\sin\left[2\delta kl_1 \cos\left(\frac{\phi+\phi'-2\alpha}{2}\right)\right]}{2\delta kl_1 \cos\left(\frac{\phi+\phi'-2\alpha}{2}\right)} \right\}. \tag{89}$$

Again using Equation (81) in (89) gives

$$U_{dominant}^{RD_1 + D_{2nd,cot}} = U_{s,h}^i e^{j\pi/4} e^{-2jkl_1\delta \sin(\phi')}$$

$$\frac{l_1}{\sqrt{\lambda}} \sin(\phi') \left\{ \frac{\sin\left[2\delta kl_1 \sin(\phi')\right]}{2\delta kl_1 \sin(\phi')} \right\}. \tag{90}$$

Had the RD_1 term been large, the result would have been the same as Equations (85) and (89). However using the condition for maximum scattering for this case ($\phi - \phi' + 2\alpha = \pi$), Equation (85) becomes

$$U_{dominant}^{D_1R+D_{1st,cot}} = U_{s,h}^i e^{j\pi/4} \frac{l_1}{\sqrt{\lambda}} \sin(2\alpha - \phi') \tag{91}$$

and (89) becomes

$$U_{dominant}^{RD_1 + D_{2nd,cot}} = U_{s,h}^i e^{j\pi/4} e^{-2jkl_1\delta \sin(2\alpha-\phi')}$$

$$\frac{l_1}{\sqrt{\lambda}} \sin(2\alpha - \phi') \left\{ \frac{\sin\left[2\delta kl_1 \sin(2\alpha - \phi')\right]}{2\delta kl_1 \sin(2\alpha - \phi')} \right\} \tag{92}$$

38

In the region where RD_2 is large, the following equation would hold

$$U_{dominant}^{RD_2+D_{1st,cot}} = U_{s,h}^i e^{j\pi/4} \frac{l_2}{\sqrt{\lambda}} \sin(\phi' + \alpha) \tag{93}$$

and

$$U_{dominant}^{D_2R+D_{2nd,cot}} = U_{s,h}^i e^{j\pi/4} e^{-2jkl_2\delta \sin(\phi'+\alpha)}$$
$$\frac{l_2}{\sqrt{\lambda}} \sin(\phi' + \alpha) \left\{ \frac{\sin[2\delta kl_2 \sin(\phi' + \alpha)]}{2\delta kl_2 \sin(\phi' + \alpha)} \right\}. \tag{94}$$

On the other hand, in the region where D_2R is large

$$U_{dominant}^{D_2R+D_{1st,cot}} = U_{s,h}^i e^{j\pi/4} \frac{l_2}{\sqrt{\lambda}} \sin(\phi' - \alpha) \tag{95}$$

and

$$U_{dominant}^{RD_2+D_{2nd,cot}} = U_{s,h}^i e^{j\pi/4} e^{-2jkl_2\delta \sin(\phi'-\alpha)}$$
$$\frac{l_2}{\sqrt{\lambda}} \sin(\phi' - \alpha) \left\{ \frac{\sin[2\delta kl_2 \sin(\phi' - \alpha)]}{2\delta kl_2 \sin(\phi' - \alpha)} \right\}. \tag{96}$$

It is important to emphasize that Equations (84) to (96) are present over regions as given by Equations (72) to (75) and are valid for one of the two cases of maximum scattering as mentioned earlier. Figures 19, 20 and 21 are for equal length strip dihedrals of $\alpha = 92°$ (4° bistatic), 95° (10° bistatic) and 110° (40° bistatic), respectively, and compare the results obtained by the dominant UTD terms with that obtained by the UTD computer code. Good agreements are obtained in all regions except where the speculars from the strips are present, which are not included in the dominant UTD terms.

3 Specular Return From Dihedral Strips

As pointed out earlier, the specular from the individual strip faces is produced by D from the ends of the strips and the DR and DRD terms between the strips.

The importance of D and the DR terms is illustrated by the following. Consider the geometry shown in Figure 22. It is observed that the singly diffracted field
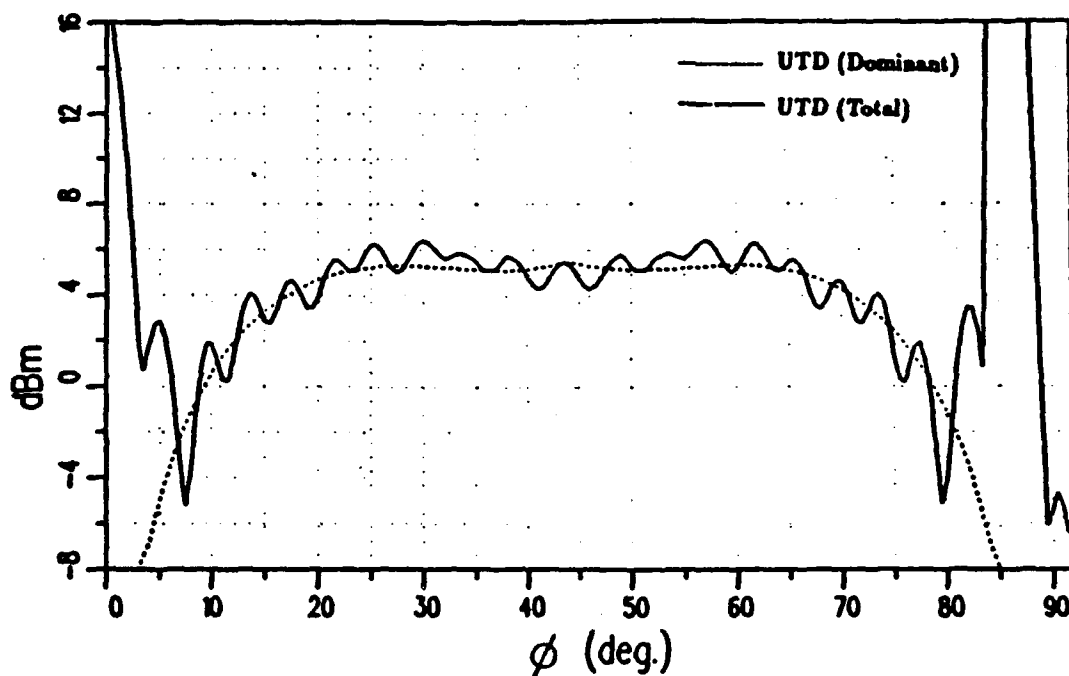
Figure 19: The dominant UTD terms and the UTD computer code results for 9 in 92° 2-D dihedral at 10 GHz (4° bistatic).
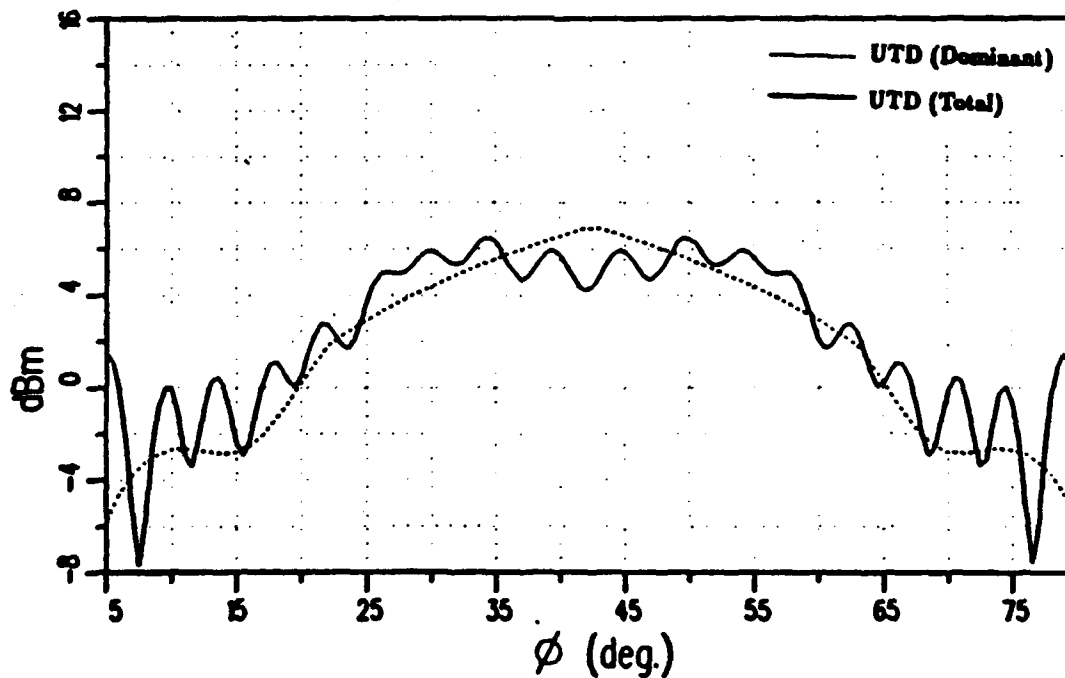
Figure 20: The dominant UTD and the UTD computer code results for 9 in 95° 2-D dihedral at 10 GHz (10° bistatic).

40
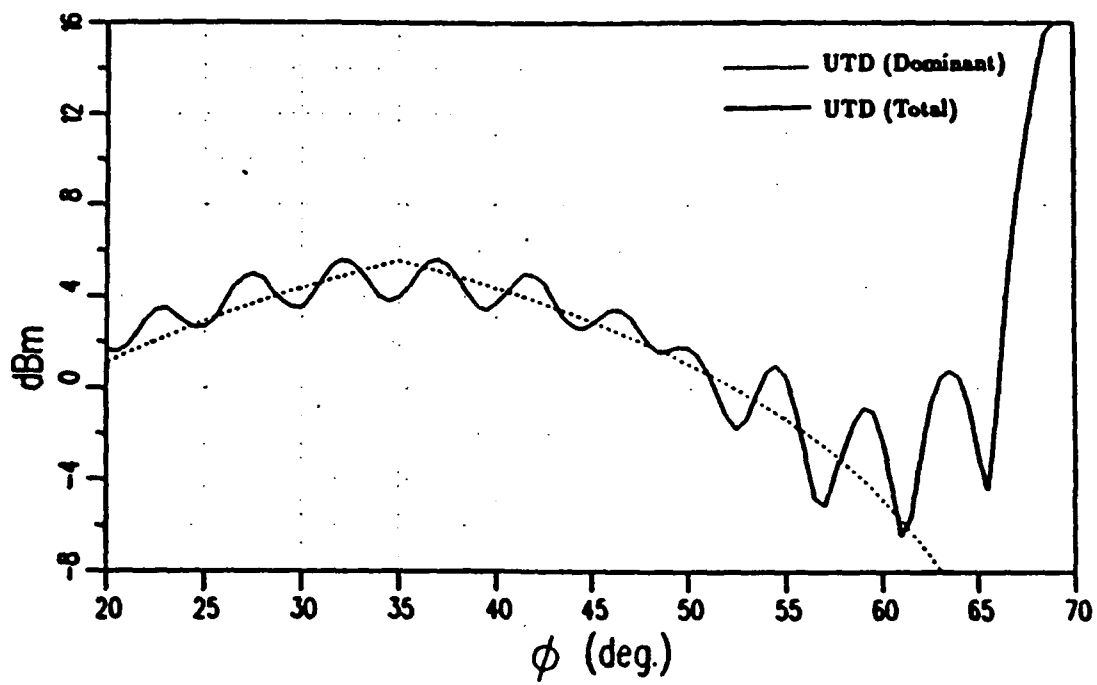
Figure 21: The dominant UTD terms and the UTD computer code results for 9 in 110° 2-D dihedral at 10 GHz (40° bistatic).
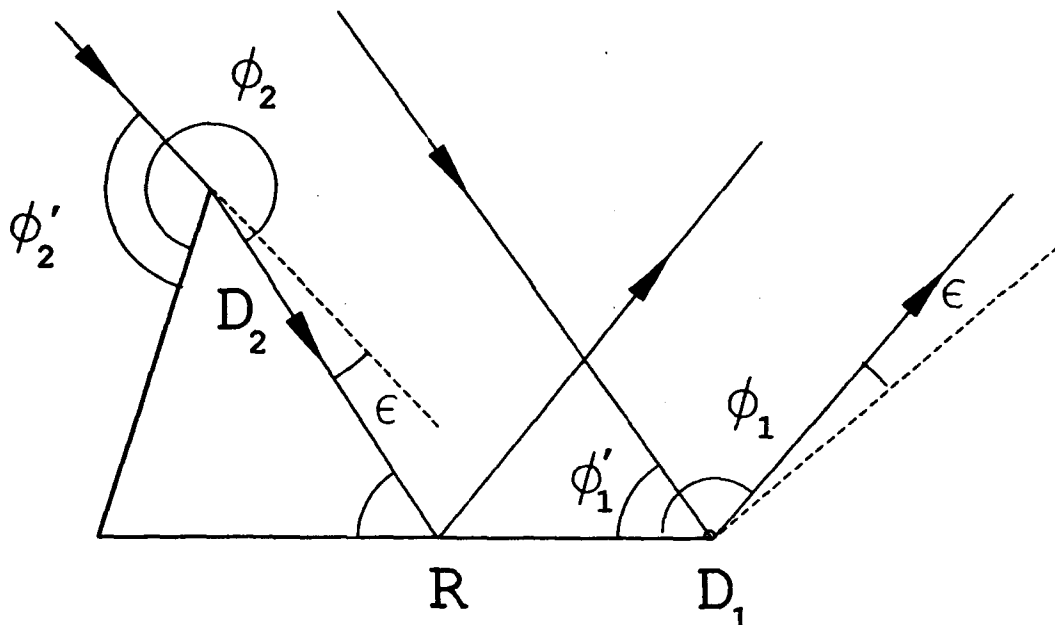
Figure 22: Cancellation of infinities of diffracted and diffracted-reflected terms.

D_1 appears to leave an infinity at the reflection shadow boundary. The diffracted - reflected field D_2R also appears to leave an infinity along the incident shadow boundary. However D_1 and D_2R combine to give a bounded result.

The diffracted field is

$$U^{D_1} = U^i_{s,h} D_{s,h}(Q_{e1}) e^{-jk\rho_1}, \tag{97}$$

where

$$U^i_{s,h} = \begin{cases} E^i, & \text{E parallel to wedge} \\ H^i, & \text{E perpendicular to wedge} \end{cases} \tag{98}$$

and

$$D_{s,h}(Q_{e1}) = \frac{-e^{-j\pi/4}}{2\sqrt{2\pi k}} \left(\frac{1}{\cos\left(\frac{\phi_1 - \phi'_1}{2}\right)} + R_{s,h} \frac{1}{\cos\left(\frac{\phi_1 + \phi'_1}{2}\right)} \right), \tag{99}$$

where the reflection coefficient, $R_{s,h} = \mp 1$. Along the reflection shadow boundary,

$$\cos\left(\frac{\phi_1 + \phi'_1}{2}\right) = \cos(\pi/2 - \epsilon/2) = \epsilon/2. \tag{100}$$

42

For the DR field,

$$U^{D_2R} = U'_{s,h}R_{s,h}D_{s,h}(Q_{r2})e^{-jk\rho_2}, \tag{101}$$

where

$$D_{s,h}(Q_{r2}) = \frac{-e^{-j\pi/4}}{2\sqrt{2\pi k}}\left(\frac{1}{\cos\left(\frac{\phi_2-\phi'_2}{2}\right)} + R_{s,h}\frac{1}{\cos\left(\frac{\phi_2+\phi'_2}{2}\right)}\right). \tag{102}$$

Along the incident shadow boundary,

$$\cos\left(\frac{\phi_2-\phi'_2}{2}\right) = \cos(\pi/2 + \epsilon/2) = -\epsilon/2. \tag{103}$$

By adding the *singular* terms of D_1 and D_2R, the following is obtained

$$U^{singular\ total} = U'_{s,h}R_{s,h}\frac{-e^{-j\pi/4}}{2\sqrt{2\pi k}}\left(\frac{2}{\epsilon}\right)e^{-jk\rho_1} + U'_{s,h}R_{s,h}\frac{-e^{-j\pi/4}}{2\sqrt{2\pi k}}\left(\frac{-2}{\epsilon}\right)e^{-jk\rho_2}, \tag{104}$$

where the phase contributions (see Figure 23) are

$$e^{-jk\rho_1} = e^{-jkr}e^{-jk[d\cos(\epsilon)+(x+l)\cos(\phi)]}, \tag{105}$$

and

$$e^{-jk\rho_2} = e^{-jkr}e^{-jk[d+(\frac{d\sin(\epsilon)}{\sin(\phi)}+l)\cos(\phi+\epsilon)]}. \tag{106}$$

Equation (104) can be written as

$$U^{singular\ total} = U'_{s,h}R_{s,h}\frac{e^{-j\pi/4}}{2\sqrt{2\pi k}}e^{-jk\left[d+l\cos(\phi)+\frac{d\epsilon}{\sin(\phi)}\cos(\phi)+\frac{\epsilon}{2}l\sin(\phi)\right]}$$
$$\left\{2jkl\sin(\phi)\left[\frac{\sin(kl\frac{\epsilon}{2}\sin(\phi))}{kl\frac{\epsilon}{2}\sin(\phi)}\right]\right\}. \tag{107}$$

As ϵ approaches zero, Equation (107) becomes

$$U^{singular\ total} = U'_{s,h}R_{s,h}\frac{e^{j\pi/4}}{\sqrt{2\pi k}}e^{-jk[d+l\cos(\phi)]}\left\{kl\sin(\phi)\right\}. \tag{108}$$

Note that this gives the PO result for a strip of length l.

It is observed that for the backscatter case from a 90° dihedral, the DR term is shadowed due to the diffraction reflection shadow boundary ($\phi = 90°$). As pointed out in the next section, it is the DRD term that takes care of this discontinuity. Figure 24 shows that the inclusion of DRD term ensures the continuity and gives the correct result. Note that at $\phi = 90°$ only the 9 in strip is visible, which by PO gives a result of 10.39 dBm. The result obtained by Figure 24 is 10.26 dBm.

43
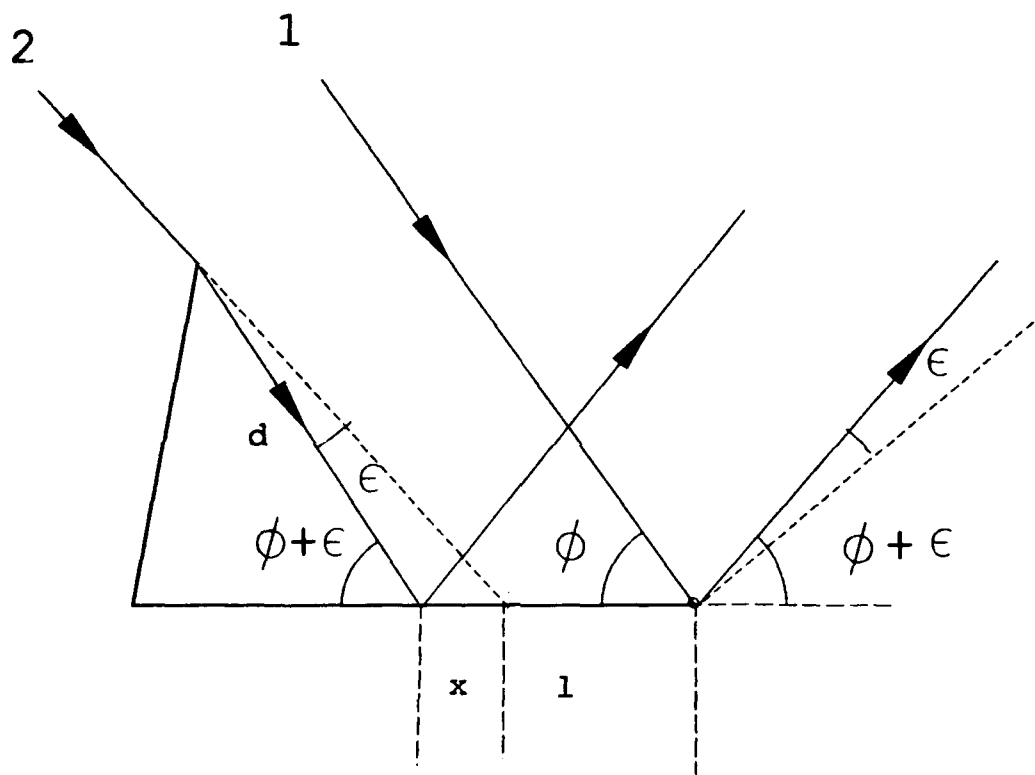
Figure 23: Phase of D, and DR terms.
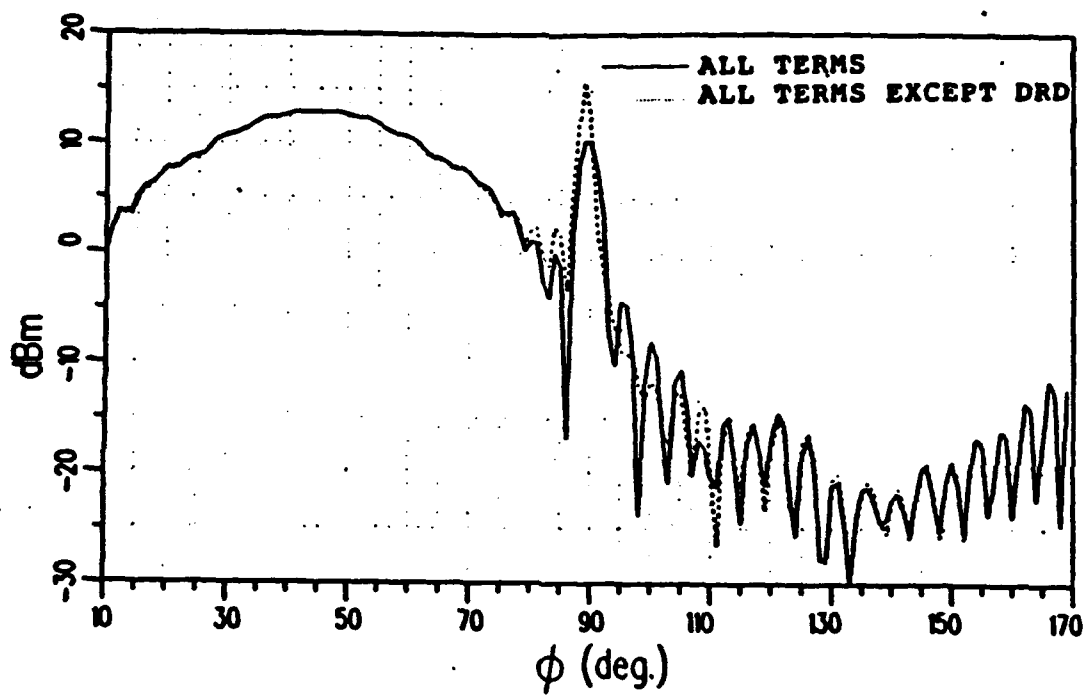
Figure 24: Importance of DRD term. The results are for a 9 in 90° 2-D dihedral at 10 GHz.

4 Continuity of Fields by Including Double Diffraction

Figure 25 shows the shadow boundaries that can result after the first diffraction. The diffracted field is discontinuous across the diffraction incident shadow boundary (DSB), and the diffracted -reflected field is discontinuous across the diffraction reflection shadow boundary (DRSB). The $D_1 D_2$ field compensates for the discontinuity of D_1 and $D_1 R$ fields. The double diffraction formulation, for separate wedges, as given by Equation (51), has 16 terms. Across the DSB or DRSB one of the terms becomes infinite. This term is determined by the values of Φ_p and Φq (Equations (49) and (50)) which make the cotangent ($\cot\left(\frac{\Phi_p}{2n_1}\right)$ and $\cot\left(\frac{\Phi_q}{2n_2}\right)$) unbounded. Thus, any term can become singular depending on the geometry and the position of the source and the receiver. As shown in an example below, the same holds true if the wedges are joined.

Consider the case when the two wedges are not joined, as shown in Figure 26. Since $\pi - (\phi_1 - \phi_1') = 0$, $\cot(0) = \infty$, and $\pi + (\phi_2 + \phi_2') = 4\pi$, $\cot(\pi) = \infty$, at the boundaries, thus the term $P(\Phi_{p=1}, \Phi_{q=4})$ will balance the singularity of the singly diffracted field. The terms $P(\Phi_{p=1}, \Phi_{q=1}) + P(\Phi_{p=1}, \Phi_{q=2}) + P(\Phi_{p=1}, \Phi_{q=3})$ balance the discontinuity that results from the diffraction by the edge Q_2 being shadowed by edge Q_1. The terms $P(\Phi_{p=2}, \Phi_{q=4}) + P(\Phi_{p=3}, \Phi_{q=4}) + P(\Phi_{p=4}, \Phi_{q=4})$ balance the discontinuity that results from the diffraction by edge Q_1 being shadowed by edge Q_2.

In the above sections, the doubly diffracted field was necessary to get the continuity of the fields in two cases. (See Figures 24 and 18.) In both of these cases the discontinuity is a result of being on the DRSB. In this section, a case where the discontinuity is along the DSB is considered. It is shown mathematically, as well as by plots, how the inclusion of doubly diffracted field compensates for the singularities and discontinuities. In Figure 27, $\epsilon_1 \simeq 0$ and $\epsilon_2 \simeq 0$ i.e., both incidence and observation aspects are close to grazing. Note that for $\epsilon_1 < 0$ and $\epsilon_2 > 0$,

46

$$\phi_2^r + \phi_2' = \pi$$

$$\phi_2^i - \phi_2' = \pi$$
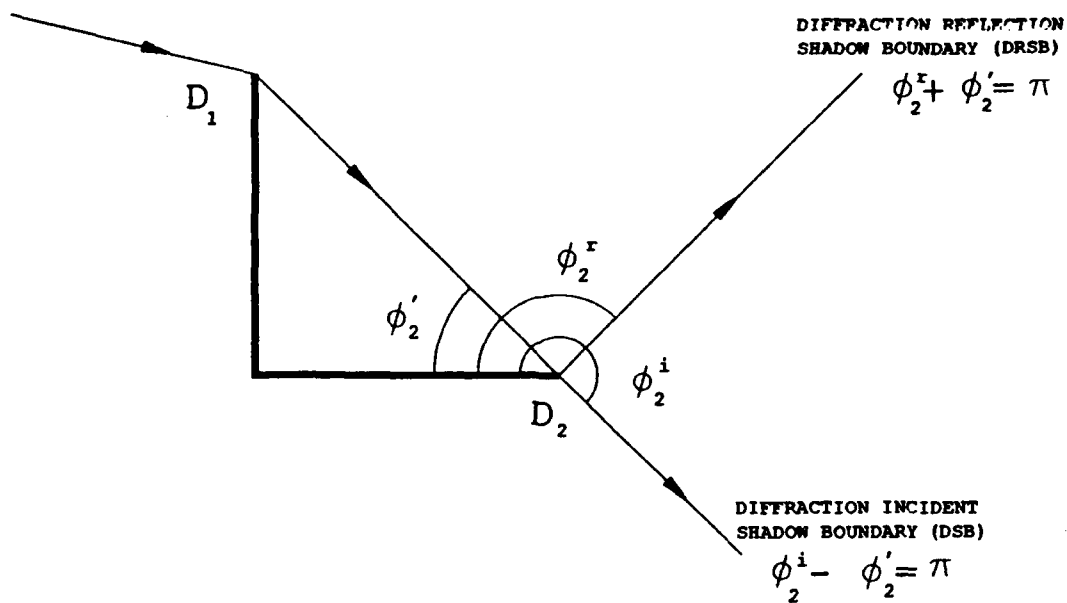
Figure 25: Illustration of diffraction incident (DSB) and diffraction-reflection shadow boundary (DRSB).
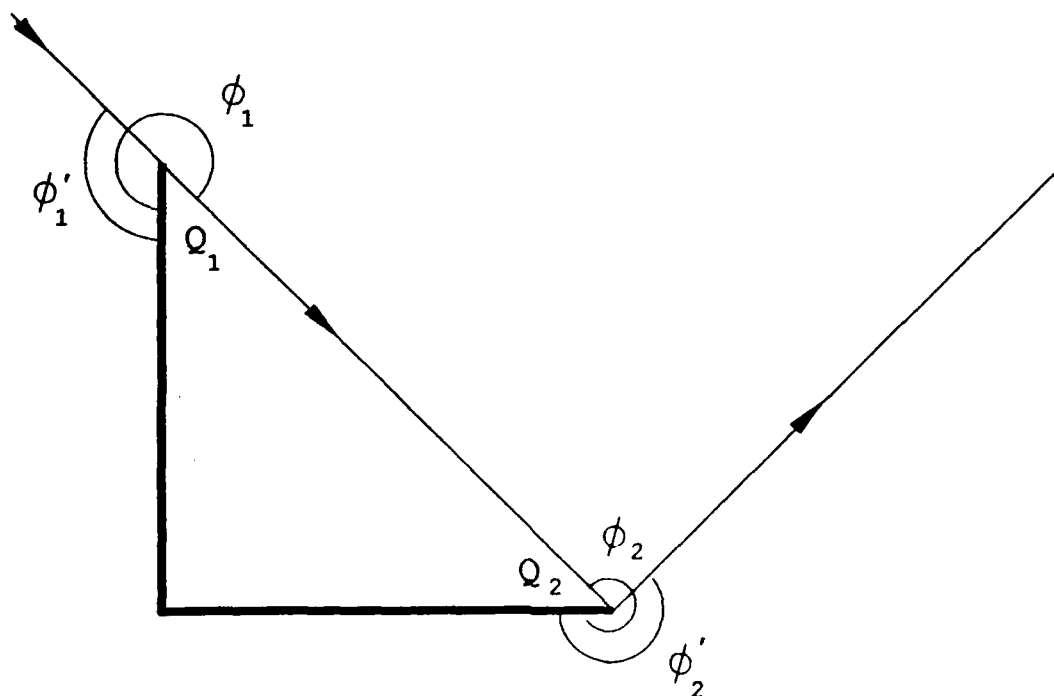
Figure 26: Balancing of fields for disjoined wedges.
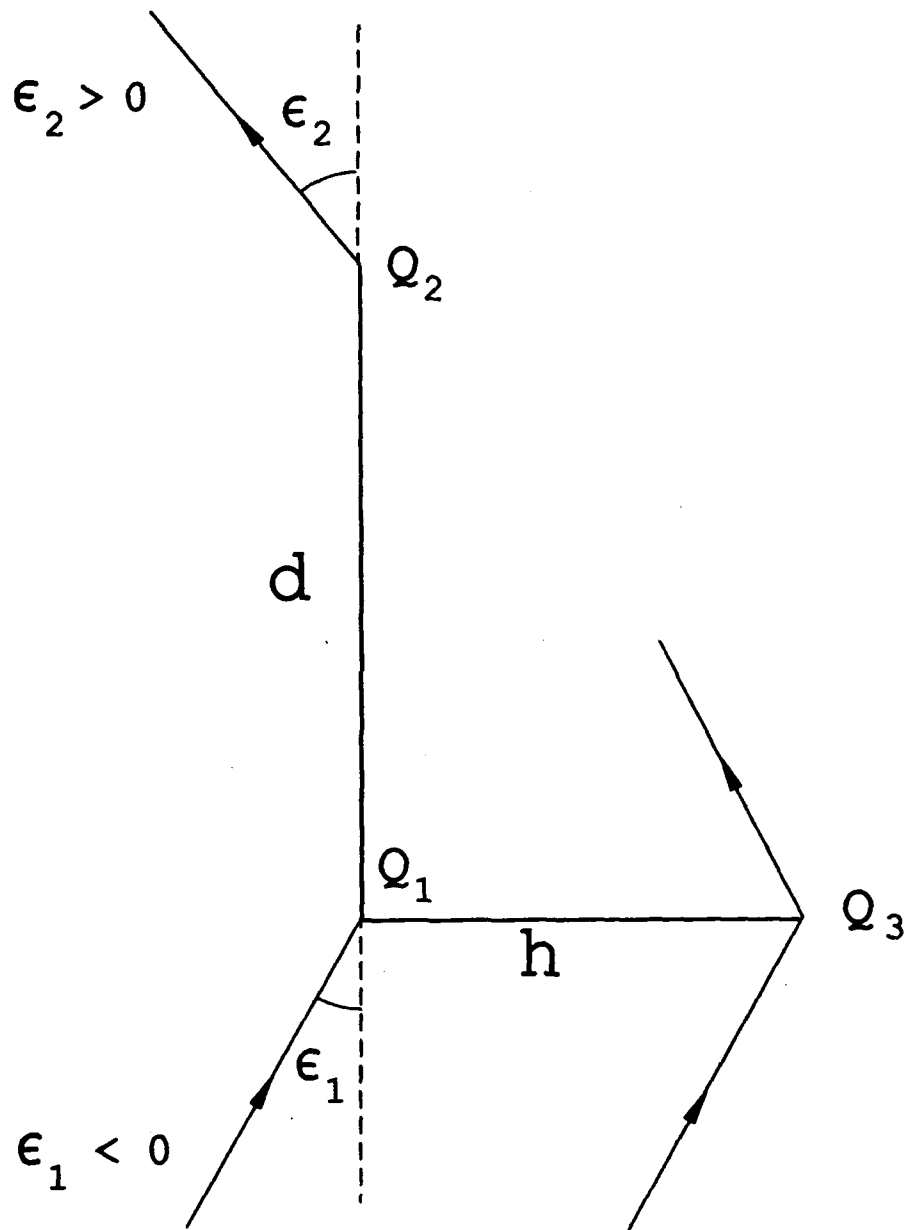
Figure 27: Balancing of fields for joined wedges.

diffraction from D_1, D_2 and D_3 is present. But for $\epsilon_1 < 0$ and $\epsilon_2 < 0$, only diffraction from D_2 and D_3 is observed. Details of the equations below are given in Appendix A. The contribution of the fields singly diffracted by Q_1 can be expressed as a singular contribution given by

$$P'_{e,m}(Q_1) = \frac{e^{-j\pi/4}}{\sqrt{2\pi k}} \left[\frac{\epsilon_2}{\epsilon_1^2 - \epsilon_2^2} \right] e^{-jkd} [1 + sgn(\epsilon_2)] \tag{109}$$

and a non-singular contribution of

$$P''_{e,m}(Q_1) = \frac{-e^{-j\pi/4}}{2n\sqrt{2\pi k}} \left[\cot\left(\frac{2\pi + \epsilon_1 - \epsilon_2}{2n} \right) \right.$$
$$\left. \mp \cot\left(\frac{2\pi + \epsilon_1 + \epsilon_2}{2n} \right) \right] e^{-jkd} \frac{1}{2} [1 + sgn(\epsilon_2)]. \tag{110}$$

Similarly, separating $P_{e,m}(Q_2)$ into a singular and a non-singular part, where the singular part is given as

$$P'_{e,m}(Q_2) = \frac{e^{-j\pi/4}}{\sqrt{2\pi k}} \left[\frac{\epsilon_1}{\epsilon_1^2 - \epsilon_2^2} \right] e^{-jkd} [1 - sgn(\epsilon_1)] \tag{111}$$

and the non-singular part is

$$P''_{e,m}(Q_2) = \frac{-e^{-j\pi/4}}{2n\sqrt{2\pi k}} \left[\cot\left(\frac{2\pi - \epsilon_2 + \epsilon_1}{2n} \right) \right.$$
$$\left. \mp \cot\left(\frac{2\pi - \epsilon_2 - \epsilon_1}{2n} \right) \right] e^{-jkd} \left[\frac{1}{2} \right] [1 - sgn(\epsilon_1)]. \tag{112}$$

For the single diffracted field from Q_3, the singular term is given as

$$P'_{e,m}(Q_3) = \frac{-e^{-j\pi/4}}{\sqrt{2\pi k}} \left[\frac{1}{\epsilon_1 - \epsilon_2} \right] e^{jkh(\epsilon_1 - \epsilon_2)} e^{-jkd}. \tag{113}$$

The double diffraction term obtained by setting $p = 1$ and $q = 1$ in Equation (44) compensates for the discontinuity and singularities of the single diffracted fields. This term is given as

$$P_{s,h}(\Phi_{p=1}, \Phi_{q=1}) = \frac{-e^{-j\pi/4}}{\sqrt{2\pi k}} \left\{ \frac{\epsilon_2 sgn(\epsilon_2) - \epsilon_1 sgn(\epsilon_1)}{\epsilon_1^2 - \epsilon_2^2} \right\} e^{-jkd}$$
$$- \frac{1 \pm 1}{2} \frac{\sqrt{d}}{r} e^{-jkd}. \tag{114}$$

Adding all the *singular* terms of singly diffracted fields from Q_1, Q_2 and Q_3, and doubly diffracted field from Q_1 and Q_2, Equations (109), (111), (113) and (114), the following is obtained

$$P_{e,m}^{singular\ total} = \frac{e^{-j\pi/4}}{\sqrt{2\pi k}} \left[\frac{1}{\epsilon_1 - \epsilon_2} - \frac{e^{jkh(\epsilon_1 - \epsilon_2)}}{\epsilon_1 - \epsilon_2} \right] - \frac{1 \pm 1}{2} \frac{\sqrt{d}}{\pi} e^{-jkd}. \tag{115}$$

Now for ϵ_1 and ϵ_2 zero, the above equation becomes

$$P_{e,m}^{singular\ total} = -e^{j\pi/4} \frac{h}{\sqrt{\lambda}} - \frac{1 \pm 1}{2} \frac{\sqrt{d}}{\pi} e^{-jkd}. \tag{116}$$

Note that the first term is equivalent to a PO result of the strip of length h. The second term is the correction to the PO. Figure 28 shows that the inclusion of the diffracted-diffracted term ensures continuity. Thus, the UTD formulation of the double diffraction presented in [2] provides the compensation of the singularities, so that the leading term of the total scattered far field is well behaved in the neighborhood of the shadow boundary (DSB) of the diffracted incident field.

Now, consider the continuity of the non-singular part of the diffracted terms. It is also noted that $P_{e,m}''(Q_1)$ vanishes due to shadowing by the edge Q_2 ($\epsilon_2 < 0$), and similarly, $P_{e,m}''(Q_2)$ vanishes due to shadowing by the edge Q_1 ($\epsilon_1 > 0$). From the discussion in the beginning of this section, it is expected that the term $P_h(\Phi_{p=2}, \Phi_{q=1} = \epsilon_2)$ ensures continuity of $P_{e,m}''(Q_1)$. From Equation (110), when $\epsilon_2 \simeq 0$,

$$P_m'' = -\frac{e^{-j\pi/4}}{2n_1 \sqrt{2\pi k}} \cot \left(\frac{2\pi + \epsilon_1}{2n} \right) \{1 + sgn(\epsilon_2)\} e^{-jkd} \tag{117}$$

and from Equation (42) and (43),

$$\Phi_{p=2} = \pi + (n_1 \pi - (n_1 \pi - \pi - \epsilon_1)) = 2\pi + \epsilon_1 \tag{118}$$

$$\Phi_{q=1} = \pi - (n_2 \pi - (n_2 \pi - \pi - \epsilon_2)) = \epsilon_2 \tag{119}$$

$$N_{i=2} = \frac{2\pi + \epsilon_1}{2n\pi} = 1 \quad for \ \ 0.67 < n < 2 \tag{120}$$

$$a_{p=2} = 2\cos^2 [(2\pi + \epsilon_1)/2 - \pi/2 - 2n\pi/2] = 2\sin^2 [\pi(1 - n) + \epsilon_1/2] \tag{121}$$
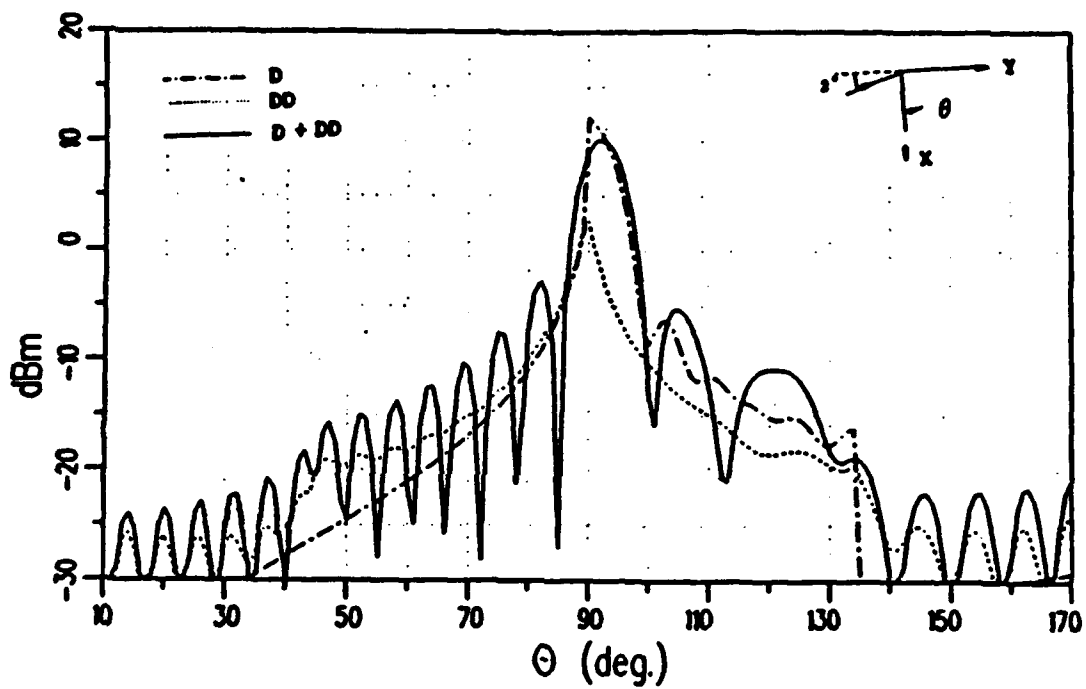
Figure 28: Importance of the doubly diffracted term for the field to be continuous for TE case.

for $n=3/2$

$$P_h = \frac{-1}{4\pi j n_1 n_2} \cot\left(\frac{2\pi + \epsilon_1}{2n_1}\right)\left(\frac{2n_2}{\epsilon_2}\right)$$

$$\left\{\frac{\epsilon_2^2/2 - 2\sqrt{2\pi k d \epsilon_2^2/4}e^{j\pi/4}}{2 - \epsilon_2^2/2}\right\}\frac{e^{-jkd}}{k\sqrt{d}} \qquad (122)$$

again neglecting terms of order ϵ_1^2 and ϵ_2^2,

$$P_h = \frac{e^{-j\pi/4}}{2n_1\sqrt{2\pi k}}e^{-jkd}\cot\left(\frac{2\pi + \epsilon_1}{2n_1}\right)sgn(\epsilon_2)e^{-jkd}. \qquad (123)$$

Thus $P_m'' + P_h$ (Equations (117) and (123)) is continuous across the shadow boundary. Similarly it may be shown that the term $P_h(\Phi_{p=1}, \Phi_{q=2})$ ensures continuity of $P_m''(Q_2)$.

However, for a TM plane wave illumination, $P_e''(Q_1)$ and $P_e''(Q_2)$ vanishes rapidly at $\epsilon_1 = \epsilon_2 = 0$, so that no discontinuity occurs due to the shadowing by Q_1 and Q_2. However, the terms $P_s(\Phi_{p=2}, \Phi_{q=1})$ and $P_s(\Phi_{p=1}, \Phi_{q=2})$ provide a contribution which, as expected, is continuous across the DSB and provides a smoother transition from the lit into the shadow region of the field for rays singly diffracted from edges.

From Equation (45),

$$P_s(\phi_{p=2}, \phi_{q=1}) = -\frac{1}{8\pi j(n_1 n_2)^2}\left\{\frac{2\epsilon_2^2/4}{sin^2\left(\frac{2\pi + \epsilon_1}{2n_1}\right)\left(\frac{\epsilon_2^2}{4n_2^2}\right)}\right\}\left\{\begin{array}{c}1\\2\end{array}\right\}\frac{e^{-jkd}}{k\sqrt{d}} \qquad (124)$$

$$= -\frac{1}{8\pi j n_1^2}\left(\frac{1}{sin^2\left(\frac{2\pi + \epsilon_1}{2}\right)}\right)\frac{e^{-jkd}}{k\sqrt{d}}. \qquad (125)$$

Figure 29 shows how the result is affected by including the DD field for the case when the TM plane wave is incident.

5 More Multiple Plate UTD Terms

The previous sections discussed the plate interaction terms that provide the basic dihedral characteristic pattern. This section briefly outlines other higher order mechanisms that contribute to the pattern. Depending on the angle of the dihedral
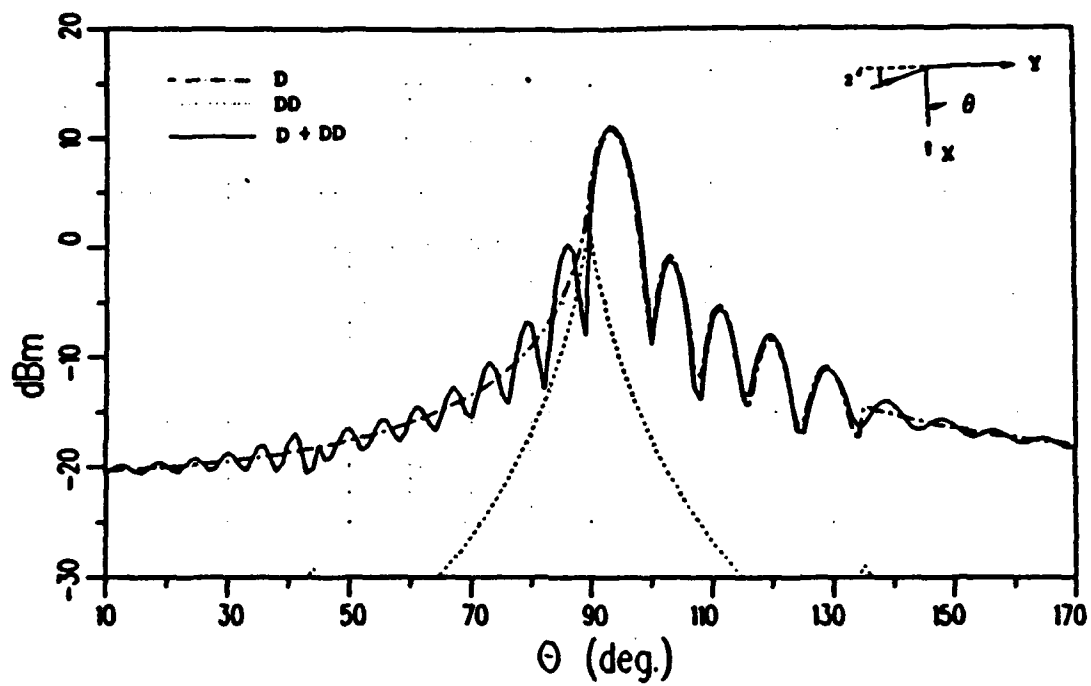
Figure 29: For the TM case, the doubly diffracted field provides a smoother transition.

and on the bistatic angle any one of these terms can be important. In general, as the frequency decreases, that is, as the size of the object in wavelengths gets smaller, more higher order terms need to be added.

The various UTD terms can be derived by using combinations of the theory in Section 2. The importance of single diffraction (D), DR and RD terms in giving rise to the main beam of the pattern, and the single diffracted, DR and the DRD terms in giving the specular from the strips has already been considered. The RRD and the DRR terms are present when the angle of the dihedral is less than 90°. Of course, these two terms are most significant when the diffraction is along a reflection shadow boundary RSB. Although the RDR term is present for all angles of the dihedral, its significance is greatest when the angle of the dihedral is less than 90° and the diffraction is along a reflection shadow boundary.

A discontinuity will result if a reflection falls off the edge for which a diffraction must be included to balance the fields. Therefore, the DDR term compensates for the discontinuity of the DRR and RDR terms. The RDD term compensates for the discontinuity of the RRD and RDR terms. Also the DRD compensates for the discontinuity of the RRD and DRR terms. Discontinuities of the DDR, DRD, and RDD are balanced by the triply diffracted fields. Thus, one term may be balanced by a number of different terms and vice versa depending on the geometry.

6 Results of Rectangular Dihedral

In this section, the theory and computer code are validated by comparing the UTD results to the results based on a 2-D method of moments [18, 19] solution of the rigorous integral equation for the currents induced on the target by the illumination. Unless explicitly shown in the pattern, the geometry of the dihedral is as shown in Figure 12. In order to calculate the backscatter results, a slight bistatic angle is used to avoid numerical limit difficulties when approaching indeterminate forms on the computer; alternatively, one could calculate the limits analytically using

L'Hopital's rule and calculate the fields without requiring one to use slight bistatic angles. Method of Moments is chosen to validate the results as an independent check, since both are two-dimensional. Fairly large sized dihedrals can be calculated using Method of Moments in the 2-D case. In 3-D, limits on computer memory restrict the size of dihedral that can be analyzed using Method of Moments. A 9 in 2-D dihedral is analyzed at 2 GHz and 10 GHz which means the dihedral is 1.52 and 7.62 wavelengths on a side, respectively. All the patterns are normalized to dB below a meter, that is a two dimensional cross section.

For the vertically polarized incident field, the backscatter from a 90° dihedral, Figure 30 shows the singly diffracted (D) term, DR, and RD terms. Figure 31 shows the D, RD and DR terms combined, the DRD term, and the DD term. This is all that is required to get the complete result for the 90° dihedral. Figure 32 shows the result obtained by the D, DR, RD, DRD, and DD terms combined. Notice that the result obtained by Figure 32 is the same as that obtained by all the terms of the UTD computer code. (See Figure 45.)

For the backscatter case with strips of equal lengths, based on simple reflection concepts, the order of interactions required to get the pattern in between the strips is $\text{INT}\left(\frac{180°}{\alpha}\right)$. Where INT denotes the integral value of $\left(\frac{180°}{\alpha}\right)$. Thus, for $\alpha = 60°$ third order terms are required to get the pattern in between the strips. Figure 33 shows how only the third order terms for a dihedral of 60° combine to give the correct result in between the strips. Figure 34 compares the Method of Moments results with that of the UTD computer code (with all terms present) for a dihedral of 60°. Notice that the discontinuity at $\phi = 60°$ in Figure 33 and Figure 34 is due the triply diffracted field which has not been included in the computer code. Our formulation indicates that for $\alpha = 45°$, fourth order interactions are required. Since the UTD computer code does not take into account all the fourth order interactions, we expect no agreement of the results in between the strips. This is shown in Figure 36. However, even for this case, notice the excellent agreement for ϕ greater then 50°. Thus, for the
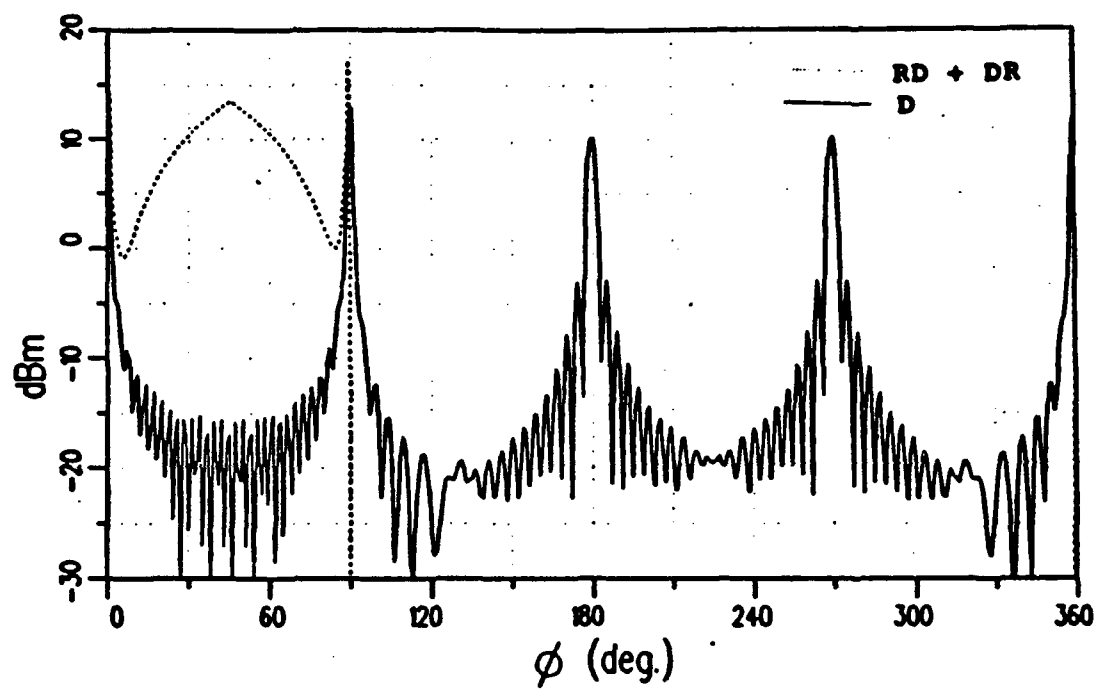
Figure 30: D, DR, and RD terms for the backscatter for 9 in 90° rectangular dihedral at 10 GHz (vertically polarized).

56
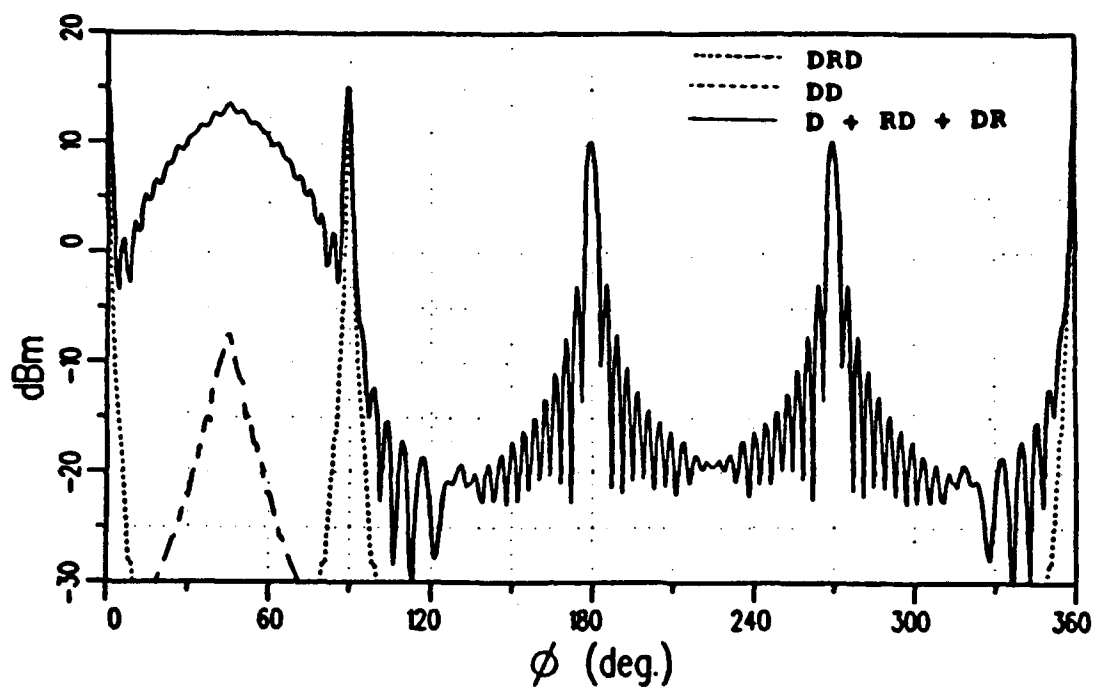
Figure 31: All terms of the above figure, DRD, and DD terms for the backscatter for 9 in 90° rectangular dihedral at 10 GHz (vertically polarized).
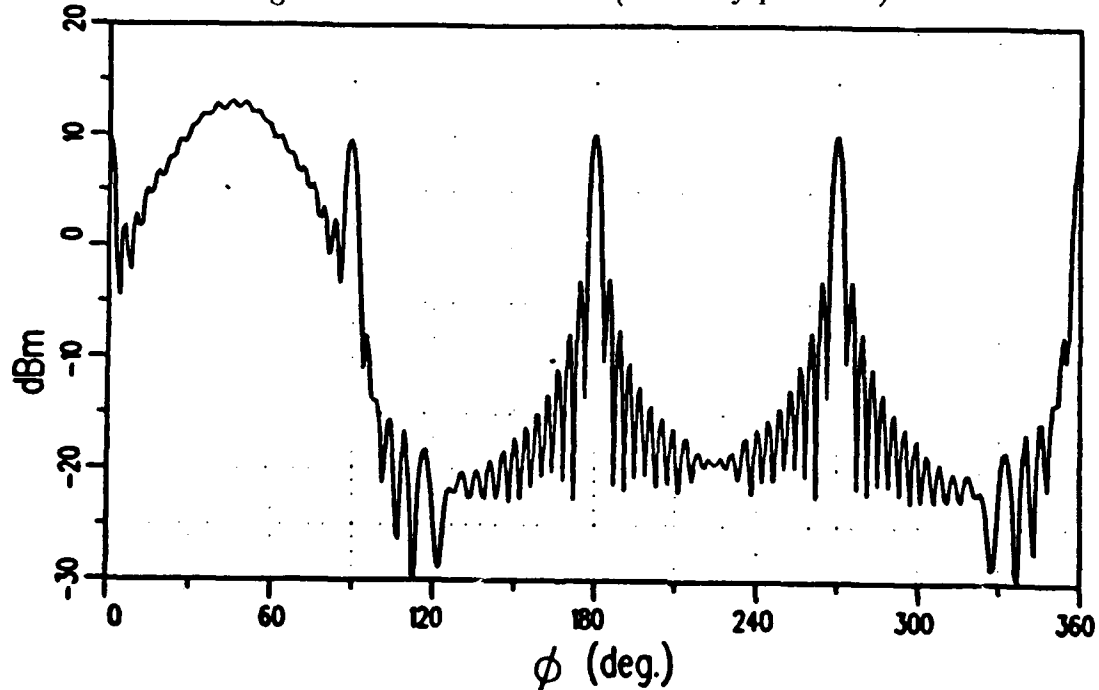
Figure 3'. All terms required to get the backscatter result for 9 in 90° rectangular dihedral at 10 GHz (vertically polarized).

terms present in the computer code, the pattern would worsen gracefully in between the strips for α less then 60°. As the angle of the dihedral becomes smaller, more terms are required to give the correct result in between the strips and a "cavity" effect results.

From here on, the UTD results contain all of the terms discussed above. For the backscatter case, from Geometrical Optics, a main beam is expected when the angle of the dihedral is such that $\left(\frac{180°}{\alpha}\right)$ is an integer. This is clearly evident in Figures 32, 35 and 36. Also, as the angle of the dihedral diverts from α, which makes $\left(\frac{180°}{\alpha}\right)$ an integer, the main beam falls. Figures 37 to 41 show backscatter results for $\alpha = 85, 92, 94, 95,$ and 120° with the incident field horizontally polarized. As expected, the main beam of the pattern for $\alpha = 90°$ falls as α is decreased or increased.

The backscatter field for the 2 GHz case is shown in Figure 42 for horizontal polarization and in Figure 43 for vertical polarization. The 10 GHz backscatter case is shown in Figures 44 and 45 for the horizontal and vertical polarizations, respectively. Patterns for a fixed bistatic angle of 90° are shown next. The 2 GHz case is shown in Figure 46 for horizontal polarization and in Figure 47 for vertical polarization. The 10 GHz patterns are shown in Figures 48 and 49 for horizontal and vertical polarizations, respectively. In all cases the agreement is excellent. The small dihedrals have slightly more disagreement due to the fact that the higher order interactions are more important. It is assumed that even better agreement and/or smaller sized dihedrals could be achieved by including more interactions. For engineering accuracy, however, this would not seem to be necessary in this application.
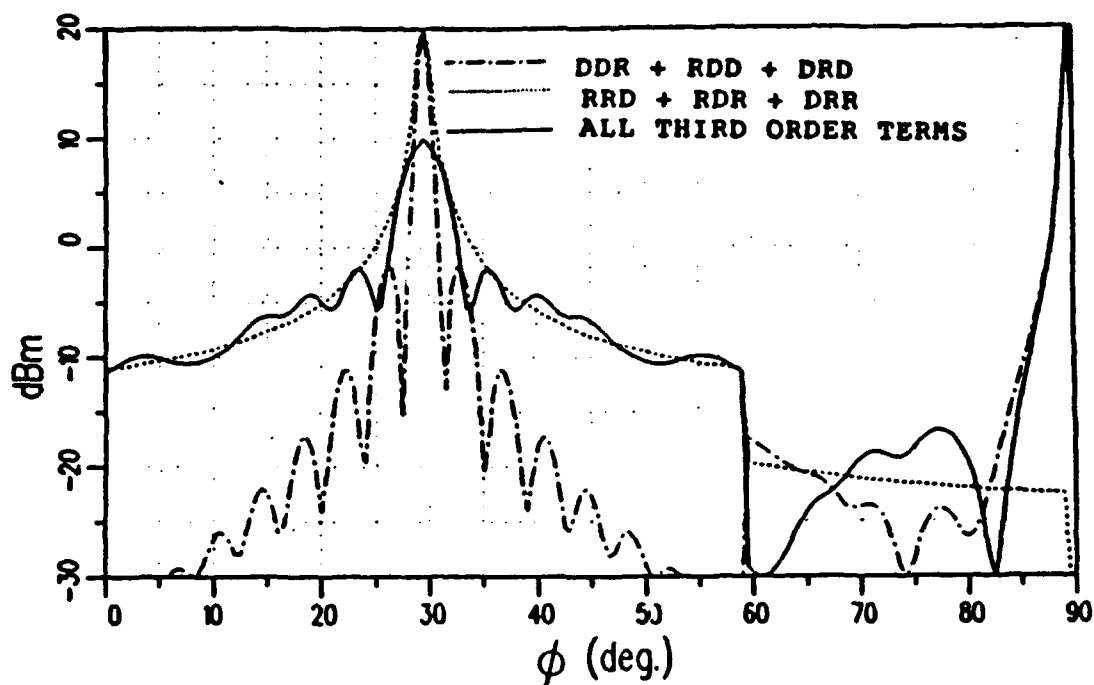
Figure 33: Only third order terms give continuous result for 9 in 60° rectangular dihedral at 10 GHz for horizontally polarized field (backscatter).
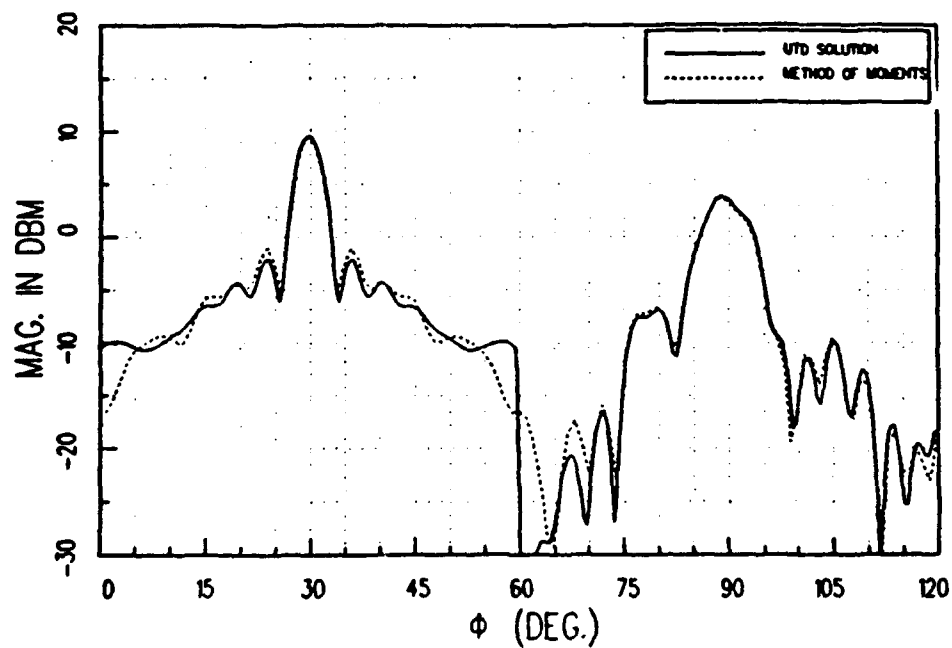
Figure 34: Backscatter field from a 9 in 60° rectangular dihedral at 10 GHz for horizontally polarized field.
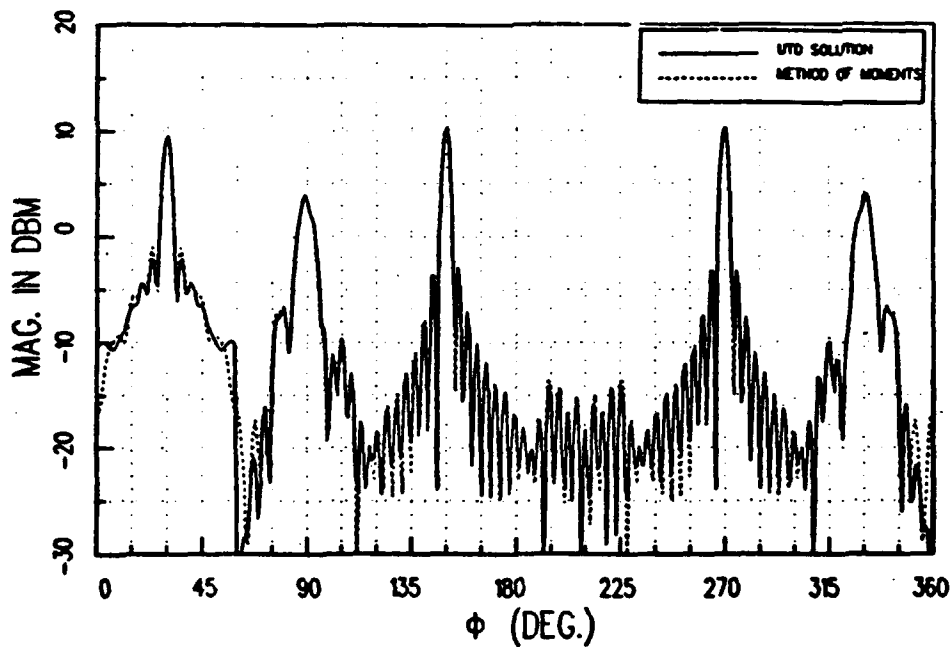
Figure 35: Backscatter result for 9 in 60° rectangular dihedral at 10 GHz for horizontally polarized field.
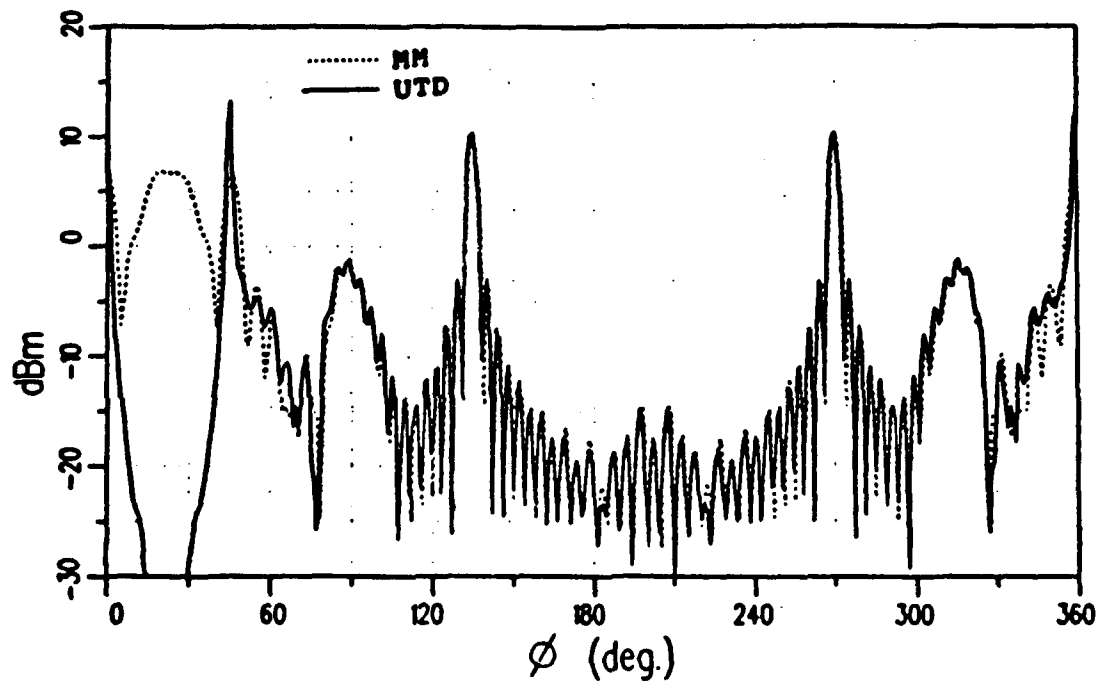
Figure 36: Backscatter field from a 9 in 45° rectangular dihedral at 10 GHz for horizontally polarized field.

60
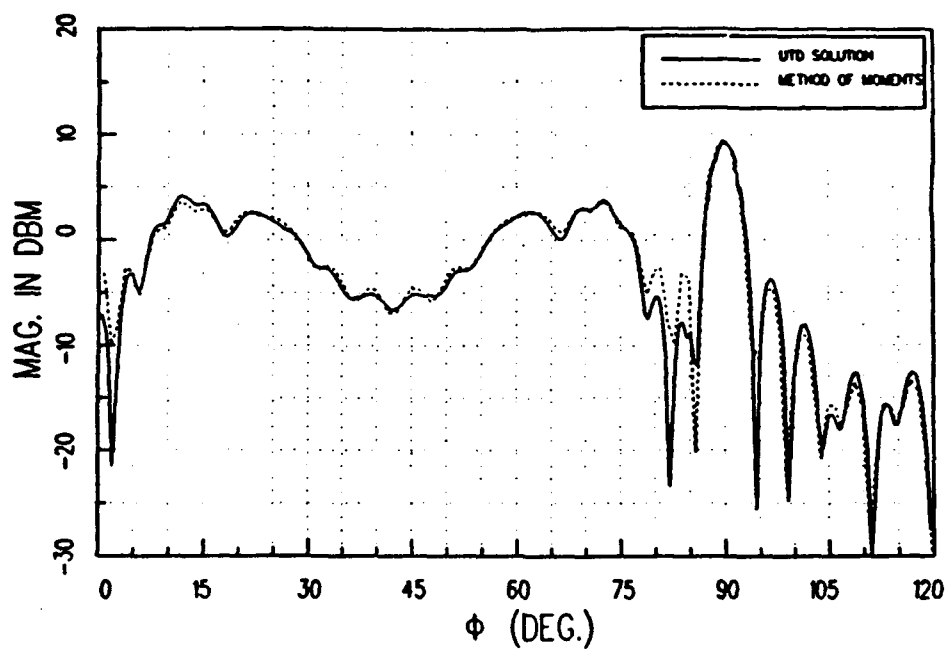
Figure 37: Backscatter result for 9 in 85° rectangular dihedral at 10 GHz for horizontally polarized field.
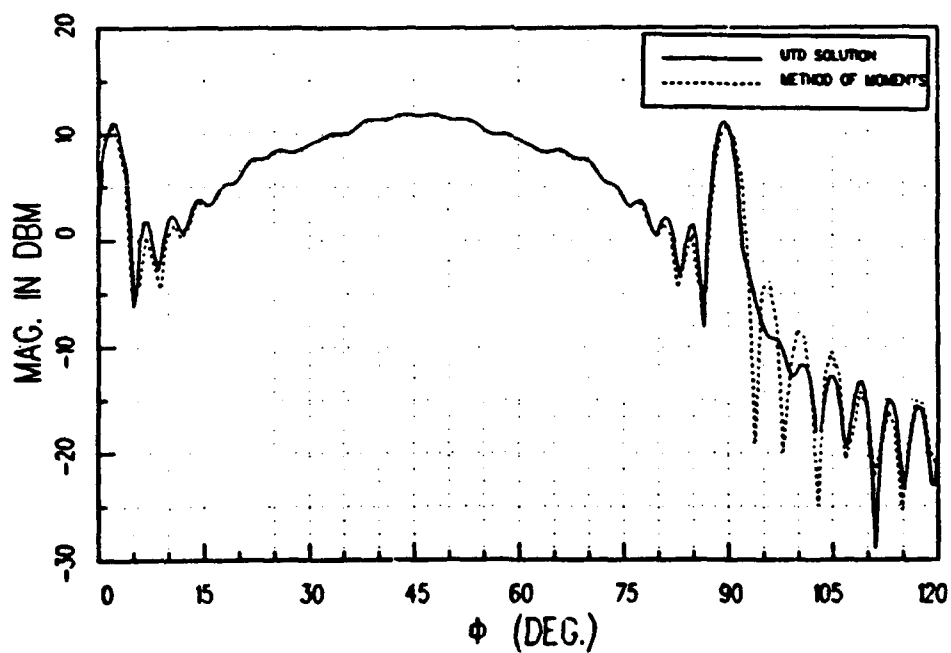
Figure 38: Backscatter result for 9 in 92° rectangular dihedral at 10 GHz for horizontally polarized field.

61
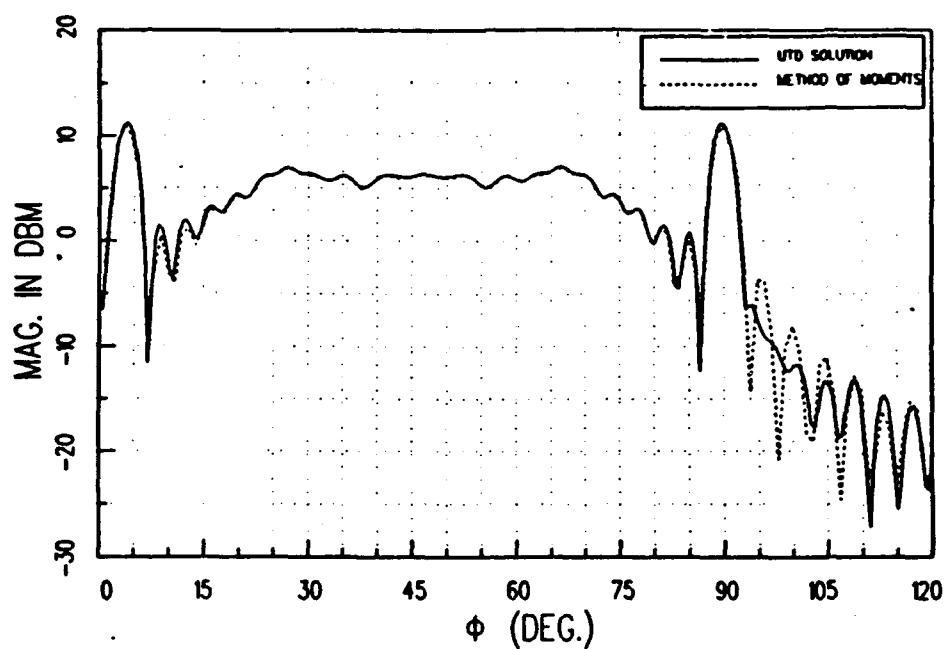
Figure 39: Backscatter result for 9 in 94° rectangular dihedral at 10 GHz for horizontally polarized field.
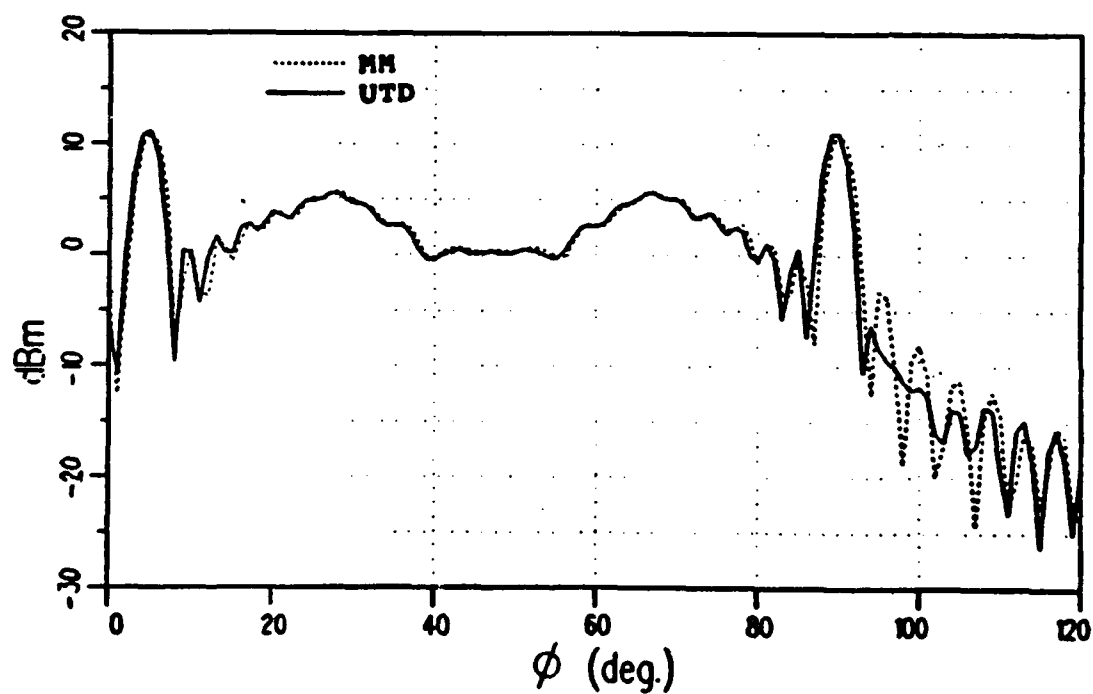
Figure 40: Backscatter result for 9 in 95° rectangular dihedral at 10 GHz for horizontally polarized field.
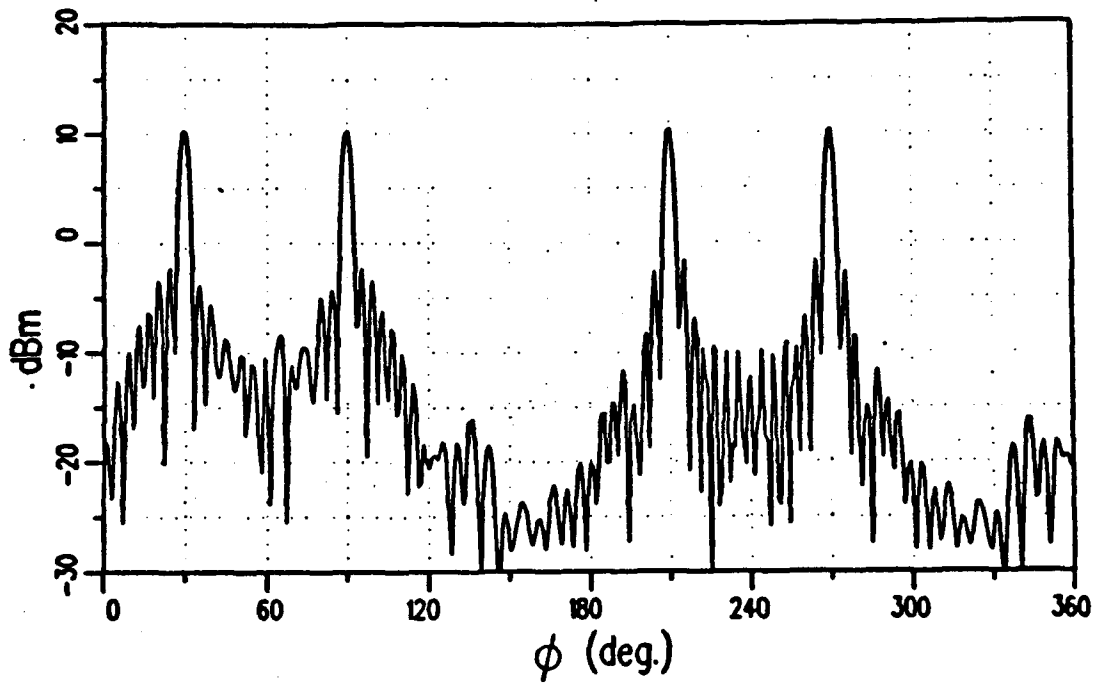
Figure 41: Backscatter result for 9 in 120° rectangular dihedral at 10 GHz for horizontally polarized field.
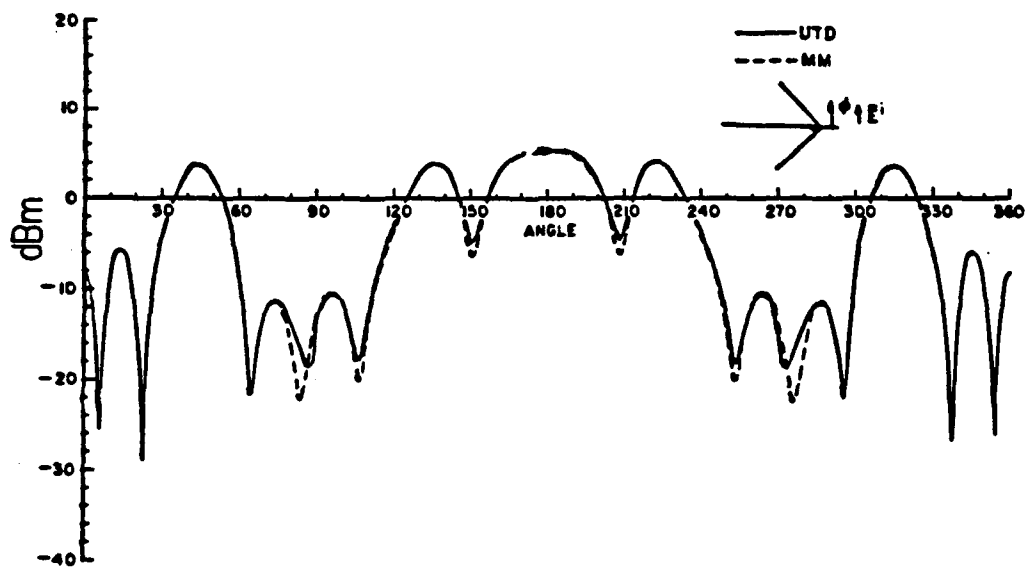
Figure 42: Backscatter field from a 9 in rectangular dihedral at 2 GHz for horizontally polarized field.

63
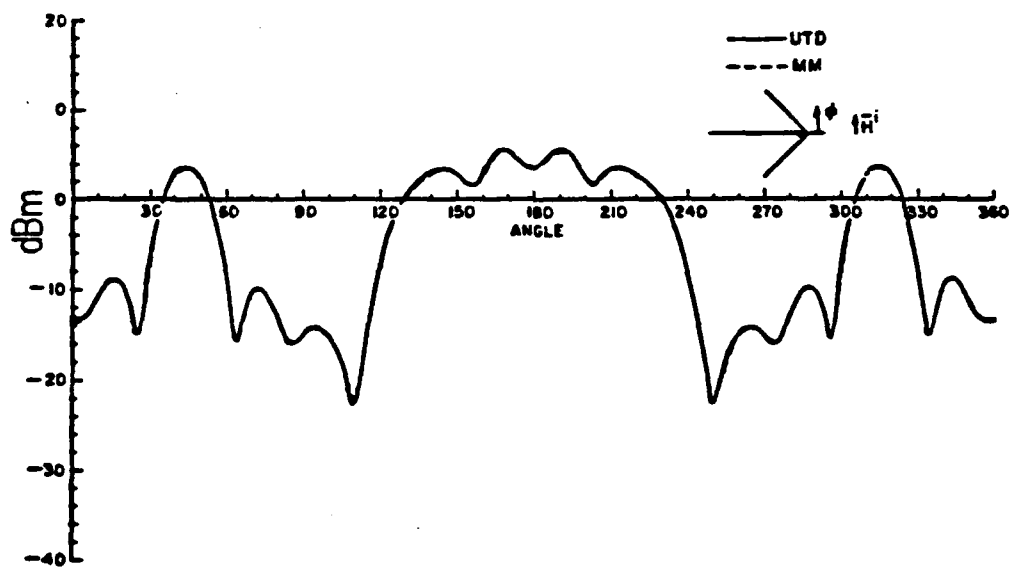
Figure 43: Backscatter field from a 9 in rectangular dihedral at 2 GHz for vertically polarized field.
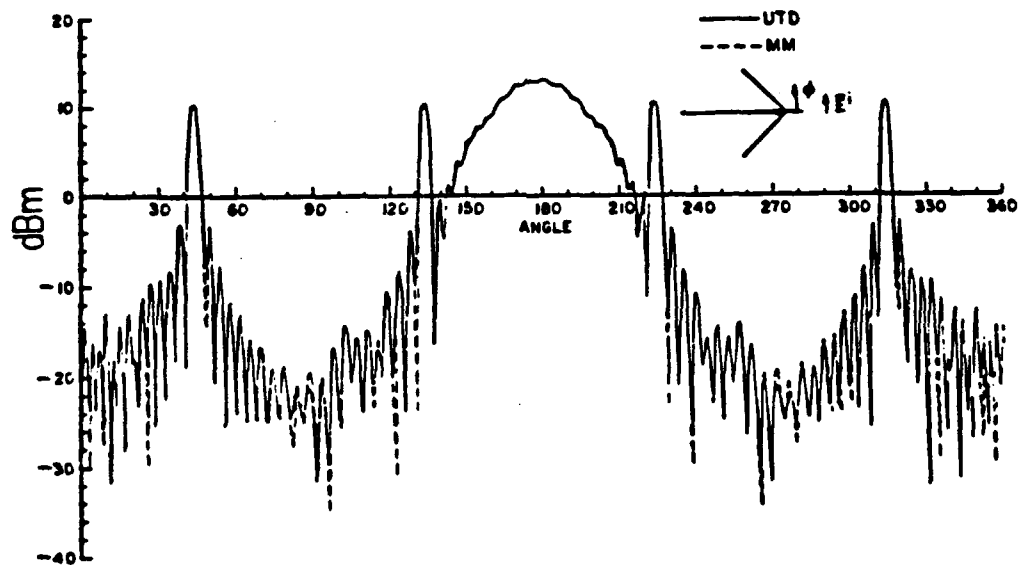
Figure 44: Backscatter field from a 9 in rectangular dihedral at 10 GHz for horizontally polarized field.

64
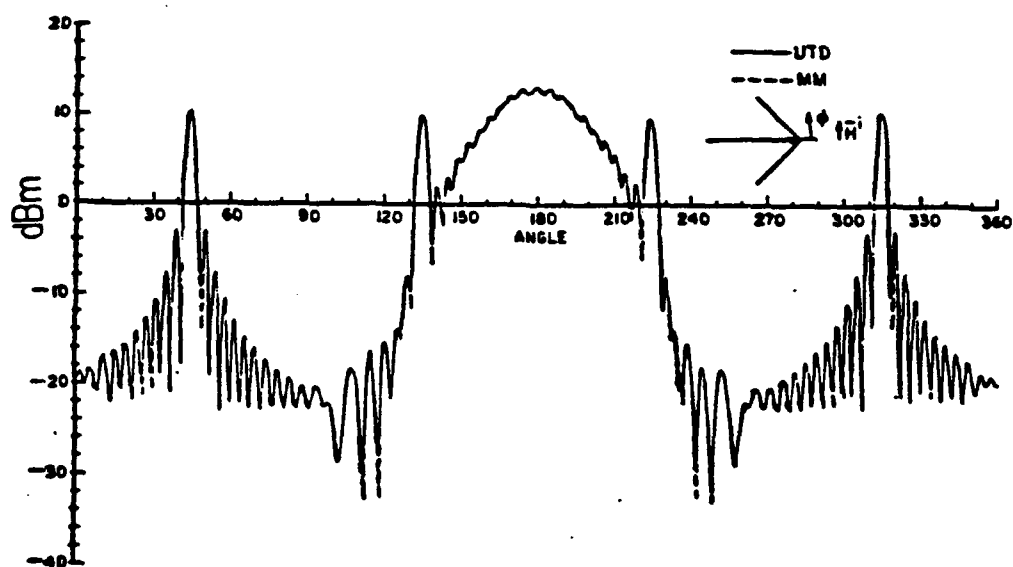
Figure 45: Backscatter field from a 9 in rectangular dihedral at 10 GHz for vertically polarized field.
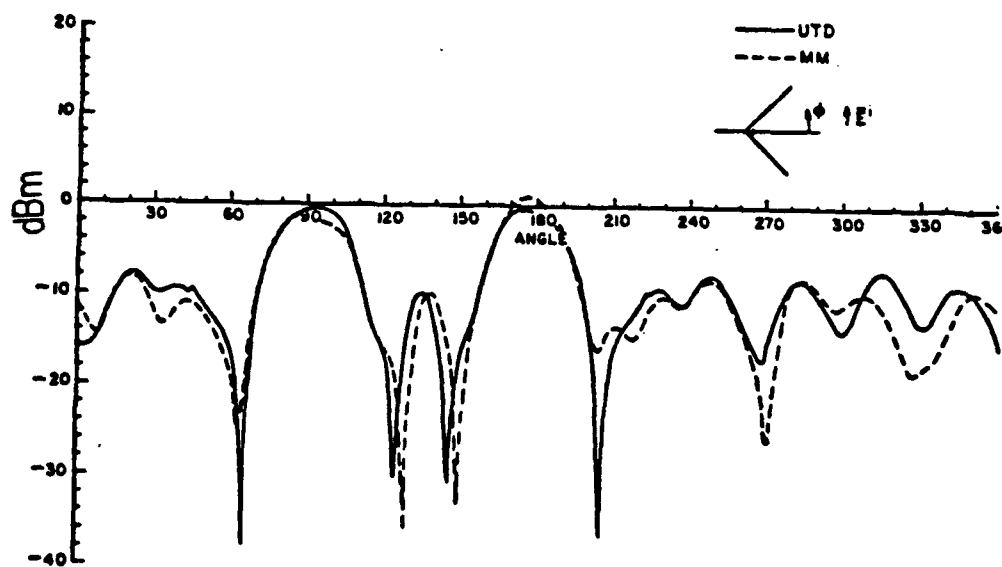
Figure 46: Ninety-degree bistatic field from a 9 in rectangular dihedral at 2 GHz for horizontally polarized field.

65
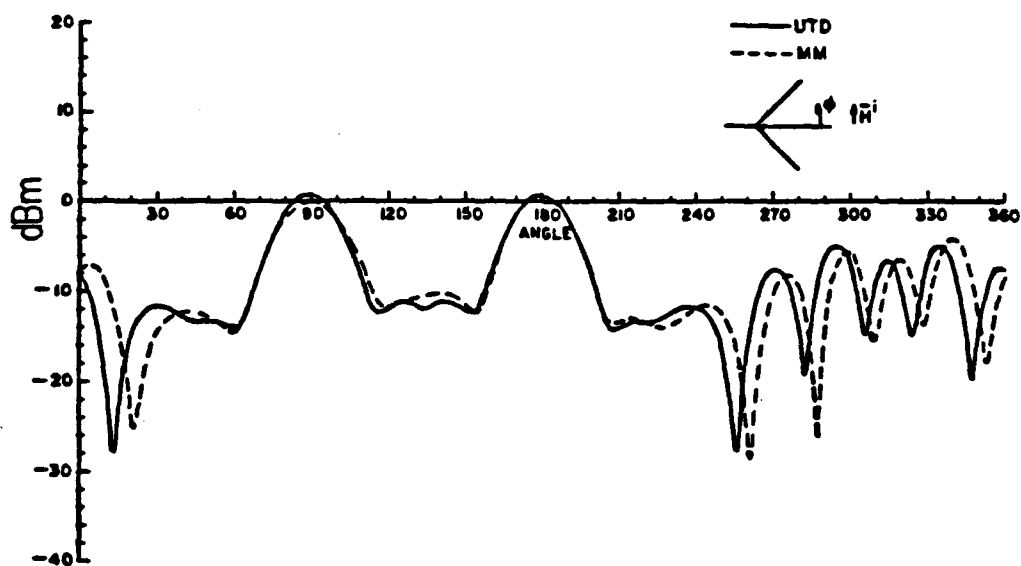
Figure 47: Ninety-degree bistatic field from a 9 in rectangular dihedral at 2 GHz for vertically polarized field.
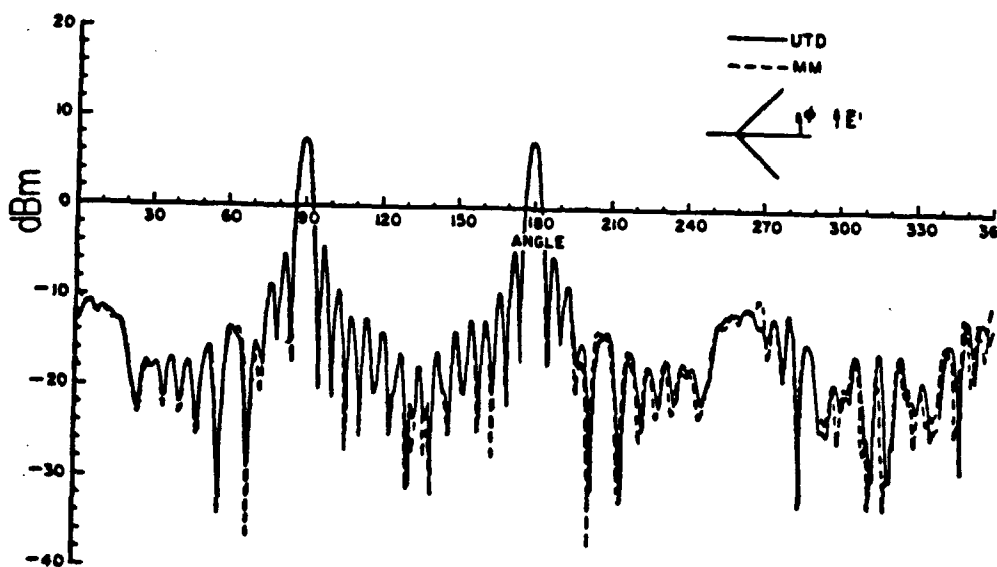
Figure 48: Ninety-degree bistatic field from a 9 in rectangular dihedral at 10 GHz for horizontally polarized field.

66
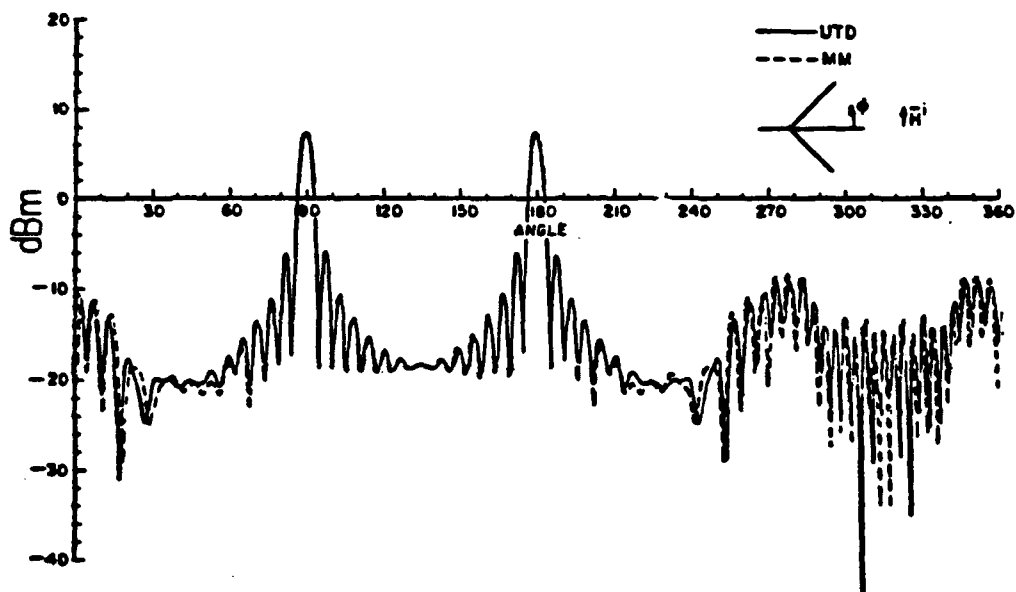
Figure 49: Ninety-degree bistatic field from a 9 in rectangular dihedral at 10 GHz for vertically polarized field.

SECTION 4

Rim and Curved-Surface Caustic Corrections

1 Introduction

The Geometrical Theory of Diffraction predicts infinite fields at ray caustics. The occurrence of a caustic requires that the erroneous ray field infinities be "corrected" with transition functions which blend the well behaved wide-angled ray field predictions smoothly into the corrected or bounded values at the caustic. Details of rim and curved-surface caustic corrections can be found in References [20, 21, 22]. Although theses solutions are based on equivalent edge and line currents, the modern MEC (Michaeli et al) provides essentially the same result.

Ryan and Peters [20] developed a solution in the rim-caustic regions based on the field radiated by equivalent edge currents on the rim. This result goes to the diffraction point solution outside the caustic region; thus, it is a uniform solution. In Reference [21], this technique is extended by the use of the "stripping concept" [23, 24] in addition to using a small argument approximation to the diffraction coefficient in the specular caustic region of the radiation integral. This solution referred to as the "Bessel-Struve function extension," provides an accurate uniform result in the rim-caustic region that is associated with a specular or forward-scatter direction of disks, end caps of cylinders, cones etc.

68

The need for the curved-surface specular correction arises from the fact that the classical edge diffraction coefficient, being a local phenomenon, has no a priori knowledge of the variation in curvature along a curved-surface away from the edge. If the radius of curvature is equal at both the edges of the curved-surface, as in the case of the cylinder, the total field along the specular direction will be correct. However, if the radii of curvature are different at the two edges of the curved-surface (for example, cones), the energy spreads differently at every point on the curved-surface, depending on the radii of curvature. Since this information is not built into the classic edge diffraction coefficient, the edge diffracted field is not able to match into the reflected field in the specular direction whose dominant behavior is as predicted by physical optics (PO). Using procedures similar to References [20, 21] and extending them by asymptotically matching the PO solution for the reflection from the curved face into the UTD solution, Ebihara [22] extracted a transition function useful in the curved-surface specular region.

In Section 4.2, the equivalent-line current solution procedure [25] is presented. In Section 3.1, the equivalent-edge-current solution of Ryan and Peters is presented. Next, in Section 3.2, the Bessel-Struve function extension is examined. Finally, the curved-surface specular correction will be considered in Section 4.

2 Equivalent-Line Current Solution Procedure

The following steps are used to find the equivalent-line solution:

1. The field of a canonical problem is obtained (a two-dimensional solution).

2. Next, the radiated fields from infinite travelling-wave line currents, I^r and I^m, are determined. I^r is an electric current and I^m is a magnetic current.

3. The currents I^r and I^m are substituted for the two-dimensional solution, and the currents I^r and I^m are then adjusted to give the same field as the two-dimensional solution. In the principal plane, I^r gives the horizontally polarized

field, and I''' gives the vertically polarized field. These are "fictitious" currents that vary with the incident and observation positions.

4. These equivalent line currents are broken up into infinitesimal current elements. The current elements are placed at the equivalent locations on the surface.

5. The radiated fields due to the above currents are evaluated. This involves a line integral. The resulting expression is the equivalent-line current solution. It gives the correct value of the field away from the caustic direction.

3   Rim Caustic Correction

3.1   Ryan/Peters Equivalent-Edge-Current Solution

Ebihara [22] used the original work by Ryan and Peters [20] to get the standard diffraction coefficient with rim caustic correction function, Figure 50. There appear to be some sign discrepancies early in the derivation in [22] which result in inconsistencies in the final result for the hard polarization using Equation 5.225 in [22]. In this section, the standard diffraction coefficient with the transition functions are defined for consistency.

The equivalent edge current used by Ryan and Peters are

$$I^r = \frac{2jG'}{\eta k \sin \beta_o \sin \beta_o'} \left(\hat{e} \cdot \vec{E}'(0) \right) e^{jk\vec{r}_r \cdot r'} \tag{126}$$

and

$$I_r''' = \frac{2jG'''}{k \sin \beta_o \sin \beta_o'} \eta \left(\hat{e} \cdot \vec{H}'(0) \right) e^{jk\vec{r}_r \cdot r'}, \tag{127}$$

where

$$G' \left(\Phi, \Phi' \right) = -\frac{1}{2n} \left(A - B \right), \tag{128}$$

$$G''' \left(\Phi, \Phi' \right) = -\frac{1}{2n} \left(A + B \right) \tag{129}$$

and

$$A \left(\Phi, \Phi' \right) = \cot \left(\frac{\pi + (\Phi - \Phi')}{2n} \right) + \cot \left(\frac{\pi - (\Phi - \Phi')}{2n} \right), \tag{130}$$
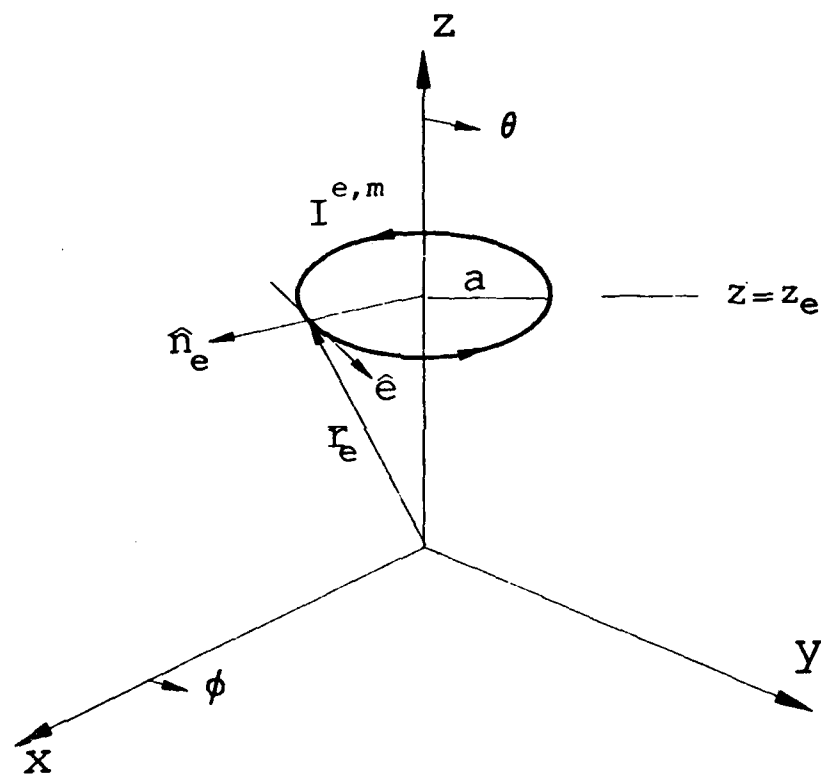
Figure 50: Geometry for rim caustic correction.

$$B(\Phi, \Phi') = \cot\left(\frac{\pi + (\Phi + \Phi')}{2n}\right) + \cot\left(\frac{\pi - (\Phi + \Phi')}{2n}\right). \tag{131}$$

These currents are distributed on the illuminated edge of the rim. The radiated fields due to the electric and magnetic equivalent edge currents on a circular rim are

$$E_\theta^c = \frac{a\cos\theta}{2\pi}\frac{e^{-jkr}}{r}\int_0^{2\pi}\frac{G^c}{\sin\beta_o}\left(\hat{e}\cdot\vec{E}^i(0)\right)\sin(\phi - \phi_c)e^{jk\vec{r}_c\cdot(\hat{r}+\hat{r}')}d\phi_c, \tag{132}$$

$$E_\theta^m = \frac{a\eta}{2\pi}\frac{e^{-jkr}}{r}\int_0^{2\pi}\frac{G^m}{\sin\beta_o}\left(\hat{e}\cdot\vec{H}^i(0)\right)\cos(\phi - \phi_c)e^{jk\vec{r}_c\cdot(\hat{r}+\hat{r}')}d\phi_c, \tag{133}$$

$$E_\phi^c = \frac{a}{2\pi}\frac{e^{-jkr}}{r}\int_0^{2\pi}\frac{G^c}{\sin\beta_o}\left(\hat{e}\cdot\vec{E}^i(0)\right)\cos(\phi - \phi_c)e^{jk\vec{r}_c\cdot(\hat{r}+\hat{r}')}d\phi_c, \tag{134}$$

and

$$E_\phi^m = \frac{-a\eta\cos\theta}{2\pi}\frac{e^{-jkr}}{r}\int_0^{2\pi}\frac{G^m}{\sin\beta_o}\left(\hat{e}\cdot\vec{H}^i(0)\right)\sin(\phi - \phi_c)e^{jk\vec{r}_c\cdot(\hat{r}+\hat{r}')}d\phi_c. \tag{135}$$

The diffracted field is the sum of the fields radiated from both electric and magnetic equivalent currents, so that

$$\vec{E}_{rim}^d = \hat{\theta}E_\theta + \hat{\phi}E_\phi, \tag{136}$$

where

$$E_\phi = E_\phi^c + E_\phi^m \tag{137}$$

and

$$E_\theta = E_\theta^c + E_\theta^m. \tag{138}$$

To simplify the integration in (132)-(135), Ryan and Peters used the approximation that the diffraction coefficients remained relatively constant with respect to the variable of integration, so that

$$\frac{G^{c,m}}{\sin\beta_o} \approx constant\ in\ \phi_c. \tag{139}$$

Let

$$\psi_c = ka\hat{n}_c(\phi_c)\cdot(\hat{r}+\hat{r}') \tag{140}$$

$$= ka\left[\sin\theta'\cos(\phi' - \phi_c) + \sin\theta\cos(\phi - \phi_c)\right]. \tag{141}$$

and

$$\gamma_c = kz_c \hat{z} \cdot (\hat{r} + \hat{r}') .$$ (142)

Using the previously mentioned approximation and the fact that

$$\int_0^{2\pi} \sin \phi_c \cos \phi_c e^{j\psi} d\phi_c = 0,$$ (143)

the expressions for the radiated fields become

$$E_\phi = \frac{a}{2\pi} \frac{e^{j\gamma_c}}{\sin \beta_o} \frac{e^{-jkr}}{r} E_\phi^i \left\{ G^c \int_0^{2\pi} \cos^2 \phi_c e^{j\psi_c} d\phi_c \right.$$
$$\left. - G''' \cos \theta \cos \theta' \int_0^{2\pi} \sin^2 \phi_c e^{j\psi_c} d\phi_c \right\},$$ (144)

and

$$E_\theta = \frac{a}{2\pi} \frac{e^{j\gamma_c}}{\sin \beta_o} \frac{e^{-jkr}}{r} E_\theta^i \left\{ G^c \cos \theta \cos \theta' \int_0^{2\pi} \sin^2 \phi_c e^{j\psi_c} d\phi_c \right.$$
$$\left. - G''' \int_0^{2\pi} \cos^2 \phi_c e^{j\psi_c} d\phi_c \right\},$$ (145)

where

$$\psi_c = U \cos \phi_c.$$ (146)

Let the following integrals be defined by:

$$F_1(U) = \int_0^{2\pi} \cos^2 \phi_c e^{j\psi_c} d\phi_c$$ (147)

$$f_1(U) = \int_{-\frac{\pi}{2}}^{\frac{\pi}{2}} \cos^2 \phi_c e^{j\psi_c} d\phi_c$$ (148)

$$f_1^*(U) = \int_{\frac{\pi}{2}}^{\frac{3\pi}{2}} \cos^2 \phi_c e^{j\psi_c} d\phi_c$$ (149)

$$F_2(U) = \cos \theta \cos \theta' \int_0^{2\pi} \sin^2 \phi_c e^{j\psi_c} d\phi_c$$ (150)

$$f_2(U) = \cos \theta \cos \theta' \int_{-\frac{\pi}{2}}^{\frac{\pi}{2}} \sin^2 \phi_c e^{j\psi_c} d\phi_c$$ (151)

$$f_2^*(U) = \cos \theta \cos \theta' \int_{\frac{\pi}{2}}^{\frac{3\pi}{2}} \sin^2 \phi_c e^{j\psi_c} d\phi_c$$ (152)

73

These integrals can be evaluated in closed form as follows:

$$f_1(U) = \pi\left[\left(J_0(U) - \frac{J_1(U)}{U}\right) + j\left(H_0(U) - \frac{H_1(U)}{U}\right)\right] \tag{153}$$

$$f_1^*(U) = \pi\left[\left(J_0(U) - \frac{J_1(U)}{U}\right) - j\left(H_0(U) - \frac{H_1(U)}{U}\right)\right] \tag{154}$$

$$f_2(U) = \pi\cos\theta\cos\theta'\left(\frac{J_1(U)}{U} + j\frac{H_1(U)}{U}\right) \tag{155}$$

$$f_2^*(U) = \pi\cos\theta\cos\theta'\left(\frac{J_1(U)}{U} - j\frac{H_1(U)}{U}\right), \tag{156}$$

where J_1 and H_1 are the first order Bessel and Hankel functions, respectively. The expressions for the radiated fields are

$$E_\phi = \frac{a}{2\pi}\frac{e^{j\gamma_c}}{\sin\beta_o}\frac{e^{-jkr}}{r}E_\phi'\frac{1}{2n}\left\{-(A-B)F_1 + (A+B)F_2\right\} \tag{157}$$

$$E_\theta = \frac{a}{2\pi}\frac{e^{j\gamma_c}}{\sin\beta_o}\frac{e^{-jkr}}{r}E_\theta'\frac{1}{2n}\left\{-(A-B)F_2 + (A+B)F_1\right\}. \tag{158}$$

The above can be rearranged into

$$E_\phi = \frac{-a}{2\pi}\frac{e^{j\gamma_c}}{\sin\beta_o}\frac{e^{-jkr}}{r}E_\phi'\frac{1}{2n}\left\{A(F_1-F_2) - B(F_1+F_2)\right\} \tag{159}$$

$$E_\theta = \frac{a}{2\pi}\frac{e^{j\gamma_c}}{\sin\beta_o}\frac{e^{-jkr}}{r}E_\theta'\frac{1}{2n}\left\{A(F_1-F_2) + B(F_1+F_2)\right\}. \tag{160}$$

Breaking the integral apart into

$$F_1(U) = f_1(U) + f_1^*(U) \tag{161}$$

$$F_2(U) = f_2(U) + f_2^*(U) \tag{162}$$

and further manipulating them gives

$$E_\phi = \frac{-a}{2\pi}\frac{e^{j\gamma_c}}{\sin\beta_o}\frac{e^{-jkr}}{r}E_\phi'\frac{1}{2n}\left\{A(f_1-f_2) - B(f_1+f_2)\right. $$
$$\left. + A(f_1^*-f_2^*) - B(f_1^*+f_2^*)\right\} \tag{163}$$

$$E_\theta = \frac{a}{2\pi}\frac{e^{j\gamma_c}}{\sin\beta_o}\frac{e^{-jkr}}{r}E_\theta'\frac{1}{2n}\left\{A(f_1-f_2) + B(f_1+f_2)\right.$$
$$\left. + A(f_1^* - f_2^*) + B(f_1^*+f_2^*)\right\}. \tag{164}$$

74

Now, consider associating a half-rim integral with the points at $\phi_c = 0,\ \pi$, the stationary points for a large ψ_c; they are also the diffraction points on the rim for the principal plane. From the above equations, the field contributions from the half rim associated with $\phi_c = 0$ are

$$E_{1\phi} = \frac{-a}{2\pi} \frac{e^{j\gamma_c}}{\sin\beta_o} \frac{e^{-jkr}}{r} E_\phi^i \{A(f_1 - f_2) - B(f_1 + f_2)\} \tag{165}$$

$$E_{10} = \frac{a}{2\pi} \frac{e^{j\gamma_c}}{\sin\beta_o} \frac{e^{-jkr}}{r} E_\theta^i \{A(f_1 - f_2) + B(f_1 + f_2)\} \tag{166}$$

$$\vec{E}_1^d = \hat{\phi} E_{1\phi} + \hat{\theta} E_{10}. \tag{167}$$

Comparing this with the expression for the edge-diffracted field from a point on the rim,

$$\vec{E}_c^d = \vec{E}^i(Q_c) \sqrt{\rho^d(Q_c)} e^{jk\vec{r}_c \cdot \hat{r}} \frac{e^{jkr}}{r}, \tag{168}$$

the new diffraction coefficients may be expressed as:

$$\overline{\overline{D}}(Q_c) = -\hat{\beta}' \hat{\beta} D_s(Q_c) - \hat{\Phi}' \hat{\Phi} D_h(Q_c), \tag{169}$$

where

$$D_s = \frac{-e^{-j\frac{\pi}{4}}}{2n\sqrt{2\pi k} \sin\beta_o} \left(AT_{c1}(U) - BT_{c2}(U)\right) \tag{170}$$

$$D_h = \frac{-e^{-j\frac{\pi}{4}}}{2n\sqrt{2\pi k} \sin\beta_o} \left(AT_{c1}(U) + BT_{c2}(U)\right) \tag{171}$$

where

$$T_{c1}(U) = \frac{1}{\pi} (f_1(U) - f_2(U)) \sqrt{\frac{\pi U}{2}} e^{-j(U - \frac{\pi}{4})} \tag{172}$$

$$T_{c2}(U) = \frac{1}{\pi} (f_1(U) + f_2(U)) \sqrt{\frac{\pi U}{2}} e^{-j(U - \frac{\pi}{4})} \tag{173}$$

and

$$U(Q_c) = ka_c \hat{n}_c \cdot (\hat{r} + \hat{r}'). \tag{174}$$

The functions T_{c1} and T_{c2} are the transition functions through the rim caustic region based on the Ryan/Peters equivalent-edge-current solution. The transition functions

75

have small and large argument forms which are obtained using the series and the asymptotic forms of the Bessel and Struve functions, so that for

$|U| \ll 1$

$$
T_{c1}(U) \approx \sqrt{\frac{\pi U}{2}} e^{-j(U - \frac{\pi}{4})}
$$
$$
\cdot \left\{ \frac{1}{2} \left[1 - \frac{3U^2}{8} + \frac{U^4}{32} - \cos\theta \cos\theta' \left(1 - \frac{U^2}{8} \right) \right] \right.
$$
$$
\left. + j\frac{2U}{3\pi} \left[2 \left(1 - \frac{2U^2}{15} \right) - \cos\theta \cos\theta' \left(1 - \frac{U^2}{15} \right) \right] \right\}
\tag{175}
$$

$$
T_{c2}(U) \approx \sqrt{\frac{\pi U}{2}} e^{-j(U - \frac{\pi}{4})}
$$
$$
\cdot \left\{ \frac{1}{2} \left[1 - \frac{3U^2}{8} + \frac{U^4}{32} + \cos\theta \cos\theta' \left(1 - \frac{U^2}{8} \right) \right] \right.
$$
$$
\left. + j\frac{2U}{3\pi} \left[2 \left(1 - \frac{2U^2}{15} \right) + \cos\theta \cos\theta' \left(1 - \frac{U^2}{15} \right) \right] \right\}
\tag{176}
$$

$|U| \gg 1$

$$
T_{c1}(U) \sim 1 - \frac{j9}{8U} + \frac{39}{128U^2} - \frac{j45}{1024U^3}
$$
$$
- \cos\theta \cos\theta' \left(-\frac{j}{U} + \frac{3}{8U^2} - \frac{j15}{128U^3} \right)
$$
$$
- \sqrt{\frac{\pi U}{2}} e^{-j(U - \frac{\pi}{4})} \left[\cos\theta \cos\theta' \left(1 + \frac{1}{U^2} \right) + \frac{2}{U^2} \right]
\tag{177}
$$

$$
T_{c2}(U) \sim 1 - \frac{j9}{8U} + \frac{39}{128U^2} - \frac{j45}{1024U^3}
$$
$$
+ \cos\theta \cos\theta' \left(-\frac{j}{U} + \frac{3}{8U^2} - \frac{j15}{128U^3} \right)
$$
$$
+ \sqrt{\frac{\pi U}{2}} e^{-j(U - \frac{\pi}{4})} \left[\cos\theta \cos\theta' \left(1 + \frac{1}{U^2} \right) - \frac{2}{U^2} \right].
\tag{178}
$$

Associating a half rim to the stationary points Q_1 and Q_2, the total field radiated by the equivalent edge currents on the rim may be written in the diffraction-point form

$$
\vec{E}_{rim}^d = \vec{E}_1^d + \vec{E}_2^d,
\tag{179}
$$

76

where

$$\vec{E}_1^d = \vec{E}^i \cdot \overline{\overline{D}}(Q_1)\sqrt{\rho^d(Q_1)}e^{jk\vec{r}_1 \cdot \hat{r}}\frac{e^{-jkr}}{r} \qquad (180)$$

and

$$\vec{E}_2^d = \vec{E}^i \cdot \overline{\overline{D}}(Q_2)\sqrt{\rho^d(Q_2)}e^{jk\vec{r}_2 \cdot \hat{r}}\frac{e^{-jkr}}{r}. \qquad (181)$$

3.2   Bessel-Struve Function Extension

One problem associated with the Ryan/Peters result is that the approximation (139) becomes invalid for a rim caustic associated with an end cap's specular or forward-scatter direction. To overcome this difficulty, a modified edge vector $\hat{e}^*$ is used. It is defined by

$$\hat{e}^* = \hat{p}\left(\hat{e} \cdot \hat{p}\right), \qquad (182)$$

where

$$\hat{p} = \frac{(\hat{r}' + \hat{r}) \times \hat{n}_o}{|(\hat{r}' + \hat{r}) \times \hat{n}_o|} \qquad (183)$$

$\hat{n}_o$ = normal to the end cap

$\hat{r}'$ = direction of source, and

$\hat{r}$ = direction of receiver.

By using the modified edge vector, only the perpendicular components to the plane of incidence of the equivalent edge currents are considered. This is called the "stripping concept." The equivalent edge currents with this modification are given by

$$I_s^e = \frac{2jG^e}{\eta k \sin \beta_o \sin \beta_o'} \left(\hat{e}^* \cdot \vec{E}'(0)\right) e^{jk\vec{r}_e \cdot \hat{r}'} \qquad (184)$$

$$I_s^m = \frac{2jG^m}{k \sin \beta_o \sin \beta_o'}\eta \left(\hat{e}^* \cdot \vec{H}'(0)\right) e^{jk\vec{r}_e \cdot \hat{r}'}. \qquad (185)$$

The modified equivalent-edge-current solution is obtained in the same way as before. To simplify the evaluation of the integral, the following small argument approximations are used:

$$\theta \approx \theta' - \epsilon \ , \ in \ the \ specular \ region, \ or \qquad (186)$$

77

$$\theta \approx \pi - \theta' - \epsilon \,, \text{ in the forward scatter region.} \tag{187}$$

This results in

$$\frac{G^{e,m}}{\sin \beta_o \sin \beta'_o} \approx \frac{1}{\epsilon \cos \phi_r} \tag{188}$$

and the integral

$$F_o(U) = \int_0^{2\pi} \cos \phi_c e^{jU \cos \phi_c} d\phi_c, \tag{189}$$

which can be evaluated by using

$$f_o(U) = \int_{-\frac{\pi}{2}}^{\frac{\pi}{2}} \cos \phi_c e^{jU \cos \phi_c} d\phi_c$$
$$= \pi \left[\frac{2}{\pi} - H_1(U) + jJ_1(U) \right]. \tag{190}$$

Associating a half rim to the stationary points Q_1 and Q_2, the total field radiated by the equivalent edge currents on the rim may be written in the diffraction-point form

$$\vec{E}_{rim}^d = \vec{E}_1^d + \vec{E}_2^d \tag{191}$$

where

$$\vec{E}_1^d = \vec{E}^i . \overline{\overline{D}}(Q_1) \sqrt{\rho^d(Q_1)} e^{jk\vec{r}_1 . \hat{r}} \frac{e^{-jkr}}{r} \tag{192}$$

$$\vec{E}_2^d = \vec{E}^i . \overline{\overline{D}}(Q_2) \sqrt{\rho^d(Q_2)} e^{jk\vec{r}_2 . \hat{r}} \frac{e^{-jkr}}{r}. \tag{193}$$

The modified diffraction coefficient is

$$\overline{\overline{D}}(Q_c) = -\hat{\beta}'\hat{\beta} D_s(Q_c) - \hat{\Phi}'\hat{\Phi} D_h(Q_c) \tag{194}$$

$$D_{s,h} = \frac{-e^{-j\pi/4}}{2n\sqrt{2\pi k}} \left[\cot\left(\frac{\pi + \beta^-}{2n}\right) + \cot\left(\frac{\pi - \beta^-}{2n}\right) \right.$$
$$\left. \mp \left\{ \cot\left(\frac{\pi + \beta^+}{2n}\right) + \cot\left(\frac{\pi - \beta^+}{2n}\right) \right\} \right] T_c(U), \tag{195}$$

where

$$\beta = \beta^\pm = \phi \pm \phi', \tag{196}$$

$$U = ka\hat{n}_c \cdot (\hat{r} + \hat{r}'), \tag{197}$$

$$T_r(U) = \frac{1}{\pi} f_o(U) \sqrt{\frac{\pi U}{2}} e^{-j\left(U - \frac{\pi}{4}\right)} \tag{198}$$

and

$$f_o(U) = \pi \left[\frac{2}{\pi} - H_1(U) + jJ_1(U) \right]. \tag{199}$$

J_1 and H_1 are the first order Bessel and Struve functions, respectively. The transition function is $T_r(U)$, k is the wave number, a and $\hat{n}_c$ are the radius of curvature and the normal to the edge at the point of diffraction, and $\hat{r}$ and $\hat{r}'$ are the directions to the source and the receiver, respectively. The transition function has small and large argument forms given as:

for $|U| << 1$

$$T_r(U) \approx \sqrt{\frac{\pi U}{2}} e^{-j\left(U - \frac{\pi}{4}\right)} \left\{ \frac{\pi}{2} - \frac{2U^2}{3\pi} \left(1 - \frac{U^2}{15}\right) + j\frac{U}{2} \left(1 - \frac{U^2}{8}\right) \right\} \tag{200}$$

for $|U| >> 1$

$$T_r(U) \sim 1 + \frac{j3}{8U} - \frac{1}{U}\sqrt{\frac{2}{\pi U}} e^{-j\left(U - \frac{\pi}{4}\right)} + \frac{15}{128U^2} - \frac{j105}{1024U^3}. \tag{201}$$

4 Curved-Surface Specular Region Correction

Details of the curved-surface specular region correction are presented in [22]. Referring to Figure 51, the term of the diffraction coefficient which "blows" up in the specular direction is corrected by the inclusion of a transition function. This result goes to the diffraction point solution outside the caustic region, making it a uniform solution. The specular terms from the two diffraction points with the correction are given as

$$D_{s,h}^{rn-} = R_{s,h} \frac{-e^{-j\pi/4}}{2n\sqrt{2\pi k}\sin\beta_o} \cot\left(\frac{\pi - (\phi_1 + \phi_1')}{2n}\right) T_r(+jXa_r) \tag{202}$$

and

$$D_{s,h}^{rn+} = R_{s,h} \frac{-e^{-j\pi/4}}{2n\sqrt{2\pi k}\sin\beta_o} \cot\left(\frac{\pi - (\phi_2 + \phi_2')}{2n}\right) T_r(-jXa_r). \tag{203}$$
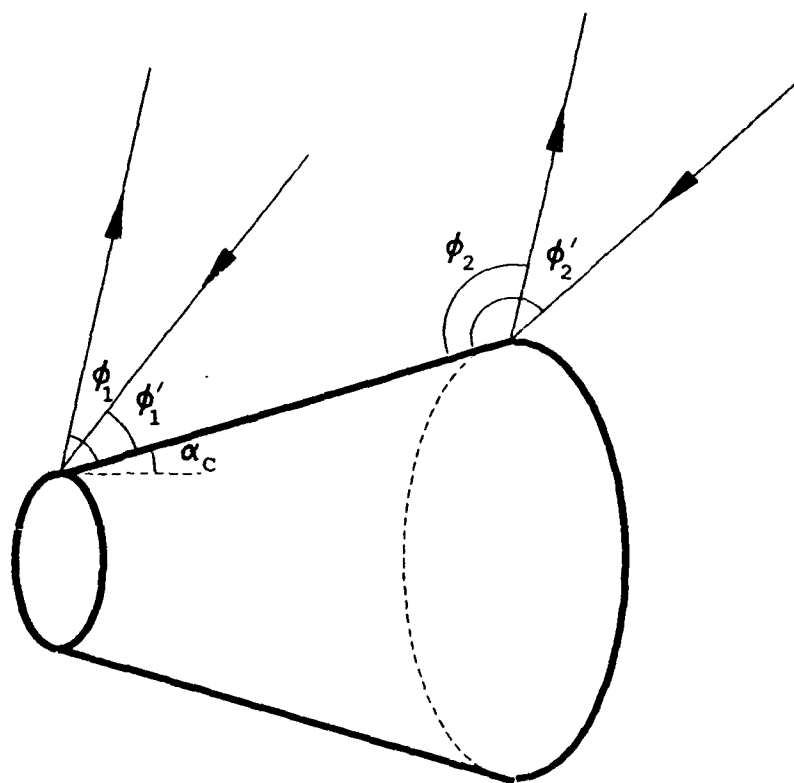
Figure 51: Geometry for curved-surface caustic correction.

The radius of curvature of the diffracting edge is a_r, and

$$X = K \cot \alpha_r \left[\tan^2 \alpha_c \left(\cos^2 v + \epsilon_c^2 \sin^2 v \right) + 1 \right]^{1/2} \sin \beta_o$$
$$2 \cos \left(\frac{\phi + \phi'}{2} \right) \cos \left(\frac{\phi - \phi'}{2} \right), \qquad (204)$$

where the ϕ's are measured from the curved surface, as shown in Figure 51 and ϵ_r is the ellipticity of the curved surface. The transition function is given as

$$T(z) = T_1(z) = \frac{2}{3} z M(1, 2.5, -z) \qquad (205)$$

or

$$T(z) = T_2(z) = -z U(1, 2.5, -z), \qquad (206)$$

where

$$U(1, 2.5, -z) = -\frac{2}{3} M(1, 2.5, -z) + \frac{\sqrt{\pi}}{2} (-z)^{-\frac{3}{2}} e^{-z}, \qquad (207)$$

and M and U are confluent hypergeometric functions. The small and the large argument of the transition function are the following:

for $|z| << 1$,

$$T_1(z) \approx e^{-z} \left(\frac{2z}{3} + \frac{2z^2}{5} + \frac{z^3}{7} \right) \qquad (208)$$

$$T_2(z) \approx e^{-z} \left(\frac{\sqrt{\pi}}{2\sqrt{-z}} + \frac{2z}{3} + \frac{2z^2}{5} + \frac{z^3}{7} \right) \qquad (209)$$

for $|z| >> 1$,

$$T_1(z) \sim 1 + \frac{\sqrt{\pi}}{2} e^{\pm j \frac{3}{2} \pi} \frac{e^{-z}}{\sqrt{z}} - \frac{1}{2z} - \frac{1}{4z^2} \qquad (210)$$

$$T_2(z) \sim 1 - \frac{1}{2z} - \frac{1}{4z^2}. \qquad (211)$$

The new diffraction coefficient can be expressed as:

$$\overline{\overline{D}}^{\mp}(Q_r) = -\hat{\beta}'\hat{\beta} D_s^{\mp}(Q_r) - \hat{\Phi}'\hat{\Phi} D_h^{\mp}(Q_r), \qquad (212)$$

where

$$D_{s,h}^{\mp} = \frac{-e^{-j\frac{\pi}{4}}}{2n\sqrt{2\pi k}\sin\beta_o} \left\{ \cot\left(\frac{\pi + (\Phi - \Phi')}{2n}\right) + \cot\left(\frac{\pi - (\Phi - \Phi')}{2n}\right) + \right.$$
$$\left. R_{s,h}\left[\cot\left(\frac{\pi + (\Phi + \Phi')}{2n}\right) + \cot\left(\frac{\pi - (\Phi + \Phi')}{2n}\right) T\left(\pm jXa_r\right)\right] \right\} \quad (213)$$

$$R_{s,h} = \mp 1. \quad (214)$$

SECTION 5

Top-Hat

1 Introduction

The study of scattering from the top-hat has been of interest for a long time. Among some of the latest work is [26]. Which uses physical optics to get an approximate backscatter result. In order to get a more accurate UTD result, the 2-D dihedral discussed in Section 3 can be extended to get 3-D results for a wide variety of problems. The solution of the triangular dihedral in the principal plane is discussed in [13] is the starting point. A few modifications are required to the UTD 2-D analysis of the dihedral in order to obtain the solution to the top-hat. The high frequency solution is validated against a moment method body of revolution result [27]. For a 90° dihedral, as seen in Section 2, the number of important terms decreases significantly for the backscatter case. It is shown that a complete solution can be obtained by including the D, DR and RD, DD, and DRD terms.

For the top-hat, a UTD result is obtained from the important terms which is valid in all regions for backscatter and is reasonably simple to program. Also, in the dihedral region, the dominant result is further simplified to provide approximate results. The parameters for the top-hat are shown in Figure 52.
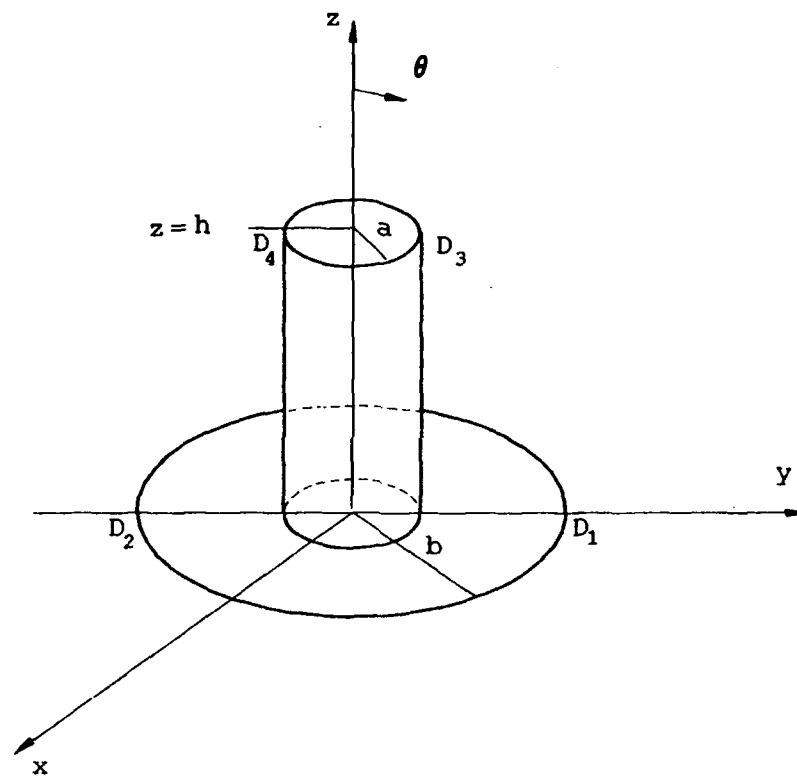
Figure 52: Top-hat geometry.

2 Double Diffraction Simplified to Retain the Significant Part

In order to obtain a result which is valid in all regions and is simple to program, it is necessary to extract the dominant part of the double diffraction for the backscatter case when the two diffractions are occurring from the same point. This is only possible in terms such as DRD.

The double diffraction formulation for the joint wedge, discussed in Section 6, is used to get the dominant part of the the double diffraction coefficient. In this case, $n_1 = n_2 = n$, $a_p = a_q = a$, $\Phi_p = \Phi_q = \Phi$, and d are the same as defined in Section 6 for the joint wedge. In order to get the dominant contribution, it is necessary to choose $\Phi = \pi - (n\pi - \phi)$, where the angle, ϕ, is measured from the 'o' face, as shown in Figure 9. Also, the distance parameter, d, is the distance traced by the ray between the first and the second diffraction points. For this case, the double diffraction coefficients, P_s and P_h, Equations (45) and (46), can be simplified to

$$P_r(Q_1, Q_1) = P_s(\Phi, n, d) = \frac{1}{8\pi j n^1} \frac{a^2}{\sin^1(\frac{\Phi}{2n})}$$
$$d\left[\left(j + \frac{1}{2kda}\right) F[kda] - j\right]\left(\frac{e^{-jkd}}{\sqrt{d}}\right), \tag{215}$$

for a TM plane wave (with the electric field parallel to the wedge), and for a TE plane wave (with the electric field perpendicular to the wedge),

$$P_m(Q_1, Q_1) = P_h(\Phi, n, d) = -\frac{1}{4\pi j n^2} \cot^2\left(\frac{\Phi}{2n}\right)$$
$$da\left[\left(j - \frac{1}{2kda}\right) F[kda] - j\right]\left(\frac{e^{-jkd}}{\sqrt{d}}\right). \tag{216}$$

For the top-hat, these equations are used to get the dominant contribution from $D_1 RD_1$, $D_3 RD_3$ and $D_4 RD_4$ terms.

3 Modifications Required

Basically, rim caustic correction and spread factors are required to modify the 2-D dihedral solution to obtain the solution for the top-hat. In Section 3, it is shown that, for the backscatter case, the most dominant terms for the 90° dihedral are diffraction, diffracted-reflected (DR), reflected-diffracted (RD), and diffracted-reflected-diffracted (DRD). The dominant contribution from these terms are used to get the result for the top-hat.

3.1 D, RD, DR and DRD terms

For the backscatter case, referring to Figure 52, using Equation (25), the diffracted terms from the disk is given by

$$U_{disk}^{D_1} = U_{s,h}^i \frac{-e^{-j\pi/4}}{2\sqrt{2\pi k}} \left[1 - R_{s,h} \frac{1}{\sin(\theta)} \right] T_c \left(2kb \sin(\theta) \right)$$

$$\sqrt{\frac{b}{2\sin(\theta)}} e^{j2k(b-a)\sin(\theta)}, \tag{217}$$

and

$$U_{disk}^{D_2} = U_{s,h}^i \frac{-e^{-j\pi/4}}{2\sqrt{2\pi k}} \left[1 + R_{s,h} \frac{1}{\sin(\theta)} \right] T_c \left(-2kb \sin(\theta) \right)$$

$$\sqrt{\frac{b}{2\sin(\theta)}} e^{j\frac{\pi}{2}} e^{j2k(b-a)\sin(\theta)} e^{-j4kb\sin(\theta)};$$

$$\begin{cases} 0 < \theta < \tan^{-1} \left[\frac{b-a}{h} \right], \\ \frac{\pi}{2} < \theta < \pi, \end{cases} \tag{218}$$

where $R_{s,h} = \mp 1$ and

$$U_{s,h} = \begin{cases} E, & \text{E field perpendicular to the pattern plane} \\ H, & \text{H field perpendicular to the pattern plane.} \end{cases} \tag{219}$$

Using Equation (13), the diffracted terms from the cylindrical surface are

$$U_{cyl}^{D_3} = U_{s,h}^i \frac{2e^{-j\pi/4} \sin\left(\frac{2\pi}{3}\right)}{3\sqrt{2\pi k}} \left[\frac{1}{\cos\left(\frac{2\pi}{3}\right) - 1} + \right.$$

86

$$R_{s,h}\frac{1}{\cos\left(\frac{2\pi}{3}\right)-\cos\left(\frac{2\pi+\theta}{3}\right)}\Bigg]\,T_r\left(2ka\sin\left(\theta\right)\right)$$

$$\sqrt{\frac{a}{2\sin\left(\theta\right)}}e^{j2kh\cos(\theta)};$$

$$\theta<\frac{\pi}{2}+\tan^{-1}\left[\frac{h}{b-a}\right],\tag{220}$$

and

$$U_{cyl}^{D_4}=U_{s,h}'\frac{2e^{-j\pi/4}\sin\left(\frac{2\pi}{3}\right)}{3\sqrt{2\pi k}}\left[\frac{1}{\cos\left(\frac{2\pi}{3}\right)-1}+\right.$$

$$R_{s,h}\frac{1}{\cos\left(\frac{2\pi}{3}\right)-\cos\left(\frac{4(\pi+\theta)}{3}\right)}\Bigg]\,T_r\left(-2ka\sin\left(\theta\right)\right)$$

$$\sqrt{\frac{a}{2\sin\left(\theta\right)}}e^{j\frac{\pi}{2}}e^{j2kh\cos(\theta)}e^{-j4ka\sin(\theta)};$$

$$0<\theta<\frac{\pi}{2}.\tag{221}$$

The diffracted-reflected terms, obtained by simplifying Equations (79) and (80) and modifying for curvature and the caustic correction are given as

$$U^{RD_3}+U^{D_3R}=U_{s,h}'\frac{e^{-j\pi/4}}{\sqrt{2\pi k}}T_r\left(2ka\sin\left(\theta\right)\right)$$

$$\left\{R_{s,h}\frac{4\sin\left(\frac{2\pi}{3}\right)}{3\left[\cos\left(\frac{\pi-2\theta}{3}\right)-\cos\left(\frac{2\pi-\theta}{3}\right)\right]}+j2kh\sin\left(\theta\right)\right\}\sqrt{\frac{a}{2\sin\left(\theta\right)}};$$

$$0<\theta<\tan^{-1}\left[\frac{b-a}{h}\right],\tag{222}$$

and

$$U^{D_4R}+U^{RD_4}=U_{s,h}'\frac{-e^{-j\pi/4}}{2\sqrt{2\pi k}}$$

$$\left\{2R_{s,h}\frac{1}{\cos\left(\theta\right)}-j4k\left(b-a\right)\cos\left(\theta\right)\right\}\sqrt{\frac{a}{2\sin\left(\theta\right)}};$$

$$\tan^{-1}\left[\frac{b-a}{h}\right]<\theta<\frac{\pi}{2}.\tag{223}$$

For the DRD terms, as discussed in Section 2, only the dominant part is retained. The dominant part of DRD, where the diffractions are from the disk, is

$$U^{D,RD_4}=R_{s,h}U_{s,h}'P_{s,h}\left(\Phi=\theta-\frac{\pi}{2},n=2,d=2\left(b-a\right)\right)$$

87

$$\sqrt{\left(\frac{\rho_1}{\rho_1 + (b-a)}\right)\left(\frac{\rho^r}{\rho^r + (b-a)}\right)}\,\rho_2\, e^{j2k(b-a)\sin(\theta)}, \qquad (224)$$

where

$$\rho_1 = \frac{b}{\sin(\theta) - 1}, \qquad (225)$$

$$\rho^r = \frac{((b-a) + \rho_1)a}{a + 2((b-a) + \rho_1)}, \qquad (226)$$

$$\rho_2 = \frac{b((b-a) + \rho^r)}{b + [\sin(\theta) - 1]\,[(b-a) + \rho^r]}, \qquad (227)$$

and $P_{s,h}(\Phi, n, d)$ is given by Equations (215) and (216). The dominant part of DRD terms, where the diffractions are from the cylindrical surface, are

$$U^{D_3 R D_3} = R_{s,h} U_{s,h}^i P_{s,h}\left(\Phi = \theta, n = 2, d = 2h\right) T_r\left(2ka\sin\left(\theta\right)\right)$$

$$\sqrt{\frac{a^2}{2\left(a + h\sin(\theta)\right)\sin(\theta)}}\, e^{j2kh\cos(\theta)};$$

$$0 < \theta < -\frac{\pi}{2} - \tan^{-1}\left[\frac{h}{b-a}\right], \qquad (228)$$

and

$$U^{D_4 R D_4} = R_{s,h} U_{s,h}^i P_{s,h}\left(\Phi = \frac{\pi}{2} + \theta, n = 2, d = 2h\right) T_r\left(-2ka\sin\left(\theta\right)\right)$$

$$\sqrt{\frac{a^2}{2\left(a + h\sin(\theta)\right)\sin(\theta)}}\, e^{j\frac{\pi}{2}} e^{j2kh\cos(\theta)} e^{j4ka\sin(\theta)};$$

$$0 < \theta < \frac{\pi}{2}. \qquad (229)$$

4 Dominant Result in the Double Bounce Region

It is shown in Section 2 that the diffracted-reflected type terms, RD and DR, may be combined to give a dominant result in the double bounce region for the dihedral. For the top-hat, a result in the double bounce region can be obtained by modifying Equations (79) and (80),to take into account the curvature, so that

$$U_{dominant}^{RD_3 + D_3 R} = U_{s,h}^i e^{j\frac{\pi}{4}} \sqrt{\frac{2a\sin(\theta)}{\lambda}}\, h; \quad \theta_{cut} < \theta < \tan^{-1}\left[\frac{b-a}{h}\right], \qquad (230)$$

and

$$U_{dominant}^{D_1R+RD_1} = U'_{s,h} e^{j\frac{\pi}{4}} \sqrt{\frac{2a}{\lambda \sin(\theta)}} (b-a)\cos(\theta); \quad \tan^{-1}\left[\frac{b-a}{h}\right] < \theta < \frac{\pi}{2} - \theta_{cut}. \quad (231)$$

In Equations (230) and (231), θ_{cut} is an angle that is chosen such that the specular from the disk and the top of the cylindrical rim are not significant. This is necessary since these equations do not consider singly diffracted fields. A reasonable choice for θ_{cut} is approximately $10°$.

5 PO on the Axis of the Top-Hat

Along the axis of the top-hat, the cotangent terms of the diffraction coefficients that tend to "blow" up and combine to give the dominant result. Not surprisingly, the dominant result obtained is exactly as one would predict from physical optics [20].

As expected, at the z-axis, the reflection boundary cotangent terms associated with the diffraction from the disk (Equations (217) and (218)), give the area of the disk. The reflection boundary cotangent terms associated with the diffraction from the upper face of the cylinder (Equations (220) and (221)), give the area of the end cap. The incident boundary terms from D_3R, RD_3 and D_3RD_3 (Equations (222), (228) and (229)), give the negative area of the end cap. Thus the apparent "infinites" combine to give a result which equals the area of the disk minus the area of the end cap of the cylinder plus the area of the end cap of the cylinder with the phase taking into account twice the electrical distance of the cylinder. The RCS along the axis of the top-hat is appropriately given as

$$\sigma_{top,hat}^{po}\bigg|_{\theta=0°} = 4\pi \left|\frac{\pi(b^2-a^2)}{\lambda} + \frac{\pi a^2}{\lambda} e^{-jk2h}\right|^2. \quad (232)$$

6 Results

Figures 53 and 54 compare the results obtained for the $\theta\theta$ and $\phi\phi$ polarizations by the UTD computer code and the Body of Revolution code at 10 GHz for a top-hat
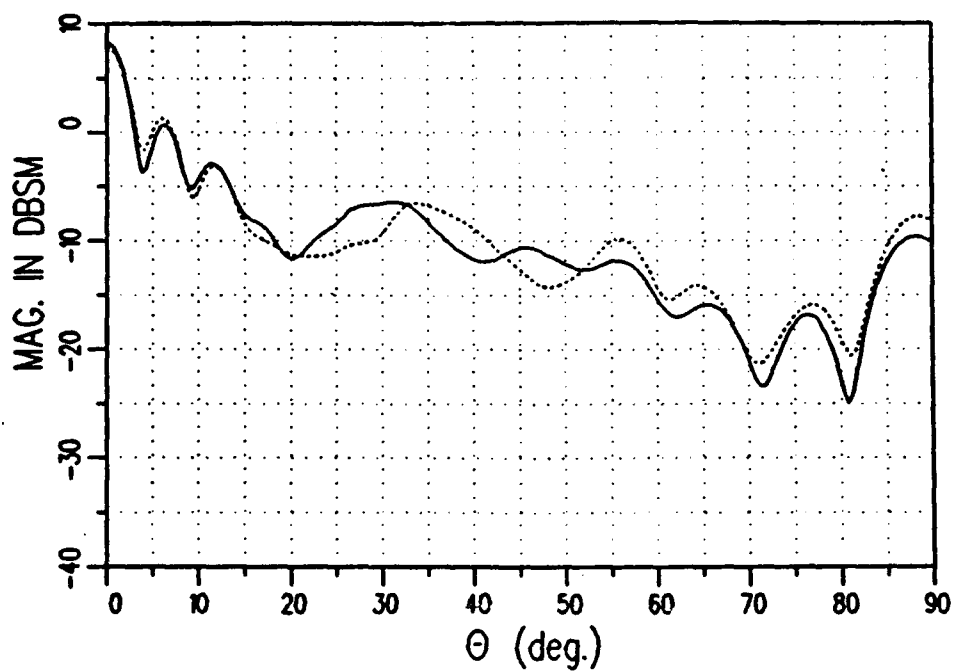
Figure 53: Backscatter field with $\theta\theta$ polarized field. The solid line is UTD solution and the dashed line is the BOR solution.
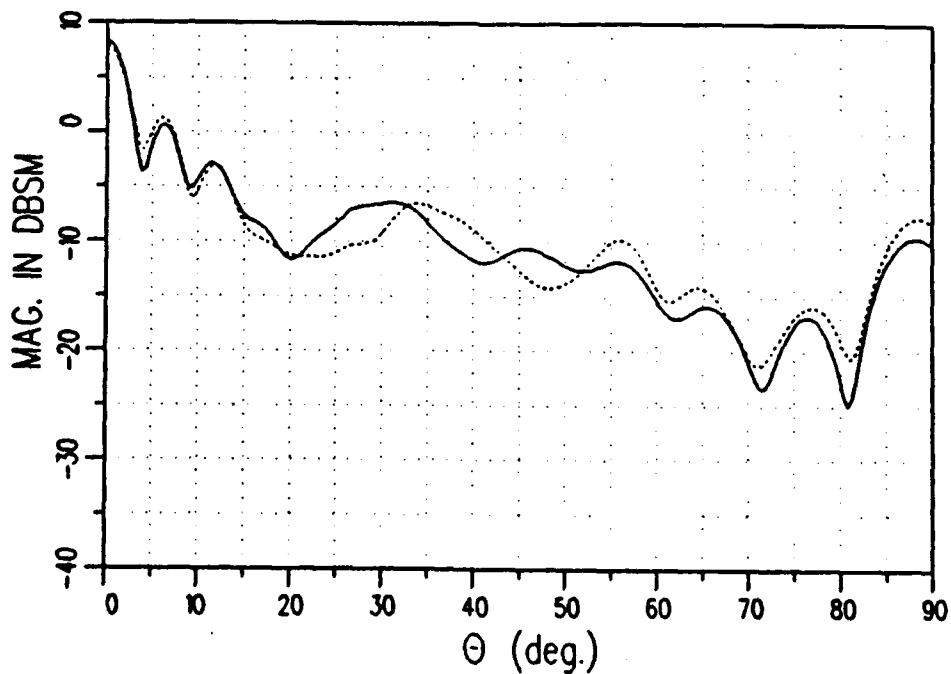
Figure 54: Backscatter field with $\phi\phi$ polarized field. The solid line is UTD solution and the dashed line is the BOR solution.

of cylinder of dimensions $a= 2$ in, $b= 4$ in, and $h= 4$ in. The results compare well with the body of revolution code.

7   Bruderhedral

A bruderhedral is a reflector that is an angular sector of a top-hat. (See Figure 55.) Fundamentally, the solution to the bruderhedral is the same as that of the top-hat, discussed above. In the region, $0 < \theta < 90°$, the scattered fields are determined from Equations (217), (220), (222), (223), (224) and (228) with $T_e(U)$ replaced by $T_{partial}(U)$ which is defined as:

$$T_{partial}(U) = \frac{1}{\pi}(U)\sqrt{\frac{\pi U}{2}}e^{-j\left(U-\frac{\pi}{4}\right)}\int_{-\phi_{bound}}^{\phi_{bound}} \cos\phi_e e^{jU\cos\phi_e}d\phi_e, \qquad (233)$$

where $-\phi_{bound} < \phi < \phi_{bound}$ is the angle made by the sector of the bruderhedral.

8   Results

Figures 56 and 57 compare the results obtained for the $\theta\theta$ and $\phi\phi$ polarizations by the UTD computer code and the measurements at 10 GHz for a bruderhedral of dimensions $a= 107$ cm, $b= 115.9$ cm, $c= 30.5$ cm and $h= 8.9$ cm. The measurements are courtesy of D. Blejer of MIT, Lincoln Laboratory. The lip of the model used in the actual measurements is believed to have edges parallel to the y-axis, as shown in Figure 55. The UTD results have edges along constant radial lines. The differences are expected to be minimal since a is much larger than the difference between b and a. The results compare well with the measurements.

91
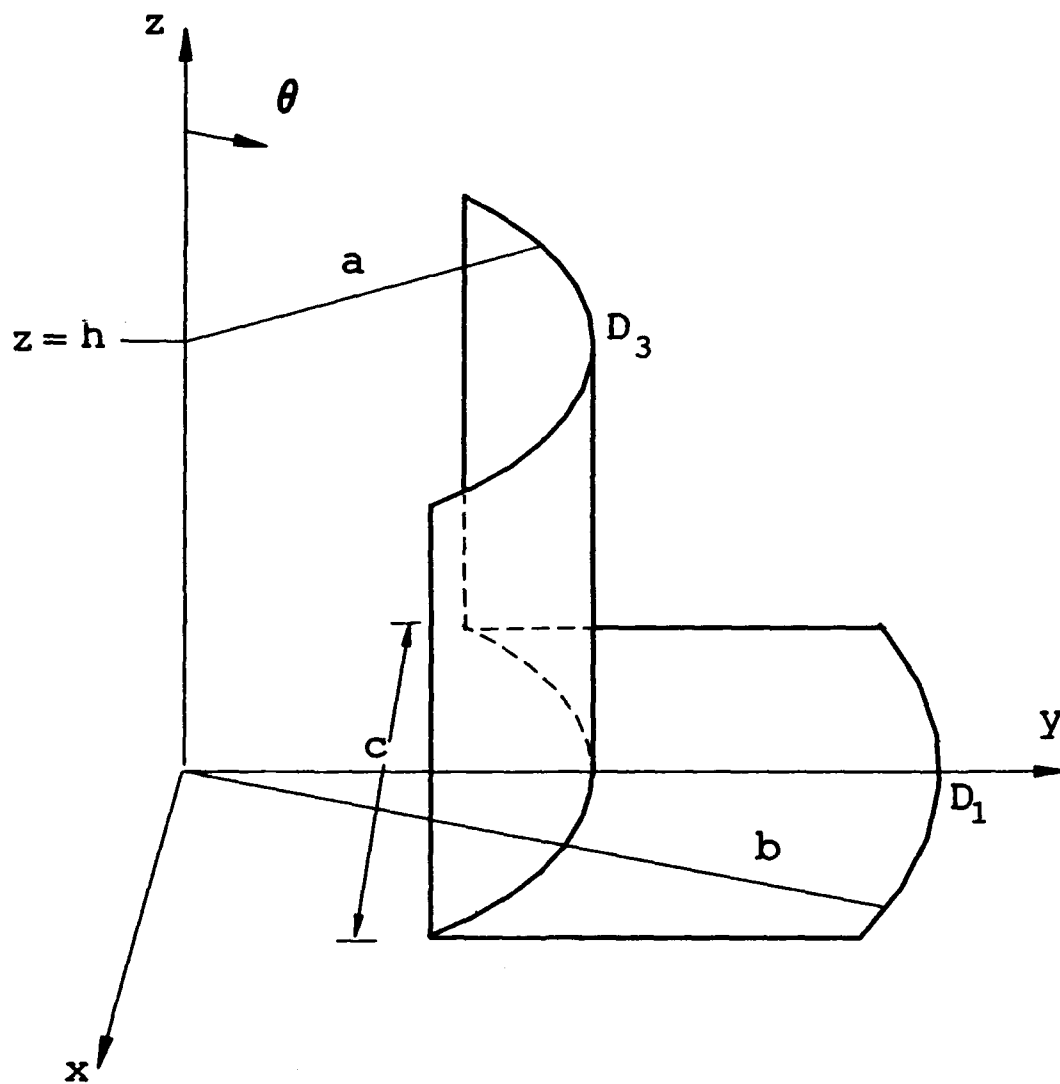
Figure 55: Bruderhedral geometry.
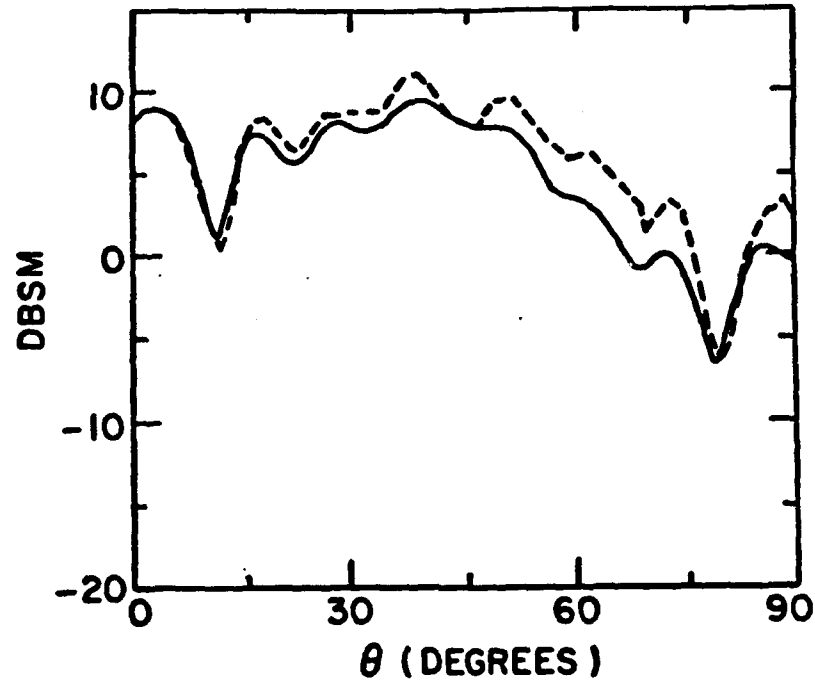
Figure 56: Backscatter field with $\theta\theta$ polarized field. The solid line is UTD solution and the dashed line is the measurement.
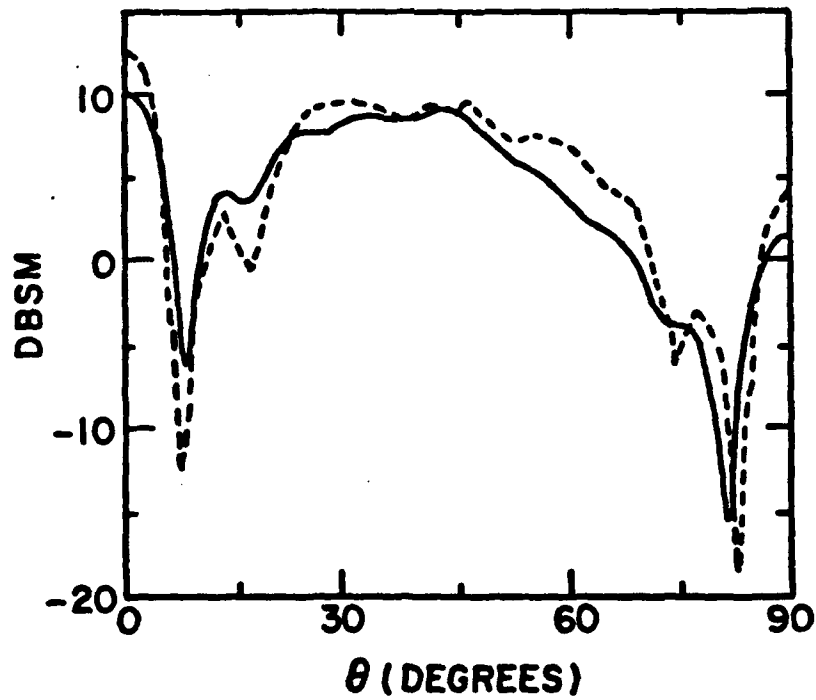
Figure 57: Backscatter field with $\phi\phi$ polarized field. The solid line is UTD solution and the dashed line is the measurement.

93

SECTION 6

Bi-Cone

1 Introduction

The methods used to analyze the top-hat in the previous section are very similar to those required to obtain the scattered fields in the far-zone from the bi-cone. In general, all the terms discussed for the UTD 2-D solution of the dihedral in Section 3 have to be modified to take into account curvature and specular caustics. However, by putting a restriction on the bi-cone that the sum of the cone angles, $\alpha_{r,1}$ and $\alpha_{r,2}$ in Figure 58, is a right angle, for the backscatter case, the number of important terms decreases significantly as seen in Section 6. For this case, a dominant UTD result is obtained which is valid in all regions and is simple to program. Also, in the dihedral region, the dominant result is further simplified by using only the double bounce terms to provide approximate results. Figure 58 shows the parameters for the bi-cone.

2 Modifications Required

Basically, it is only necessary to change the caustic corrections and spread factors in the 2-D dihedral solution to obtain a result for the bi-cone. Two types of caustic corrections are needed. One is the rim caustic which is discussed in Section 3 and

94
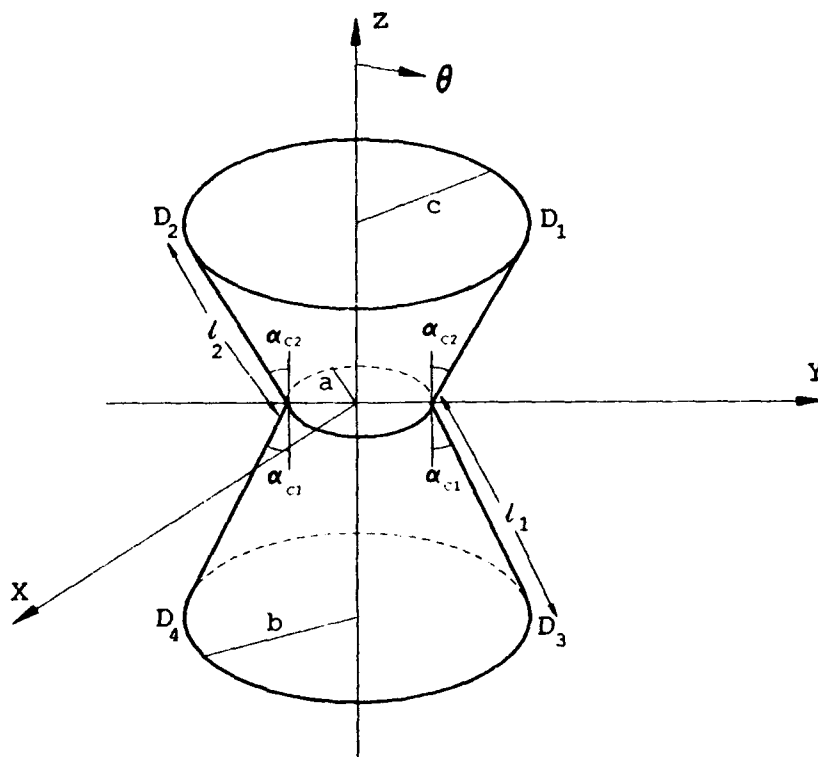
Figure 58: Bi-Cone geometry.

used in the solution of the top-hat in Section 5, and the other is the curved-surface specular region correction which is examined in Section 4.

3 Dominant Result

The bi-cone has the same type of dominant mechanisms as the 2-D dihedral. In order to simplify the problem, it is necessary to choose cone angles such that $\alpha_{r1} + \alpha_{r2} = 90°$. Thus, as for the 2-D dihedral discussed in Section 6, the dominant result is obtained from diffracted (D), RD, RD and DRD terms for the bi-cone.

3.1 D, RD, DR and DRD terms

The expressions shown below are for backscatter from a bi-cone of parameters given in Figure 58. Also note that

$$\alpha_{r1} = \sin^{-1}\left[\frac{b-a}{l_1}\right], \tag{234}$$

$$\alpha_{r2} = \sin^{-1}\left[\frac{c-a}{l_2}\right], \tag{235}$$

$$n_1 = \frac{3}{2} + \frac{\alpha_{r1}}{\pi}, \tag{236}$$

and

$$n_2 = \frac{3}{2} + \frac{\alpha_{r2}}{\pi}. \tag{237}$$

Using Equations (25) and (26), the diffracted fields from the upper rim of the bi-cone of radius c is given by

$$U^{D_1} = U'_{s,h}\frac{-e^{-j\frac{\pi}{4}}}{2n_2\sqrt{2\pi k}}\left[2\cot\left(\frac{\pi}{n_2}\right) + R_{s,h}\left\{-\cot\left(\frac{\theta}{n_2}\right)\right.\right.$$
$$\left.\left. + \cot\left(\frac{\pi+\theta}{n_2}\right)T_r\left(-jkc\left(\frac{l_2}{c-a}\right)2\cos\left(2\alpha_{r2}-2\theta\right)\right)\right\}\right]T_r\left(2kc\sin\theta\right)$$
$$\sqrt{\frac{c}{2\sin\theta}}e^{j2kl_2\cos(\theta-\alpha_{r2})}, \tag{238}$$

96

and

$$U^{D_2} = U^i_{s,h} \frac{e^{-j\frac{\pi}{4}} \sin\left(\frac{\pi}{n_2}\right)}{n_2\sqrt{2\pi k}} \left[\frac{1}{\cos\left(\frac{\pi}{n_2}\right) - 1} + \right.$$

$$\left. R_{s,h} \frac{1}{\cos\left(\frac{\pi}{n_2}\right) - \cos\left(\frac{\pi - 2\theta}{n_2}\right)} \right] T_c\left(-2kc\sin\theta\right)$$

$$\sqrt{\frac{c}{2\sin\theta}}\, e^{j\frac{\pi}{2}} e^{j2kl_2\cos(\theta - \alpha_{c2})} e^{-j\, lkc\sin\theta};$$

$$\theta < \frac{\pi}{2}. \tag{239}$$

The diffracted field from the lower rim of the bi-cone of radius b is given by

$$U^{D_3} = U'_{s,h} \frac{-e^{-j\frac{\pi}{4}}}{2n_1\sqrt{2\pi k}} \left[2\cot\left(\frac{\pi}{2n_1}\right) + R_{s,h}\left\{ \cot\left(\frac{\theta - \pi}{n_1}\right) \right. \right.$$

$$\left. \left. + \cot\left(\frac{2\pi - \theta}{n_1}\right) T_c\left(-jkb\left(\frac{l_1}{b - a}\right) 2\cos\left(2\alpha_{c1} + 2\theta\right)\right) \right\} \right] T_c\left(2kb\sin\theta\right)$$

$$\sqrt{\frac{b}{2\sin\theta}} e^{-j2kl_1\cos(\theta + \alpha_{c1})}, \tag{240}$$

and

$$U^{D_4} = U^i_{s,h} \frac{e^{-j\frac{\pi}{4}} \sin\left(\frac{\pi}{n_1}\right)}{n_1\sqrt{2\pi k}} \left[\frac{1}{\cos\left(\frac{\pi}{n_1}\right) - 1} + \right.$$

$$\left. R_{s,h} \frac{1}{\cos\left(\frac{\pi}{n_1}\right) - \cos\left(\frac{2\theta - \pi}{n_1}\right)} \right] T_c\left(-2kb\sin\theta\right)$$

$$\sqrt{\frac{b}{2\sin\theta}}\, e^{\frac{\pi}{2}} e^{-j2kl_1\cos(\theta + \alpha_{c1})} e^{-j\, lkb\sin\theta};$$

$$\theta > \frac{\pi}{2}. \tag{241}$$

The purpose of the curved surface specular caustic correction for the DR and DRD terms is twofold: to ensure continuity of the fields, and to obtain the physical optics result for the visible part of the cone in the specular direction. This requires that for the diffraction-reflection type terms, the caustic correction is associated with the incident shadow boundary. After simplifying Equations (70) and (71) and modifying for curvature and caustic, the diffraction-reflection terms are given as

$$U^{D_1 R} + U^{RD_1} = U^i_{s,h} \frac{-e^{-j\frac{\pi}{4}}}{n_2\sqrt{2\pi k}} \left[R_{s,h}\left\{ \cot\left(\frac{\pi - \theta + \alpha_{c1}}{n_2}\right) \right. \right.$$

97

$$+ \cot\left(\frac{\theta - \alpha_{c2}}{n_2}\right) T_c\left(jka\left(\frac{l_1}{b-a}\right) 2\cos(2\alpha_{c1} + 2\vartheta)\right)\Bigg\}$$

$$+ \cot\left(\frac{\pi}{n_2}\right) - j2n_2 kl_2 \sin(\theta - \alpha_{c2})\Bigg] \sqrt{\frac{\rho_2^{r1}\rho^{d1}}{(\rho_2^{r1} + s_1)}};$$

$$\alpha_{c2} < \theta < \alpha_{c2} + \tan^{-1}\left[\frac{l_1}{l_2}\right], \qquad (242)$$

and

$$U^{D_3 R} + U^{RD_3} = U^i_{s,h}\frac{-e^{-j\frac{\pi}{4}}}{n_1\sqrt{2\pi k}}\left[R_{s,h}\left\{\cot\left(\frac{\pi - \theta - \alpha_{c2}}{n_1}\right)\right.\right.$$

$$+ \cot\left(\frac{\theta + \alpha_{c1}}{n_1}\right) T_c\left(jka\left(\frac{l_2}{c-a}\right) 2\cos(2\alpha_{c2} - 2\theta)\right)\Bigg\}$$

$$+ \cot\left(\frac{\pi}{n_1}\right) - j2n_1 kl_1 \sin(\theta + \alpha_{c1})\Bigg] \sqrt{\frac{\rho_2^{r2}\rho^{d2}}{(\rho_2^{r2} + s_2)}};$$

$$\alpha_{c2} + \tan^{-1}\left[\frac{l_1}{l_2}\right] < \theta < \pi - \alpha_{c1}. \qquad (243)$$

In the above equation for $D_1 R$ and RD_1 terms

$$\rho_2^{r1} = \frac{R_{r1}}{2\sin(\theta + \alpha_{c1})}, \qquad (244)$$

$$R_{r1} = \frac{a - l_2\cot(\theta + \alpha_{c1})\sin\alpha_{c1}}{\cos\alpha_{c1}}, \qquad (245)$$

$$\rho^{d1} = \frac{c\left(s + \rho_2^{r1}\right)}{c + \left(s_1 + \rho_2^{r1}\right)\left(\sin\theta + \sin(\theta - 2\alpha_{c2})\right)} \qquad (246)$$

and

$$s_1 = \frac{l_2}{\sin(\theta + \alpha_{c1})}, \qquad (247)$$

and for $D_3 R$ and RD_3 terms

$$\rho_2^{r2} = \frac{R_{r2}}{2\sin(\theta + \alpha_{c2})}, \qquad (248)$$

$$R_{r2} = \frac{a + l_1\cot(\theta - \alpha_{c2})\sin\alpha_{c2}}{\cos\alpha_{c2}}, \qquad (249)$$

$$\rho^{d2} = \frac{b\left(s + \rho_2^r\right)}{b + \left(s_2 + \rho_2^r\right)\left(\sin\theta + \sin(\theta + 2\alpha_{c2})\right)} \qquad (250)$$

and

$$s_2 = \frac{l_1}{\sin\left(\theta - \alpha_{c2}\right)}. \tag{251}$$

For the DRD terms, as discussed in Section 2, only the dominant part is retained for the joined wedges solution. The dominant part of the DRD term in the region where z is positive (especially around $\theta = \alpha_{c2}$) is

$$U^{D_1 RD_1} = R_{s,h} U^i_{s,h} P_{s,h} \left(\Phi = \theta - \alpha_{c2}, n = n_2, d = 2l_2\right)$$
$$\frac{T_c \left(jka\left(\dfrac{l_1}{b-a}\right) 2\cos\left(2\theta + 2\alpha_{c1}\right)\right)}{\sqrt{\left(\dfrac{\rho^{d1}}{\rho^{d1}+l_2}\right)\left(\dfrac{\rho^{r1}}{\rho^{r1}+l_2}\right)} \, \rho^{d2}} \, e^{j2kl_2\cos(\theta - \alpha_{c2})}, \tag{252}$$

and in the region where z is negative (especially around $\theta = \pi - \alpha_{c1}$)

$$U^{D_3 RD_3} = R_{s,h} U^i_{s,h} P_{s,h} \left(\Phi = \theta - (\pi - \alpha_{c1}), n = n_1, d = 2l_1\right)$$
$$\frac{T_c \left(jka\left(\dfrac{l_2}{c-a}\right) 2\cos\left(2\alpha_{c2} - 2\theta\right)\right)}{\sqrt{\left(\dfrac{\rho^{d3}}{\rho^{d3}+l_1}\right)\left(\dfrac{\rho^{r2}}{\rho^{r2}+l_1}\right)} \, \rho^{d4}} \, e^{-j2kl_1\cos(\theta + \alpha_{c1})}. \tag{253}$$

In Equation (252)

$$\rho^{d1} = \frac{c}{\sin\theta - \sin\alpha_{c2}}, \tag{254}$$

$$\rho^{r1} = \frac{\left(\rho^{d1}+l_2\right)a}{a + \left(\rho^{d1}+l_2\right)2\cos\alpha_{c1}}, \tag{255}$$

$$\rho^{d2} = \frac{\left(\rho^{r1}+l_2\right)c}{c + \left(\rho^{r1}+l_2\right)\left(\sin\theta - \sin\alpha_{c2}\right)}, \tag{256}$$

and in Equation (253)

$$\rho^{d3} = \frac{b}{\sin\theta - \sin\alpha_{c1}}, \tag{257}$$

$$\rho^{r2} = \frac{\left(\rho^{d3}+l_1\right)a}{a + \left(\rho^{d3}+l_1\right)2\cos\alpha_{c2}} \tag{258}$$

and

$$\rho^{d4} = \frac{\left(\rho^{r2}+l_1\right)c}{c + \left(\rho^{r2}+l_1\right)\left(\sin\theta - \sin\alpha_{c1}\right)}. \tag{259}$$

99

4 Dominant Result in the Double Bounce Region

It is shown in Section 2 that the diffracted-reflected type terms, RD and DR, may be combined to give a dominant result in the double bounce region for the dihedral. Modifying Equations (79) and (80), to take into account the curvature, a result in the dihedral region for the bi-cone can be given as

$$U_{dominant}^{RD_1+D_1R} = U_{s,h}^i e^{j\frac{\pi}{4}} \frac{2l_2}{\sqrt{\lambda}} \sqrt{\frac{\rho_2^{r1}\rho^{d1}}{(\rho_2^{r1}+s_1)}} \sin(\theta - \alpha_{c2});$$

$$\alpha_{c2} + \theta_{cut} < \theta < \alpha_{c2} + \tan^{-1}\left[\frac{l_1}{l_2}\right], \quad (260)$$

and

$$U_{dominant}^{D_3R+RD_3} = U_{s,h}^i e^{j\frac{\pi}{4}} \frac{2l_1}{\sqrt{\lambda}} \sqrt{\frac{\rho_2^{r2}\rho^{d2}}{(\rho_2^{r2}+s_2)}} \sin(\theta + \alpha_{c1});$$

$$\alpha_{c2} + \tan^{-1}\left[\frac{l_1}{l_2}\right] < \theta < \pi - \alpha_{c1} - \theta_{cut}. \quad (261)$$

Using Equations (244) to (247) in Equation (260), and using Equations (248) to (251) in Equation (261), the dominant contribution from the double bounce is obtained. An angle, θ_{cut}, is chosen so that the specular from the curved sides of the cones are not significant. This is necessary since these equations do not consider singly diffracted fields. A reasonable choice for θ_{cut} is approximately 10°.

5 Results

Figures 59 and 60 show the results obtained for the $\theta\theta$ and $\phi\phi$ polarizations by the UTD computer code and the moment method body of revolution code [27] at 10 GHz for bi-cone of $a = 0.5$ in (0.42 λ), $b = c = 2.0$ in (1.69 λ), and $l_1 = l_2 = 1.5\sqrt{2}$ in (1.8 λ). Considering the small size of the bi-cone, the results compare well with the body of revolution moment method code.
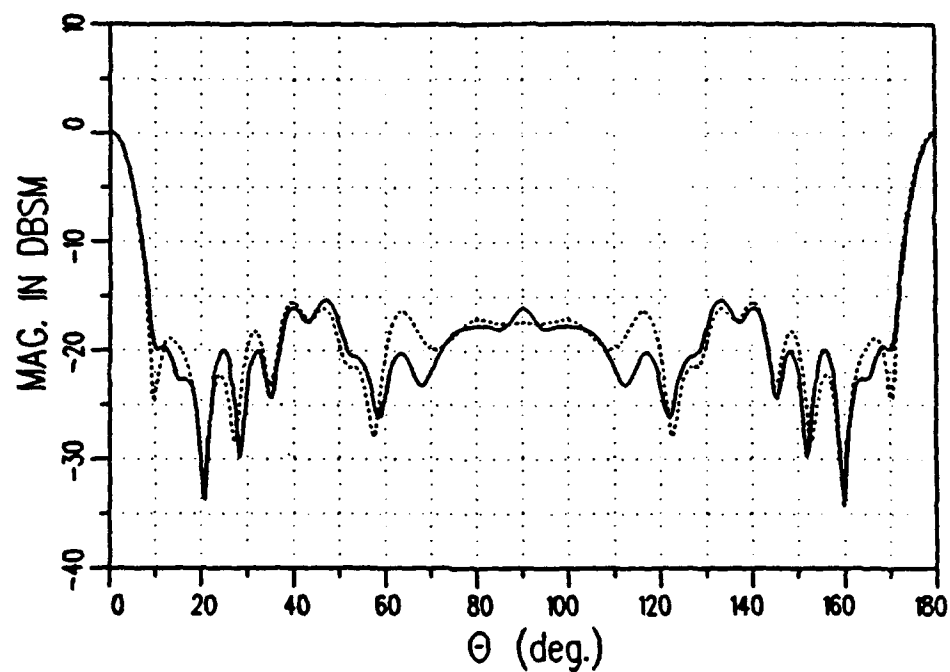
Figure 59: Backscatter field with $\theta\theta$ polarized field. The solid line is UTD solution and the dashed line is the BOR solution.
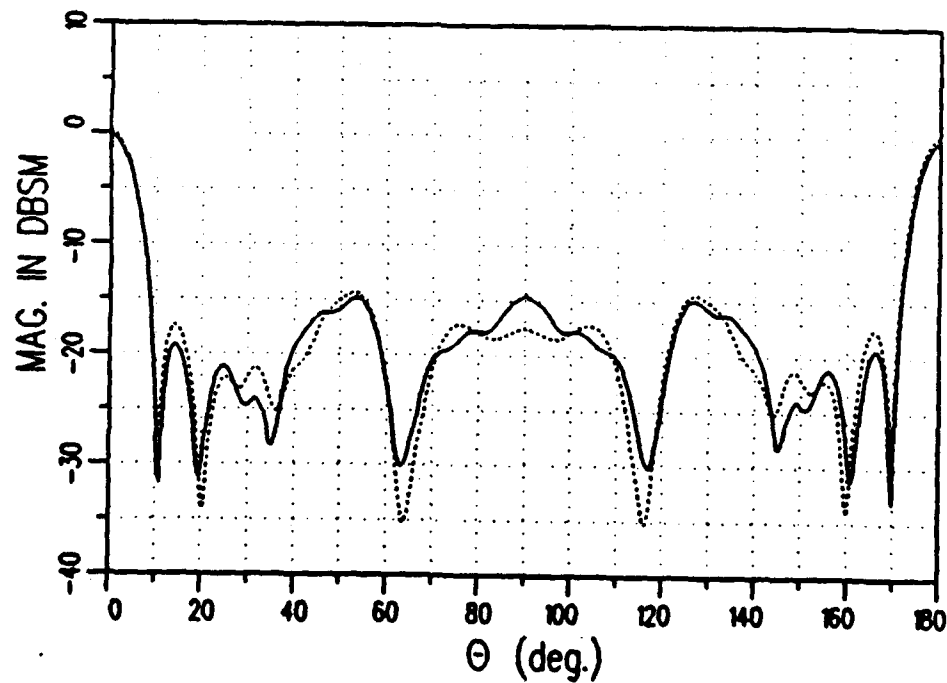
Figure 60: Backscatter field with $\phi\phi$ polarized field. The solid line is UTD solution and the dashed line is the BOR solution.

SECTION 7

Parallel Plate Cavity and Circular Cavity

1   Introduction

The study of scattering from a parallel plate cavity and its three-dimensional counterpart, a circular cavity, has been of much interest lately [28, 29]. These shapes may be used to model many common objects. For example, the parallel plate cavity can be used to represent the dominant scattering from a truck bed and the shallow circular cylinder cavity resembling a cake pan can be used to represent the dominant scattering from a wheel hub, cannon barrels, jet inlet structure, et cetera. The theory and the results discussed in this section are valid for cavities of arbitrary depths. However, since the terms in the non principal plane are not included, the smaller the height to width ratio of the cavity, the wider the range of angles over which the result is valid. Also, the dominant terms of a shallow cavity are the same over much of the region (the smaller the height to width ratio of the cavity, the larger is the region) as for a dihedral, which has been studied in detail in Section 3. In this section, three dots, "···", will represent one or more reflections within the cavity.

2   Dominant Terms for the Parallel Plate Cavity

Consider the two-dimensional geometry shown in Figure 61. For the backscatter
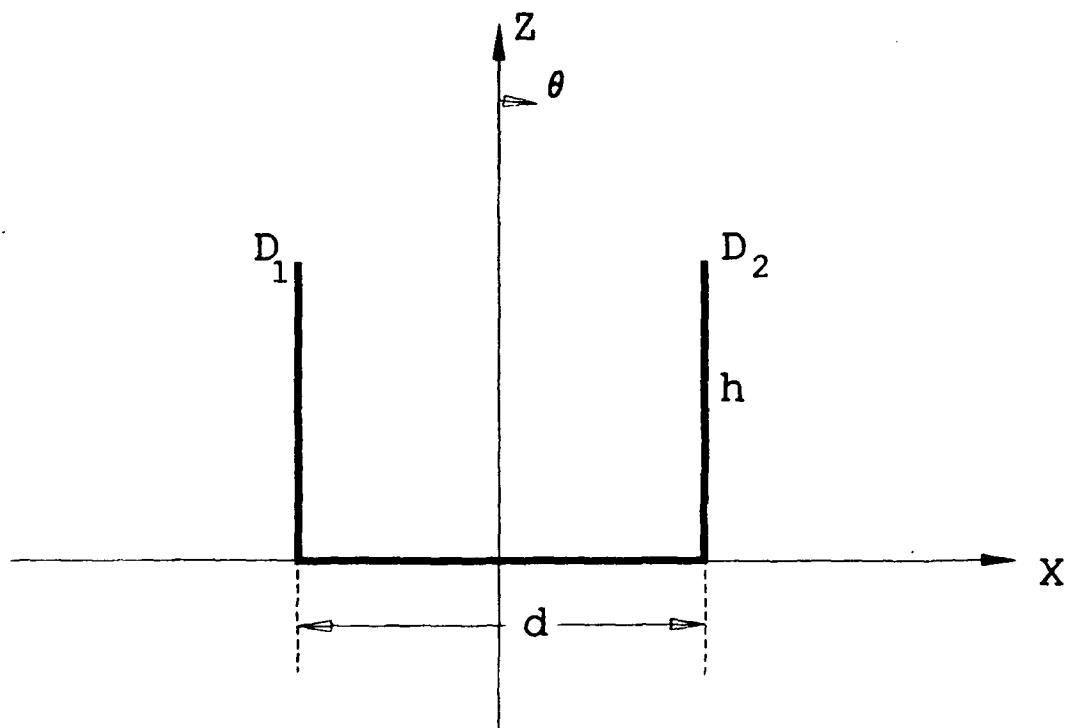
Figure 61: Two-dimensional parallel plate cavity geometry.

case, looking along the z-axis ($\theta = 0''$), the important terms are the diffractions (D_1 and D_2), diffracted-reflected ($D_1 R_b$ and $R_b D_1$) and the diffracted- reflected-diffracted ($D_1 R_b D_1$ and $D_2 R_b D_2$) terms. See Figure 62. R_b refers to the reflection from the base of the cavity. From the study of the basic dihedral mechanisms in Section 2, it is expected that as θ departs from $0°$, the diffracted-reflected ($D_1 R_b$ and $R_b D_1$) terms will dominate the solution. However, the angular range over which the diffracted-reflected terms dominate, will depend on the ratio of the height to the width of the cavity. The shallower and wider the cavity the larger is the angular range.

As θ increases, one set of terms get shadowed and another set of higher order terms appear. For example, once the DR and RD terms get shadowed the DRR and RRD terms appear, upon shadowing of DRR and RRD terms, DRRR and RRRD terms appear, et cetera. From a geometrical point of view, the $D_1 R \cdots$ and $\cdots R D_1$ terms are visible in the region ($\cdots$ represent reflections)

$$\tan^{-1}\left[\frac{md}{h}\right] < \theta < \tan^{-1}\left[\frac{(2m+1)d}{2h}\right], \tag{262}$$

where m is the number of reflections before reflecting from the base of cavity. For example, $m=0$ represents $D_1 R_b$, $m=1$ represents $D_1 R R_b R$, $m=2$ represents $D_1 R R R_b R R$ and so on. R_b refers to the reflection from the base. (See Figure 62.) Also, the $D_2 R \cdots$ and $\cdots R D_2$ terms are visible in the region

$$\tan^{-1}\left[\frac{(2m+1)d}{2h}\right] < \theta < \tan^{-1}\left[\frac{(m+1)d}{h}\right], \tag{263}$$

where m is the number of reflections before reflecting from the base of cavity. For example, $m=0$ represents $D_1 R_b R$, $m=1$ represents $D_1 R R_b R R$, $m=2$ represents $D_1 R R R_b R R R$ and so on. Again, R_b refers to the reflection from the base (see Figure 62). Given the angle θ, the value of m (number of reflections before reflecting from the base of the cavity) may be determined using Equations (262) and (263). Rearranging Equation (262),

$$\frac{2h\tan\theta - d}{2d} < m < \frac{h\tan\theta}{d} \tag{264}$$

104
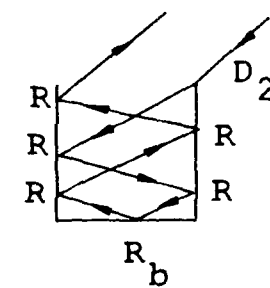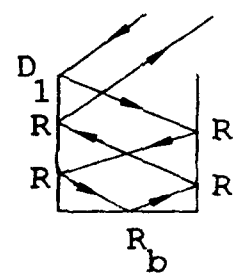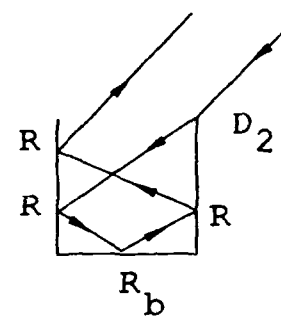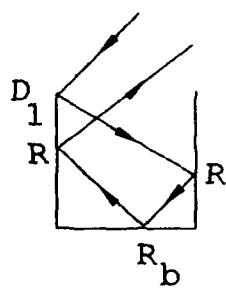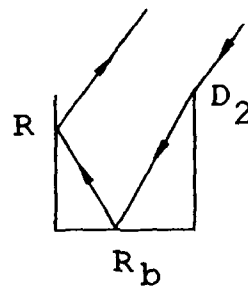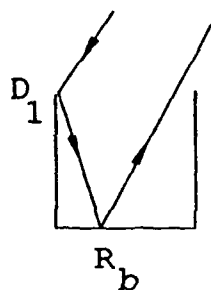
Figure 62: Some of the terms of the cavity problem.

and if the range of m includes an integer, then for the given angle, θ, the $D_1 \cdots$ term is present. Thus, the diffraction occurs from the upper left edge of the parallel plate cavity, and the integral value of m is the number of reflections before reflecting from the base of the cavity. Rearranging Equation (263),

$$\frac{h\tan\theta - d}{d} < m < \frac{2h\tan\theta - d}{2d}, \tag{265}$$

and if the range of m includes an integer, then for the given angle, θ, the $D_2 \cdots$ term is present. Thus, the diffraction occurs from the upper right edge of the parallel plate cavity, and the integral value of m is the number of reflections before reflecting from the base of the cavity. Note, in general, for a particular θ either Equation (264) or (265) will have an integral value in its range. If both the equations have an integral value in the range, then there is a shadow boundary at that angle.

2.1 $D_1 \cdots$ and $\cdots D_1$ Terms

Consider the case of diffraction from the top left edge (D_1) shown in Figure 63. The field from $D_1 \cdots$ for a bistatic angle of ϵ, where ϵ is a small number, valid in the region defined by Equation (262), is given as

$$U^{D_1 \cdots} \sim -\frac{e^{-j\frac{\pi}{4}}}{4\sqrt{2\pi k}} R_{s,h}^{(2m+2)} \cot\left(\frac{\pi - (\Phi + \Phi')}{4}\right) e^{jk(\vec{r}_1 \cdot \hat{r}' + \vec{r}_i \cdot \hat{r})}, \tag{266}$$

where m is the number of reflections before reflecting from the base of the parallel plate cavity, and

$$\hat{r}' = \sin\theta\,\hat{x} + \cos\theta\hat{z}, \tag{267}$$

$$\hat{r} = \sin(\theta - \epsilon)\,\hat{x} + \cos(\theta - \epsilon)\,\hat{z}, \tag{268}$$

$$\vec{r}_l = -a\,\hat{x} + h\,\hat{z} \tag{269}$$

is the position vector of the diffraction point (D_1),

$$\vec{r}_i = -(4m + 2)\,a\,\hat{x} - h\,\hat{z} \tag{270}$$

106
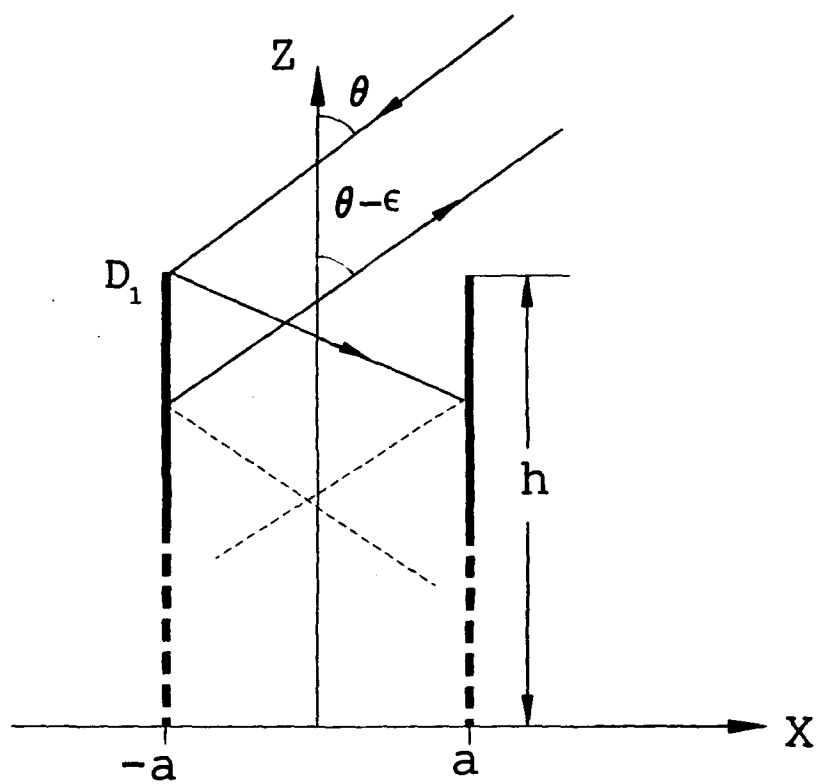
Figure 63: $D_1 \cdots$ type terms.

is the position vector of the diffraction point (D_1) imaged through all reflection,

$$\Phi = (\theta - \epsilon), \tag{271}$$

and

$$\Phi' = \pi - \theta. \tag{272}$$

Using Equations (267) to (272) in Equation (266),

$$U^{D_1 \cdots} \sim -\frac{e^{-j\frac{\pi}{4}}}{\sqrt{2\pi k}} \left(\frac{1}{\epsilon}\right) e^{-jk(4m+2)a\sin\theta} e^{jk[(4m+1)a\cos\theta - h\sin\theta]}. \tag{273}$$

The field from $\cdots D_1$, valid in the region defined by Equation (262), is given as

$$U^{\cdots D_1} \sim -\frac{e^{-j\frac{\pi}{4}}}{4\sqrt{2\pi k}} R_{s,h}^{(2m+2)} \cot\left(\frac{\pi - (\Phi + \Phi')}{4}\right) e^{jk(\vec{r}_1 \cdot \hat{r} + \vec{r}_i \cdot \hat{r}')}, \tag{274}$$

with Equations (267) to (270) the same as above and

$$\Phi = \pi - (\theta - \epsilon) \tag{275}$$

and

$$\Phi' = \theta. \tag{276}$$

Equation (274) may now be simplified to

$$U^{\cdots D_1} \sim -\frac{e^{-j\frac{\pi}{4}}}{\sqrt{2\pi k}} \left(\frac{1}{\epsilon}\right) e^{-jk(4m+2)a\sin\theta} e^{jk[a\cos\theta + h\sin\theta]}. \tag{277}$$

Thus, the total field from the diffraction occurring from the terms with D_1, for the backscatter case, (Equations (273)+(277) in the limit as $\epsilon \to 0$), valid in the region defined by Equation (262), is

$$U^{total\ left} \sim e^{-jk(4m+2)a\sin\theta} e^{j\frac{\pi}{4}} \sqrt{\frac{2k}{\pi}} \left[h\sin\theta - 2ma\cos\theta\right]. \tag{278}$$

2.2 $D_2 \cdots$ and $\cdots D_2$ Terms

Consider the terms with diffraction from the top right edge (D_2) shown in Figure 64. The field from $D_2 \cdots$ for a bistatic angle of ϵ, where ϵ is a small number, valid
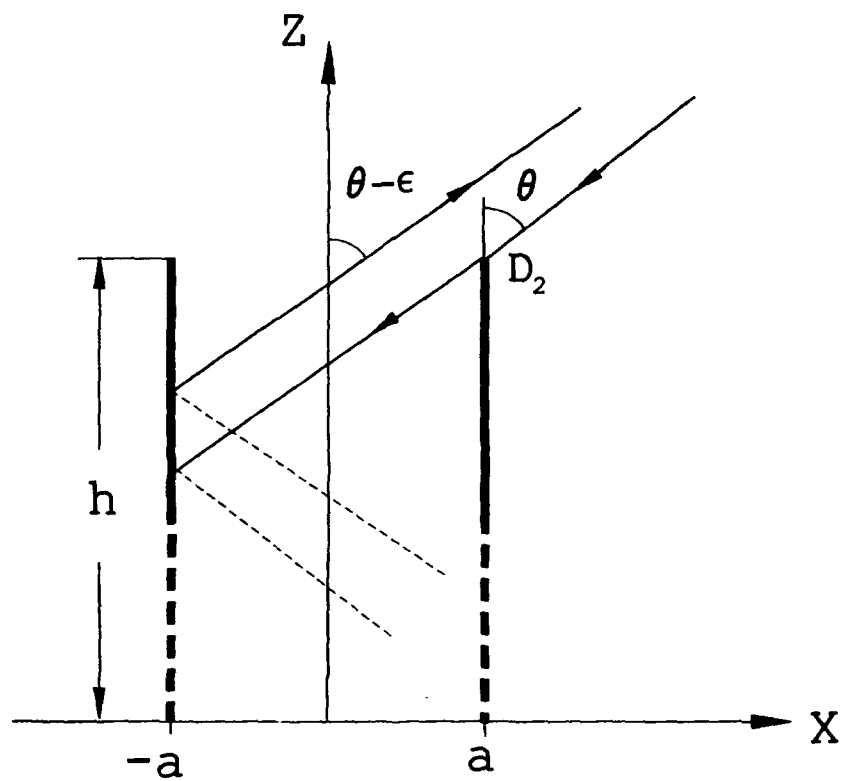
Figure 64: $D_2 \cdots$ type terms.

in the region defined by Equation (263), is given as

$$U^{D_2\cdots} \sim -\frac{e^{-j\frac{\pi}{4}}}{4\sqrt{2\pi k}} R_{s,h}^{(2m+2)} \cot\left(\frac{\pi + (\Phi - \Phi')}{4}\right) e^{jk(\vec{r}_1 \cdot \vec{r}' + \vec{r}_i \cdot \vec{r})}, \qquad (279)$$

where m is the number of reflections before reflecting from the base of the parallel plate cavity and Equations (267) and (268) are the same as before, and

$$\vec{r}_1 = a\,\hat{x} + h\,\hat{z} \qquad (280)$$

is the position vector of the diffraction point (D_2),

$$\vec{r}_i = -(4m+3)\,a\,\hat{x} - h\,\hat{z} \qquad (281)$$

is the position vector of the diffraction point (D_2) imaged through all reflection,

$$\Phi = (\theta - \epsilon), \qquad (282)$$

and

$$\Phi' = \pi + \theta. \qquad (283)$$

Equation (279) can now be simplified to

$$U^{D_2\cdots} \sim -\frac{e^{-j\frac{\pi}{4}}}{\sqrt{2\pi k}} \left(\frac{1}{\epsilon}\right) e^{-jk(4m+2)a\sin\theta} e^{jk[(4m+3)a\cos\theta - h\sin\theta]}. \qquad (284)$$

The field from $\cdots D_2$, valid in the region defined by Equation (263), is given as

$$U^{\cdots D_2} \sim -\frac{e^{-j\frac{\pi}{4}}}{4\sqrt{2\pi k}} R_{s,h}^{(2m+2)} \cot\left(\frac{\pi + (\Phi - \Phi')}{4}\right) e^{jk(\vec{r}_1 \cdot \vec{r} + \vec{r}_i \cdot \vec{r}')}. \qquad (285)$$

Using Equations (267), (268), (280), (281),

$$\Phi = \pi + (\theta - \epsilon), \qquad (286)$$

and

$$\Phi' = \theta. \qquad (287)$$

Equation (285) may be simplified to

$$U^{\cdots D_2} \sim -\frac{e^{-j\frac{\pi}{4}}}{\sqrt{2\pi k}} \left(\frac{1}{\epsilon}\right) e^{-jk(4m+2)a\sin\theta} e^{-jk[a\cos\theta - h\sin\theta]}. \qquad (288)$$

110

The total field from the diffraction occurring from the terms with D_2, for the backscatter case, (Equations (284)+(288) in the limit as $\epsilon \to 0$), valid in the region defined by Equation (263), is

$$U^{total\ right} \sim e^{-jk(4m+2)a\sin\theta} e^{j\frac{\pi}{4}} \sqrt{\frac{2k}{\pi}} \left[2(m+1)a\cos\theta - h\sin\theta \right]. \qquad (289)$$

It can easily be shown that when both the diffractions of $D_1 \cdots$ and $D_2 \cdots$ are at the shadow boundaries defined by Equations (262) and (263), the terms $D_1 \cdots$ and $D_2 \cdots$ are continuous, and Equations (278) and (289) may be further simplified. At the boundary,

$$\theta = \theta_l = \cot^{-1} \left[\frac{2h}{(2m+1)d} \right]; \ m = 0, 1, \cdots, \qquad (290)$$

the field from $D \cdots R$ type terms is

$$U^{D\cdots + \cdots D}|_{\theta=\theta_l} = \frac{2}{\sqrt{\lambda}} a \cos\theta_l e^{j\frac{\pi}{4}} e^{-jk2h\tan\theta_l\sin\theta_l}. \qquad (291)$$

At the shadow boundary,

$$\theta = \theta_u = \cot^{-1} \left[\frac{h}{(m+1)d} \right]; \ m = 0, 1, \cdots, \qquad (292)$$

the field from $D \cdots R$ type terms is

$$U^{D\cdots + \cdots D}|_{\theta \approx \theta_u} = 0. \qquad (293)$$

From Equations (264) and (265), as θ approaches $90°$, more and more terms are required. However, from Equation (291) it is observed that as θ increases towards $90°$ the result approaches zero, so it is no longer necessary to include these higher order terms. This should be expected physically since less and less of the cavity is visible and the broadside reflection from the outer cylinder becomes dominant.

2.3 $D \cdots D$ Terms

Also of importance are the $D_1 \cdots D_2$ and $D_2 \cdots D_1$ terms. Although, for the backscatter case, these terms do not contribute to the continuity of the fields, they

are as important as the $D \cdots$ and $\cdots D$ type terms. It is found that the dominant part of the terms, $D_1 \cdots D_2$ and $D_2 \cdots D_1$, associated with *both* the diffractions being near the shadow boundaries, cancels. However, a significant part remains from the non-dominant part of the terms, $D_1 \cdots D_2$ and $D_2 \cdots D_1$, associated with *only* *one* of the diffractions being on the shadow boundary.

Typical results from terms of the type $D \cdots$ and $\cdots D$ (Equations (278) and (289) valid in the regions given by Equations (262) and (263), respectively) are shown in Figure 65. At the boundaries, Equations (290) and (292), the $D \cdots$ and $\cdots D$ terms go through peaks (Equation (291)) and nulls (Equation (293)), respectively. In general, as shown in Figure 65, the $D \cdots D$ terms relatively smooth out the peaks and the nulls of the $D \cdots$ and $\cdots D$ terms.

3   Parallel Plate Cavity Verses Dihedral

From the dihedral study in Section 2, and Figures 15 and 16, it is observed that the DD across the face of the dihedral balances the slope discontinuity of the DR and RD terms for the backscatter case. However, as seen in the above section, for the parallel plate cavity, the $D \cdots D$ terms relatively smooth out the ripple due to the $D \cdots$ and $\cdot\cdot\ D$ terms. Thus, the response of a parallel plate cavity is not as sharp as compared to that of the dihedral.

4   Results

Figures 66 and 67 compare the results obtained by including terms up to 12 reflections after diffraction and the Method of Moments at 10 GHz. The dimensions of the cavity are d=4 *in* (3.387 λ) and h=8 *in* (6.773 λ). As expected, the results compare well with the method of moments.
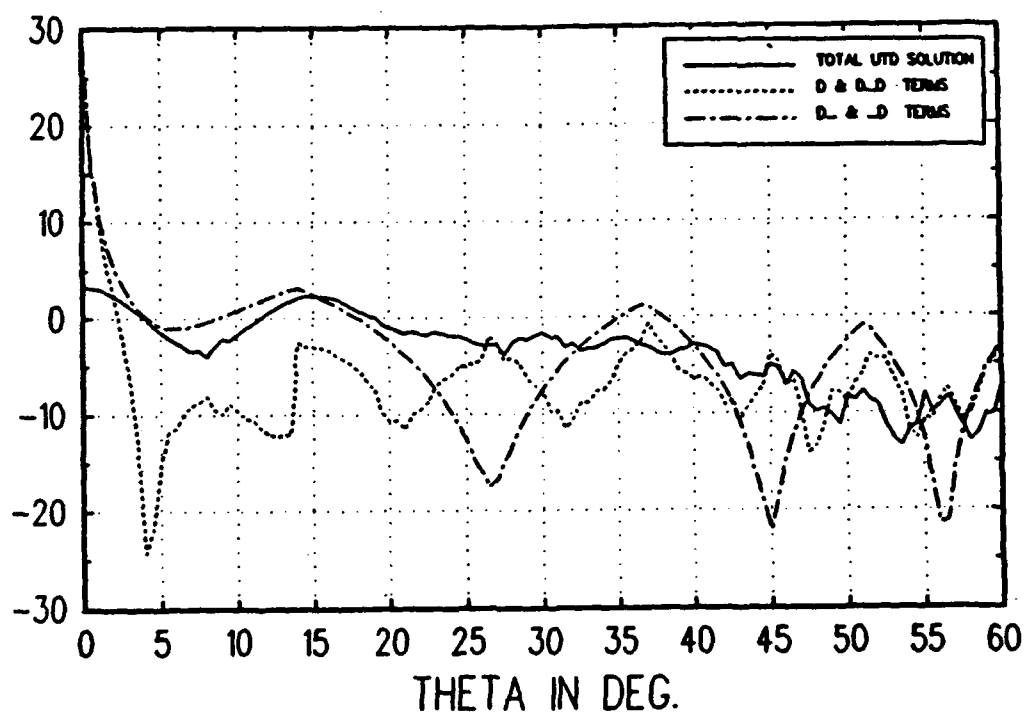
Figure 65: Importance of $D \cdots D$ terms for a parallel cavity d=4 in and h=8 in with $\phi\phi$ polarized field.
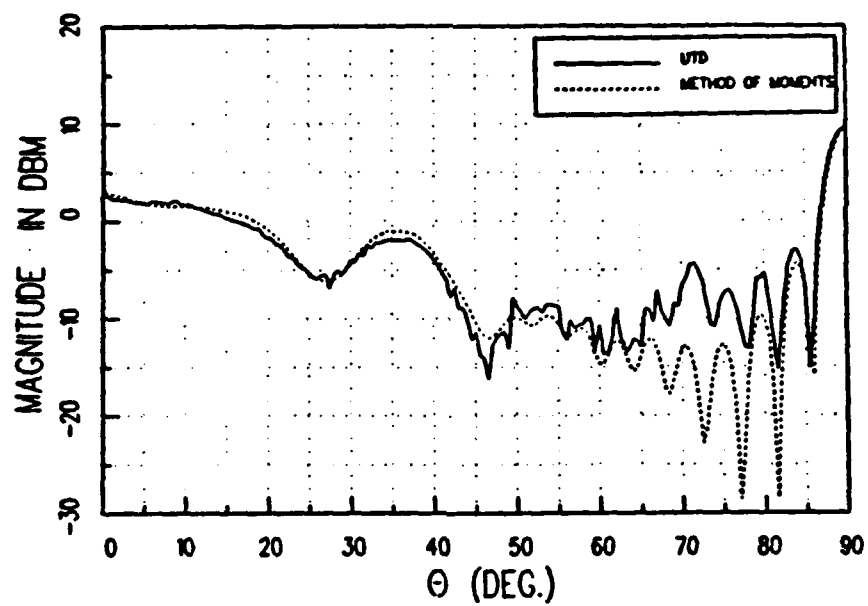
Figure 66: Backscatter field for a parallel cavity d=4 *in* and h=8 *in* with $\phi\phi$ polarized field.
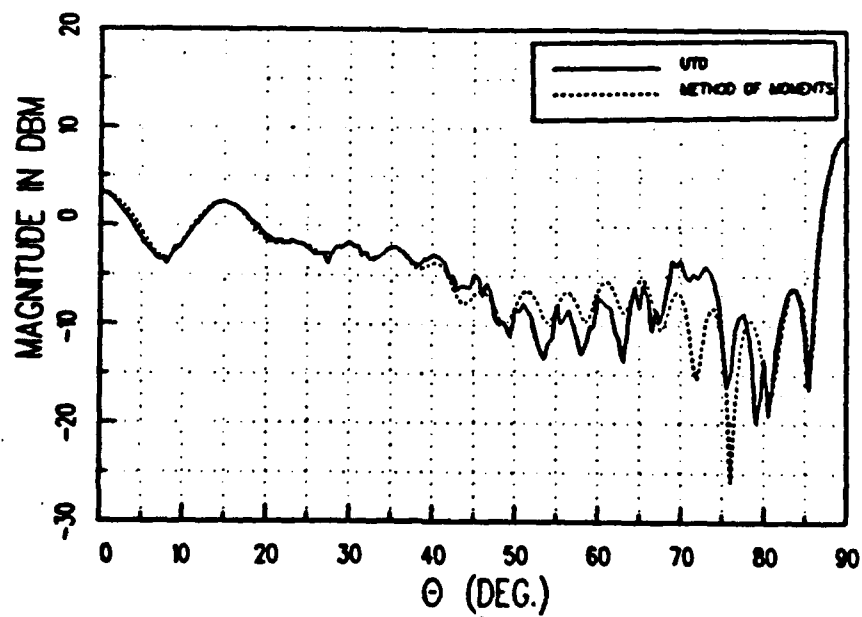
Figure 67: Backscatter field for a parallel cavity d=4 *in* and h=8 *in* with $\theta\theta$ polarized field.

114

5 Circular Cavity

Consider the circular cavity shown in Figure 68. Apart from the terms present in the parallel plate cavity, terms with single and double diffractions and reflections are present that are not in the principal plane of the cavity. However, terms with diffraction points not in the principal plane are not considered in this study. It is found that for circular cavities, the smaller the height to width ratio, the larger is the region over which the terms in the non-principal plane are insignificant. The circular cavity result is obtained by modifying the terms of the parallel plate cavity by the spread factor and the caustic correction. The caustic corrections are basically the same as that for the top-hat discussed in detail in Section 5.

6 Spread Factor Modification

In order to account for the concave geometry, the spread factor has to be modified to take into consideration each bounce on the circular cavity.

6.1 Spread Factor for $R \cdots D_2$

Referring to Figure 69, the spread factor for $R \cdots D_2$ will be derived. For the backscatter case, the spread factor for $R \cdots D_1$ is the same as for $D_1 \cdots$. In general, for m reflections after reflecting from the base of the cavity, the spread factor may be represented as

$$\rho_{spread\ factor} = \left[\frac{\rho_1^{r1} \rho_2^{r1}}{(\rho_1^{r1} + s)(\rho_2^{r1} + s)} \frac{\rho_1^{r2} \rho_2^{r2}}{(\rho_1^{r2} + s)(\rho_2^{r2} + s)} \cdots \right.$$

$$\left. \cdots \frac{\rho_1^{r(2m+1)} \rho_2^{r(2m+1)}}{\left(\rho_1^{r(2m+1)} + s\right)\left(\rho_2^{r(2m+1)} + s\right)} \rho \right]^{\frac{1}{2}}, \tag{294}$$

where

$$\rho_1^{r1} = \rho_1^{r2} = \cdots = \rho_1^{r(2m+1)} = \infty, \tag{295}$$

$$\rho_2^{r1} = \frac{-a}{2\sin\theta}, \tag{296}$$

115
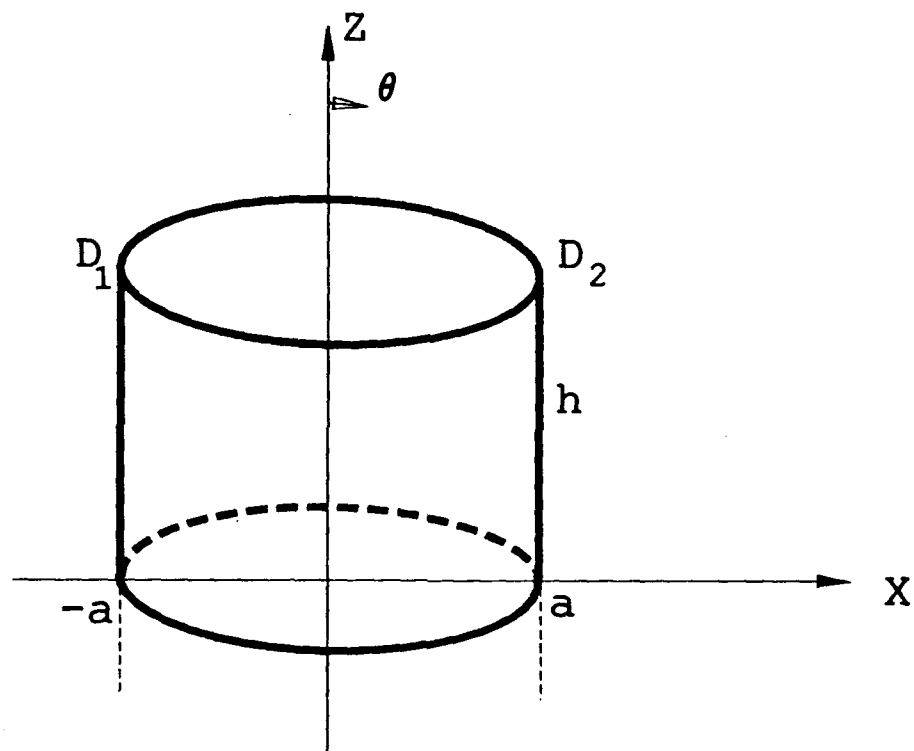
Figure 68: Circular cavity geometry.
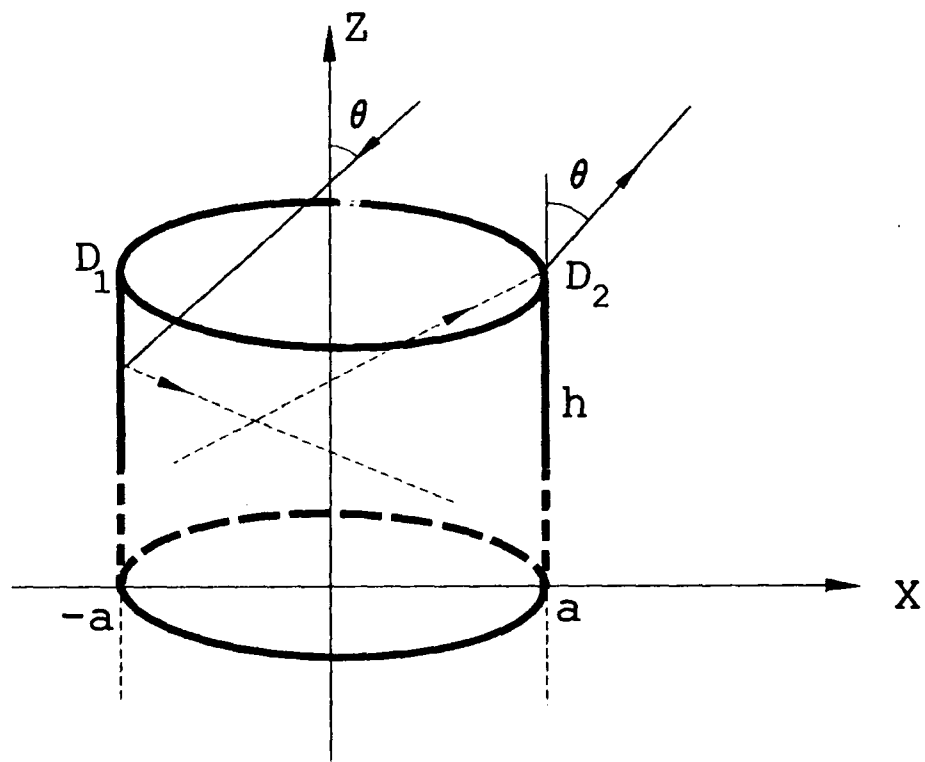
Figure 69: $R \cdots D_2$ type terms in circular cavity.

and

$$s = \frac{2a}{\sin\theta}, \tag{297}$$

is the distance between two points of contact on the circular part of the cavity. For the second reflection,

$$\rho_2^{r2} = \frac{s + \rho_2^{r1}}{1 - \frac{2\sin\theta}{a}\left(s + \rho_2^{r1}\right)}, \tag{298}$$

$$\rho_2^{r2*} = \frac{1}{1 - \frac{2\sin\theta}{a}\left(s + \rho_2^{r1}\right)}, \tag{299}$$

and for the n th reflection

$$\rho_2^{rn} = \frac{s + \rho_2^{r(n-1)}}{1 - \frac{2\sin\theta}{a}\left(s + \rho_2^{r(n-1)}\right)}, \tag{300}$$

$$\rho_2^{rn*} = \frac{1}{1 - \frac{2\sin\theta}{a}\left(s + \rho_2^{r(n-1)}\right)}, \tag{301}$$

and for the diffraction,

$$\rho = \rho_2^{r(2m+1)} + s. \tag{302}$$

Using Equations (295) to (302) in Equation (294), the spread factor becomes

$$\rho_{spread\ factor} = \left[\rho_2^{r1}\rho_2^{r2*}\rho_2^{r3*}\cdots\rho_2^{r(2m+1)*}\right]^{\frac{1}{2}}. \tag{303}$$

6.2   Spread Factor for $R\cdots D_1$

Referring to Figure 70, the spread factor for $R\cdots D_1$ will be derived. For the backscatter case, the spread factor for $R\cdots D_2$ is the same as for $D_2\cdots$. In general, for m reflections after reflecting from the base of the cavity, the spread factor may be represented as

$$\rho_{spread\ factor} = \left[\frac{\rho_1^{r1}\rho_2^{r1}}{\left(\rho_1^{r1} + s\right)\left(\rho_2^{r1} + s\right)}\frac{\rho_1^{r2}\rho_2^{r2}}{\left(\rho_1^{r2} + s\right)\left(\rho_2^{r2} + s\right)}\cdots\right.$$
$$\left.\cdots\frac{\rho_1^{r2m}\rho_2^{r2m}}{\left(\rho_1^{r2m} + s\right)\left(\rho_2^{r2m} + s\right)}\rho\right]^{\frac{1}{2}}, \tag{304}$$

where

$$\rho_1^{r1} = \rho_1^{r2} = \cdots = \rho_1^{r2m} = \infty, \tag{305}$$

118
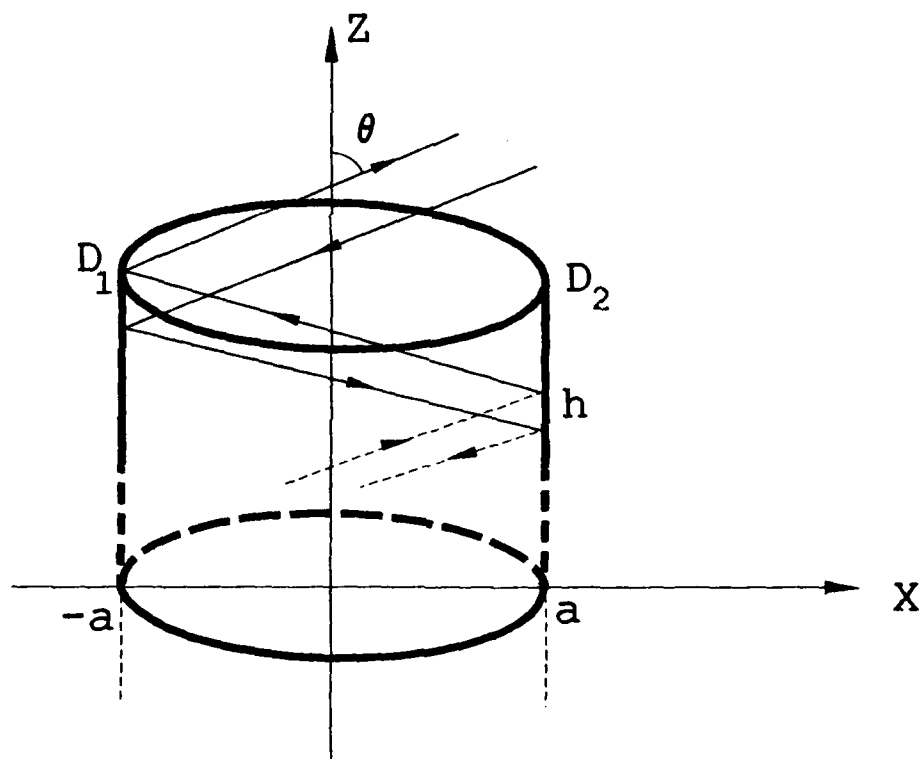
Figure 70: $R \cdots D_1$ type terms in circular cavity.

$$\rho_2^{r1} = \frac{-a}{2\sin\theta},\tag{306}$$

and

$$s = \frac{2a}{\sin\theta},\tag{307}$$

is the distance between two contact points in the circular part of the cavity. For the second reflection,

$$\rho_2^{r2} = \frac{s + \rho_2^{r1}}{1 - \frac{2\sin\theta}{a}\left(s + \rho_2^{r1}\right)},\tag{308}$$

$$\rho_2^{r2*} = \frac{1}{1 - \frac{2\sin\theta}{a}\left(s + \rho_2^{r1}\right)},\tag{309}$$

and for the n th reflection,

$$\rho_2^{rn} = \frac{s + \rho_2^{r(n-1)}}{1 - \frac{2\sin\theta}{a}\left(s + \rho_2^{r(n-1)}\right)},\tag{310}$$

$$\rho_2^{rn*} = \frac{1}{1 - \frac{2\sin\theta}{a}\left(s + \rho_2^{r(n-1)}\right)},\tag{311}$$

and for the diffraction,

$$\rho = \frac{\left(\rho_2^{r2m} + s\right)}{\left(\rho_2^{r2m} + s\right) - \frac{2\sin\theta}{a}},\tag{312}$$

and

$$\rho^* = \frac{1}{\left(\rho_2^{r2m} + s\right) - \frac{2\sin\theta}{a}}.\tag{313}$$

Using Equations (305) to (313) in Equation (304), the spread factor becomes

$$\rho_{spread\ factor} = \left[\rho_2^{r1}\rho_2^{r2*}\rho_2^{r3*}\cdots\rho_2^{r2m*}\rho^*\right]^{\frac{1}{2}}.\tag{314}$$

However, if $m = 0$ (i.e., for the terms $D_1 R_b$ and $R_b D_1$)

$$\rho_{spread\ factor} = \left[\frac{-a}{2\sin\theta}\right]^{\frac{1}{2}}.\tag{315}$$

6.3 Spread Factor for $D_1 \cdots D_2$

Referring to Figure 71, the spread factor for $D_1 \cdots D_2$ will be derived. For the backscatter case, the spread factor for $D_1 \cdots D_2$ is the same as for $D_2 \cdots D_1$. In
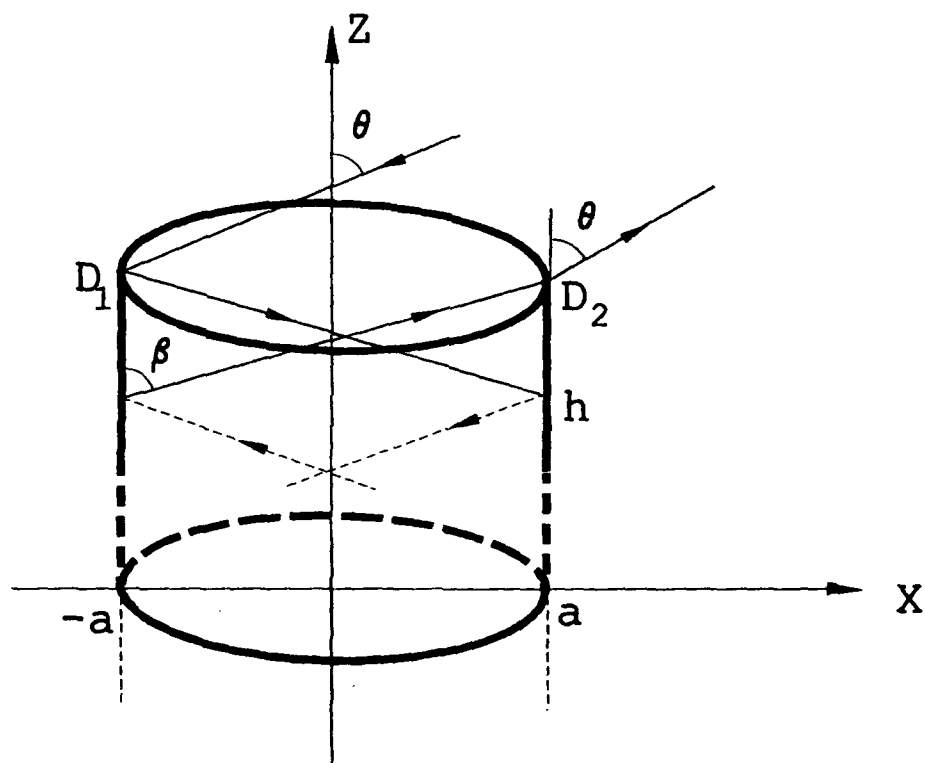
Figure 71: $D_1 \cdots D_2$ type terms in circular cavity.

general, for m reflections after reflecting from the base of the cavity, the spread factor may be represented as

$$\rho_{spread\ factor} = \left[\frac{\rho_1}{s\left(\rho_1 + s\right)} \frac{\rho_1^{r1}\rho_2^{r1}}{\left(\rho_1^{r1} + s\right)\left(\rho_2^{r1} + s\right)} \frac{\rho_1^{r2}\rho_2^{r2}}{\left(\rho_1^{r2} + s\right)\left(\rho_2^{r2} + s\right)} \cdots \right.$$

$$\left. \cdots \frac{\rho_1^{r2m}\rho_2^{r2m}}{\left(\rho_1^{r2m} + s\right)\left(\rho_2^{r2m} + s\right)}\rho_2 \right]^{\frac{1}{2}}, \qquad (316)$$

where

$$\rho_1 = \frac{-a}{\left(\sin\theta + \sin\beta\right)}, \qquad (317)$$

$$s = \frac{2a}{\sin\beta}, \qquad (318)$$

$$\rho_1^{r1} = s, \qquad (319)$$

$$\rho_1^{r2} = 2s, \qquad (320)$$

$$\rho_1^{r2m} = 2ms, \qquad (321)$$

for the first reflection,

$$\rho_2^{r1} = \frac{\rho_1 + s}{1 - \frac{2\sin\beta}{a}\left(\rho_1 + s\right)}, \qquad (322)$$

$$\rho_2^{r1*} = \frac{1}{1 - \frac{2\sin\beta}{a}\left(\rho_1 + s\right)}, \qquad (323)$$

for the second reflection,

$$\rho_2^{r2} = \frac{\rho_2^{r1} + s}{1 - \frac{2\sin\beta}{a}\left(\rho_2^{r1} + s\right)}, \qquad (324)$$

$$\rho_2^{r2*} = \frac{1}{1 - \frac{2\sin\beta}{a}\left(\rho_2^{r1} + s\right)}, \qquad (325)$$

and for the $n\,th$ reflection,

$$\rho_2^{rn} = \frac{\rho_2^{r(n-1)} + s}{1 - \frac{2\sin\beta}{a}\left(\rho_2^{r(n-1)} + s\right)}, \qquad (326)$$

$$\rho_2^{rn*} = \frac{1}{1 - \frac{2\sin\beta}{a}\left(\rho_2^{r(n-1)} + s\right)}, \qquad (327)$$

$$\rho_2 = \frac{\rho_2^{r2m} + s}{1 - \left(\frac{\sin\beta - \sin\theta}{a}\right)\left(\rho^{r2m} + s\right)}, \qquad (328)$$

122

and

$$\rho_2^{\cdot} = \frac{1}{1 - \left(\frac{\sin\beta - \sin\theta}{a}\right)(\rho^{r2m} + s)}. \tag{329}$$

Using Equations (317) to (329) in Equation (316), the spread factor is

$$\rho_{spread\ factor} = \left[\rho_1 \rho_2^{r1} \rho_2^{r2*} \rho_2^{r3*} \cdots \frac{\rho_2^{r2m*}}{(2m+1)s} \rho_2^{\cdot}\right]^{\frac{1}{2}}. \tag{330}$$

7   Cake Pan Results

In this section, the results obtained by the UTD method mentioned above are compared with the modal theory. The results for the modal theory are obtained from [29]. Figures 72 and 73 are for backscatter with $\phi\phi$ and $\theta\theta$ polarizations for a cake pan of both the radius and the height of two wavelengths. Figures 74 and 75 are for backscatter with $\phi\phi$ and $\theta\theta$ polarizations for a cake pan of radius two wavelengths and a height of four wavelengths. Figures 76 and 77 are for backscatter with $\phi\phi$ and $\theta\theta$ polarizations for a cake pan of radius two wavelengths and a height of ten wavelengths. Figures 78 and 79 are for backscatter with $\phi\phi$ and $\theta\theta$ polarizations for a cake pan of radius five wavelengths and a height of ten wavelengths.

From a simple ray picture it may be shown that the first $D\cdots$ term which is not in the principal plane and hence not considered in this solution, appears at

$$\theta = \tan^{-1}\left[\frac{a}{h\sqrt{2}}\right]. \tag{331}$$

Note that this is a boundary, and the solution may begin to deteriorate even before it. This corresponds to $\theta \sim 54°$ for Figures 80 and 81, $\theta \sim 35°$ for Figures 72 and 73, $\theta \sim 19°$ for Figures 74, 75, 78 and 79, and $\theta \sim 8°$ for Figure 76 and 77. Taking this into consideration, it is observed that the results compare well with the modal theory.

Figure 72: Backscatter field for a circular cylinder with radius 2λ and height 2λ with $\phi\phi$ polarized field (UTD solution valid for $\theta < 35°$).
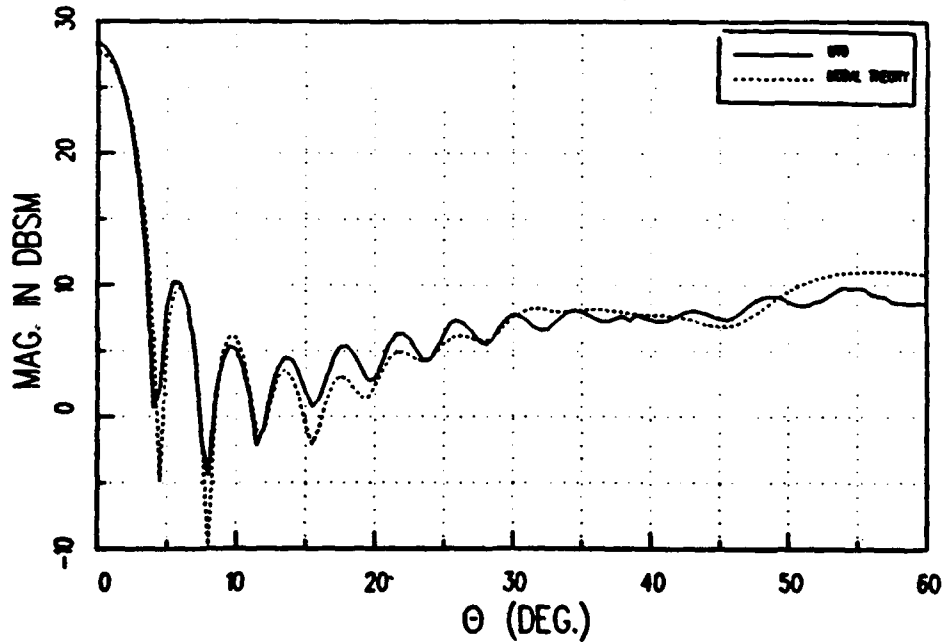
Figure 73: Backscatter field for a circular cylinder with radius 2λ and height 2λ with $\theta\theta$ polarized field (UTD solution valid for $\theta < 35°$).

124
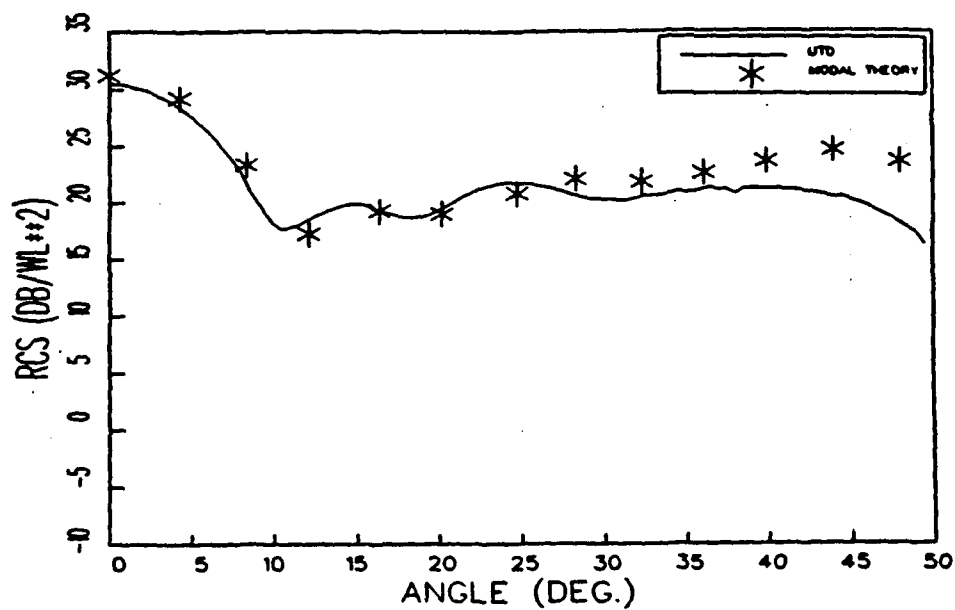
Figure 74: Backscatter field for a circular cylinder with radius 2λ and height 4λ with $\phi\phi$ polarized field (UTD solution valid for $\theta < 19°$).
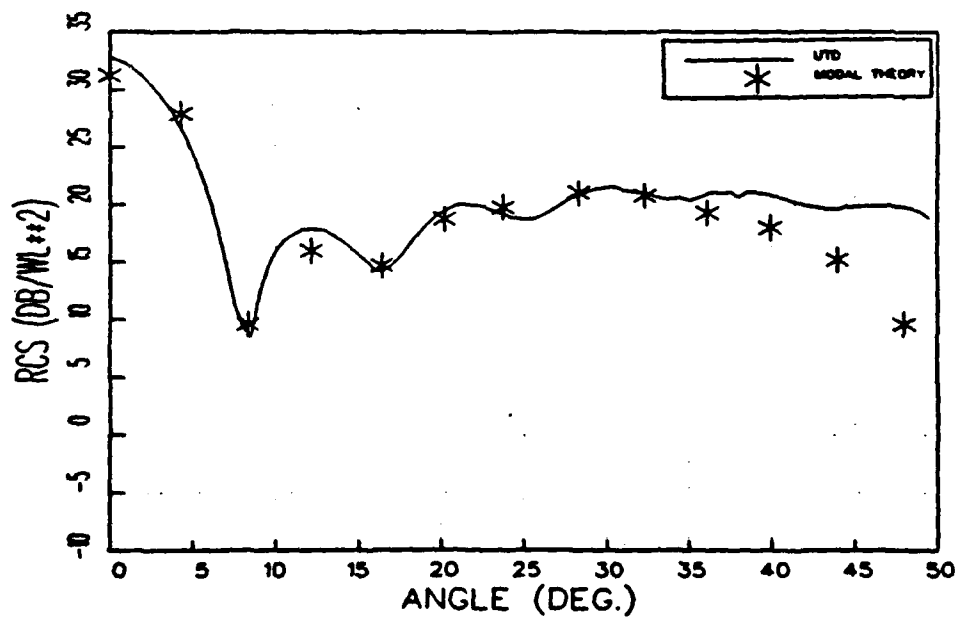
Figure 75: Backscatter field for a circular cylinder with radius 2λ and height 4λ with $\theta\theta$ polarized field (UTD solution valid for $\theta < 19°$).

125
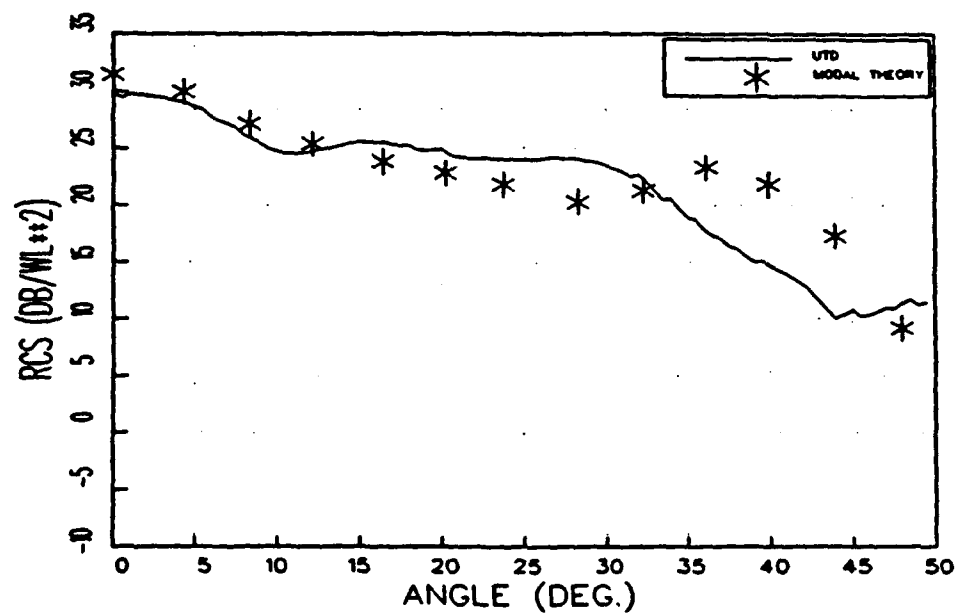
Figure 76: Backscatter field for a circular cylinder with radius 2λ and height 10λ with $\phi\phi$ polarized field (UTD solution valid for $\theta < 8°$).
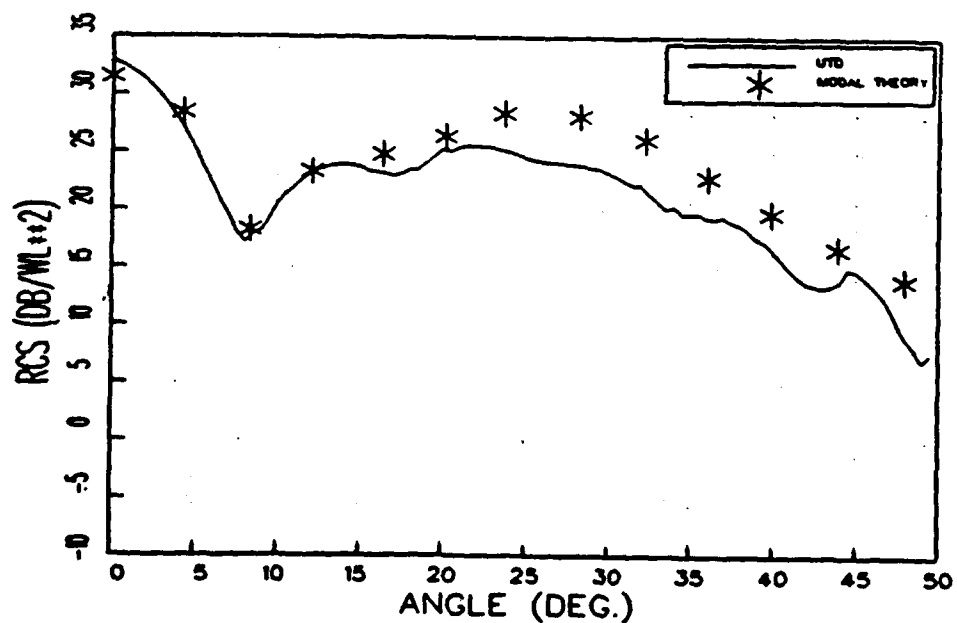
Figure 77: Backscatter field for a circular cylinder with radius 2λ and height 10λ with $\theta\theta$ polarized field (UTD solution valid for $\theta < 8°$).
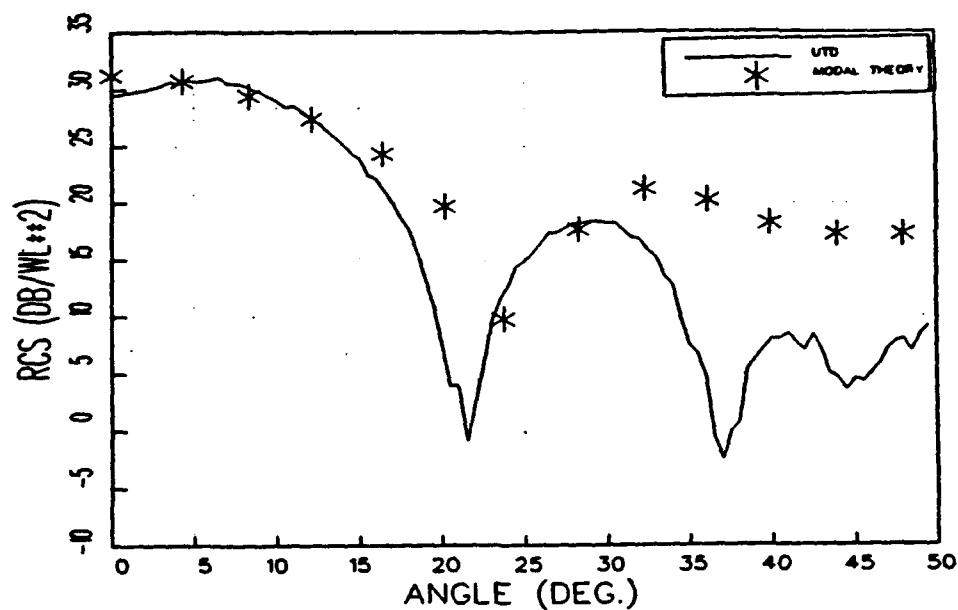
Figure 78: Backscatter field for a circular cylinder with radius 5λ and height 10λ with $\phi\phi$ polarized field (UTD solution valid for $\theta < 19°$).
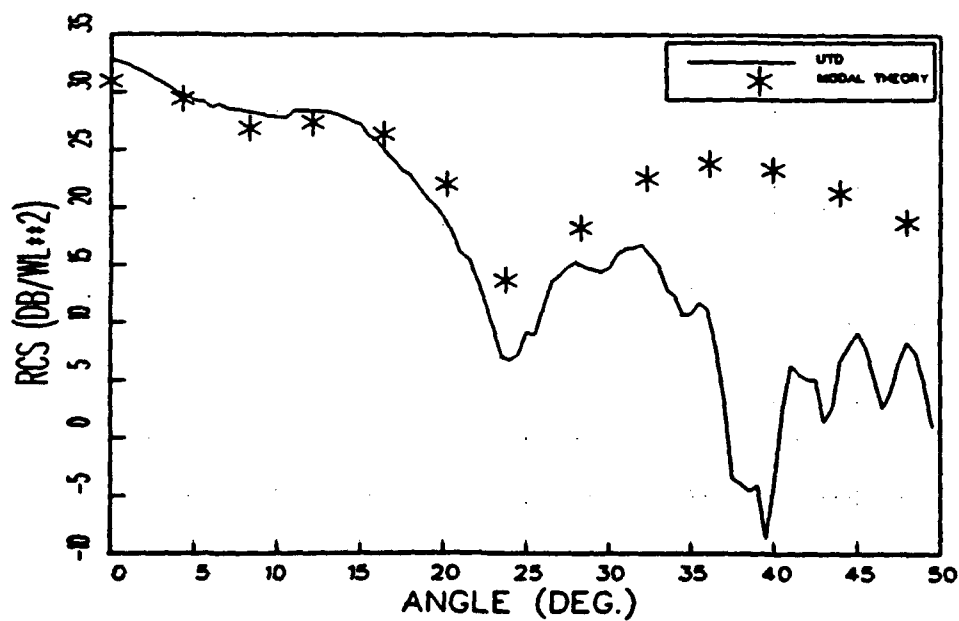
Figure 79: Backscatter field for a circular cylinder with radius 5λ and height 10λ with $\theta\theta$ polarized field (UTD solution valid for $\theta < 19°$).
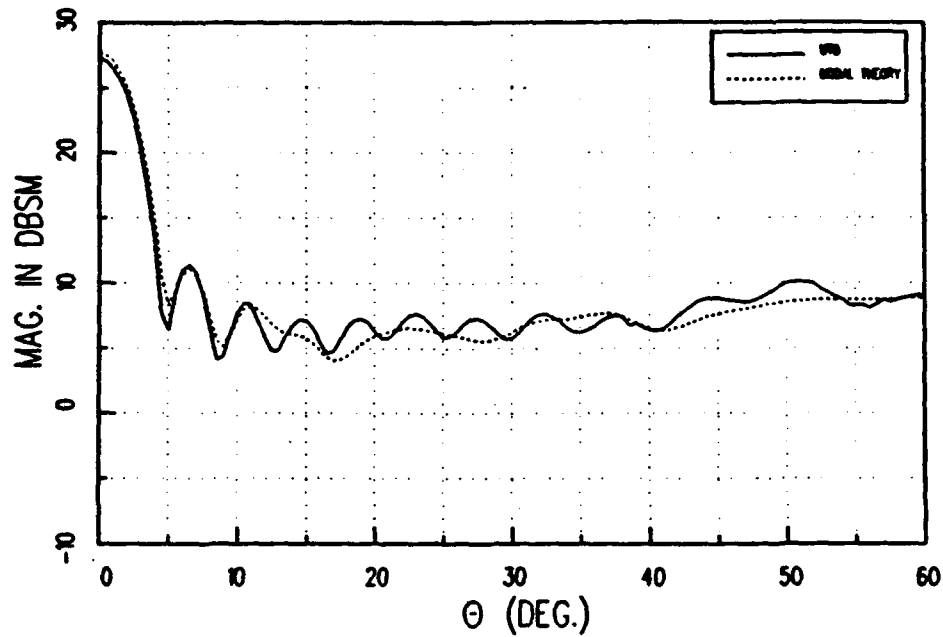
127
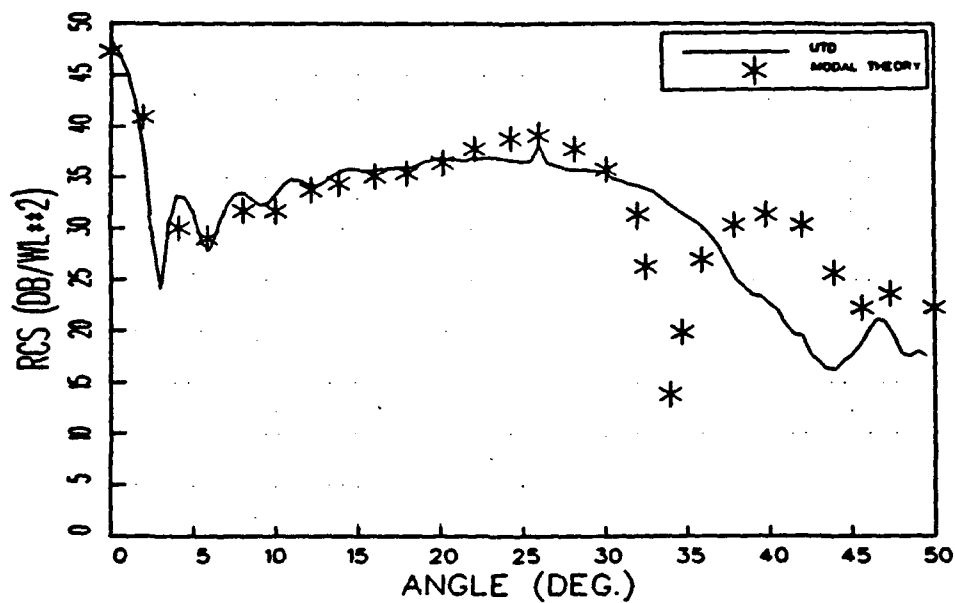
Figure 80: Backscatter field for a circular cylinder with radius 4λ and height 2λ with $\phi\phi$ polarized field (UTD solution valid for $\theta < 54°$).
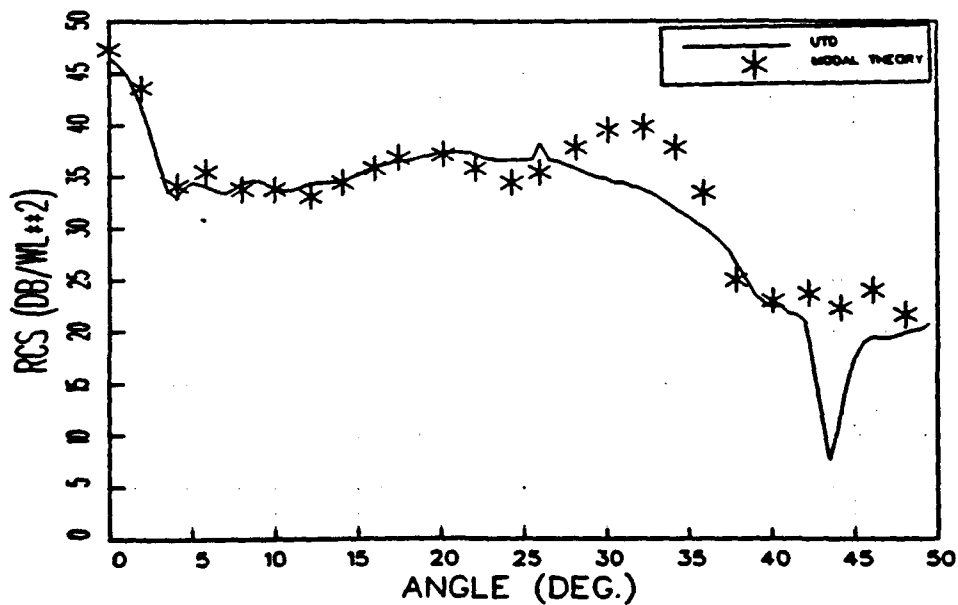
Figure 81: Backscatter field for a circular cylinder with radius 4λ and height 2λ with $\theta\theta$ polarized field (UTD solution valid for $\theta < 54°$).

128

SECTION 8

Donut

1 Introduction

First and second order Geometrical Optics solution and their caustic corrections for the donut are obtained in this section. This is a special case of scattering from elliptical cylinders discussed in detail in [30]. This configuration is of interest since it can represent tires on a vehicle and with Section 7 a wheel hub. It is observed in [30] that a fourth order equation has to be solved in order to determine the reflection points from such a geometry. However, working the other way around, with one of the reflection points assumed known, a simple solvable equation can be obtained to get the angle of incidence. Interpolation can then be used to determine the reflection points for a given angle of incidence. In Section 2, for a general bistatic case, the points of reflections for the double bounce are determined.

The rest of the section deals with backscatter. First, the GO term for the 2-d cylinder-cylinder doubly reflected term is obtained in Section 3. This is used later to get GO field for the donut. The first order GO solution for the donut and its caustic correction are obtained in Sections 4 and 5, respectively. In Section 6, the second order GO solution for the donut and its caustic correction is discussed.

2 Cylinder-Cylinder Interaction

Consider the two-dimensional geometry shown in the Figure 82. In order to compute the spread factors, it is necessary to determine the points of reflection. It was found in Section 3, that for the double bounce to occur, the angle of the dihedral must be $\alpha = \frac{\pi}{2} + \left|\frac{\theta - \theta'}{2}\right|$ or $\alpha = \frac{\pi}{2} - \left|\frac{\theta - \theta'}{2}\right|$. Thus, for a given bistatic angle, two dihedral angles are possible which will result in a double bounce. Of the two double bounces, one is for the case when the first reflection occurs from cylinder of radius a_1, $R_1 R_2$, and the other is for the case when the first reflection occurs from cylinder of radius a_2, $R_2 R_1$ (R_1 and R_2 refers to reflections from the cylinders of radius a_1 and a_2, respectively). However, for the backscatter case, there is only one dihedral angle, $\alpha = \frac{\pi}{2}$, and the two ray paths, $R_1 R_2$ and $R_2 R_1$, are the same. We will determine the
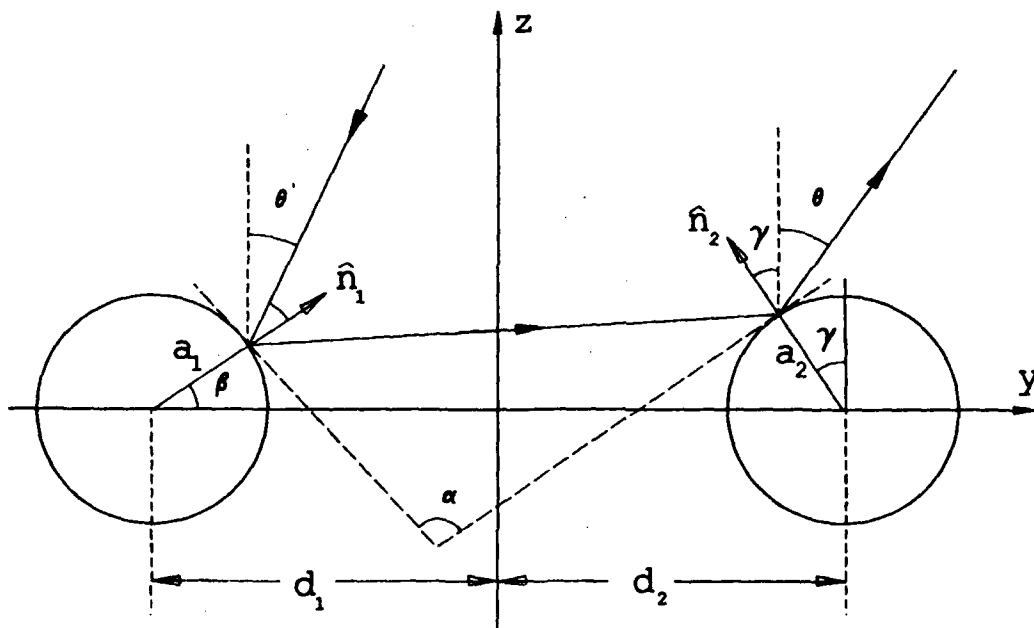
Figure 82: Cylinder Cylinder interaction.

reflection points for one of the rays, $R_1 R_2$ or $R_2 R_1$, and use that result to determine the reflection points for the other ray path. First, the ray path that results is the dihedral angle being greater then $\frac{\pi}{2}$ will be considered; i.e., $\alpha = \frac{\pi}{2} + \left| \frac{\theta - \theta'}{2} \right|$. This choice is necessary in order to avoid the ambiguity in the relationship between sides and angles, the sine rule.

From Figure 82, it is observed that if $\theta > \theta'$, α is greater then $\frac{\pi}{2}$ (i.e., $\alpha = \frac{\pi}{2} + \left| \frac{\theta - \theta'}{2} \right|$), we will determine the angle β for $R_1 R_2$. However, if $\theta < \theta'$, we will determine the angle β for $R_2 R_1$. From Figure 82, one gets

$$\gamma = \beta - \alpha + \frac{\pi}{2}. \tag{332}$$

Using the sine rule on the triangle formed by $\hat{n}_1$, $\hat{n}_2$ and the y-axis,

$$\frac{d_1 + d_2}{\sin(\pi - \alpha)} = \frac{s_1}{\sin(\frac{\pi}{2} - \gamma)} = \frac{s_2}{\sin \beta}, \tag{333}$$

where s_1 and s_2 are the length made by sides $\hat{n}_1$ and $\hat{n}_2$, respectively. Using Equation (333) and applying sine rule on the triangle formed by $\hat{n}_1$, $\hat{n}_2$ and the two points of reflection,

$$\Pi = \frac{(d_1 + d_2) \cos \gamma - a_1 \sin \alpha}{(d_1 + d_2) \sin \beta - a_2 \sin \alpha} = \frac{\sin(\theta' + \gamma)}{\cos(\theta + \beta)}. \tag{334}$$

Rearranging Equation (334) and solving for the incident angle, θ,

$$\theta = \tan^{-1} \left[\frac{\Pi \cos \beta - \cos(\beta - \alpha - \theta_b)}{\Pi \sin \beta - \sin(\beta - \alpha - \theta_b)} \right], \tag{335}$$

where θ_b is the bistatic angle,

$$\theta_b = \theta - \theta'. \tag{336}$$

Equation (335) may be used to obtain the incident angle, θ, if the point of first reflection, or β, is known. However if θ is known, which is normally the case, then β may be found by trial and error. A more reasonable approach may be to find θ's for particular values of β, using Equation (335), and then interpolating to find β for a particular θ. Now, γ may be found from Equation (332).

131

Now, consider the other case, when $\alpha = \frac{\pi}{2} - \left| \frac{\theta - \theta'}{2} \right|$, referring to the *other* double bounce, it can be shown that

$$\beta_{other} = \beta - |\theta_b| \tag{337}$$

and

$$\gamma_{other} = \beta - \left| \frac{\theta - \theta'}{2} \right|. \tag{338}$$

Thus, one double bounce occurs at reflection points defined by angles β and γ, and the *other* double bounce occurs at the reflection points defined by angles β_{other} and γ_{other}.

3 Two-Dimensional Cylinder-Cylinder Doubly Reflected Term

Referring to the two-dimensional geometry shown in Figure 83. The backscatter doubly reflected term $R_1 R_2$, using Equation (1), is given as

$$\overline{E}^{rr} = \left(\overline{E}'(0) \cdot \overline{\overline{R_1}} \right) \cdot \overline{\overline{R_2}} \sqrt{ \frac{\rho_1^{r_1} \rho_1^{r_2}}{(\rho_1^{r_1} + s)} } \; e^{-jk s} e^{jk\bar{r}_{c1} \cdot \bar{r}'} e^{jk\bar{r}_{c2} \cdot \bar{r}}. \tag{339}$$

$\overline{\overline{R_1}}$ and $\overline{\overline{R_2}}$ are defined in Equation (1) at the first and second reflection points, respectively, and $\rho_1^{r_1}$ and $\rho_1^{r_2}$, the caustic distances for the first and the second reflected rays, are given as

$$\rho_1^{r_1} = \frac{a \sin (\theta + \beta)}{2}, \tag{340}$$

and

$$\frac{1}{\rho_1^{r_2}} = \frac{1}{s + \rho_1^{r_1}} + \frac{2}{a \cos (\theta + \gamma)}. \tag{341}$$

132
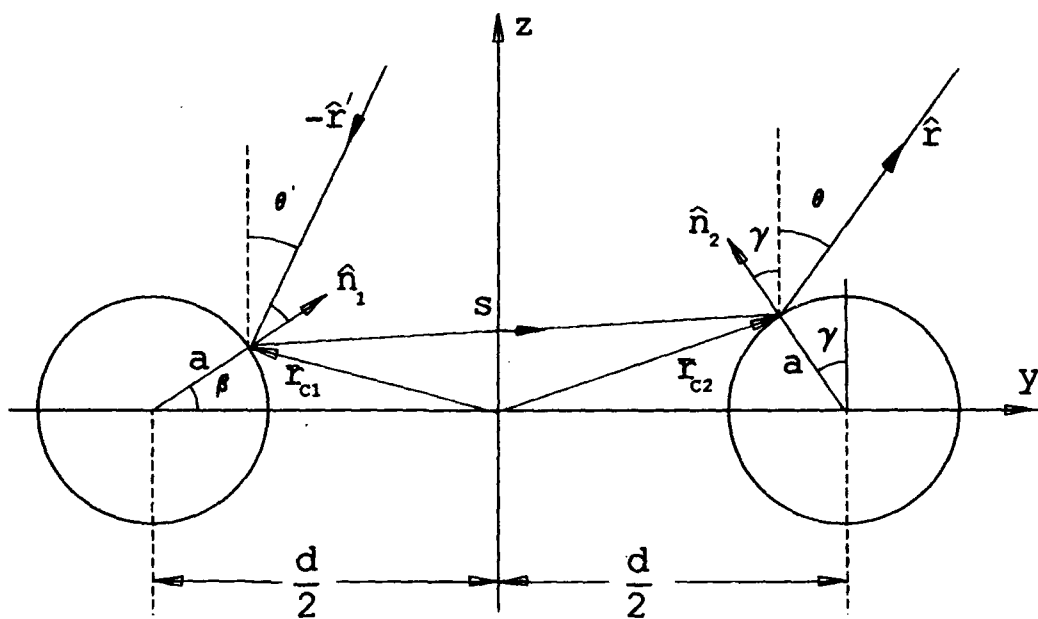
Figure 83: Two-dimensional Cylinder-Cylinder showing $R_1 R_2$ interaction.

4 Donut: First Order Solution

Consider modifying the 2-D double cylinder to a donut, shown in Figure 84. For the backscatter case, the two single reflected fields, from Equation (1), are given as

$$\vec{E}^r = \vec{E}^i(0) \cdot \overline{\overline{R}} \sqrt{\rho_1^r \rho_2^r} \; e^{jk\vec{r}_c \cdot (\hat{r} + \hat{r}')}, \tag{342}$$

where ρ_1^r and ρ_2^r are obtained using Equation (5). The radii of curvatures are $R_1 = \mp \frac{d}{2\sin\theta} + a$ and $R_2 = a$. Also, using $\theta' = 0$, $\theta_1 = \frac{\pi}{2}$ and $\theta_2 = \frac{\pi}{2}$ in Equation (5), the caustic distances become

$$\rho_1^r = \frac{a}{2}, \tag{343}$$

$$\rho_2^r = \mp \frac{d}{4\sin\theta} + \frac{a}{2}. \tag{344}$$

In Equation (342), $\vec{r}_c = \vec{r}_{c_1}$ for the reflection from the donut on the $-$ y-axis, and for the reflection from the donut on the $+$ y-axis $\vec{r}_c = \vec{r}_{c_2}$. In Equation (344) and in the radius of curvature, R_1, $-$ and $+$ signs refer to reflection from the donut on the $-$ and $+$ y-axis, respectively. Note that a first order caustic occurs when $\theta \to 0$ and $\rho_2^r \to \infty$. This caustic correction may be done much the same way as the first order diffracted caustic is corrected, which is discussed in detail in Section 4.

5 Caustic Correction to the First Order Solution

The concept of using equivalent currents for caustic correction discussed here have also been used in References [31, 32]. The equivalent line currents for a cylinder are obtained by setting the infinite cylinder's GO reflected field equal to the field radiated by the infinite line currents. The equivalent line currents for a cylinder are

$$I^r = \hat{\beta} \cdot \left(\vec{E}^i(0) \cdot \overline{\overline{R}} \right) \sqrt{\frac{8\pi}{k}} \frac{e^{-j\frac{\pi}{4}}}{\eta} \sqrt{\rho_1^r} e^{jk\vec{r}_c \cdot \hat{r}'}, \tag{345}$$

and

$$I^m = -\hat{\beta} \cdot \left(\vec{H}^i(0) \cdot \overline{\overline{R}} \right) \sqrt{\frac{8\pi}{k}} \eta e^{-j\frac{\pi}{4}} \sqrt{\rho_1^r} e^{jk\vec{r}_c \cdot \hat{r}'}, \tag{346}$$

134
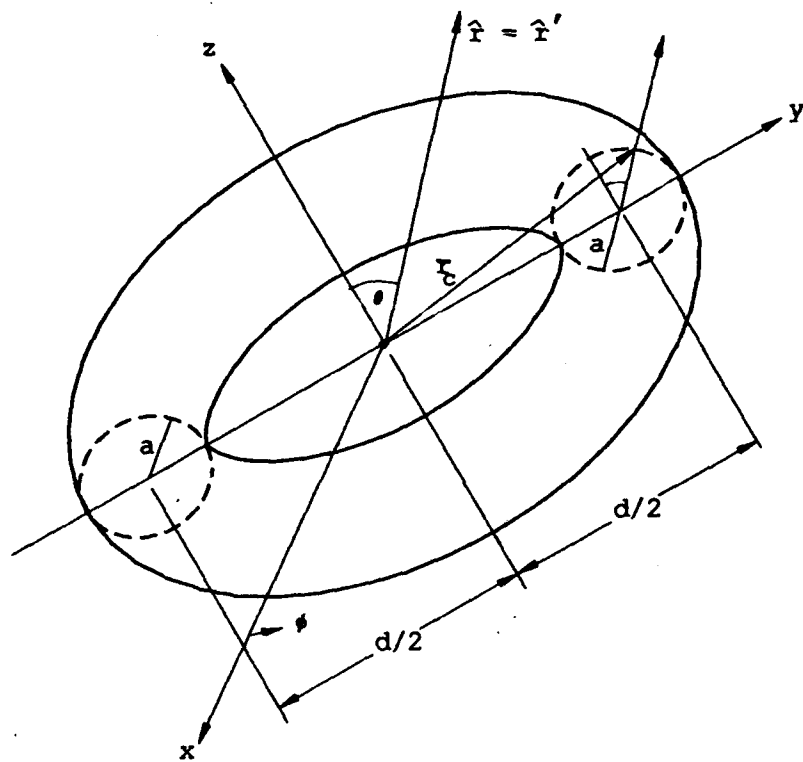
Figure 84: Geometry used to get first order caustic corrected fields.

where

$$\rho_1^r = \frac{a}{2} \frac{\hat{r} \cdot \hat{n}_r}{sin^2\beta}, \tag{347}$$

a is the radius, and $\hat{n}_r$ is the normal to the 2-D cylinder as shown in Figure 84. First, the caustic correction from half of the donut on the $+$ y-axis will be considered. The result from this caustic correction will be used to get the result from the whole donut. Referring to Figure 84,

$$\vec{r}_c = \left(\frac{d}{2} + a\sin\theta\right)\cos\phi\,\hat{x} + \left(\frac{d}{2} + a\sin\theta\right)\sin\phi\,\hat{y} + a\cos\theta\,\hat{z}, \tag{348}$$

$$\hat{n}_r = \cos\theta\,\hat{z} + \sin\theta\,\hat{y}, \tag{349}$$

$$\hat{\beta} = \sin\phi\,\hat{x} - \cos\phi\,\hat{y}, \tag{350}$$

$$\hat{r} = \sin\theta\,\hat{y} + \cos\theta\,\hat{z}, \tag{351}$$

and

$$\hat{r}' = \sin\theta'\,\hat{y} + \cos\theta'\,\hat{z}. \tag{352}$$

Let

$$\vec{E}^i = E_o\hat{x} \tag{353}$$

and $E_o = 1$. The far-zone fields, due to the equivalent line currents, are

$$\vec{E}_r = \hat{\beta}j\eta k\sin\beta\frac{e^{-jkr}}{4\pi r}\int_0^\pi I^r(\phi)\,e^{jk\vec{r}_c\cdot\hat{r}}d\phi, \tag{354}$$

and

$$\vec{E}_m = \left(\hat{\beta}\times\hat{r}\right)jk\sin\beta\frac{e^{-jkr}}{4\pi r}\int_0^\pi I^m(\phi)\,e^{jk\vec{r}_c\cdot\hat{r}}d\phi. \tag{355}$$

Equations (354) and (355) may be simplified to

$$\vec{E}_r = \frac{e^{-jkr}}{r}\frac{k}{2\pi}e^{j\frac{\pi}{4}}\sqrt{\frac{a}{2}}e^{jk2a\cos^2\theta}\int_0^\pi\sin^2\phi e^{jk(d+2a\sin\theta)\sin\theta\sin\phi}d\phi, \tag{356}$$

and

$$\vec{E}_m = \frac{e^{-jkr}}{r}\frac{k}{2\pi}e^{j\frac{\pi}{4}}\sqrt{\frac{a}{2}}e^{jk2a\cos^2\theta}\int_0^\pi\cos^2\phi e^{jk(d+2a\sin\theta)\sin\theta\sin\phi}d\phi. \tag{357}$$

136

Combining Equations (356) and (357) and after some manipulation, it may be shown that the first order reflected field with the caustic correction, is given as

$$\vec{E}^r = \vec{E}^i(0).\overline{\overline{R}}\sqrt{\rho_1^r \rho_2^r} e^{jk\vec{r}_c.(\hat{r}+\hat{r}')} T_r(U),$$ (358)

where

$$T_r(U) = \frac{1}{\pi} f_0 \sqrt{\frac{\pi U}{2}} e^{j(U-\frac{\pi}{4})},$$ (359)

$$f_0 = \pi \left[J_0(U) + j H_0(U) \right],$$ (360)

and

$$U = k \left(\frac{d}{2} \pm a \sin\theta \right) \hat{n}_r.(\hat{r}+\hat{r}').$$ (361)

In Equation (360), J_0 and H_0 refer to the Bessel and Hankel functions, respectively, and in Equation (361), the $+$ and the $-$ signs refer to the reflection from donut of the $+$ and $-$ sides of the y-axis, respectively. The normal at the point of reflection as defined in Equation (349), is $\hat{n}_r$. The transition function is $T_r(U)$. The following are the small and large argument forms which are obtained using the series and the asymptotic forms, respectively, of the Bessel and Hankel functions, so that for

$|U| << 1$,

$$T_r(U) \approx \sqrt{\frac{\pi U}{2}} e^{-j(U-\frac{\pi}{4})} \left\{ 1 - \frac{U^2}{4} + \frac{U^4}{64} + j\frac{2U}{\pi} \left[1 - \frac{U^2}{15} \right] \right\},$$ (362)

and for $|U| >> 1$,

$$T_r(U) \sim 1 - \frac{j17}{8U} + \frac{55}{128U^2} - \frac{j53}{1024U^3} - \sqrt{\frac{\pi U}{2}} e^{-j(U-\frac{\pi}{4})} \left[1 - \frac{1}{U^2} \right].$$ (363)

6   Second Order Solution and its Caustic Correction

The second order solution to the donut (Figure 85) obtained by modification to the double bounce on the two-dimensional cylinder-cylinder, discussed in Section 3, is given as

$$\vec{E}^{rr} = \left(\vec{E}^i(0) \cdot \overline{\overline{R_1}} \right) \cdot \overline{\overline{R_2}} \sqrt{\frac{\rho_1^{r_1}}{(\rho_1^{r_1}+s)} \frac{\rho_2^{r_1}}{(\rho_2^{r_1}+s)}} \rho_1^{r_2} \rho_2^{r_2} e^{-jks} e^{jk\vec{r}_{c_1}.\hat{r}'} e^{jk\vec{r}_{c_2}.\hat{r}},$$ (364)

137
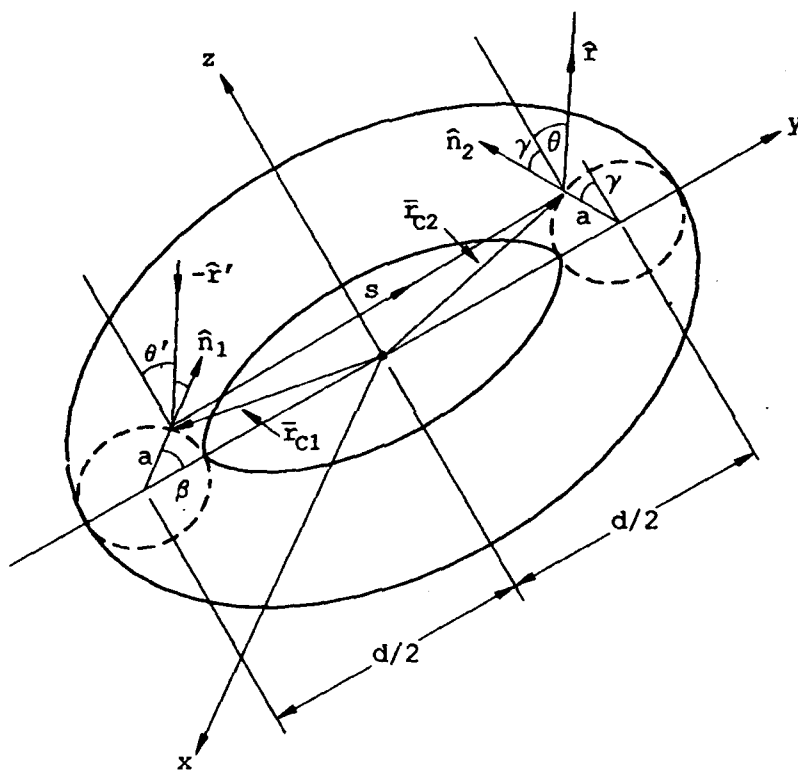
Figure 85: Geometry showing the term $R_1 R_2$ from a donut.

where $\overline{\overline{R_1}}$ and $\overline{\overline{R_2}}$ are as defined in Equation (1) at the first and second reflection points, $\rho_1^{r_1}$ and $\rho_1^{r_2}$ are as defined in Equations (340) and (341), and

$$\rho_2^{r_1} = \frac{\left(a\cos\beta - \frac{d}{2}\right)}{2\sin\left(\theta + \beta\right)\cos\beta},\tag{365}$$

and

$$\frac{1}{\rho_2^{r_2}} = \frac{1}{s + \rho_2^{r_1}} + \frac{2\cos\left(\theta + \beta\right)\sin\beta}{\left(a\sin\beta - \frac{d}{2}\right)}\tag{366}$$

are obtained using Equation (2).

It is observed that as $\theta \to 0$, $\rho_2^{r_2} \to \infty$, Equation (364) appears to become infinite. This is expected since we are at a double reflection caustic. However a careful evaluation of Equation (364) at the caustic shows that the double reflected field *vanishes* at the caustic. One simple way to see this is to look at two double reflected terms that are $\phi = 90°$ apart on the donut. It is observed that along the z-axis, these two terms cancel each other. Thus, the total resultant field from the double reflected caustic, along the z-axis, vanishes. However, near the caustic, $\theta \approx 0$, it is necessary to set up equivalent currents on half rims that are associated with the two reflection points and integrating the equivalent currents along half-circles, the radius of which are determined by the two reflection points (GO), in order to obtain the doubly reflected field. This interaction could not be written in closed form because of the complexity of the distance parameter, s, the distance between the two reflection points. (See Figure 85.) Performing this integration numerically, it was found that the doubly reflected term hardly made any contribution to the total result, at least for the dimensions of the donut considered. (See Figures 86 and 87.)

7   Results

Figures 86 and 87 compare the soft and the hard backscatter at 10 GHz from a donut of solid radius, $a = \frac{7}{2\pi}$ *in* (0.943 λ) and the ring radius, $\frac{d}{2} = \frac{a}{2\sin 10°}$ *in* (2.7 λ). Since

139

the result for the soft polarization, Figure 86, is better than for the hard polarization, Figure 87, it is expected that the creeping waves, which have not been considered in this solution, are important for this dimension of the donut. Since the result worsen as θ increases, it may be expected that double bounce mechanisms that are not in the principal plane become more important.
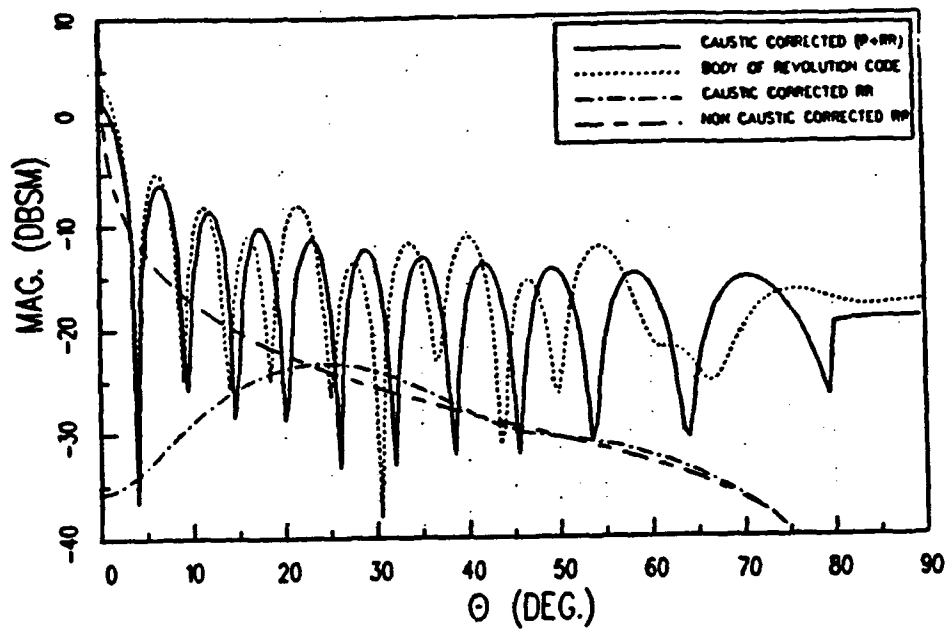
Figure 86: Backscatter from Donut with $\phi\phi$ polarized field.
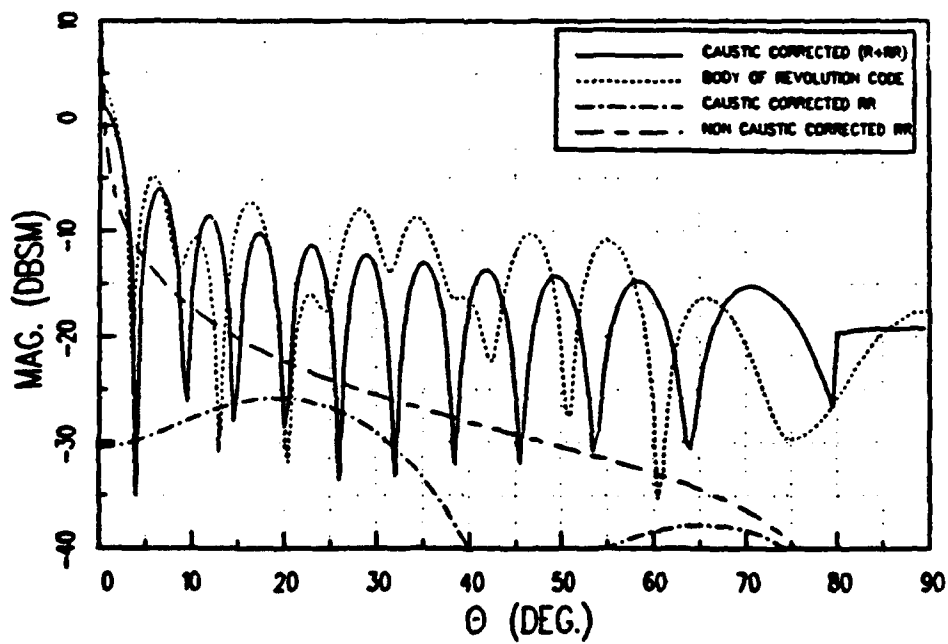
Figure 87: Backscatter from Donut with $\theta\theta$ polarized field.

141

SECTION 9

UTD Scattering from Multi-Joined Cylinders

1 Introduction

The multi-joined cylinder model for the scattering of the electromagnetic fields is developed for the purpose of studying radar remote sensing of forested areas. The top-hat, discussed in Section 5, can be used to study the tree trunk and ground interaction. In this section, the multi-joined cylinders model, see Figure 88, is used to investigate the scattering from tree trunks and branches. Concentric dielectric layers are used to represent the material characteristic of the trunks and branches, and their shape is represented by using more than one cylinder to create bends.

Uniform Theory of Diffraction (UTD) is employed to obtain the scattered fields. The dihedral study done in Reference [13] and outlined in Section 3 is used as the building block for modeling the cylinder-cylinder interactions. The main differences being that the reflection coefficients are modified to take into account the dielectric layers, see Appendix B or Reference [33], and the standard two dimensional UTD diffraction coefficients are modified to take into account the spread factors and caustic corrections. The caustic corrections are basically the same as discussed in References [21, 22] and summarized in Section 4. Also, junction characteristics, not
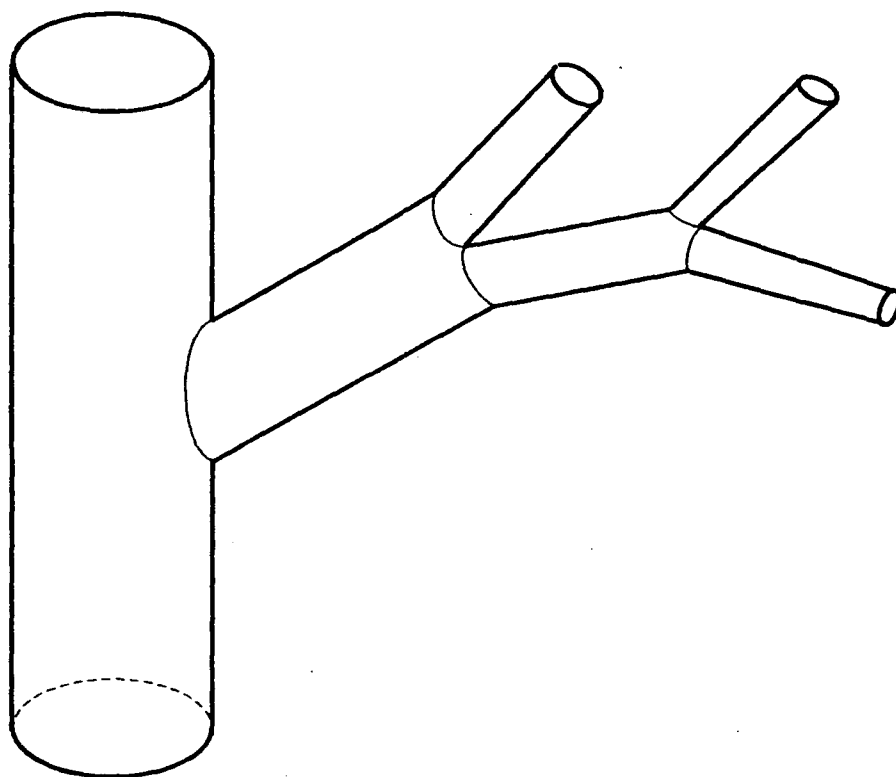
Figure 88: Multi-joined cylinder model.

discussed in the literature, such as radius of curvature and edge normal, are required to obtain the diffracted field from a junction.

2 Theoretical Background

2.1 Modified Diffraction Coefficient

In order to find the scattered fields from dielectric surfaces, the edge diffraction coefficient for the perfectly-conducting case (Equation (25)) discussed in Section 3, has to be modified to take into account a junction of two dielectric plates. It is shown in References [34, 35] that the modified diffraction coefficient for an electrically thin dielectric is

$$D_{s,d} = \frac{-e^{-j\frac{\pi}{4}}}{2n\sqrt{2\pi k}} \left[\left(1 - T_o^{s,h}\right) \cot \left(\frac{\pi - (\Phi - \Phi')}{2n} \right) + \left(1 - T_n^{s,h}\right) \cot \left(\frac{\pi + (\Phi - \Phi')}{2n} \right) \right.$$
$$\left. + R_o^{s,h} \cot \left(\frac{\pi - (\Phi + \Phi')}{2n} \right) + R_n^{s,h} \cot \left(\frac{\pi + (\Phi + \Phi')}{2n} \right) \right],$$

$$(367)$$

where $R_o^{s,h}$ and $R_n^{s,h}$ are the reflection coefficient for the vertical and horizontal polarization for the 'o' and the 'n' faces, respectively, and $T_o^{s,h}$ and $T_n^{s,h}$ are the transmission coefficient for the vertical and horizontal polarization for the 'o' and the 'n' faces, respectively. Details of the reflection and transmission coefficient are presented in Appendix B or Reference [33]. To generalize the edge diffraction coefficient to include diffraction due to dielectric plates, the following assumptions are made [34]

(a) $n \approx 1$, or $n = 2$ and

(b) the width of the dielectric plates is a small fraction of a wavelength.

Note that this is not the case for the multi-cylinder model. However, if the cylinders are assumed to be lossy, the transmission coefficients, $T_{o,n}^{s,h}$, are negligible. In general, for the backscatter case, the incident boundary cotangent terms have a much smaller contribution as compared to the reflection boundary cotangent terms.

Hence, for the backscatter case the transmission coefficient may be assumed *zero*. Therefore, under the assumption of backscatter and lossy cylinders, Equation (367) can be simplified to

$$D_{s,d} = \frac{-e^{-j\frac{\pi}{4}}}{2n\sqrt{2\pi k}} \left[\cot\left(\frac{\pi - (\Phi - \Phi')}{2n}\right) + \cot\left(\frac{\pi + (\Phi - \Phi')}{2n}\right) \right.$$
$$\left. + R_o^{s,h} \cot\left(\frac{\pi - (\Phi + \Phi')}{2n}\right) + R_n^{s,h} \cot\left(\frac{\pi + (\Phi + \Phi')}{2n}\right) \right]. \qquad (368)$$

2.2 The Junction Edge Normal Vector and Curvature

In order to find the diffracted caustic distance, ρ_d, in Equation (22), from a typical cylinder-cylinder junction, it is necessary to determine the edge normal vector, $\hat{n}_c$, and the radius of curvature, a_c. Here, the right hand x-y-z coordinate system is defined so that the x-axis is along the normal to the end cap of the main cylinder (trunk) and the y-axis is in the plane formed by the end cap normals (also the pattern plane) in the direction of the junction of interest, Figure 89. It is shown in Appendix C that for a cylinder-cylinder junction angle α (the dihedral angle) and equal radii of cylinders, a, the junction edge normal is

$$\hat{n}_c = \cos\left(\frac{\alpha}{2}\right) \hat{y} + \sin\left(\frac{\alpha}{2}\right) \hat{x}, \qquad (369)$$

and the radius of curvature is

$$a_c = a \cos\left(\frac{\alpha}{2}\right). \qquad (370)$$

3 Modification to the Two-Dimensional Dihedral

The only caustic that needs to be considered is that of single diffractions from the end caps. Thus, its correction is the same as that of the cylindrical part of the top-hat, which has been discussed in Section 3.1. Note that even if the junction angle, α, is 90° the diffracted-reflected and the diffracted-reflected-diffracted terms do not exhibit caustics at broadside.

145
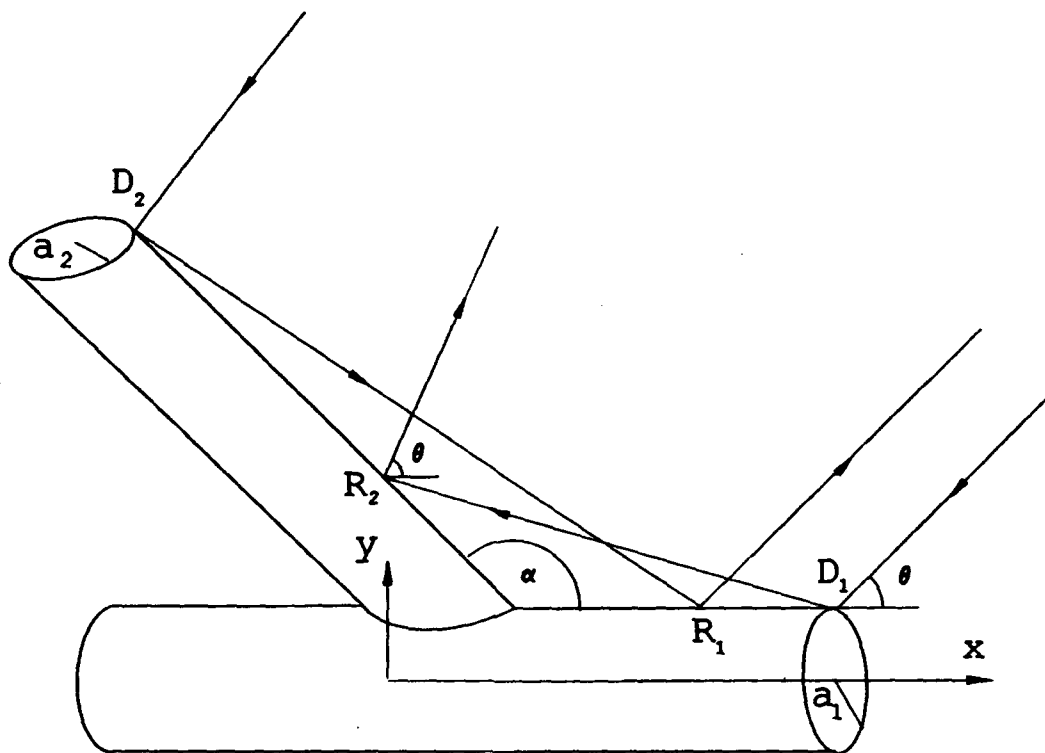
Figure 89: Cylinder-cylinder diffracted-reflected terms.

3.1 Spread Factor and Caustic Correction for Diffracted Terms

Equation (22) is used to get the spread factor for single diffractions. However, if the single diffraction is from a junction, $\hat{n}_r$ and a_c used in Equation (22) are defined by Equations (369) and (370), respectively.

3.2 Spread Factor for Diffracted-Reflected Type Terms

For the backscatter case, the spread factor due to the diffracted-reflected (DR) and reflected-diffracted (RD) terms are the same since the two ray paths are the same. For details, see Section 2.

146

The spread factor for the $D_1 R_2$ term (or $R_2 D_1$), see Figure 89, may be represented as

$$\rho^{D_1 R_2}_{spread\ factor} = \left[\frac{\rho^d}{s\left(\rho^d + s\right)} \rho^r_1 \rho^r_2 \right]^{\frac{1}{2}}, \tag{371}$$

where ρ^d, using Equation (22), is

$$\rho^d = \frac{a}{\sin\theta + \sin\left(2\alpha - \theta\right)}, \tag{372}$$

and the principal radii of curvature of the reflected wavefront are

$$\rho^r_1 = s, \tag{373}$$

and

$$\frac{1}{\rho^r_2} = \frac{1}{s + \rho^d} + \frac{2\sin\left(\alpha - \theta\right)}{a} \tag{374}$$

or

$$\rho^r_2 = \frac{a\left(s + \rho^d\right)}{a + \left(s + \rho^d\right)2\sin\left(\alpha - \theta\right)}. \tag{375}$$

Using Equations (372) to (375) in (371),

$$\rho^{D_1 R_2}_{spread\ factor} = \left[\frac{\rho^d a}{a + \left(s + \rho^d\right)2\sin\left(\alpha - \theta\right)} \right]^{\frac{1}{2}}. \tag{376}$$

The spread factor for the $D_2 R_1$ term (or $R_1 D_2$), see Figure 89, may be represented as

$$\rho^{D_2 R_1}_{spread\ factor} = \left[\frac{\rho^d}{s\left(\rho^d + s\right)} \rho^r_1 \rho^r_2 \right]^{\frac{1}{2}}, \tag{377}$$

where ρ^d, using Equation (22), is

$$\rho^d = \frac{a}{\sin\left(\alpha + \theta\right) + \sin\left(\alpha - \theta\right)}, \tag{378}$$

and the principal radii of curvature of the reflected wavefront are

$$\rho^r_1 = s, \tag{379}$$

and

$$\rho^r_2 = \frac{a\left(s + \rho^d\right)}{a + \left(s + \rho^d\right)2\sin\theta}. \tag{380}$$

Using Equations (378) to (380) in (377)

$$\rho^{D_2 R_1}_{spread\ factor} = \left[\frac{\rho^d a}{a + \left(s + \rho^d\right)2\sin\theta} \right]^{\frac{1}{2}}. \tag{381}$$

147

3.3 Spread Factor for Diffracted-Reflected-Diffracted Terms

The spread factor for the $D_2 R_1 D_2$ term, see Figure 90, may be represented as

$$\rho_{spread\ factor}^{D_2 R_1 D_2} = \left[\frac{\rho_1^d}{s\left(\rho_1^d + s\right)} \frac{\rho_1^r \rho_2^r}{\left(\rho_1^r + s\right)\left(\rho_2^r + s\right)} \rho_2^d \right]^{\frac{1}{2}}, \tag{382}$$

where ρ_1^d, using Equation (22), is

$$\rho_1^d = \frac{a}{\cos\alpha + |\sin(\alpha - \theta)|}, \tag{383}$$

and the principal radii of curvature of the reflected wavefront are

$$\rho_1^r = s, \tag{384}$$

and

$$\frac{1}{\rho_2^r} = \frac{1}{s + \rho_1^d} + \frac{2}{a}, \tag{385}$$

and for the second diffraction, ρ_2^d, using Equation (22), is

$$\rho_2^d = \frac{1}{\left(\rho_2^r + s\right)} + \frac{\cos\alpha + |\sin(\alpha - \theta)|}{a}. \tag{386}$$

The spread factor for the $D_1 R_2 D_1$ term, see Figure 90, may be represented as

$$\rho_{spread\ factor}^{D_1 R_2 D_1} = \left[\frac{\rho_1^d}{s\left(\rho_1^d + s\right)} \frac{\rho_1^r \rho_2^r}{\left(\rho_1^r + s\right)\left(\rho_2^r + s\right)} \rho_2^d \right]^{\frac{1}{2}}, \tag{387}$$

where ρ_1^d, using Equation (22), is

$$\rho_1^d = \frac{a}{\cos\alpha + \sin\theta}, \tag{388}$$

and the principal radii of curvature of the reflected wavefront are

$$\rho_1^r = s, \tag{389}$$

and

$$\frac{1}{\rho_2^r} = \frac{1}{s + \rho_1^d} + \frac{2}{a}, \tag{390}$$

and for the second diffraction, ρ_2^d, using Equation (22), is

$$\rho_2^d = \frac{1}{\left(\rho_2^r + s\right)} + \frac{\cos\alpha + \sin\theta}{a}. \tag{391}$$
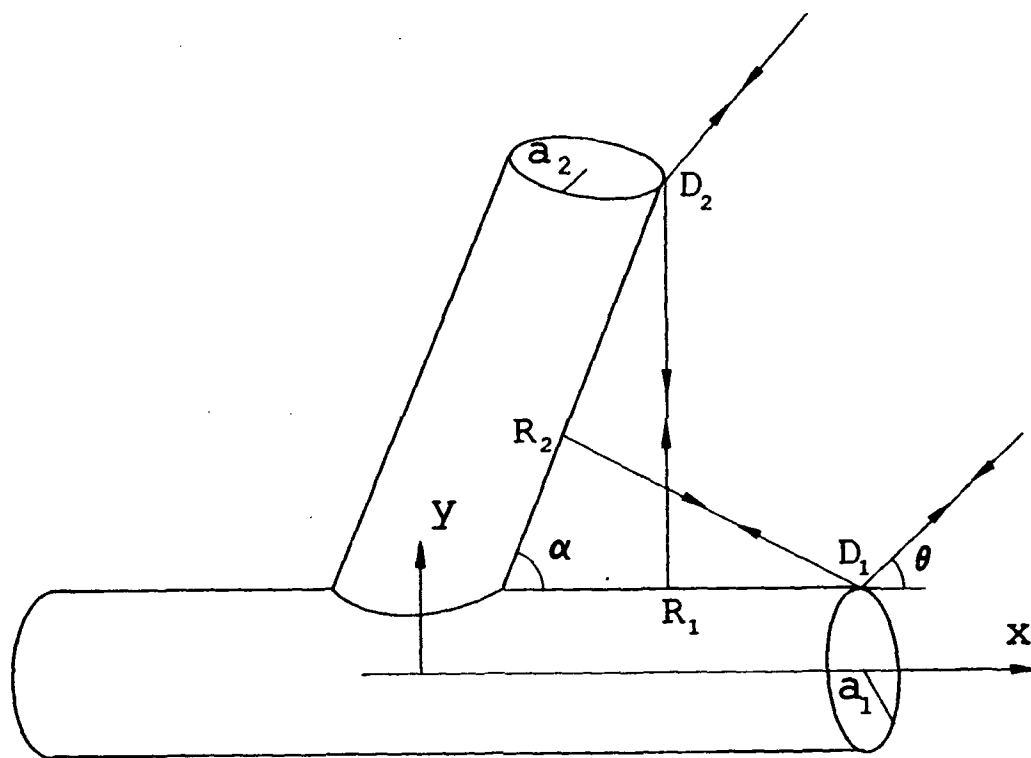
Figure 90: Cylinder-cylinder DRD terms.

4 Model Types and Results

Two types of models are considered, as shown in Figures 91 and 92. The models are made of PVC pipes with absorber placed inside because it is inexpensive and easy to piece together into various configurations. They are chosen to validate the dielectric aspects of the code. The dielectric properties of the PVC and the absorber are well known. The configurations are chosen to resemble the crooks of trees. It is not suggested that the results from these models are directly comparable to those from trees.

To determine the effects of terminations while comparing the Uniform Theory of Diffraction and the measurement results, the following order of analysis is carried out. All the results are for the backscatter case. First, the plastic cylinders and the end caps are covered with aluminum foil: Figures 93 and 94 show the vertically and horizontally polarized fields for the T-junction at 2 GHz, and Figures 95 and 96 show the vertically and horizontally polarized fields for the Y-junction at 2 GHz. Second, the plastic cylinders are covered in aluminum foil, but flat absorbers are inserted in the end caps: Figures 97 and 98 show the vertically and horizontally polarized fields for the T-junction at 2 GHz, and Figures 99 and 100 show the vertically and horizontally polarized fields for the Y-junction at 2GHz. Next, the cylinders are the same as above, but cone pyramid absorbers are inserted in the end caps: Figures 101 and 102 show the vertically and horizontally polarized fields for the T-junction at 2 GHz, and Figures 103 and 104 show the vertically and horizontally polarized fields for the Y-junction at 2 GHz.

4.1 Specular from PVC Cylinder with Absorber

Figure 105 shows the real and the imaginary parts of the dielectric constants for the absorber used to fill the PVC pipe. The dielectric constant of the PVC pipe is taken to be that of Polystyrene given as $\epsilon = 2.55 - j8.5E - 04$ [36] and is assumed fixed over 2-18 GHz.
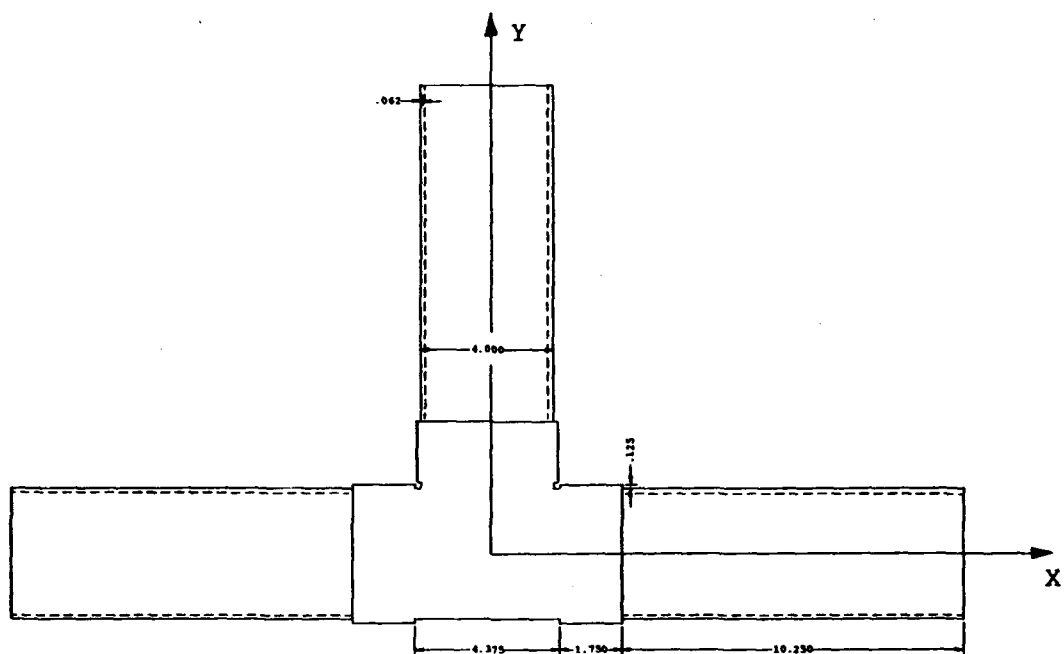
Figure 91: The T-junction model.
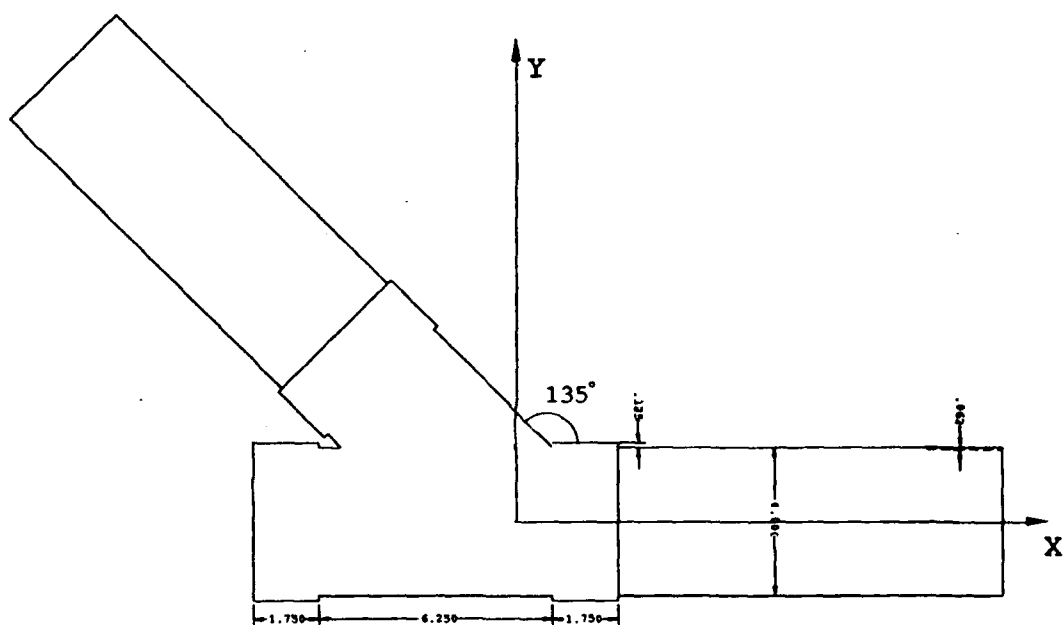
Figure 92: The Y-junction model.

151
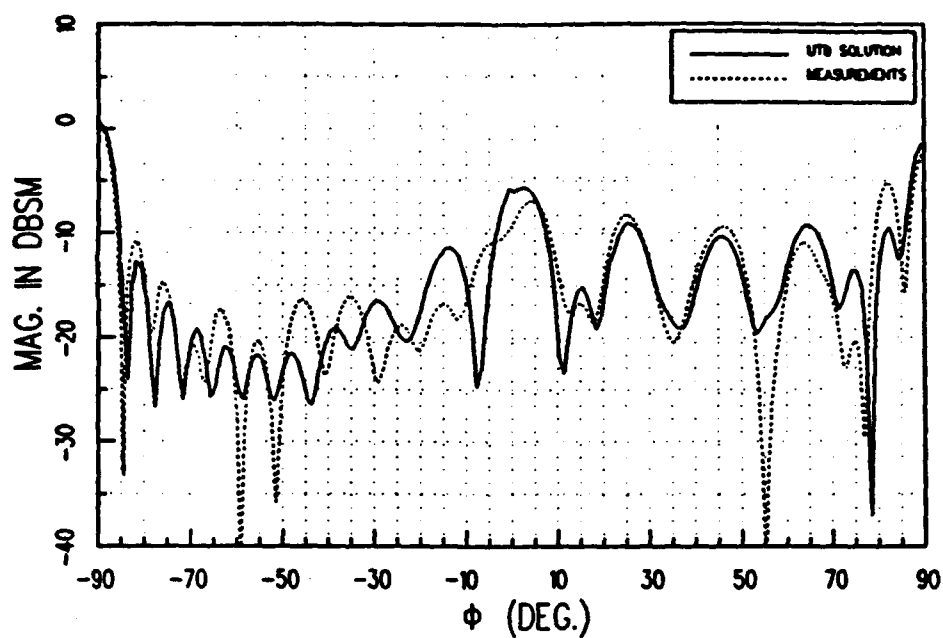
Figure 93: Backscatter from T-junction covered in aluminum foil at 2 GHZ for vertically polarized field.
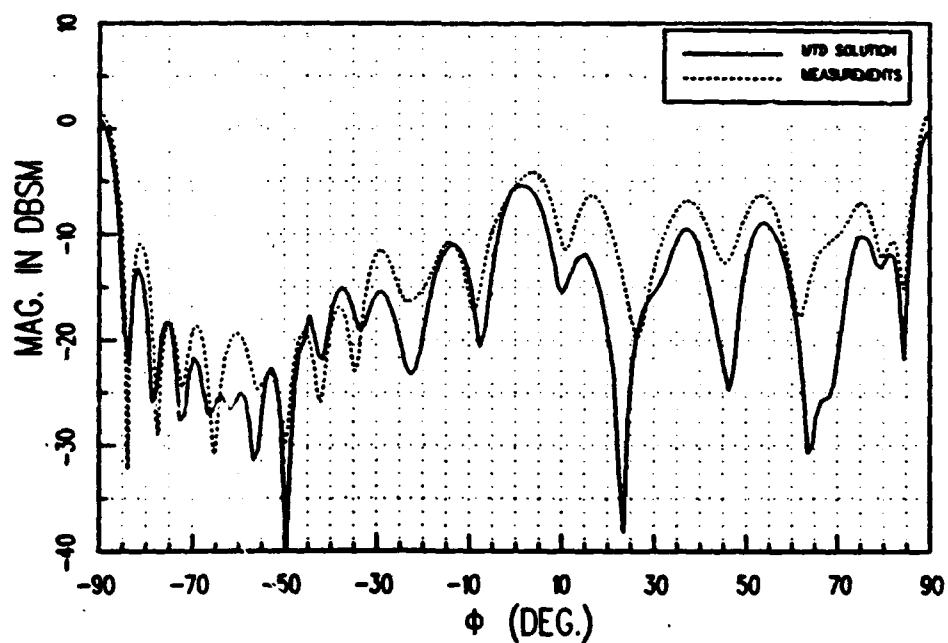
Figure 94: Backscatter from T-junction covered in aluminum foil at 2 GHZ for horizontally polarized field.

152
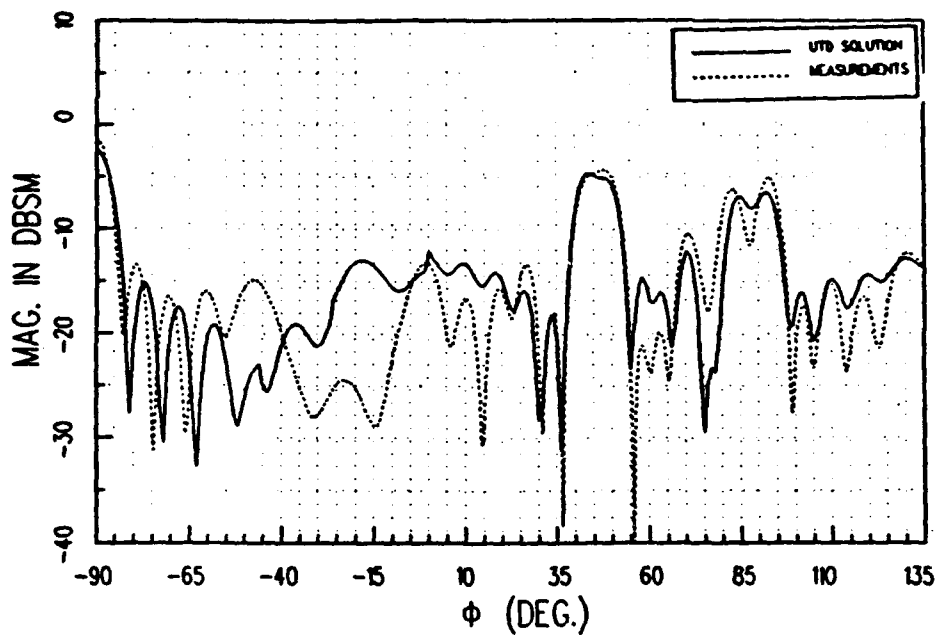
Figure 95: Backscatter from Y-junction covered in aluminum foil at 2 GHZ for vertically polarized field.
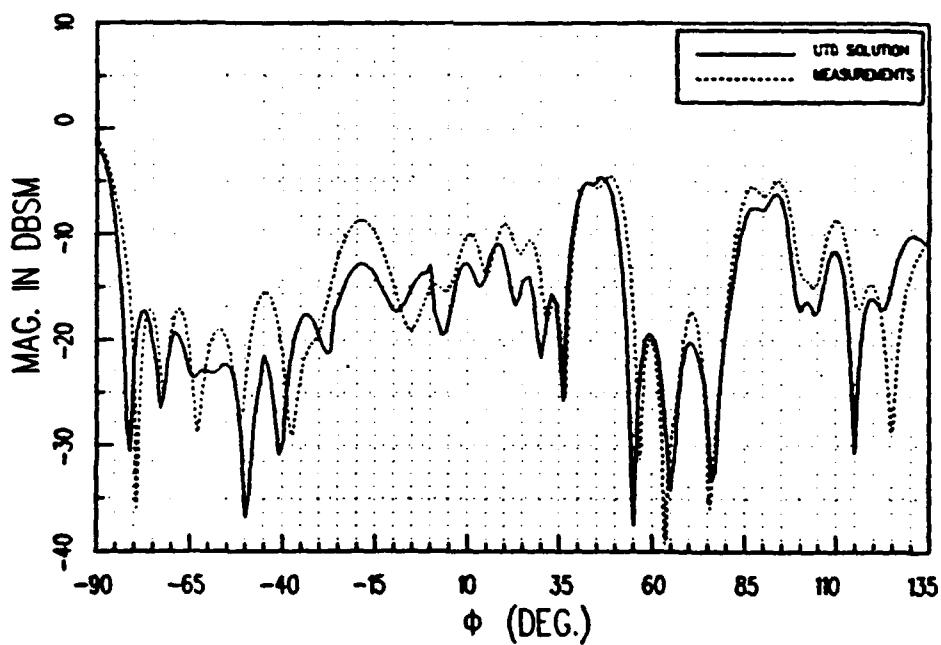
Figure 96: Backscatter from Y-junction covered in aluminum foil at 2 GHZ for horizontally polarized field.

Figure 97: Backscatter from T-junction covered in aluminum foil, but flat absorbers inserted in end caps, at 2 GHZ for vertically polarized field.

Figure 98: Backscatter from T-junction covered in aluminum foil, but flat absorbers inserted in end caps, at 2 GHZ for horizontally polarized field.

154
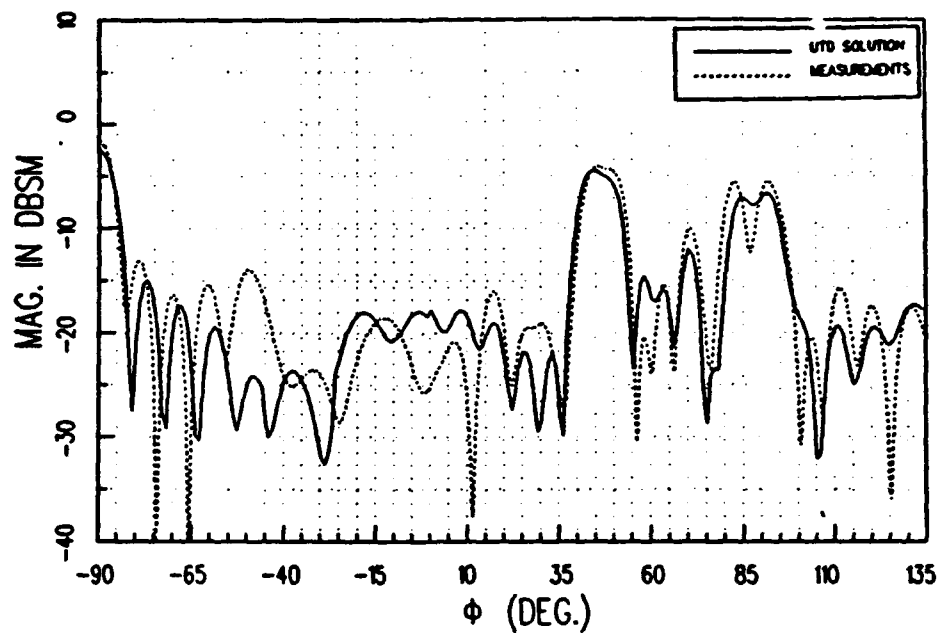
Figure 99: Backscatter from Y-junction covered in aluminum foil, but flat absorbers inserted in end caps, at 2 GHZ for vertically polarized field.
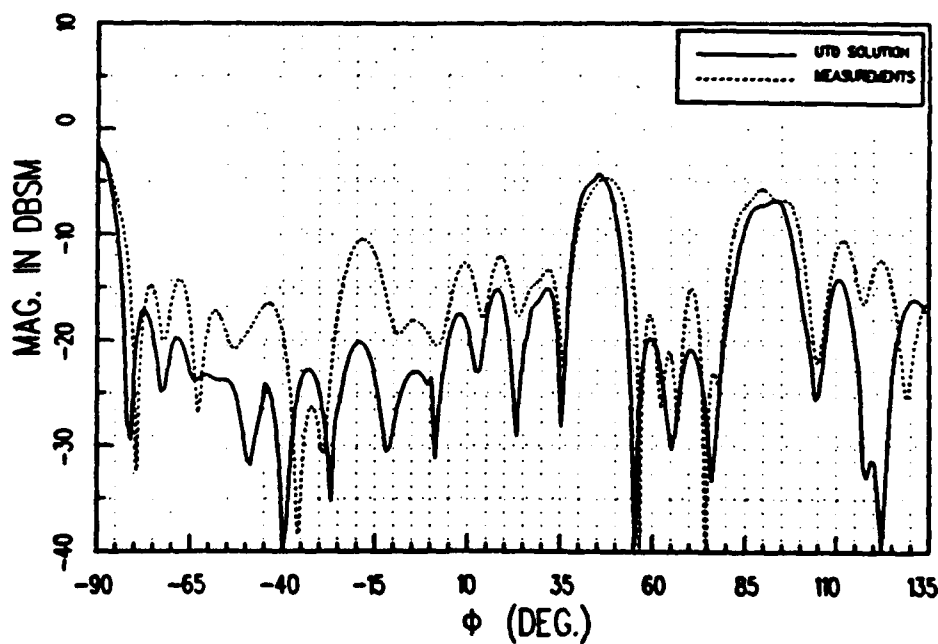
Figure 100: Backscatter from Y-junction covered in aluminum foil, but flat absorbers inserted in end caps, at 2 GHZ for horizontally polarized field.

155
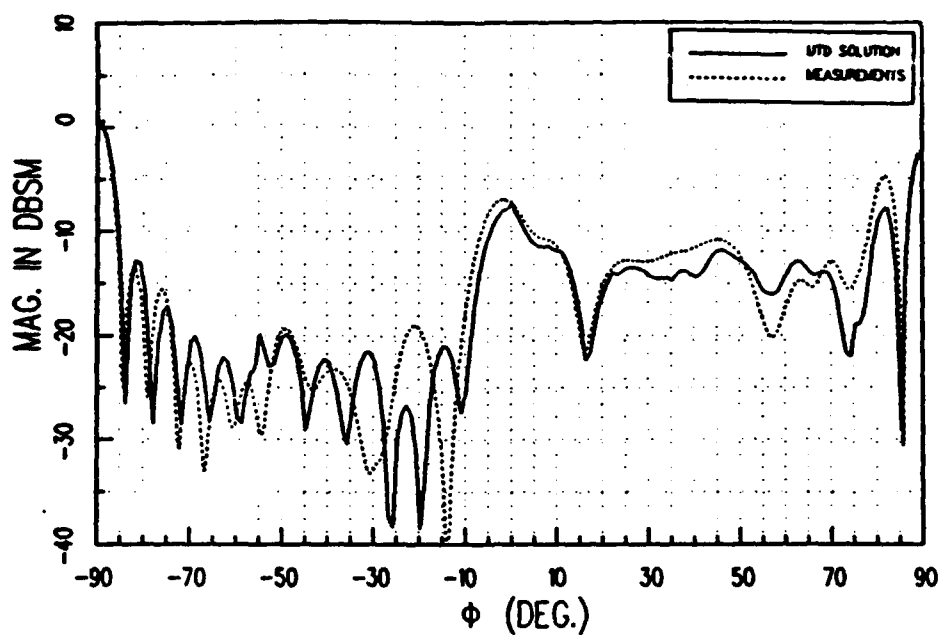
Figure 101: Backscatter from T-junction covered in aluminum foil, but cone pyramid absorbers inserted in end caps, at 2 GHZ for vertically polarized field.

Figure 102: Backscatter from T-junction covered in aluminum foil, but cone pyramid absorbers inserted in end caps, at 2 GHZ for horizontally polarized field.

156
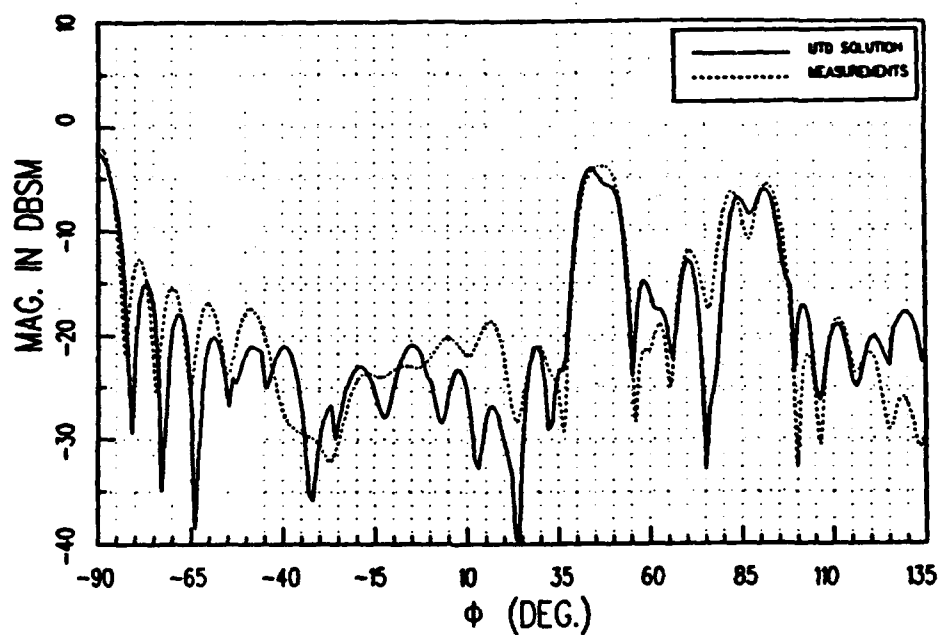
Figure 103: Backscatter from Y-junction covered in aluminum foil, but cone pyramid absorbers inserted in end caps, at 2 GHZ for vertically polarized field.
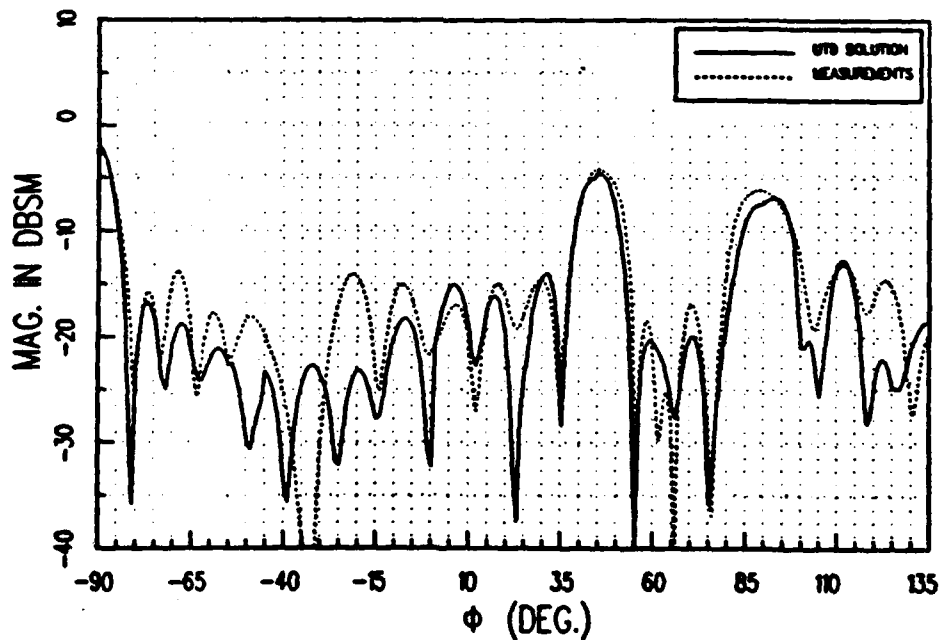
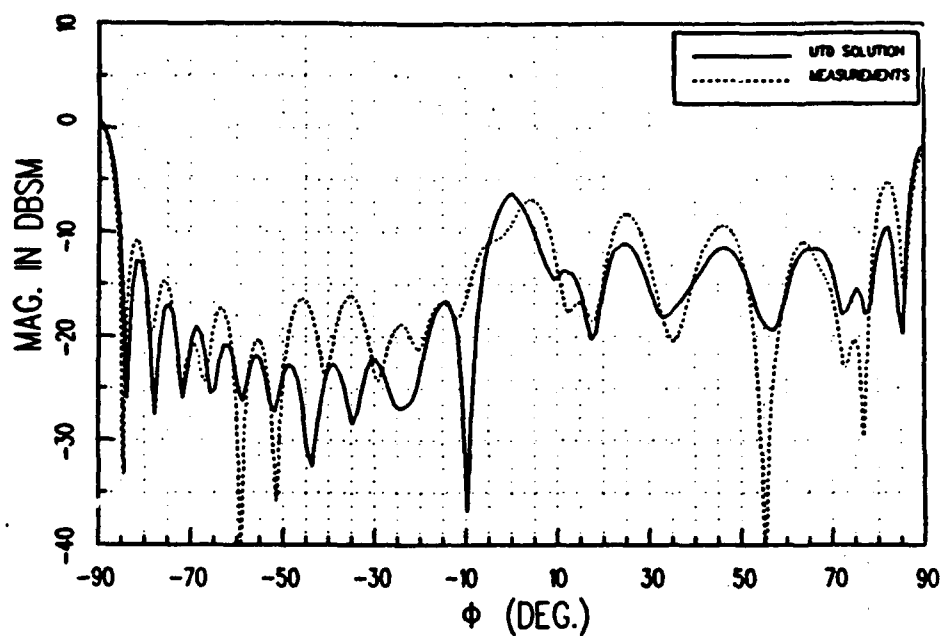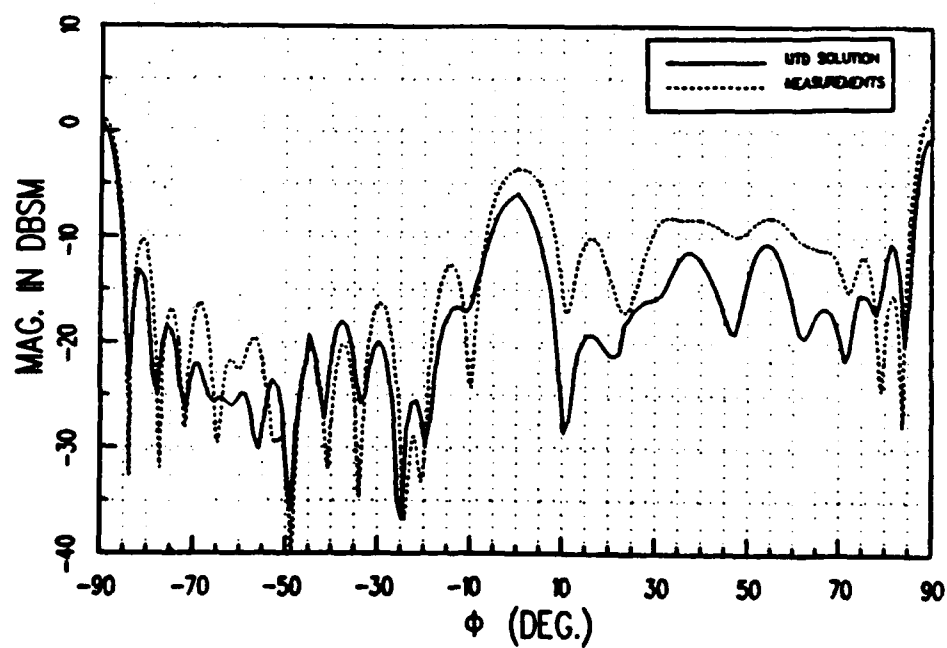Figure 104: Backscatter from Y-junction covered in aluminum foil, but cone pyramid absorbers inserted in end caps, at 2 GHZ for horizontally polarized field.
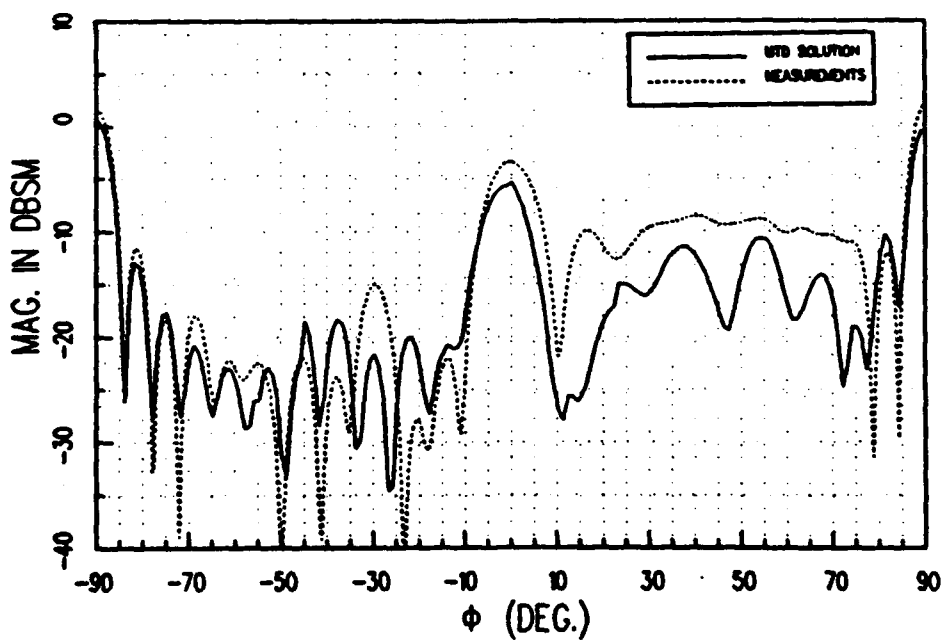
157
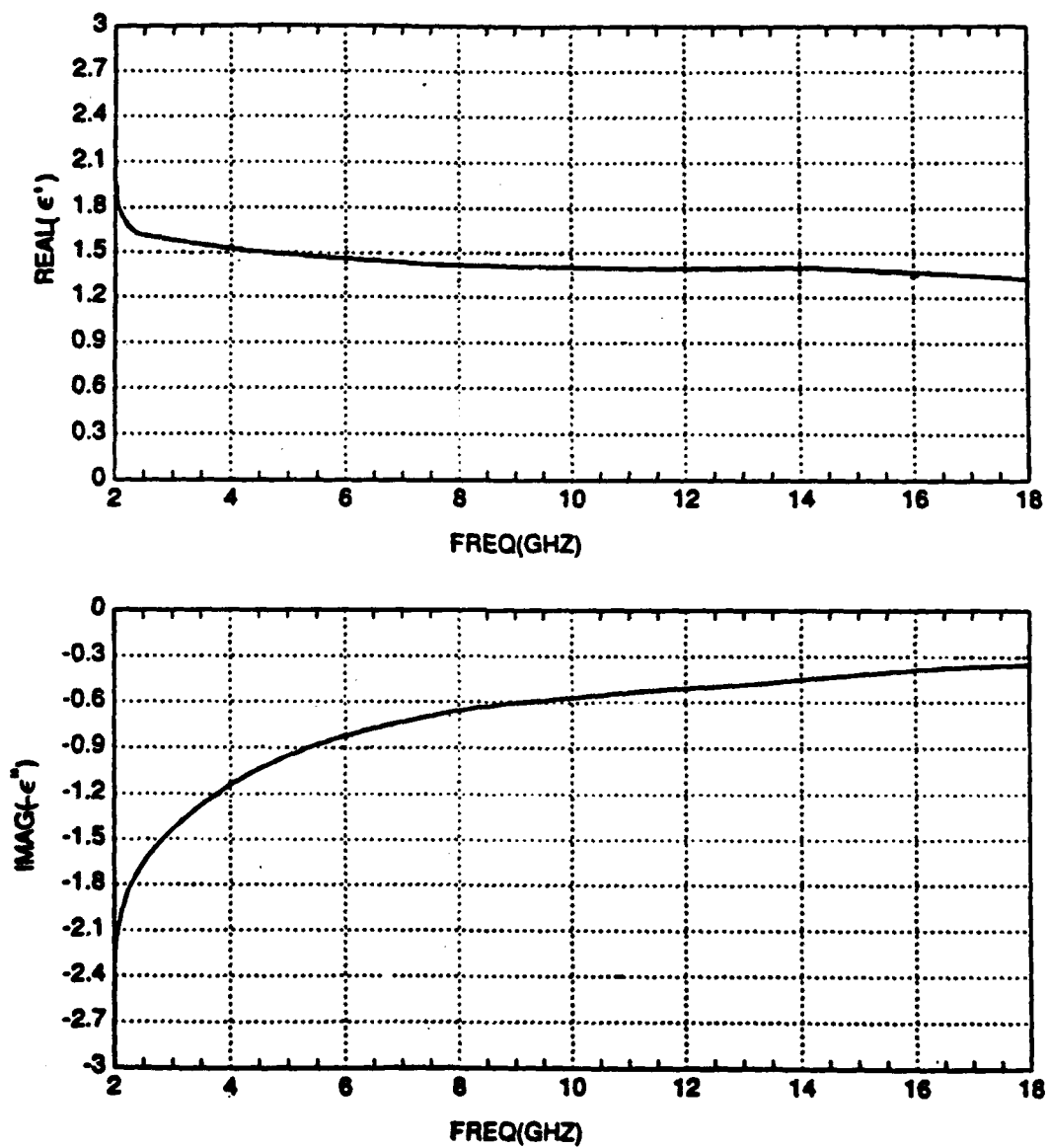
Figure 105: Real and the imaginary parts of the dielectric constant of the absorber used.

In order to match the theory with the measurements in the specular region broadside to the PVC pipe with absorber flat at the end caps it is necessary to set an air gap between the PVC and absorber in both the UTD and the eigenfunction solution. This may be explained by the fact that the absorber is not tightly fitted into the PVC pipe. Figures 106 and 107 show the horizontal and the vertical polarizations from a 24 *in* long cylindrical pipe of radius 1.5 *in*. An air gap of 0.18 *in* is chosen for the theory to match the measured results. It is observed that the PVC pipe was slightly elliptical which can explain why the ripple in the eigenfunction solution due to the creeping wave does not match with the creeping wave ripple in the measurement.

4.2   Results of PVC pipe with absorber

In the modified diffraction coefficient, Equation (368), one face of the wedge is unaware of the characteristics of the other face. This suggests that simplifying Equation (368) to retain information of only one face at a particular direction should provide even better results. The diffraction coefficient is simplified as

if $\quad \left| R_o^{s,h} \cot\left(\frac{\pi - (\Phi + \Phi')}{2n}\right) \right| > \left| R_n^{s,h} \cot\left(\frac{\pi + (\Phi + \Phi')}{2n}\right) \right|$,

$$D_{s,h} = \frac{-e^{-j\frac{\pi}{4}}}{2n\sqrt{2\pi k}} R_o^{s,h} \cot\left(\frac{\pi - (\Phi + \Phi')}{2n}\right) ;$$

if $\quad \left| R_o^{s,h} \cot\left(\frac{\pi - (\Phi + \Phi')}{2n}\right) \right| < \left| R_n^{s,h} \cot\left(\frac{\pi + (\Phi + \Phi')}{2n}\right) \right|$,

$$D_{s,h} = \frac{-e^{-j\frac{\pi}{4}}}{2n\sqrt{2\pi k}} R_n^{s,h} \cot\left(\frac{\pi + (\Phi + \Phi')}{2n}\right) . \tag{392}$$

It is found that patterns and signatures of cylinders, T and Y junctions, obtained by using the simplified diffraction coefficient, Equation (392), compare better with measurements than those obtained by using the modified diffraction coefficient, Equation (368). For all the results shown in this subsection, the simplified diffraction coefficient of Equation (392) is used and an air gap of 0.18 *in* is assumed between the PVC pipe and the absorber. Also, all the results are for the backscatter case at

159
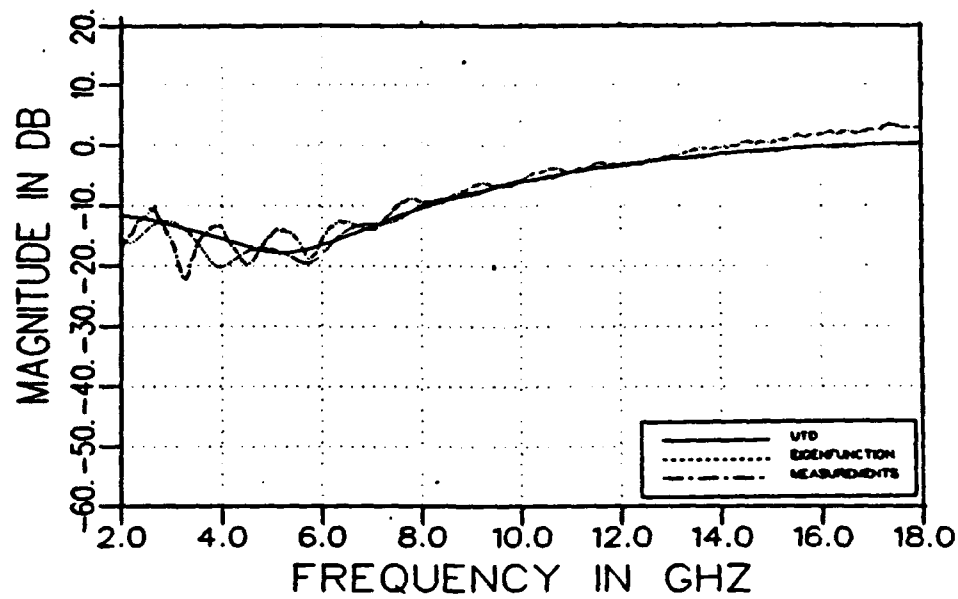
Figure 106: Specular from 24 *in* long cylinder of radius 1.5 *in* for horizontally polarized field.
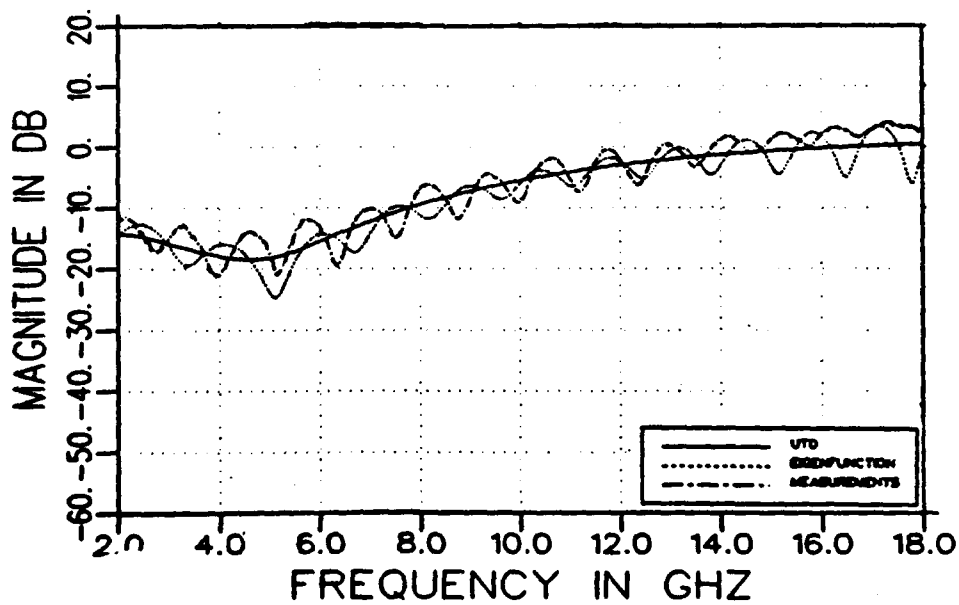
Figure 107: Specular from 24 *in* long cylinder of radius 1.5 *in* for vertically polarized field.

160

2 GHz. For a 24 *in* long cylindrical pipe of radius 1.5 *in*, Figures 108 and 109 show the vertical and the horizontal polarizations, respectively. Figures 110 and 111 show the vertical and the horizontal polarizations, respectively, for a cylindrical pipe of the same length but of radius 2 *in*. For the T-junction model, shown in Figure 91, Figures 112 and 113 show the vertical and the horizontal polarizations, respectively. Figures 114 and 115 show the vertical and the horizontal polarizations, respectively, for the Y-junction model, shown in Figure 92.

5 More Realistic Modeling

The PVC models studied above have been chosen simply to validate the theory and the computer code. More work needs to be done to come up with a reasonable model for a tree. Certain conclusions from this study, however, may be pointed out. Since the PVC pipe is not lossy, it is expected that better results can be obtained for actual trunks and branches. This is because the surface waves will dampen out due the wood being lossy. Also, in general, it is expected, that the truncations of the cylinders which are considered in this study only approximately model the actual shapes of the trunks and branches. One needs to come up with an equivalent length in order to model a trunk or a branch.
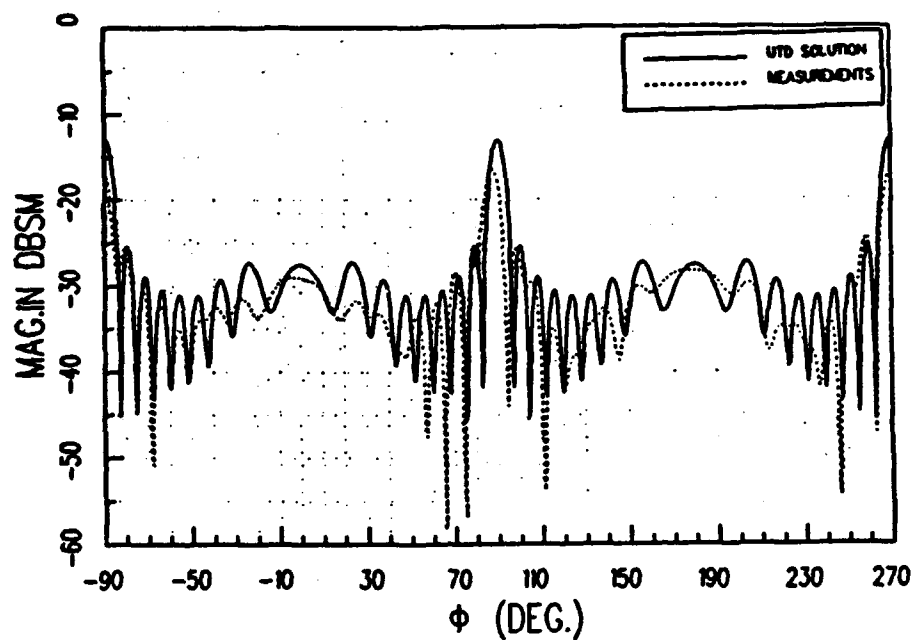
Figure 108: Backscatter from 24 *in* cylinder of radius 1.5 *in* at 2 GHZ for vertically polarized field.
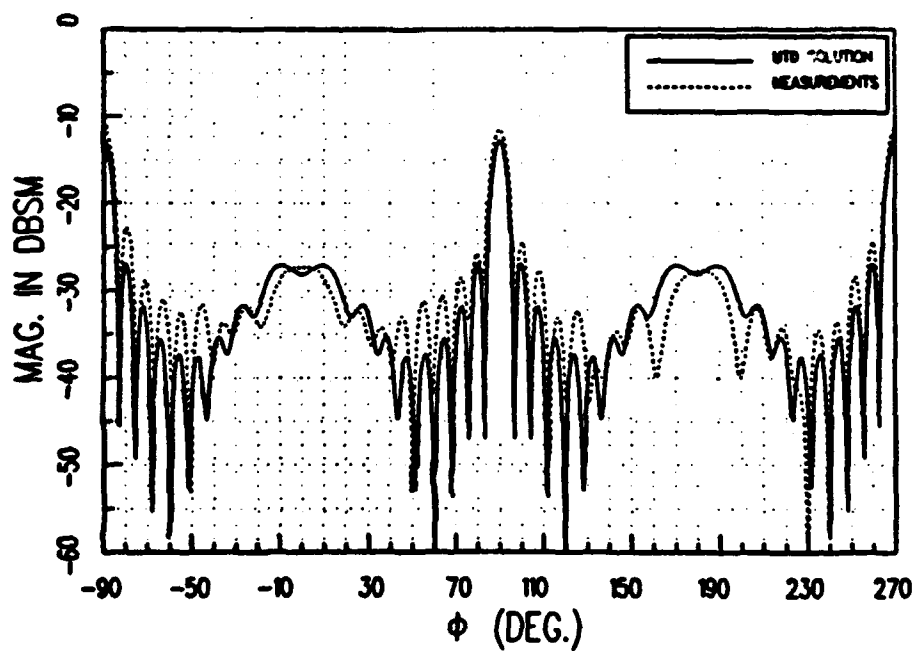
Figure 109: Backscatter from 24 *in* cylinder of radius 1.5 *in* at 2 GHZ for horizontally polarized field.
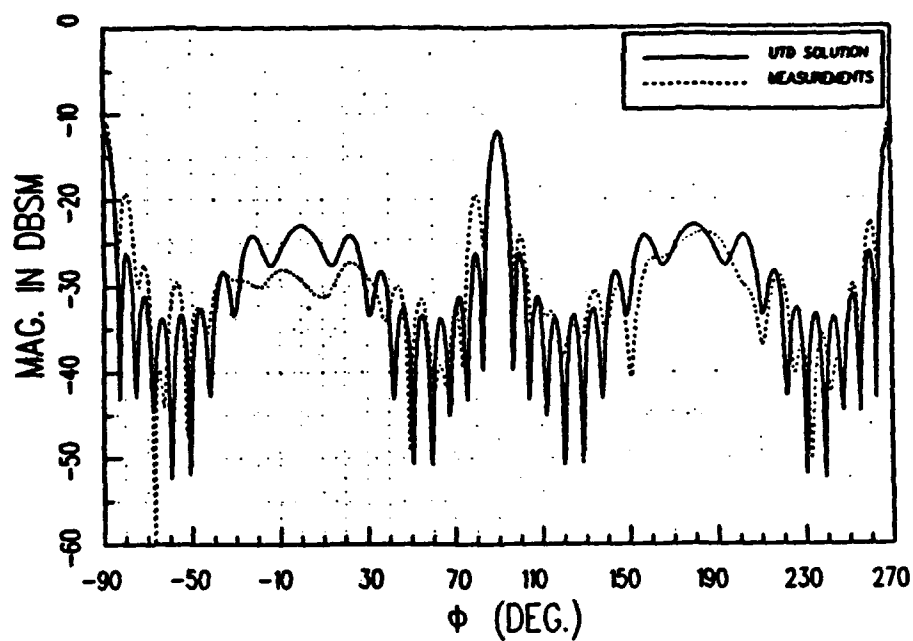
Figure 110: Backscatter from 24 *in* cylinder of radius 2.0 *in* at 2 GHZ for vertically polarized field.
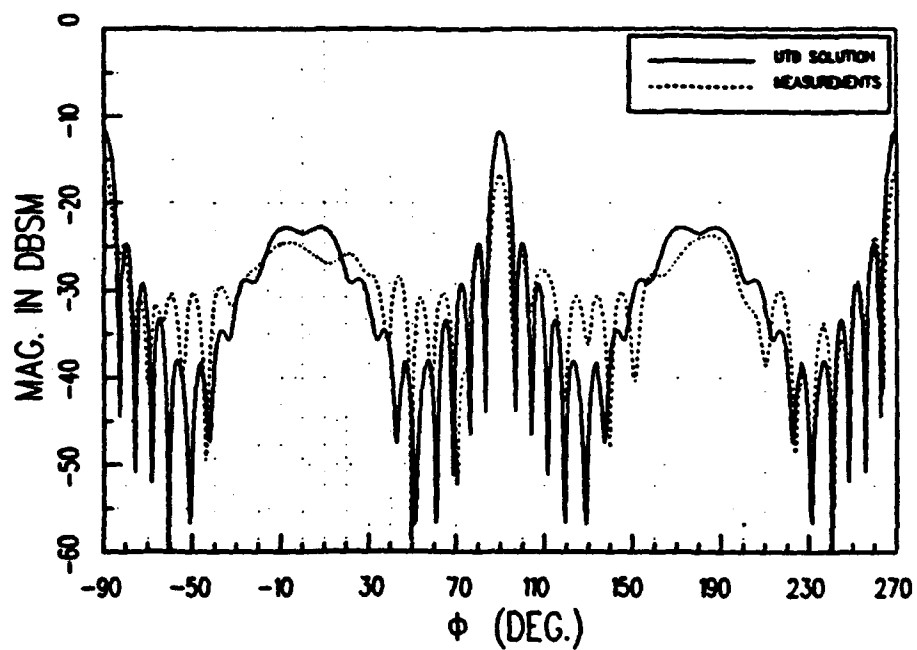
Figure 111: Backscatter from 24 *in* cylinder of radius 2.0 *in* at 2 GHZ for horizontally polarized field.

163
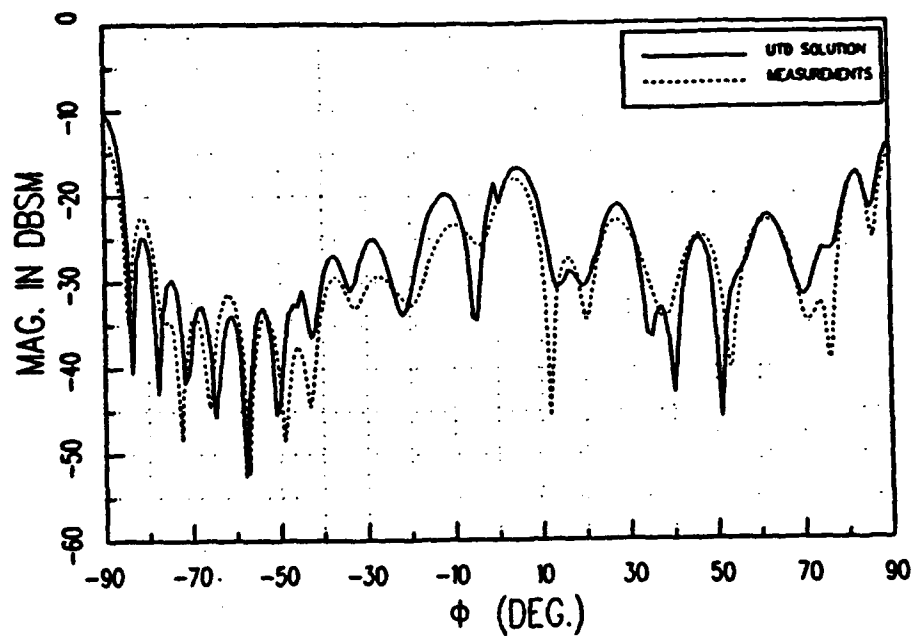
Figure 112: Backscatter from T-junction at 2 GHZ for vertically polarized field.
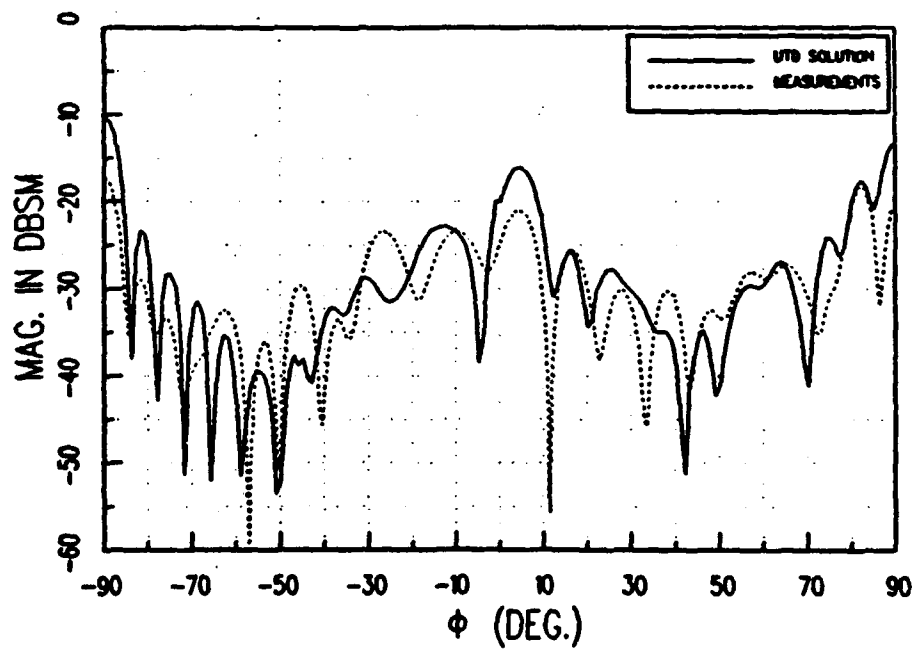
Figure 113: Backscatter from T-junction at 2 GHZ for horizontally polarized field.

164
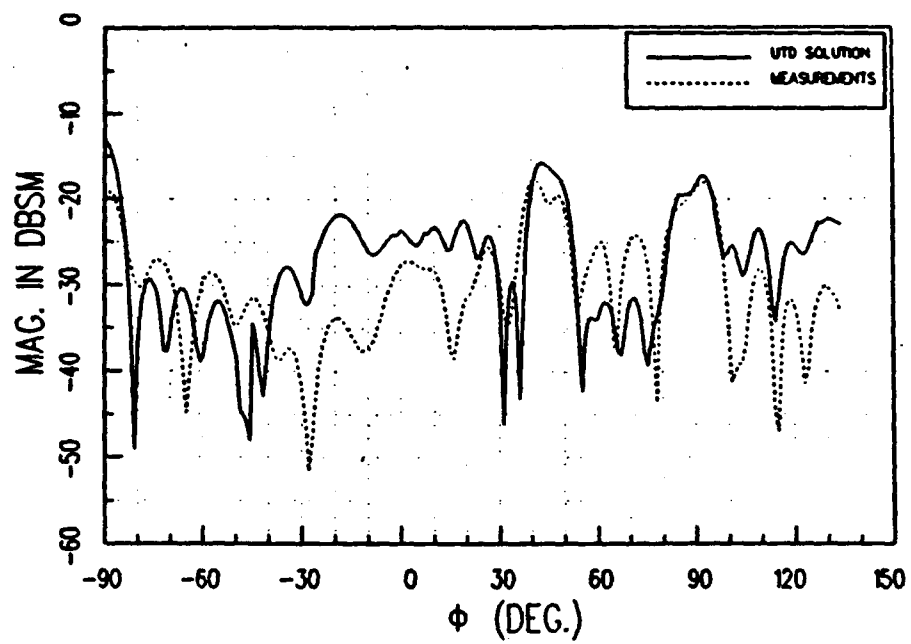
Figure 114: Backscatter from Y-junction at 2 GHZ for vertically polarized field.
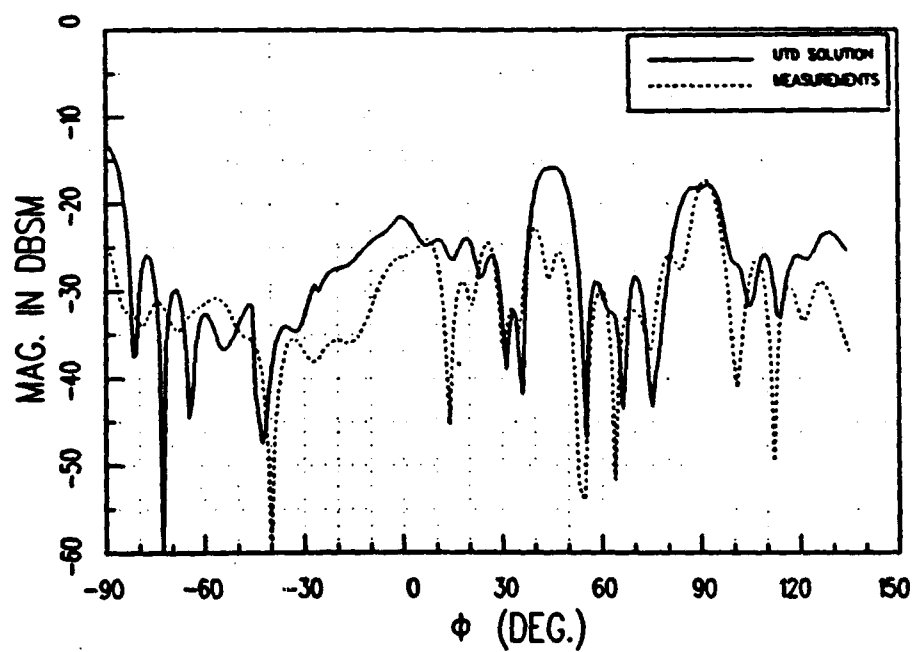
Figure 115: Backscatter from Y-junction at 2 GHZ for horizontally polarized field.

165

SECTION 10

Conclusion

In general, the high frequency EM scattering from complicated physical structures such as aircraft, tanks, trucks etc. can be analyzed using ray techniques by building up such complex structures from simpler shapes such as cylinders, cones, dihedrals etc.. Therefore a complex problem may be analysed piece by piece and then applying superposition. In this work, classical Uniform Theory of Diffraction (UTD) with modifications for the caustics and curvatures is used to get the scattered fields. Shapes where the second and higher order interactions are important over a wide range of angle are considered.

It is shown that for the rectangular dihedral in the principal plane, the order of interactions required to get the pattern in the dihedral region, for a dihedral of angle α, is found to be the integral value of $\left(\frac{180°}{\alpha}\right)$, for the backscatter case. Since the computer code developed for this analysis contains all interactions up to third order except the triple diffractions, the solution discussed here is valid for backscatter for dihedrals of $\alpha = 60°$ or greater. This solution is expected to degrade gracefully in the dihedral region for α less than 60°. In general, as the angle of the dihedral diverts from α which makes $\left(\frac{180°}{\alpha}\right)$ an integer, the main beam amplitude falls fairly rapidly. The UTD formulation provides excellent results compared with the method of moments. For the case of maximum scattering, from a GO point of view, and for a general angled dihedral and bistatic angle, the dominant UTD terms in the

dihedral region are reduced to simple forms. Comparisons of these dominant UTD results with the total UTD solutions show good agreement.

The two-dimensional result of the rectangular dihedral is modified by caustic corrections and spread factors, to get three-dimensional results for the top-hat, bicone, and parallel plate and circular cavities. It is found that the response of cavities is not as sharp as compared to that of the $90°$ dihedral. The results compare well with the those obtained from body of revolution moment method solution.

Scattering from the donut is considered in Section 8. The first and second order GO field caustics are corrected by using equivalent currents. Again, the results compare well with the body of revolution moment method solution.

Scattering from cylindrical pipes that form a T and Y-junctions of perfect electric conductor and dielectric materials are considered. It is shown that by using the modified diffraction coefficients, the UTD results compare well with measurements and an eigenfunction solution. Some more work is required to extend these results for scattering from tree trunks and branches.

It is observed that a few underlying principles are all that is required to get scattered fields from many different shapes. It is expected that even better agreement and/or results for small-sized models could be achieved by including more interactions.

REFERENCES

[1] R. G. Kouyoumjian and P.H. Pathak, "A Uniform Geometrical Theory of Diffraction for an Edge in a Perfectly Conducting Surface," *Proc. IEEE*, Vol. 62, pp. 1448-1461, Nov. 1974.

[2] R. Tiberio, G. Manara, G. Pelosi and R.G. Kouyoumjian, "High-frequency Electromagnetic Scattering of plane waves from double wedges," *IEEE Trans. on Antennas and Propagation*, Vol. 37, pp. 1172-1180, Sept. 1989.

[3] J. B. Keller, *"Geometrical Theory of Diffraction,"* J. Opt. Soc. of America, vol. 52, no. 2, Feb. 1962.

[4] R. G. Kouyoumjian, "Asymptotic High-Frequency Methods," *Proc IEEE*, Vol. 53, pp. 864-876, Sept. 1965.

[5] P. H. Pathak, W. D. Burnside, and R. J. Marhefka, "A Uniform GTD Analysis for the diffraction of Electromagnetic Waves by a smooth Convex Surface," *IEEE Trans. on Antennas and Propagation*, Vol. AP-28, pp. 631-642, Sept. 1980.

[6] R. Tiberio and R. G. Kouyoumjian, "An Analysis of Diffraction at Edges Illuminated by Transition Region Fields," *Radio Science*, Vol. 17, pp. 323-336, 1982

[7] R. Tiberio, and R. G. Kouyoumjian, "Calculation of the High-Frequency Diffraction by Two Nearby Edges Illuminated at Grazing Incidence,"*Proc. IEEE*, Vol. 32, pp.933-941, Nov. 1984.

[8] A. Michaeli, "A closed form Physical Theory of Diffraction solution for the electromagnetic scattering by Strips and 90° Dihedrals",*Radio Science*, Vol. 19, pp. 609-616, 1984.

[9] R. Tiberio and R. C. Kouyoumjian, "A Uniform GTD Solution for the Diffraction by Strips Illuminated at Grazing Incidence," *Radio Science*, Vol. 14, pp. 933-941, 1979.

[10] J. N. Hines and J. A. McEntee, "Echo Area of Acute-angle Dihedral Corner reflectors," Contract AF 30(635)-2811, October 1956.

[11] L. Peters, Jr., "Theory of Corner Reflectors as Bistatic Radar Enhancement Devices," Task No. 62561,May 1959.

[12] L. Peters, Jr., "Theory of spherical reflectors for bistatic radar enhancement," Task No. 62561, July 1959.

[13] N. Akhter and R. J. Marhefka, "Far Zone Scattering from Rectangular and Triangular Dihedral in the Principal Plane." *Technical Report 721198-1*, February 1989.

[14] D. J. Blejer "Physical Optics Polarization Scattering Matrix and Impulse Response of a Right Dihedral Corner Reflector," ADT Project Memorandum No. 47PM-ADT-0052, December 1986. MIT, Lincoln Laboratory.

[15] T. Griesser and C. A. Balanis,"Backscatter Analysis of Dihedral Corner Reflectors Using Physical Optics and the Physical Theory of Diffraction," *IEEE Trans. on Antennas and Propagation*, Vol. 35, pp. 1137-11 , Oct 1987.

[16] T. Griesser and C. A. Balanis,"Dihedral Corner Reflector Backscatter Using Higher Order Reflections and Diffractions," *IEEE Trans. on Antennas and Propagation*, Vol. 35, pp. 1235-1247, Nov. 1987.

[17] K. R. Aberegg and R. J. Marhefka, "UTD interaction between plates for backscatter." *Technical Report 71573-1*, August 1986.

[18] J. H. Richmond, "A Integral-equation Solution for TE Radiation and Scattering from Conducting Cylinders," *Technical Report 2902-7*, October 1972.

[19] N. N. Wang, "Reaction formulation for Radiation and Scattering from Plates Corner Reflectors and Dielectric Coated Cylinders," *Technical Report 2902-15*, April 1974.

[20] C. E. Ryan and L. Peters, Jr., "Evaluation of Edge Diffracted Field Including Equivalent Currents for the Caustic Regions," *IEEE Trans. on Antennas and Propagation.* vol. AP-17, May 1969, p. 292-299; see also correction to this paper in vol. AP-18, p. 275, 1970.

[21] K. C. Chiang and R. J. Marhefka, "Bistatic Scattering from a finite Circular Cylinder." *Technical Report 714614-4*, July 1984.

[22] W. Ebihara and R. J. Marhefka, "Bistatic Scattering from a Cone Frustum." *Technical Report 716148-16*, August 1986.

[23] F. A. Sikta, W. D. Burnside, T. T. Chu, and L. Peters, Jr, "First Order Equivalent Current and Corner Diffraction Scattering form Flat Plate Structures," *IEEE Trans. on Antennas and Propagation*, vol. AP-31, July 1983, p. 584-589.

[24] T. T. Chu, "First Order Uniform Geometrical Theory of Diffraction Analysis of the Scattering of Smooth Structures."*Ph.D. dissertation*, The Ohio State University, Department of Electrical Engineering, Columbus, Ohio, 1982.

[25] C. A. Balanis, *Antenna Theory: Analysis and Design*, New York: Harper and Row Publishers, Inc., 1982.

[26] D. J. Blejer, "Physical Optics Polarization Scattering Matrix for a Top Hat Reflector," *IEEE Trans. on Antennas and Propagation*, vol. 39, No. 6, June 1991, p. 857-859.

[27] C. W. Chuang, "Scattering by a Rotationally Conducting Body," *Technical Report 714614-2*, August 1983.

[28] R. J. Burkholder, and P. H. Pathak, "Analysis of EM Penetration into and Scattering by Electrically Large Open Waveguide Cavities Using Gaussian Beam Shooting," *Proc. IEEE*, Vol. 79, No. 10, pp. 1401-1412, Oct. 1991.

[29] H Ling, R. C. Chou, S. W. Lee, "Shooting and Bouncing Rays: Calculating the RCS of an Arbitrary Shaped Cavity," *IEEE Trans. on Antennas and Propagation*, vol. AP-37, No. 2, February 1989, p. 194-205.

[30] E. D. Greer, "High Frequency Scattering from Multiple Finite Elliptical Cylinders." *Technical Report 712242-7*, June 1981.

[31] J. L. Volakis, and L. Peters, Jr., "Evaluation of Reflected Fields at Caustic Regions Using a Set of GO Equivalent Line Currents," *IEEE Trans. on Antennas and Propagation*, Vol. AP-33, pp. 860-866, August 1985.

[32] J. L. Volakis, "Electromagnetic Scattering from Inlets and Plates Mounted on Arbitrary Smooth Surface," *Ph. D. dissertation*, Ohio State University, Dept. Elec. Eng., 1982.

[33] J. H. Richmond, "Efficient Recursive Solution For Plane and Cylindrical Multilayers," *Technical Report 1968-1*, August 1965.

[34] R. G. Rojas-Teran, and W. D. Burnside, "GTD Analysis of Airborne Antennas Radiating in the Presence of Lossy Dielectric Layers," Semi-Annual Report 710964-8, August 1981. The Ohio State University ElectroScience Laboratory, Department of Electrical Engineering;

[35] Short course notes on "The Modern Geometrical Theory of Diffraction," Vols. 1, 2 and 3, The Ohio State University, ElectroScience Laboratory, Department of Electrical Engineering, 1982.

[36] R. F. Harrington, "Time-Harmonic Electromagnetic Fields," New York, McGraw-Hill Book Company, 1961.

[37] R. J. Marhefka, personal communication.

[38] R. J. Marhefka, "Numerical Electromagnetic Code - Basic Scattering Code," *Technical Report 712242-15 (713742)*, December 1982.

[39] J. D. Young and R. J. Marhefka, "Bistatic Scattering Signatures of a 90° Dihedral," Bistatic Radar Symposium, Adelphi, Maryland, Sept. 16-18, 1986. memorandum, June 1986.

[40] N. Akhter, J. S. Gwynne, R. J. Marhefka and J. D. Young, "Modeling and Analysis of Polarization Effects in Coherent Radar." *Technical Report 717756-3*, October 1988.

[41] C. S. Lee and S. W. Lee, "Radar Cross Section of an Open-ended Circular Waveguide: Calculation of Second-order Diffraction terms," *Radio Science, volume 22, Number 1, Jan.-Feb. 1987, p. 2-12.*

[42] Ching-Chao Huang, "Ray Analysis of EM Backscatter from a Cavity Configuration." *Ph.D. dissertation*, The Ohio State University, Department of Electrical Engineering, Columbus, Ohio, 1982.

[43] J. D. Young and J. S. Gwynne, "An Evaluation of the Small Dihedral for the Purpose of Radar Backscattering Calibration," Technical Report 717756-2, April 1988. The Ohio State University ElectroScience Laboratory, Department of Electrical Engineering; prepared under contract No. F33615-85-C-1771 for Wright - Patterson Air Force Base.

[44] P. E. Mast and R. G. Kouyoumjian, "On the GTD scattering by a polygonal cylinder," *IEEE Trans. on Antennas and Propagation*, Vol. 24, pp. 94-95, Jan 1976.

Appendix A

Balancing of Fields for Joined Wedges

In this appendix, a detailed mathematical analysis is carried out in order to obtain various diffracted terms which are then used in Section 4 to show continuity of the fields. Reference is made to Figure 27. For diffraction from Q_1 the angles are

$$\phi' = \pi + \epsilon_1 \quad and \quad \phi = \epsilon_2. \tag{393}$$

Thus diffraction from Q_1 is given as

$$D_{s,h}^1 = P_{c,m}(Q_1) = \frac{-e^{-j\pi/1}}{2n\sqrt{2\pi k}} \left[\frac{2n}{\epsilon_2 - \epsilon_1} + \cot\left(\frac{2\pi + \epsilon_1 - \epsilon_2}{2n}\right) \right.$$
$$\left. \mp \left\{ \cot\left(\frac{2\pi + \epsilon_1 + \epsilon_2}{2n}\right) + \frac{2n}{-\epsilon_2 - \epsilon_1} \right\} \right] e^{-jkd}. \tag{394}$$

Since the diffracted field is taken close to the incident shadow boundary, $P_{c,m}(Q_1)$ may be split into a term, $P'_{c,m}(Q_1)$, which is singular at the shadow boundary, and non - singular term that is denoted by $P''_{c,m}(Q_1)$.

$$P'_{c,m}(Q_1) = \frac{-e^{-j\pi/1}}{\sqrt{2\pi k}} \left[\frac{1}{\epsilon_2 - \epsilon_1} \pm \frac{1}{\epsilon_2 + \epsilon_1} \right] e^{-jkd} \tag{395}$$

Noting that $P_{c,m}(Q_1)$ is present only when $\epsilon_2 > 0$

$$P'_{c,m}(Q_1) = \frac{e^{-j\pi/1}}{\sqrt{2\pi k}} \left[\frac{\epsilon_2}{\epsilon_1^2 - \epsilon_2^2} \right] e^{-jkd} \left[1 + sgn(\epsilon_2) \right] \tag{396}$$

and

$$P_{c,m}''(Q_1) = \frac{-e^{-j\pi/4}}{2n\sqrt{2\pi k}}\left[\cot\left(\frac{2\pi + \epsilon_1 - \epsilon_2}{2n}\right)\right.$$
$$\left.\mp\cot\left(\frac{2\pi + \epsilon_1 + \epsilon_2}{2n}\right)\right]e^{-jkd}\frac{1}{2}\left[1 + sgn(\epsilon_2)\right]. \tag{397}$$

The angle parameters for Q_2 are

$$\phi' = -\epsilon_1 \quad and \quad \phi = \pi - \epsilon_2 \tag{398}$$

and the diffraction from Q_2 is

$$D_{s,h}^2 = P_{c,m}(Q_2) = \frac{-e^{-j\pi/4}}{2n\sqrt{2\pi k}}\left[\cot\left(\frac{2\pi - \epsilon_2 + \epsilon_1}{2n}\right) + \frac{2n}{-\epsilon_1 + \epsilon_2}\right.$$
$$\left.\mp\left\{\cot\left(\frac{2\pi - \epsilon_2 - \epsilon_1}{2n}\right) + \frac{2n}{\epsilon_2 + \epsilon_1}\right\}\right]e^{-jkd} \tag{399}$$

Again separating $P_{c,m}(Q_2)$ in to singular and the non-singular parts and noting that $P_{c,m}(Q_2)$ is only present when $\epsilon_1 < 0$.

$$P_{c,m}'(Q_2) = \frac{-e^{-j\pi/4}}{\sqrt{2\pi k}}\left[\frac{1}{\epsilon_2 - \epsilon_1} \mp \frac{1}{\epsilon_1 + \epsilon_2}\right]e^{-jkd}\frac{1}{2}\left[1 - sgn(\epsilon_1)\right] \tag{400}$$

$$= \frac{e^{-j\pi/4}}{\sqrt{2\pi k}}\left[\frac{\frac{\epsilon_1}{2}}{\epsilon_1^2 - \epsilon_2^2}\right]e^{-jkd}\left[1 - sgn(\epsilon_1)\right] \tag{401}$$

$$P_{c,m}''(Q_2) = \frac{-e^{-j\pi/4}}{2n\sqrt{2\pi k}}\left[\cot\left(\frac{2\pi - \epsilon_2 + \epsilon_1}{2n}\right)\right.$$
$$\left.\mp\cot\left(\frac{2\pi - \epsilon_2 - \epsilon_1}{2n}\right)\right]e^{-jkd}\left[\frac{1}{2}\right]\left[1 - sgn(\epsilon_1)\right] \tag{402}$$

The angle parameter for Q_3 are

$$\phi' = \pi/2 + \epsilon_1 \quad and \quad \phi = 3\pi/2 + \epsilon_2 \tag{403}$$

For the single diffracted field from Q_3. Note ONLY the term that is singular for diffraction form Q_3 is shown below. This term is associated with $\pi - (\phi - \phi')$.

$$P_{c,m}'(Q_3) = \frac{-e^{-j\pi/4}}{\sqrt{2\pi k}}\left[\frac{1}{\epsilon_1 - \epsilon_2}\right]e^{jkh(\epsilon_1 - \epsilon_2)}e^{-jkd} \tag{404}$$

173

From Figure 27 and Equation (394), we note that for the diffraction from edge Q_1, the term associated with $\pi - (\phi - \phi')$ blows up. From double diffraction formulation, $\pi - (\phi - \phi')$ is obtained by setting $p = 1$ in Equation (42). Again from Figure 27 and Equation (399), it is noted that for diffraction from edge Q_2 the term associated with $\pi + (\phi - \phi')$ blows up. Note that in the double diffraction formulation, the angles ϕ and ϕ' on the second edge (Q_2) are defined in the reverse to those defined for single diffraction. With this in mind, for double diffraction, $\pi - (\phi - \phi')$ is obtained by setting $q = 1$ in Equation (43). Thus, we expect the double diffraction term obtained by setting $p = 1$ and $q = 1$ in Equation (44) to compensate for the discontinuity and singularities of the single diffracted fields.

For the double diffraction formulation

$$\phi'_1 = (n_1 - 1)\pi - \epsilon_1 \tag{405}$$

and

$$\phi'_2 = (n_2 - 1)\pi + \epsilon_2. \tag{406}$$

Thus

$$\Phi_{p=1} = \pi - [n_1\pi - (n_1 - 1)\pi + \epsilon_1] = -\epsilon_1 \tag{407}$$

$$\Phi_{q=1} = \pi - [n_2\pi - (n_2 - 1)\pi - \epsilon_2] = \epsilon_2 \tag{408}$$

$$a_{p=1} = 2\cos^2[-\epsilon_1/2 - \pi/2] = 2\sin^2(\epsilon_1/2) \tag{409}$$

$$a_{q=1} = 2\cos^2[\epsilon_2/2 - \pi/2] = 2\sin^2(\epsilon_2/2) \tag{410}$$

Using the above equations in Equation (46)

$$P_h(\Phi_{p=1}, \Phi_{q=1}) = -\frac{1}{4\pi j n_1 n_2} \left(\frac{-2n_1}{\epsilon_1} \right) \left(\frac{2n_2}{\epsilon_2} \right)$$
$$\frac{2\sin^2(\epsilon_2/2)F[kd2\sin^2(\epsilon_1/2)] - 2\sin^2(\epsilon_1/2)F[kd2\sin^2(\epsilon_2/2)]}{2\sin^2(\epsilon_1/2) - 2\sin^2(\epsilon_2/2)}$$
$$\left(\frac{e^{-jkd}}{k\sqrt{d}} \right). \tag{411}$$

For small x

$$F[x] \sim \left(\sqrt{\pi x} - 2x \cdot e^{j\pi/1} \right) e^{j(\pi/1 + x)} \tag{412}$$

174

$$F[2kd\sin^2(\epsilon_1/2)] = \left[\sqrt{2\pi kd(\epsilon_1/2)^2} - 4kd(\epsilon_1/2)^2 e^{j\pi/4}\right] e^{j(\pi/4 + 2kd\epsilon_1^2/4)} \qquad (413)$$

$$= \left[\sqrt{\pi kd/2}\,|\epsilon_1| - kd\epsilon_1^2 e^{j\pi/4}\right] e^{j(\pi/4 + 2kd\epsilon_1^2/4)} \qquad (414)$$

$$P_h(\Phi_{p=1}, \Phi_{q\approx1}) = \frac{1}{j\pi\epsilon_1\epsilon_2} \left\{ \frac{\epsilon_2^2/4\left[\sqrt{\pi kd/2}|\epsilon_1| - kd\epsilon_1^2 e^{j\pi/4}\right] e^{j(\pi/4 + 2kd\epsilon_1^2/4)}}{\epsilon_1^2/4 - \epsilon_2^2/4} \right.$$
$$\left. - \frac{\epsilon_1^2/4\left[\sqrt{\pi kd/2}|\epsilon_2| - kd\epsilon_2^2 e^{j\pi/4}\right] e^{j(\pi/4 + 2kd\epsilon_2^2/4)}}{\epsilon_1^2/4 - \epsilon_2^2/4} \right\}$$
$$\left(\frac{e^{-jkd}}{k\sqrt{d}}\right) \qquad (415)$$

neglecting terms of order ϵ_1 and ϵ_2

$$P_h(\Phi_{p=1}, \Phi_{q=1}) = \frac{-e^{-j\pi/4}}{\sqrt{2\pi k}\epsilon_1\epsilon_2} \left[\frac{\epsilon_1^2\epsilon_2 sgn(\epsilon_2) - \epsilon_2^2\epsilon_1 sgn(\epsilon_1)}{\epsilon_1^2 - \epsilon_2^2}\right] e^{-jkd} \qquad (416)$$

$$= \frac{-e^{-j\pi/4}}{\sqrt{2\pi k}} \left[\frac{\epsilon_1 sgn(\epsilon_2) - \epsilon_2 sgn(\epsilon_1)}{\epsilon_1^2 - \epsilon_2^2}\right] e^{-jkd}. \qquad (417)$$

From Equation (45)

$$P_s(\phi_{p=1}, \phi_{q=1}) = \frac{1}{8\pi j n_1^2 n_2^2} \left(\frac{\epsilon_1^2/2}{\epsilon_1^2/4n_1^2}\right) \left(\frac{\epsilon_2^2/2}{\epsilon_2^2/4n_2^2}\right)$$
$$\frac{F[kd\epsilon_1^2/2] - F[kd\epsilon_2^2/2]}{\epsilon_1^2/2 - \epsilon_2^2/2} \left(\frac{e^{-jkd}}{k\sqrt{d}}\right) \qquad (418)$$

Using Equation (414)

$$P_s(\Phi_{p=1}, \Phi_{q=1}) = \frac{1}{2\pi j} \left\{ \frac{\left(\sqrt{\pi kd/2}|\epsilon_1| - kd\epsilon_1^2 e^{j\pi/4}\right) e^{j(\pi/4 + kd\epsilon_1^2/2)}}{\epsilon_1^2/2 - \epsilon_2^2/2} \right.$$
$$\left. - \frac{\left(\sqrt{\pi kd/2}|\epsilon_2| - kd\epsilon_2^2 e^{j\pi/4}\right) e^{j(\pi/4 + kd\epsilon_2^2/2)}}{\epsilon_1^2/2 - \epsilon_2^2/2} \right\} \left(\frac{e^{-jkd}}{k\sqrt{d}}\right) \qquad (419)$$

neglecting terms of order ϵ_1 and ϵ_2

$$P_s(\phi_{p=1}, \phi_{q=1}) = \frac{-e^{-j\pi/4}}{\sqrt{2\pi k}} \left\{ \frac{\epsilon_2 sgn(\epsilon_2) - \epsilon_1 sgn(\epsilon_1)}{\epsilon_1^2 - \epsilon_2^2} \right\} e^{-jkd}$$
$$- \frac{\sqrt{d}}{\pi} e^{-jkd} \qquad (420)$$

Appendix B

Reflection and Transmission of Plane Waves in Planar, Stratified (Multi-Layered) Medium

Details of reflection and transmission of the plane wave in multi-layered medium are presented in [33]. Here a summary of [33] is presented. Suppose a plane wave in free space has oblique incidence on a plane multilayer consisting of N homogeneous isotropic slabs as shown in Figure 116. Let d_n, μ_n, and ϵ represent the thickness, permeability, and permittivity of slab n. The slabs are considered to have infinite width and hight and parallel surfaces, with unbounded free space on both sides of the multilayer. The incident plane wave impinging on the left-hand surface of the multilayer is given, in the TE case (i.e. perpendicular polarization) by

$$E_x^i = E_0 e^{jk_0 y \sin\theta} e^{jk_0 z \cos\theta}, \tag{421}$$

where θ is the angle of incidence, $k_0 = 2\pi/\lambda$, and λ is the free space wavelength. The reflected wave is given by

$$E_x^r = R E_0 e^{jk_0 y \sin\theta} e^{-jk_0 z \cos\theta}, \tag{422}$$

where R is the reflection coefficient of the multilayer. The transmitted plane wave on the right-hand side of the multilayer is represented by

$$E_x^\cdot = E_0 e^{jk_0 y \sin\theta} e^{jk_0 z \cos\theta}, \tag{423}$$
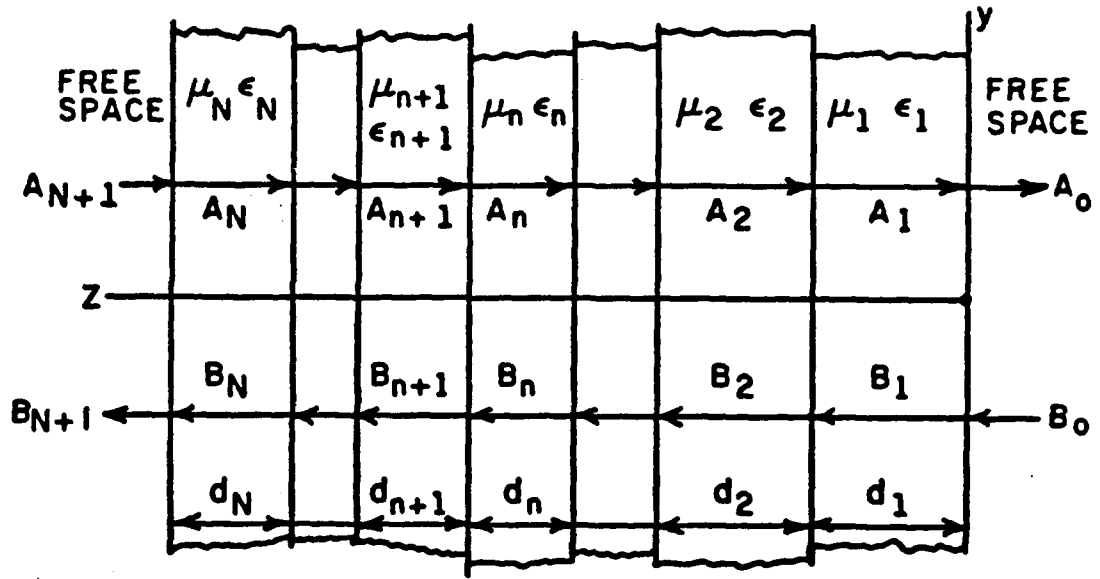
176

Figure 116: A plane multilayer, illustrating the outgoing and the reflected waves in each layer.

where T is the transmission coefficient of the multilayer. The field in each layer can be regarded as an infinite series of the plane waves bouncing back and forth, but it is more convenient (and equally valid) to consider it to be the sum of only two plane waves, one travelling outward and one reflected. In layer n, for example, the field is represented by

$$E_n = \left(A_n e^{\gamma_n z} + B_n e^{-\gamma_n z}\right) e^{jk_0 y \sin\theta}. \tag{424}$$

Similarly, in layer n+1 the electric field intensity is given by

$$E_{n+1} = \left(A_{n+1} e^{\gamma_{n+1} z} + B_{n+1} e^{-\gamma_{n+1} z}\right) e^{jk_0 y \sin\theta}. \tag{425}$$

The boundary between layers n and $n+1$ is located at

$$z_n = d_1 + d_2 + d_3 + + + d_n. \tag{426}$$

By enforcing the boundary conditions on E_x and H_y at $z = z_n$, it can show that

$$\begin{bmatrix} A_{n+1} \\ B_{n+1} \end{bmatrix} = \begin{bmatrix} P_n & Q_n \\ R_n & S_n \end{bmatrix} \begin{bmatrix} A_n \\ B_n \end{bmatrix}, \tag{427}$$

177

where

$$P_n = \frac{1}{2} \left(1 + \frac{\mu_{n+1}\gamma_n}{\mu_n\gamma_{n+1}} \right) e^{(\gamma_n - \gamma_{n+1})z_n}, \tag{428}$$

$$Q_n = \frac{1}{2} \left(1 - \frac{\mu_{n+1}\gamma_n}{\mu_n\gamma_{n+1}} \right) e^{-(\gamma_n + \gamma_{n+1})z_n}, \tag{429}$$

$$R_n = \frac{1}{2} \left(1 - \frac{\mu_{n+1}\gamma_n}{\mu_n\gamma_{n+1}} \right) e^{(\gamma_n + \gamma_{n+1})z_n}, \tag{430}$$

and

$$S_n = \frac{1}{2} \left(1 + \frac{\mu_{n+1}\gamma_n}{\mu_n\gamma_{n+1}} \right) e^{-(\gamma_n - \gamma_{n+1})z_n}. \tag{431}$$

The propagation constant γ_n for layer n will be complex if the medium is dissipative. Both the real and the imaginary parts of γ_n will be positive. If layer n is a lossless medium, γ_n will be purely imaginary. The wave equation is employed to obtain

$$\gamma_n = j\sqrt{\omega^2\mu_n\epsilon_n - k_0^2 \sin^2\theta}. \tag{432}$$

The reflection and transmission coefficient of the multilayer can be calculated in a systematic manner by setting

$$A_0 = 1 \tag{433}$$

and

$$B_0 = 0 \tag{434}$$

and then by using the recursion equations Equation (427) to calculate A_1, B_1, A_2, B_2, ... A_{N+1}, and B_{N+1} in that order.

From Eqs. (421) through (424),

$$E_0 = A_{N+1}, \tag{435}$$

$$R = \frac{B_{N+1}}{A_{N+1}}, \tag{436}$$

and

$$R = \frac{1}{A_{N+1}}. \tag{437}$$

178

In the TE case the constants A_n and B_n represent the electric field intensities of the outgoing and reflected wave in each layer. In the TM case (parallel polarization) the solution proceeds in the same manner. The equations given above apply in both cases but the A_n and B_n represent the magnetic field intensities in the TM case and μ_{n+1} and μ_n must be replaced with ϵ_{n+1} and ϵ_n in Eqs. (428) through (431).

If a perfectly conducting sheet is placed on the right-hand surface of the multilayer (i.e., on the x-y plane), the solution is again given by the equations above with the exception that the transmission coefficient T is not calculated in this case, and Eqs. (433) and (434) are replaced with

$$A_1 = 1 \ and \ B_1 = -1 \ in \ the \ TE \ case \tag{438}$$

and

$$A_1 = 1 \ and \ B_1 = 1 \ in \ the \ TM \ case. \tag{439}$$

Equations (438) and (439) are obtained by forcing the tangential electric field intensity to vanish at the perfectly conducting plane.

In the above equations, the reflection coefficient R is defined as the ratio of the reflected wave amplitude to the incident wave amplitude at the coordinate origin; that is,

$$R = \frac{E_r^r(0,0,0)}{E_r^i(0,0,0)}; \ for \ the \ TE \ case, \tag{440}$$

and

$$R = \frac{H_x^r(0,0,0)}{H_r^i(0,0,0)}; \ for \ the \ TM \ case. \tag{441}$$

Appendix C

Cylinder-Cylinder Junction Edge Normal and Curvature

Consider a "natural" cylinder-cylinder junction shown in Figure 117. The cylinders have radii a_1 and a_2 and make an angle α at the junction of interest. The position vector of cylinder 1 in cylindrical coordinates is

$$\vec{r}_1 = a_1 \left(\cos \phi_1 \hat{x}_1 + \sin \phi_1 \hat{y}_1 \right) + z_1 \hat{z}_1 \tag{442}$$

and of cylinder 2

$$\vec{r}_2 = a_2 \left(\cos \phi_2 \hat{x}_2 + \sin \phi_2 \hat{y}_2 \right) + z_2 \hat{z}_2, \tag{443}$$

where ϕ_1 is measured from x_1-axis and ϕ_2 is measured from the x_2-axis in the $x_1 - y_1$ and $x_2 - y_2$ planes, respectively. The two right handed coordinate systems (x_1, y_1, z_1 and x_2, y_2, z_2) are related so that

$$\hat{x}_2 = -\cos \alpha \hat{x}_1 - \sin \alpha \hat{z}_1, \tag{444}$$

$$\hat{z}_2 = \sin \alpha \hat{x}_1 - \cos \alpha \hat{z}_1 \tag{445}$$

and

$$\hat{y}_2 = \hat{y}_1. \tag{446}$$

Using Equations (444)-(446) in Equation (443)

$$\vec{r}_2 = \left(z_2 \sin \alpha - a_2 \cos \phi_2 \cos \alpha \right) \hat{x}_1 + a_2 \sin \phi_2 \hat{y}_1 - \left(a_2 \cos \phi_2 \sin \alpha + z_2 \cos \alpha \right) \hat{z}_1, \tag{447}$$
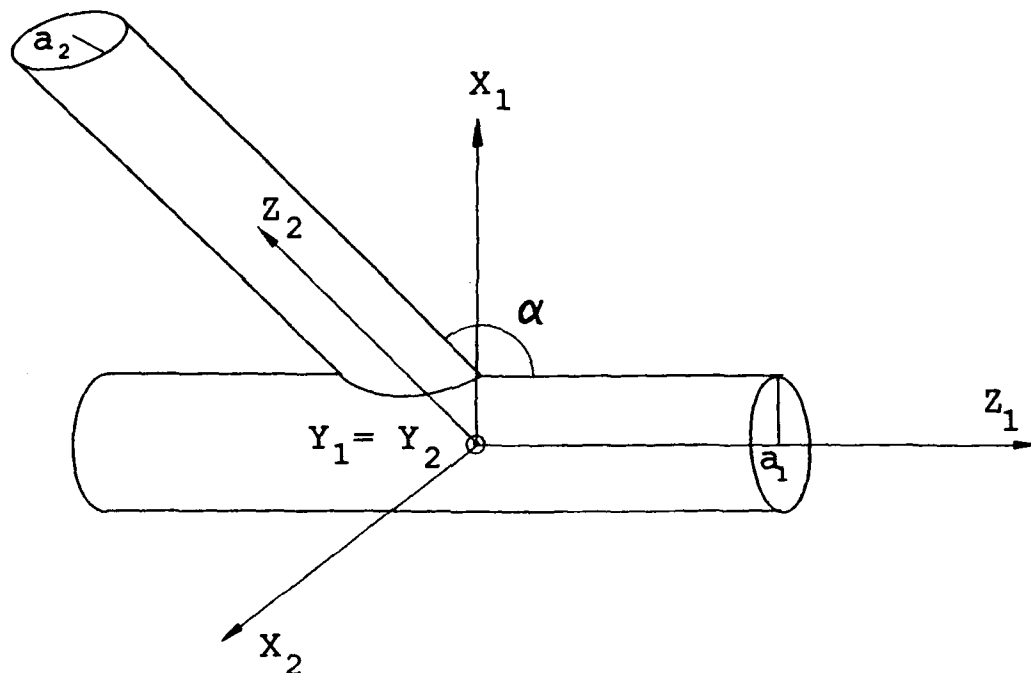
Figure 117: Cylinder-cylinder junction.

and at the junction

$$\vec{r}_1 = \vec{r}_2. \tag{448}$$

Now, the junction may be defined by:

$$a_1 \cos \phi_1 = z_2 \sin \alpha - a_2 \cos \phi_2 \cos \alpha, \tag{449}$$

$$a_1 \sin \phi_1 = a_2 \sin \phi_2 \tag{450}$$

and

$$z_1 = -\left(a_2 \cos \phi_2 \sin \alpha + z_2 \cos \alpha\right). \tag{451}$$

From Equations (449) and (450) one gets

$$0 = z_2^2 \sin^2 \alpha - z_2 a_2 \cos \phi_2 \sin (2\alpha) + a_2^2 \left(\cos^2 \phi_2 \cos^2 \alpha + \sin^2 \phi_2\right) - a_1^2. \tag{452}$$

Solving the above Equation for z_2,

$$z_2 = a_2 \cos \phi_2 \cot \alpha - \frac{1}{\sin \alpha} \sqrt{a_1^2 - a_2^2 \sin^2 \phi_2}. \tag{453}$$

If the radii of the cylinders are the same, $a_1 = a_2 = a$, then Equation (453) may be simplified to

$$z_2 = \frac{a \cos \phi_2}{\sin \alpha} \left[cos\alpha - 1 \right] \tag{454}$$

and

$$\vec{r}_2 = a \left(\cos \phi_2 \hat{x}_2 + \sin \phi_2 \hat{y}_2 \right) + \frac{a \cos \phi_2}{\sin \alpha} \left[cos\alpha - 1 \right] \hat{z}_2. \tag{455}$$

The first and the second derivatives,

$$\vec{r}_2' = \frac{d\vec{r}_2}{d\phi_2} = a \left(- \sin \phi_2 \hat{x}_2 + \cos \phi_2 \hat{y}_2 \right) - \frac{a \sin \phi_2}{\sin \alpha} \left(\cos \alpha - 1 \right) \hat{z}_2 \tag{456}$$

and

$$\vec{r}_2'' = \frac{d^2\vec{r}_2}{d\phi_2} = -a \left(\cos \phi_2 \hat{x}_2 + \sin \phi_2 \hat{y}_2 \right) - \frac{a \cos \phi_2}{\sin \alpha} \left(\cos \alpha - 1 \right) \hat{z}_2, \tag{457}$$

are needed in order to determine the curvature and the edge normal vector.

At the point of diffraction, the junction radius of curvature is

$$\rho \,|_{\phi_2 = 0} = \frac{|\vec{r}|^3}{|\vec{r}' \times \vec{r}''|} = a \cos \left(\frac{\alpha}{2} \right), \tag{458}$$

and the edge normal vector, $\hat{n}_r$, is

$$\hat{n}_r = \frac{-\vec{r}''}{|\vec{r}''|} \,|_{\phi_2 = 0} = \cos \left(\frac{\alpha}{2} \right) \hat{x}_2 - \sin \left(\frac{\alpha}{2} \right) \hat{z}_2 \tag{459}$$

or

$$\hat{n}_c = \cos \left(\frac{\alpha}{2} \right) \hat{x}_1 + \sin \left(\frac{\alpha}{2} \right) \hat{z}_1. \tag{460}$$

182